

**A Study of High Quality, Near-Infrared Spectra of Eight Spectral
Type K Stars: Precise Radial Velocities, Chromospheric
Emission, and Fundamental Stellar Parameters**

by
Ana Marie Larson

B.A., University of Washington, 1970
B.S., (Physics), B.S., (Astronomy) University of Washington, 1990

A Dissertation Submitted in Partial Fulfillment of the
Requirements for the Degree of

DOCTOR OF PHILOSOPHY

in the Department of Physics and Astronomy

We accept this thesis as conforming to the required standard.

*Dr. A. W. Irwin, Supervisor, (Department of Physics & Astronomy, Faculty of
Graduate Studies)*

Dr. D. A. Vandenberg, Co-Supervisor (Department of Physics & Astronomy)

Dr. C. D. Scarfe, Departmental Member (Department of Physics & Astronomy)

Dr. J. B. Tatum, Departmental Member (Department of Physics & Astronomy)

Dr. W. J. Balfour, Outside Member (Department of Chemistry)

Dr. G. W. Marcy, External Examiner (San Francisco State University)

© Ana Marie Larson, 1996, University of Victoria.
*All rights reserved. This thesis may not be reproduced in whole or in part,
by photocopying or other means, without the permission of the author.*

Supervisor: Dr. A. W. Irwin

Abstract

We examine the precise radial velocities and chromospheric emission and derive the fundamental parameters of eight K stars – 36 Ophiuchi A, B (K0 V, K1 V), 61 Cygni A, B (K5 V, K7 V), β Geminorum (K0 IIIb), δ Sagittarii (K2.5 IIIa), α Tauri (K5 III), and ϵ Pegasi (K2 Ib) – through analyses of high quality ($S/N > 1000$) near-infrared (864-878 nm) spectra. The spectra were obtained as part of the hydrogen fluoride precise ($\approx 15 - 30 \text{ m s}^{-1}$) radial velocity (RV) program at the Canada-France-Hawaii 3.6-m telescope (1981-1992) and the Dominion Astrophysical Observatory 1.22-m telescope (1991-1995). We define the $\Delta EW_{866.2}$ index used to quantify changes in the core flux of the Ca II 866.214 nm line and show the index is a sensitive measure of changes in chromospheric emission. We compare the “reference” spectrum for each star with synthetic spectra of the 864.7-867.7 nm region and derive the fundamental parameters: effective temperature (T_{eff}), surface gravity (g in cm s^{-2}), metallicity ($[M/H]$), and microturbulence (ξ). We describe an efficient, time-saving method which identifies and eliminates insignificant lines. Through our comparisons of the narrow spectral region for these “well-known” stars and through our development of a rapid synthesis method, we demonstrate a solid foundation for a broader, more comprehensive study of this region of the H-R diagram.

The nearly identical stars 36 Oph A and B have dissimilar chromospheric activity. For these stars, we derived $T_{eff} = 5125 \text{ K}$, $\log g = 4.67$, $[M/H] = -0.25$, and $\xi = 1.4 \text{ km s}^{-1}$, in excellent agreement with relationships

predicted by stellar interior models for $\mathcal{M}/\mathcal{M}_\odot \approx 0.75$ and $[\text{Fe}/\text{H}] = -0.3$. For 61 Cyg A, we detect a rotation period of 36.2 days in the $\Delta EW_{866.2}$ index and of 37.8 days in the radial velocities, implying that active regions are spatially and temporally coherent over long time scales for this star. For 61 Cyg A, we derived $T_{\text{eff}} = 4545$ K, $\log g = 4.55$, $[\text{M}/\text{H}] = -0.40$, and $\xi = 1.5$ km s⁻¹; for 61 Cyg B, $T_{\text{eff}} = 4150$ K, $\log g = 4.55$, $[\text{M}/\text{H}] = -0.40$, and $\xi = 0.7$ km s⁻¹. These parameters are in excellent agreement with relationships predicted by stellar interior models for $[\text{Fe}/\text{H}] = -0.4$ and $\mathcal{M}/\mathcal{M}_\odot \approx 0.65$ for 61 Cyg A, and $\mathcal{M}/\mathcal{M}_\odot \approx 0.55$ for 61 Cyg B.

Low-amplitude RV variability is a ubiquitous characteristic of the K giants. For β Gem, we find similar RV ($K = 46.23 \pm 3.9$ m s⁻¹, $P = 584.65 \pm 3.3$ dy) and $\Delta EW_{866.2}$ index ($K = 0.583 \pm 1.9$ pm, $P = 587.7 \pm 12$ dy) periods. If due to rotation modulation of some surface feature, this period is inconsistent with the most reliable $v \sin i$ value for this star. We detect a long-term (> 12 yr) change in the $\Delta EW_{866.2}$ index for this star, reminiscent of a solar-type magnetic cycle. For δ Sgr, we find significant long-term trends in the radial velocities and $\Delta EW_{866.2}$ index, and significant, but aliased, RV periods at 1.98 days ($K = 82.1 \pm 9.1$ m s⁻¹) and 293 days ($K = 68.8 \pm 9.8$ m s⁻¹). α Tauri has a 647.93-dy period ($K = 114.9 \pm 10.6$ m s⁻¹) in the radial velocities, but *no* corresponding period in the $\Delta EW_{866.2}$ index. From 1.22-m telescope observations, we find a 1.8358-dy RV period ($K = 32.0 \pm 5.0$ m s⁻¹) consistent with theoretical granulation-driven acoustic modes or a fundamental overtone ($n \approx 4$).

The supergiant ϵ Peg resembles a semi-regular RV variable. We find multiple RV periods (not aliases) of 65.2 days ($K = 415.8 \pm 59.0$ m s⁻¹), 46.3

days ($K = 559.1 \pm 57.0 \text{ m s}^{-1}$), perhaps both fundamental overtones, and 10.7 days ($K = 410.3 \pm 66.0 \text{ m s}^{-1}$), perhaps related to solar-type spicules. The 10.7-dy period is present in the $\Delta EW_{868.2}$ index for this star.

Examiners:

Dr. A. W. Irwin, Supervisor (Department of Physics & Astronomy, Faculty of Graduate Studies)

Dr. D. A. Vandenberg, Co-Supervisor (Department of Physics & Astronomy)

Dr. C. D. Scarfe, Departmental Member (Department of Physics & Astronomy)

Dr. J. B. Tatum, Departmental Member (Department of Physics & Astronomy)

Dr. W. J. Balfour, Outside Member (Department of Chemistry)

Dr. G. W. Marcy, External Examiner (San Francisco State University)

Contents

Abstract	ii
Contents	v
List of Tables	vii
List of Figures	ix
Acknowledgements	xii
Dedication	xiv
1 Introduction	1
2 PRV, $\Delta EW_{868.2}$, $\Delta(R - I)$	10
2.1 Introduction to the PRV technique	12
2.1.1 Highlights of the HF technique at the DAO	16
2.1.2 Definition of the $\Delta EW_{868.2}$ index	21
2.2 Results and Discussion	25
2.2.1 The K Dwarfs	25
2.2.2 The K Giants	45
2.2.3 The K Supergiant	97
3 Spectrum Synthesis	108
3.1 Introduction to Spectrum Synthesis	108
3.1.1 Historical overview	108
3.1.2 A general description of spectrum synthesis	110
3.1.3 A description of SSynth	113

3.2	Procedures	117
3.2.1	Pre-SSynth line list processing: description of the work	118
3.2.2	Pre-SSynth line list processing: treatment of the line haze	119
3.2.3	Post-SSynth: solar comparison	132
3.2.4	Post-SSynth: stellar comparisons	152
3.3	Gauging the Atmospheric Parameters	156
3.4	Results and Discussion	168
3.4.1	The K Dwarfs	178
3.4.2	The K Giants	185
3.4.3	The K Supergiant	190
4	Summary and Future Directions	192
4.1	The K Dwarfs	192
4.2	The K Giants and Supergiant	194
4.3	Spectrum Synthesis	200
	Bibliography	202
	A Tables of Data	214
	B Derivatives For $W'_0(\chi)$ Coefficients	236
	C Solar Intensity Atlas vs. Synthetic Spectrum	241
	D Pre-SSynth Manual Pages	249

List of Tables

1.1	The stellar sample	3
1.2	Ranges for published global parameters for stellar sample * . . .	6
1.3	Published global parameters for the stellar sample	7
2.1	61 Cygni A: periodic solution for $\Delta EW_{866.2}$ (1981 - 1992) . . .	34
2.2	61 Cygni A: periodic solution for $\langle S \rangle$ index (1967 - 1977) . . .	39
2.3	β Geminorum: periodic solution for relative radial velocities . . .	50
2.4	β Geminorum: quadratic plus periodic solution for $\Delta EW_{866.2}$. . .	52
2.5	β Geminorum: stellar properties needed to derive rotation period	59
2.6	δ Sagittarii: CFHT data linear trends and F -test results . . .	66
2.7	δ Sagittarii: relative radial velocity sinusoidal solutions	71
2.8	δ Sagittarii: stellar properties needed to derive fundamental and rotation periods	74
2.9	α Tauri: long-term radial velocity periodic solution	84
2.10	α Tauri: stellar properties needed to derive fundamental and rotation periods	85
2.11	α Tauri: short-term radial velocity periodic solution	87
2.12	ϵ Pegasi: radial velocity multi-periodic solutions	104
2.13	ϵ Pegasi: stellar properties needed to derive fundamental and rotation periods	106
3.1	Approximate execution times for the programs associated with a spectrum synthesis	129
3.2	Derived global parameters for the stellar sample	179
3.3	Published vs. derived effective temperature and surface grav- ity values	180
3.4	Published vs. derived metallicity and microturbulence values . . .	181

4.1	Summary of K giant radial velocity data and detected periods	197
A.1	δ Cygni A: $\Delta EW_{868.2}$ index data	217
A.2	β Geminorum: CFHT radial velocity and equivalent width data	218
A.3	β Geminorum: DAO radial velocity data	220
A.4	δ Sagittarii: CFHT radial velocity and equivalent width data .	221
A.5	δ Sagittarii: DAO radial velocity data	222
A.6	α Tauri: CFHT radial velocity and equivalent width data . . .	223
A.7	α Tauri: CFHT 1981 time series radial velocity and equivalent width data	226
A.8	α Tauri: DAO radial velocity data	231
A.9	α Tauri: DAO 1992 time series radial velocity data	232
A.10	ϵ Pegasi: CFHT radial velocity and equivalent width data . .	233
A.11	ϵ Pegasi: DAO radial velocity data	235

List of Figures

2.1	α Arietis: CFHT-DAO relative radial velocities	20
2.2	61 Cygni A: difference spectra defining $\Delta EW_{866.2}$ index	23
2.3	α Hydrae: $\Delta EW_{866.2}$ index vs. time	24
2.4	36 Ophiuchi A: CFHT data vs. time	28
2.5	36 Ophiuchi B: CFHT data vs. time	29
2.6	61 Cygni A: CFHT data vs. time	32
2.7	61 Cygni A: $\Delta EW_{866.2}$ phased on rotation period	35
2.8	61 Cygni A: weighted periodogram for $\Delta EW_{866.2}$ index	37
2.9	61 Cygni A: weighted periodogram for relative radial velocities	41
2.10	61 Cygni B: CFHT data vs. time	43
2.11	Weighted periodograms for 61 Cygni B CFHT data	44
2.12	β Geminorum: CFHT relative radial velocity data with model	48
2.13	β Geminorum: DAO relative radial velocity data with model	49
2.14	β Geminorum: relative radial velocities weighted periodograms	51
2.15	β Geminorum: $\Delta EW_{866.2}$ vs. time	53
2.16	β Geminorum: $\Delta EW_{866.2}$ weighted periodogram	56
2.17	β Geminorum: $\Delta EW_{866.2}$ data phased on 588-dy period	57
2.18	δ Sagittarii: CFHT data vs. time	64
2.19	δ Sagittarii: DAO radial velocity data vs. time	65
2.20	δ Sagittarii: relative radial velocities correlated periodogram	69
2.21	δ Sagittarii: radial velocities folded on aliased periods	72
2.22	α Tauri: CFHT data vs. time	77
2.23	α Tauri: 1981 CFHT time series	78
2.24	α Tauri: DAO radial velocity data vs. time	79
2.25	α Tauri: low-frequency, weighted periodograms	82
2.26	α Tauri: radial velocity data phased on 647.93-dy period	83

2.27	α Tauri: high-frequency weighted periodogram for 1992 DAO radial velocity time series	88
2.28	α Tauri: phase diagram of DAO radial velocity time series . .	89
2.29	α Tauri: theoretical radial pulsation periods	92
2.30	α Tauri: CFHT radial velocity and $\Delta EW_{866.2}$ time series with 1.84-dy model	94
2.31	α Tauri: weighted periodograms for CFHT time series data . .	96
2.32	ϵ Pegasi: CFHT data vs. time	98
2.33	ϵ Pegasi: DAO radial velocity data vs. time	99
2.34	ϵ Pegasi: low-frequency weighted periodograms for CFHT data	101
2.35	ϵ Pegasi: mid-frequency weighted periodograms for CFHT data	102
3.1	Scaled vs. actual atmospheres	116
3.2	Cumulative line blocking error vs. equivalent width	124
3.3	Fraction of retained lines for specified line-blocking errors . . .	127
3.4	Spectral comparison showing line-blocking error	130
3.5	Comparison of Fe I gf -values	139
3.6	Comparison of the calculated vs. observed solar intensity spectrum 864.7 - 867.7 nm	142
3.7	DAO and Kitt Peak solar flux comparison	146
3.8	CFHT and Kitt Peak solar flux comparison	148
3.9	β Geminorum: CFHT vs. DAO spectra 864.7 - 867.7 nm . . .	151
3.10	Synthetic flux spectrum vs. DAO solar spectrum	153
3.11	Synthetic flux spectrum vs. CFHT solar spectrum	154
3.12	T_{eff} sensitivity of Ti I 867.537 nm line	159
3.13	Line-depth ratio Ti I 867.537 : Fe I 867.474 nm	160
3.14	The Ca II 866.2 nm line broadening	162
3.15	Equivalent width of Ca II 866.2 nm line vs. $\log g$	163
3.16	Abundance sensitivity of two Fe I lines	164
3.17	Line depth vs. abundances for three Fe I lines	165
3.18	36 Ophiuchi A: synthetic vs. observed spectra	170
3.19	36 Ophiuchi B: synthetic vs. observed spectra	171
3.20	61 Cygni A: synthetic vs. observed spectra	172
3.21	61 Cygni B: synthetic vs. observed spectra	173
3.22	β Geminorum: synthetic vs. observed spectra	174
3.23	δ Sagittarii: synthetic vs. observed spectra	175
3.24	α Tauri: synthetic vs. observed spectra	176

3.25 ϵ Pegasi: synthetic vs. observed spectra	177
3.26 Evolutionary tracks for 36 Ophiuchi and 61 Cygni	183
C.1 Solar central intensity spectrum vs. synthetic intensity spectrum (864-866 nm)	242
C.2 Solar central intensity spectrum vs. synthetic intensity spectrum (866-868 nm)	243
C.3 Solar central intensity spectrum vs. synthetic intensity spectrum (868-870 nm)	244
C.4 Solar central intensity spectrum vs. synthetic intensity spectrum (870-872 nm)	245
C.5 Solar central intensity spectrum vs. synthetic intensity spectrum (872-874 nm)	246
C.6 Solar central intensity spectrum vs. synthetic intensity spectrum (874-876 nm)	247
C.7 Solar central intensity spectrum vs. synthetic intensity spectrum (876-878 nm)	248

Acknowledgements

This research has made use of data obtained from the Canada France Hawaii Telescope (CFHT), which is operated by the National Research Council of Canada, the Centre National de la Recherche Scientifique of France and the University of Hawaii; and of data obtained at the Dominion Astrophysical Observatory, Herzberg Institute of Astrophysics, National Research Council of Canada. This research has made use of the SIMBAD database, operated at CDS, Strasbourg, France.

I thank the University of Victoria for four years of support through a University of Victoria Fellowship and the R. M. Petrie Memorial Fellowship. I also thank Zonta International for choosing me as one of the International Amelia Earhart Fellows and the local club for their support.

I thank my supervisor, Dr. Alan Irwin, for an unlimited supply of ideas and conversations, and the necessary FORTRAN schooling; his original research topic grew to encompass more than one could have ever anticipated. I also thank him for his patience in his continuous, and often exasperating, push to help me achieve a higher level of excellence. I thank Dr. Don Vandenberg for convincing me to come to the University of Victoria in the first place and for his continued inspirational, academic, and financial support.

I thank Dr. Stephenson Yang for discussions regarding instrumentation and reduction procedures (without which part of this thesis could not have been written), for not allowing any HF to leak at the DAO, and for his role model as an observer. I thank Dr. Gordon Walker at UBC for his frequent encouraging words and publishing support.

There were a number of meticulous observers involved over the 12 years of the HF program at the CFHT and the 4 years at the DAO. Principal observers at the CFHT were Gordon Walker, Stephenson Yang, and Bruce Campbell. Alan Irwin and Bruce Campbell obtained the 1981 time series data for α Tauri. The principal observers at the DAO were Stephenson Yang, myself, and Andrew Walker.

To Russ Robb, thanks for the '60s comradeship, the teaching leverage, and other opportunities you gave me. To Dave Balam, thanks for the reality checks. To the other graduate students, thanks for the many lunchtime conversations, often the highlight of each day.

My family hung in there many times when life got crazy, and at other times added to the insanity by providing unexpected but ultimately beneficial distractions. My heartfelt thanks goes to daughter Kirstin Pearl, son Tor Elof, (mother's little helpers), and husband Tom "what-a-drag-it-is-getting-old" Larson. Your unfailing love and support made it all worthwhile (most of the time).

I would like to thank the people of Canada and the city of Victoria for making me and my family feel perfectly at home in this magnificent country. Our only regret from our six years of living here is that we must now leave and may only be back from time to time.

DEDICATION

To my mother, Dorothy Hene Cook Munn, who is not only my mentor and child-rearing guidance counselor but also my very best friend – my goal is to someday become as crazy as she is; and in memory of my father who was always so proud of everything his children accomplished.

Chapter 1

Introduction

The spectroscopic class K contains some of the best known and most studied stars in the sky. For example, the large proper motion of the 61 Cygni system has been known since the early 19th century. Perhaps the most famous of the K dwarfs, 61 Cygni was the first stellar system to have its trigonometric parallax measured (Bessel in 1838). This measurement laid to rest the debate regarding the magnitude of stellar distances and silenced forever geocentric-universe believers. The orange K giants are some of the brightest stars in the sky: Arcturus, Aldebaran, Pollux, Dubhe. As their color implies, these stars fill an intermediate position in the Hertzsprung-Russell Diagram between the yellow Cepheid instability strip and the red long-period variables.

This spectroscopic class also contains stars whose fundamental characteristics are the most difficult to determine. The range in effective temperatures is about 1200 K. The absolute magnitudes of the K stars range from around +7 to -7; the stellar masses, from around 0.5 to 10 times solar (or more). The stellar radii may be 0.2 or 400 times the Sun's radius. The evolutionary tracks of A, F, G, and K stars almost converge at the red-giant branch

(hydrogen shell-burning stars). Clump giants (stars burning helium in their cores) and second ascenders (hydrogen and helium shell-burning stars) are interspersed with the first ascending red giants. The outer atmospheres of these giants also differ: some show evidence of a hot chromosphere, others evidence of a cool stellar wind (mass loss), others show a blend of the two. The K stars form an enigmatic group with members in various evolutionary states.

The spectral type K stars form nearly half of the sample of 50 stars monitored as part of the HF precise radial velocity program at the CFHT and DAO (Campbell and Walker, 1979; Campbell et al., 1986; Campbell et al., 1988; Yang et al., 1993). These spectra cover the approximate range 864 - 878 nm and include the high-quality stellar “reference” spectra which are uncontaminated by the HF absorption band. The reference spectra have a typical signal-to-noise ratio per pixel in the continuum of 1800 for CFHT observations and 1200 for DAO observations. (“Pixel” is the standard abbreviation for picture element of a CCD or charge coupled device.) The resolving power, $\lambda/\delta\lambda$, is about 33,000 at 870 nm. From the spectral type K subsample, I have selected eight stars for further study in this thesis; they are listed in Table 1.1. They were selected to give a two-dimensional aspect to the radial velocity and spectroscopic research discussed here as they encompass a broad range in effective temperature and surface gravity.

The objective of the HF precise radial velocity (PRV) program at the Canada-France-Hawaii 3.6-m telescope (CFHT) was to detect planets orbiting solar-type stars. The stars, G and K dwarfs and subgiants, were sampled optimally for the detection of long-term planetary periods, $\sim 2 - 12$ yr, but

Table 1.1: The stellar sample

HR	HD	Name	SpT	RA (2000) Dec	
1475	029139	α Tauri	K5 III	4 ^h 35 ^m 55 ^s .2	+16°30'33"
2990	062509	β Geminorum	K0 III	7 ^h 45 ^m 18 ^s .9	+28°01'34"
6401	155885	36 Ophiuchi B	K1 V	17 ^h 12 ^m 16 ^s .2	-26°31'52"
6402	155886	36 Ophiuchi A	K0 V	17 ^h 12 ^m 16 ^s .2	-26°31'47"
6859	168454	δ Sagittarii	K2.5IIIa	18 ^h 20 ^m 59 ^s .7	-29°49'41"
8085	201091	61 Cygni A	K5 V	21 ^h 06 ^m 36 ^s .8	+38°42'04"
8086	201092	61 Cygni B	K7 V	21 ^h 06 ^m 54 ^s .6	+38°44'44"
8308	206778	ϵ Pegasi	K2 Ib	21 ^h 44 ^m 11 ^s .2	+ 9°52'30"

Spectral types from Garrison and Beattie (1992)

not for periods shorter than one year. Fortunately, K giants and a supergiant were also included in the program; while the dwarfs and subgiants in the program all proved remarkably stable, all of the giants and the supergiant were found to be variable, with RV variability ranging between 30 to 500 m s⁻¹ for the giants, and ~ 1000 m s⁻¹ for the supergiant. The HF technique commenced at the Dominion Astrophysical Observatory (DAO) 1.22-m telescope in 1991 and expanded the monitoring of the evolved stars. The long-term periods seen in the evolved stars may be due to rotation modulation of surface features analogous to sunspots but much larger in size and more extensive in coverage; to nonradial gravity or g modes; to global small-amplitude r modes (Wolff, 1996); or to orbiting planets. The short-term periods may be due to radial or nonradial oscillations. As predicted by Unno et al. (1979), "...it will become more difficult to find a star without nonradial oscillations

than to find a star with nonradial oscillations (as nonradial oscillations are indeed rich in the variety of the physical properties.” We are able to place some constraints on these possible underlying mechanism(s) by analyzing the $\Delta EW_{866.2}$ and $\Delta(R - I)$ index data for each star.

The chronological development of the analyses of these stars logically led to the two, semi-independent parts to this thesis. The PRV, $\Delta EW_{866.2}$, and $\Delta(R - I)$ results, obtained from an analysis of the full $\sim 864 - 878$ nm interval, for the individual stars are discussed first in Chapter 2. The discussion of the K dwarfs in the selected sample emphasizes the chromospheric activity seen in these stars and relates the $\Delta EW_{866.2}$ index to the S index from the Mount Wilson H and K survey (see discussion in Sec. 2.2.1). We search for periods of less than 40 days [the lower period cut-off used in the Walker et al. (1995) analysis] in the RV data, periods which may correspond to rotation in these stars. The discussion for the K giants emphasizes their status as a newly recognized class of radial velocity variable. Starting with the prominent paper by Walker et al. (1989), and the discussions on α Bootis (Irwin et al., 1989), γ Cephei (Walker et al., 1992), β Geminorum (Larson et al., 1993a), δ Sagittarii (Larson et al., 1996), and α Tauri (the short-term periods presented in this thesis), our work has been at the forefront of the discoveries. Though the analysis of our $\Delta EW_{866.2}$ index, our work has added stars to the list of giants which may have active regions and activity cycles similar to those of the Sun. It appears that the foundation laid by the RV group at the University of Victoria and the University of British Columbia for field giant stars has set the stage for the discovery of K giant variables in clusters, starting with the announcement by Edmonds and Gilliland (1996)

of low-amplitude RV variables in 47 Tucanae. Our analysis of the data for ϵ Pegasi indicates this supergiant is most likely a semi-regular variable, as was suggested in Walker et al. (1989). This star is one of the few where periods are found in the $\Delta EW_{866.2}$ and $\Delta(R - I)$ indices which definitely correspond to those found in the RV data.

For the second part of this thesis, Chapter 3, I extract 3 nm from each reference spectrum (the spectrum having no HF fiducial lines) centered on the Ca II 866.2 nm line and discuss the results of the comprehensive spectrum synthesis. Spectrum synthesis is the calculation of a spectrum using the fundamental physics of stellar atmospheres and line formation. There has been renewed interest in the use of spectrum synthesis, a revival due in large part to new opacity routines, the availability of extensive new line data lists, and recent exchanges of research ideas between laboratory spectroscopists and astrophysicists. We have developed an extensive suite of spectrum synthesis programs, SSynth, on line at the University of Victoria, the culmination of doctoral (1978) and post-doctoral work of Alan Irwin. The research discussed here involves the work I did to update and expand the original programs to make them more efficient, accurate, and reliable.

The stars discussed here are bright and nearby and have been the targets of numerous photometric and spectroscopic studies, with the sole exception of δ Sagittarii. There are numerous references in the literature relating to their fundamental or global properties: effective temperature (T_{eff}), surface gravity (g), metallicity¹ ($[M/H]$), and photospheric microturbulence (ξ). The

¹Astrophysically, $[M/H]$ represents the number abundance ratio of all elements heavier than helium to hydrogen; we use the standard notation, $[M/H] \equiv \log(M/H)_{star} -$

Table 1.2: Ranges for published global parameters for stellar sample *

Name	T_{eff} (K)		$\log g$ (cm s^{-2})		[Fe/H]‡	
	low	high	low	high	low	high
36 Oph B	5090	5140	4.60	4.60	-0.39	-0.09
36 Oph A	5090	5090	4.60	4.60	-0.30	-0.01
61 Cyg A	4310	4380	4.50	4.70	-0.10	+0.00
61 Cyg B	3650	4000	4.50	4.80	-0.65	+0.00
β Gem	4030	5040	2.20	3.12	-0.51	+0.16
δ Sgr †						
α Tau	3730	4130	1.01	1.5	-0.33	+0.00
ϵ Peg	3820	4380	0.75	1.25	-0.25	-0.02

* All values are from the [Fe/H] catalogue of Cayrel de Strobel et al. (1992). This catalogue gives a complete bibliography for these values.

‡ [Fe/H] $\equiv \log(\text{Fe}/\text{H})_{star} - \log(\text{Fe}/\text{H})_{Sun}$

† No values given in the Cayrel de Strobel et al. (1992) catalogue.

Table 1.3: Published global parameters for the stellar sample

Name	T_{eff} (K)	$\log g$ (cm s^{-2})	[Fe/H]	ξ (km s^{-1})	$v \sin i$ (km s^{-1})	ζ_{RT} (km s^{-1})
DWARFS						
Sun	5777 k	4.44 k	$\equiv 0.0$	1.5 k	2.0	1.0 tt
36 Oph B	5100 b	4.60 cs	-0.16 cs	1.0 cpl	1.8 v	1.5 g2
36 Oph A	5125 b	4.60 cs	-0.15 cs	1.0 cpl	2.0 v	1.5 g2
61 Cyg A	4543 b	4.50 cs	-0.05 cs	1.0 a	1.0 v	1.5 g2
61 Cyg B	4332 b	4.60 cs	-0.19 cs	1.0 a	0.7 v	1.5 g2
GIANTS						
β Gem	4850 m	2.96 m	-0.07 m	1.9 m	2.5 g1	3.5 g1
δ Sgr	4180 m	2.23 m	-0.01 m	2.7 m	2.7 li	5.0 g2
α Tau	3910 m	1.59 m	-0.34 m	2.1 m	2.7 sd	3.6 t
SUPERGIANT						
ϵ Peg	4350 sl	1.00 sl	-0.03 sl	2.5 sl	6.5 gt	9.0 gt

References:

a: Adopted value.

b: Bohlender et al. (1992)

cs: Cayrel de Strobel et al. (1992)

cpl: Cayrel de Strobel, Perrin, and Lebreton (1989)

g1: Gray (1982)

g2: Gray (1992)

gt: Gray and Toner (1986)

k: Kurucz (1993a)

li: Larson et al. (1996)

m: McWilliam (1990)

sl: Smith and Lambert (1987)

tt: Topka and Title (1991)

t: Tsuji (1986)

v: ($2\pi R/P$) from Vaughan et al. (1981)

catalogue by Cayrel de Strobel et al. (1992) is a good example of one compilation of multiple references, and Table 1.2 lists the range of values noted for the effective temperatures, surface gravities, and metallicities for most of our stellar sample (the Cayrel de Strobel et al. catalogue does not list microturbulence values). The ranges in values for these parameters are especially large for the evolved stars. Table 1.3 lists *representative* values reported in recent literature. The values from the Cayrel de Strobel et al. catalogue listed in Table 1.3 are averages. I have chosen sources other than the Cayrel de Strobel et al. catalogue where I feel a more uniform or a more reliable determination has been made; for example, where possible, the Bohlender et al. (1992) paper selected effective temperatures derived from the infrared-flux method. No further attempt has been made to judge the quality of these values. Published values for $v \sin i$ (projected rotation velocity) and radial-tangential macroturbulence, ζ_{RT} , are included with the fundamental parameters. In Sec. 3.4 I compare the results from this thesis with the values given in Table 1.3.

Given the large range in values for many of the fundamental parameters listed in Tables 1.2 and 1.3, one finds it difficult to build a coherent and comprehensive understanding of the spectral type K stars. In this thesis, we circumvent this problem by deriving the fundamental stellar parameters under a comprehensive spectrum synthesis of the pressure-broadened wings of the Ca II 866.2 nm line and adjacent spectral region. The analysis included in this thesis offers a number of improvements over previous research. Most importantly, we work with high quality spectra having a signal-to-noise ratio $\log(M/H)_{Sun}$, and assume $[M/H]$ follows $[Fe/H]$.

of up to 2000, about 10 – 15 times that of any previous work. We examine stars with a range in subclasses, 0-7, of spectral type K, and luminosity classes V-I in a consistent manner. We use the most complete atomic and diatomic line lists available to date and explicitly include the effect that literally thousands of extremely weak lines (known collectively as line haze) have on accurate determination of the pseudocontinuum. In addition, we explicitly include spectrograph light scattering in our treatment of the instrumental profile. We also explicitly test the accuracy of our adopted profile using solar observations.

Finally, in Chapter 4, I summarize the analyses of the data and discuss the opportunities for future research established as a result of the foundation laid here.

Chapter 2

PRV, $\Delta EW_{866.2}$, $\Delta(R - I)$

“The determination of periods from observations ... made at known times is difficult to describe; in many ways it is an art, acquired by practice, and varying with the peculiarities of individual stars and the distribution of observations.”

—Payne-Gaposchkin and Gaposchkin (1938)

It is perhaps an understatement to say that the ability to measure precisely (i.e., to $\leq 50 \text{ m s}^{-1}$) the changes in the relative radial velocities of the stars heralded a new dawn in stellar research. Following the introductory paper of Campbell and Walker (1979), which discusses the preliminary tests to measure radial velocities using an absorption cell and hydrogen fluoride lines as fiducial wavelengths, measurements went from a precision of $\sim 150 \text{ m s}^{-1}$ to under 20 m s^{-1} . The motivation behind the development of the HF technique was to detect sub-stellar companions: brown dwarfs and Jupiter-like planets. Although the observations at the CFHT using the HF technique did not result in any confirmed planets (Walker et al., 1995), the technique spawned the development of the iodine cell and the use of I_2 lines as fiducial wavelengths [see discussion in Butler et al. (1996)]. With the use of an echelle grating for much higher resolution, a much broader wavelength region, and

an accurate modeling of the instrumental profile, the I_2 absorption-cell technique typically reaches a precision of 3 m s^{-1} or better (Butler et al., 1996). Since fainter stars can be observed with the I_2 cell, the stellar sample has increased from around 30 to over 600. There are now a number of groups capable of achieving 15 m s^{-1} or better radial velocity (RV) precision (see Session 70 of the Bulletin of the American Astronomical Society, 1996, beginning on p. 1379), and RV variability indicative of a planetary companion has been detected in at least five solar-type stars.

Serendipitously, the runs at the CFHT also included observations of a number of cool giants, observations which filled the time when there were no program dwarf stars to be observed. All of these so-called radial velocity standards were found to be variable, with amplitudes ranging from 30 m s^{-1} to over 500 m s^{-1} . Although the low-amplitude radial velocity variability of Arcturus was discovered in the mid-1980's (Irwin et al., 1989), the paper by Walker et al. (1989) introduced this "new class of radial-velocity variable" by extending the sample to five more K giants and a supergiant. The HF program was installed at the DAO in the summer of 1991 with the stated purpose of expanding the monitoring of the bright giants of spectral types G, K, and M (Yang et al., 1993). Over 30 giants and 6 supergiants have been observed with the 1.22-m telescope at the DAO.

This chapter discusses the differential radial velocities and the changes in the chromospheric emission and photospheric temperature of four dwarfs (two binaries), three giants, and one supergiant. As mentioned in the introduction to this thesis, the stars were chosen to give a two-dimensional sample within the K spectral type and luminosity classes V-I in order to test the accu-

racy of the spectrum synthesis program for a range of effective temperatures and surface gravities. Section 2.1 of this chapter gives an overview of the HF technique, particularly the method used at the DAO, and summarizes the reduction process. This section also discusses the quantification of the $\Delta EW_{868.2}$ index used to measure the changes in the chromospheric emission of the stars. Section 2.2 discusses the PRV, $\Delta EW_{868.2}$, and $\Delta(R - I)$ results for the individual stars.

2.1 Introduction to the PRV technique

Campbell and Walker (1979), Campbell et al. (1986, the most comprehensive reference), and Campbell et al. (1988) describe the HF absorption-cell technique and the associated reduction procedure for obtaining precise radial velocities. In this section, we summarize, from these references, the description of the methods used to determine the internal and external errors. We also summarize here the techniques used to identify significant periodicity in the data for each star. The HF program was installed at the DAO in the summer of 1991; highlights of that program and a summary of the reduction procedures are discussed in 2.1.1. Pertinent details for the CFHT and DAO observations are included with the discussions of the individual stars. Bohlender et al. (1992) give the derivation of the ΔT_{eff} and $\Delta(R - I)$ indices¹

¹The $\Delta(R - I)$ and ΔT_{eff} indices are different measures of the same quantity: the relative changes in some of the temperature-sensitive lines contained in each spectrum. Thus, the $\Delta(R - I)$ and ΔT_{eff} indices are correlated (as expected). Only the relative changes in $R - I$ are discussed here since the colors of a star are generally better known than the effective temperature thus providing a better calibration of the temperature sensitive lines.

and the methods used to determine their internal errors. The derivation of the $\Delta EW_{868.2}$ index and the description of how we form the difference spectra used in the radial velocity² measurements and the $\Delta EW_{868.2}$ and $\Delta(R - I)$ indices is given in Sec. 2.1.2 and Larson et al. (1993b). All of the CFHT data have observing run corrections subtracted; these corrections are described in Appendix A. Figure 1 of Walker et al. (1995) shows the systematic offsets in the collective radial velocities between observing runs. The DAO data have not had run corrections subtracted; this is discussed in Sec. 2.1.1 and Appendix A.

The determination of the relative radial velocities from the spectra is the result of a fairly lengthy reduction process; only a few steps are mentioned here. The radial velocities for each star are derived relative to the appropriate stellar reference spectrum using the difference technique of Fahlman and Glaspey (1973). These relative line positions are then corrected for slight run-to-run changes in the instrumental profile and the imperfect cancellation of stellar lines in the star + HF spectrum. A dispersion relation is then fit to the relative positions of the HF lines in each spectrum, all stellar relative positions are adjusted to their rest values, and the stellar line positions are used to constrain the higher order components of the dispersion relation. Note that stellar lines farther than 100 pixels from the HF spectral range are used to perfect the dispersion relation but are not used in the velocity

²In this thesis, the terms precise radial velocities, velocities, radial velocities, RV, relative radial velocities, differential radial velocities, and differential velocities all pertain to the values obtained from the differenced spectra. The phrase “radial velocity of the star” means the radial component of the true space velocity of the star corrected to the barycenter of the solar system.

determination. The lines are then weighted according to their strength. After a few more iterations, the relative velocities are determined and the internal errors are established from the weighted standard errors of the velocities of the typically 10-12 non-zero-weighted stellar lines.

From the run-correction calculations, we estimate that the external errors for the CFHT RV data are approximately 20 m s^{-1} . This estimate can also be obtained from the scatter in the RV data for the most constant star in the sample, τ Ceti, shown in Fig. 2 of Walker et al. (1995). The standard deviation of these data is 17.5 m s^{-1} . We discuss the external errors for the DAO data in Sec. 2.1.1.

The method we use to determine the presence of significant periods in the stars is given in Irwin et al. (1989) and Walker et al. (1995), and briefly summarized here. Our periodogram analyses for each star rely upon the calculation of the weighted or correlated periodogram from the residuals of a parent function. The parameters for the parent function are determined by a least-squares fit to the data. Examples of parent functions are weighted means or a combination of a mean and higher order polynomial terms and/or single or multiple sinusoids (or more complicated functions). The weighted periodogram is calculated using the formula given in Irwin et al. (1989, Eq. (5)), and the correlated periodogram is calculated using the formula given in the appendix to Walker et al. (1995, Eq. (A2)). We determine the significance of a period by calculating 100 periodograms with randomized data sets having the same sampling weights as the original observations and determining the maximum periodogram power for each randomized set. The 99% confidence level is specified for each periodogram, and is defined as the level at which

99/100 randomized data sets have a maximum periodogram power below that of the observed data.

The extraction of the “true” period(s) from a given periodogram analysis may be difficult because the true period is masked by aliasing due to the observational sampling of the star. Generally, it is a simple task to identify aliases resulting from *known* periodic sampling, but it is not easy to distinguish spurious periods from real. Since the relation given in Tanner (1948) is reversible,

$$\frac{1}{P_z} = \frac{1}{P} \pm \frac{n}{k\tau}, \quad (2.1)$$

where P_z is the false period, P is the true period, n and k are integers, and τ has been predefined as the least interval of observation (e.g., the sidereal day, synodic month, or tropical year), we know only that P_z and P are aliases. As an additional means of identifying the aliased periods in our data, we determine the amplitude, period, and phase of a significant peak (usually *the* most significant peak) in the periodogram. We then include these values in the parent function, and the periodogram from the residuals is calculated. The power in the aliased periods will be significantly reduced and thus the aliasing identified. This method, which is the most common method used in period analyses of randomly sampled data, also gives information only about the aliasing and not the true period. For some periodograms, however, the periodogram power at a given frequency will be much higher than the power at any other frequency. In these cases, we are more confident that we have, in fact, isolated the true period. The periodograms for the RV data of β Gem and α Tau (discussed in Sec. 2.2.2) are examples of confident detections of

true periods.

2.1.1 Highlights of the HF technique at the DAO

The introduction of an absorption cell into the stellar light path superimposes the calibration reference lines on the stellar spectrum. The reference spectrum is coincidental in time and follows the same light path as the stellar source, advantages not shared by conventional bracketing of exposures with reference arcs. While other gases or telluric lines are being used (Campbell and Walker, 1985), hydrogen fluoride gas has some superior characteristics. The absorption lines used are the R -branch lines of the 3-0 rotation-vibration band of HF, a transition producing 7 strong lines which are widely spaced, allowing a number of unblended stellar lines to be registered in between. The HF lines are free of weak isotopic lines which would introduce an additional blending problem. The lines fall in the near infrared region, 867.0 - 877.0 nm, where there is only one strong telluric line (875.8 nm) and where the detector used (see below) has a good quantum efficiency for attaining a high signal-to-noise ratio (Campbell and Walker, 1979).

The 1.22-m telescope at the DAO is well-known for the high quality and efficiency of its coudé train and mosaic spectrograph. A description of the coudé spectrograph system is given in Richardson, Brealey, and Dancey (1970). The observations discussed here used the infrared mirror train, which has a thin coating of gold on mirrors 2-5. The focal ratio of the primary mirror is $f/4$ which is changed to $f/145$ at the secondary. Three reflections carry the light past an achromatic lens located 2 meters before the image slicer, which reduces the focal ratio to $f/30$ to match the spectrograph. An iris diaphragm

(located just past mirror 5) was used to isolate the exit pupil of the telescope (it was not exactly at the exit pupil) and help eliminate residual collimation errors. A central disc was mounted in the iris to cover the secondary mirror shadow. The HF cell, of length 90.6 cm, was located between the iris and the image slicer.

The “red” image slicer, IS32R was used in the HF program. According to Richardson et al. (1970) one may assume a gain of 2.7 times over a standard slit as the superpositioning of the slices reduces the loss of light to the spectrograph. Image slicers can be used only when sky subtraction is not necessary as all spatial information is lost. We originally intended to use the fact that the spectrograph receives these different slices to check the contribution from each grating in the mosaic and the precision of the alignment of the four gratings in order to derive the instrumental profile for each run. The contribution from each grating was obtained by simply blocking the light to the other three by means of a large mask cut especially for this task. Early attempts by Alan Irwin and Cherie Goodenough to model the instrumental profile of the CFHT were not fruitful (Irwin, private communication); no attempt has yet been made to model the instrumental profile of the 1.22-m telescope at the DAO (see discussion in Sec. 3.2.3).

The detector used was a Reticon photodiode array having 1872 elements, $15\mu\text{m}$ center-to-center by $750\mu\text{m}$ high. The advantages and disadvantages of this detector have been outlined in Campbell et al. (1986). The Reticon was ideally suited for precise radial velocity work as a signal-to-noise ratio > 1000 was needed. Even though the read-out noise was typically about 400 electrons rms, the exposures usually attained a level of between 10^6 and 10^7

electrons so that photon noise dominated. Readout of the diodes was very rapid, and thus one could immediately cycle into another exposure. However, the Reticon retained some memory of the previous exposure if a high level was reached, and thus a short “dummy read” was taken (but not recorded) between stellar exposures.

The Reticon also contained a fixed baseline pattern due to stray capacitance coupling the clock signals to the video line. This pattern could be eliminated via subtracting a short baseline exposure taken after each long exposure. The diode-to-diode variance in gain was eliminated via normal flat fielding procedures. However, under low gain, the flat field lamp exposures were often only a few times the baseline exposure and the gain variance information was lost after baseline subtraction. Under these conditions, a dark exposure was used, a procedure introduced by Stephenson Yang.

Exposures in the infrared spectral region suffer a disadvantage inherent in silicon arrays. For photon energies below the excitation energy, the silicon becomes transparent, particularly when cooled. The relatively small thickness of the diodes leads to interference between the incident radiation and that reflected from the substrate and fringing occurs (Walker, 1987, p. 290). This fringing became particularly severe in those cases where the optics were well aligned. It is generally believed that the small window of the HF cell was an additional source of fringing in the spectra. This fringing limited the precision of the radial velocity measurements from the DAO data, eliminated the use of the $\Delta EW_{868.2}$ and $\Delta(R - I)$ indices from these observations, and was one of the major factors leading to the discontinuation of the HF technique at the DAO. In addition, the Reticon was replaced by CCD detectors

which have not achieved the quantum efficiency of the Reticon.

The data from the observations were reduced in three automatic stages, as described in Campbell et al. (1986). The first stage of reduction involves preparation of the spectra through baseline subtraction, flat-fielding, and rectification of the “star + HF” spectrum to the reference stellar and HF spectra. The second stage in the reduction process determines the line positions. This technique involves very small shifts of the spectrum, subtracting the spectrum from the reference spectrum, and obtaining the sum of the squares of the residuals around each line. A third order polynomial is then fit to the sum of the squares of the residuals versus shift (Fahlman and Glaspey, 1973). In the final stage, the relative radial velocities are derived, corrected to the barycenter of the solar system.

As mentioned in Appendix A, the DAO observations were limited to evolved stars which, when compared to the dwarfs in the full CFHT program, have a relatively large velocity variability. This variability generates a large statistical error in the run corrections, and we have not applied these corrections because the corrections are not significantly different from zero. The 95% confidence intervals calculated from these corrections and their statistical errors imply typical upper limits of 40 m s^{-1} on possible systematic errors in the DAO velocities. We expect the external errors within a given run to be less than 40 m s^{-1} .

Figure 2.1 compares the RV data from the CFHT and DAO observations of α Arietis (HR 617, $\alpha = 2^{\text{h}}7^{\text{m}}10^{\text{s}}.40$, $\delta = +23^{\circ}27'44''.66$; J2000) (Hoffleit and Warren, 1991), which, although intrinsically variable, is the most “constant” star observed extensively at the DAO. The standard deviation of the

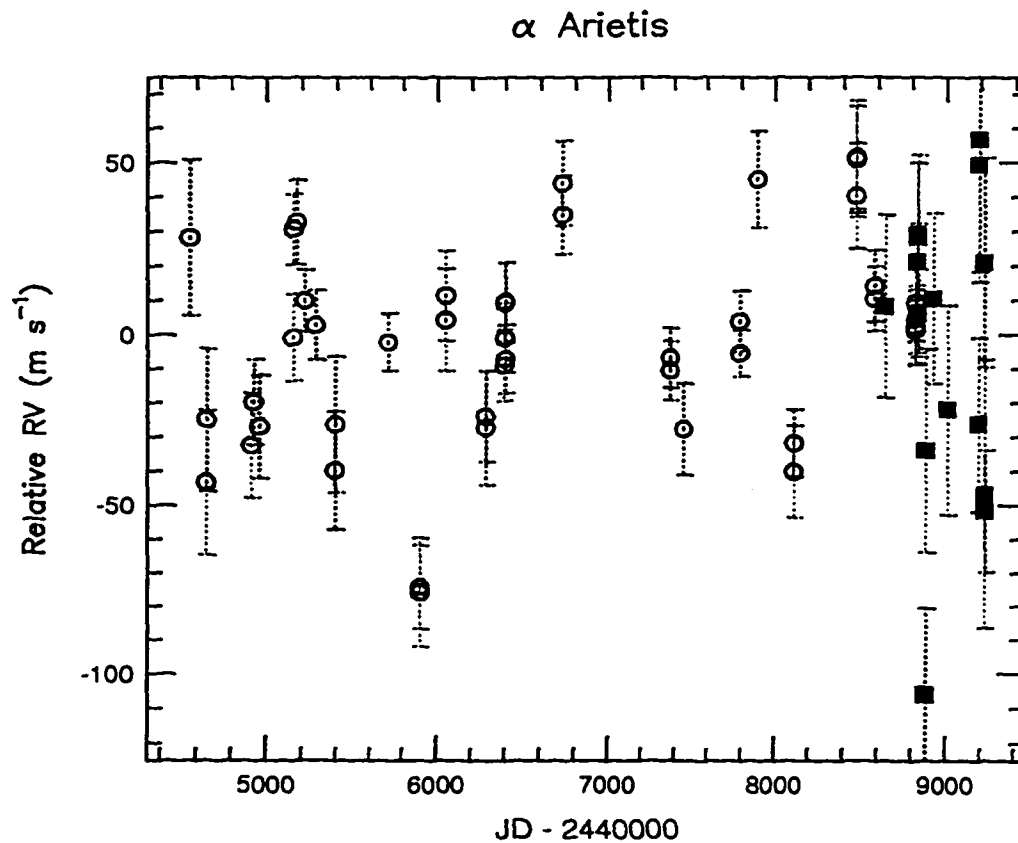


Figure 2.1: The relative radial velocities of α Arietis (HR 617) from the CFHT (open circles) and DAO (filled squares) data. The standard deviation of the CFHT data is 30.72 m s^{-1} and the mean internal error is 12.90 m s^{-1} , implying an intrinsic variability of $\sim 28 \text{ m s}^{-1}$. The standard deviation of the DAO data is 43.60 m s^{-1} and the mean internal error, 25.13 m s^{-1} , implying a $\sim 7 \text{ m s}^{-1}$ increase in the intrinsic scatter or an underestimate of the internal errors.

CFHT data is 30.7 m s^{-1} and the mean internal error is 12.9 m s^{-1} , giving an intrinsic variability of 27.9 m s^{-1} . The standard deviation of the DAO data is 43.6 m s^{-1} ; the mean internal error, 25.1 m s^{-1} . This implies that part of the increase in the long-term scatter of the DAO data is due to the increased error in each measurement. If we assume that α Ari had the same intrinsic variability during the DAO observations as for the CFHT observations, then $\sqrt{27.9^2 + 25.1^2} = 37.5$, a value not that different from the DAO external scatter of 43.6 m s^{-1} . The intrinsic variability of α Ari may have increased slightly or we may have underestimated the internal errors.

2.1.2 Definition of the $\Delta EW_{866.2}$ index

Because each spectrum includes the Ca II 866.2 nm infrared triplet line³, we are able to monitor the chromospheric activity of the program stars. Our ability to monitor simultaneously this activity and the precise velocity is critical to our understanding of any variability detected in our program stars. In this section I define the $\Delta EW_{866.2}$ index, which measures the change in the flux of the core of the 866.2 nm line (in pm), and demonstrate the viability of the index as an indicator of chromospheric activity⁴.

Shine and Linsky (1972) found that the cores of the Ca II 849.8, 854.2, and 866.2 nm triplet lines brighten in solar plage regions and show reversals in the most active plages. The relative opacities of these lines in the solar spectrum are in the ratio 1:9:5, with the least opaque line, 849.8 nm, showing

³My apologies go to those of pure heart who recognize that the Ca II infrared "triplet" is indeed not a triplet at all but technically a "compound doublet." However, astronomically, it will probably always be called a triplet.

⁴This work has been published (Larson et al., 1993b)

the greatest core reversals. Linsky et al. (1979) showed that the most opaque line, 854.2 nm, was suitable as a diagnostic of stellar chromospheric activity. The 866.2 nm line is also suitable for this purpose and, unlike 849.8 and 854.2 nm (Moore et al., 1966), is uncontaminated by atmospheric water vapor lines near the line core.

Examples of changes in the 866.2 nm line for 61 Cygni A are given in Fig. 2.2. The spectra we observe for our precise radial velocity program include a single stellar reference spectrum observed without the HF absorption cell in the telescope beam and a series of “stellar + HF” spectra observed with the HF absorption cell in the telescope beam. The difference spectrum is formed by subtracting the stellar reference spectrum from the stellar + HF spectrum after alignment of the Ca II line. Fig. 2.2 shows an example of the difference spectrum and defines the 0.135 nm core band and the adjacent 0.227 nm blue sideband used in our $\Delta EW_{866.2}$ index determination. Using these wavelength regions avoids potential contamination by the Paschen 866.5 nm line for the earlier type stars in our program. Note these wavelength regions are safely outside the HF band. The bluest HF line, which can be seen at the far right of Fig. 2.2, occurs at a rest air wavelength of 866.6 nm.

We calculate $\Delta EW_{866.2}$ using the difference spectrum defined above. To reduce the effects of variable continuum placement, we linearly extrapolate the difference spectrum sideband values to line center. Our $\Delta EW_{866.2}$ index is formed by taking the mean of the pixels in the core band of the difference spectrum with the extrapolated sideband value subtracted. An increase in our index corresponds to a filling-in of the absorption core. The standard

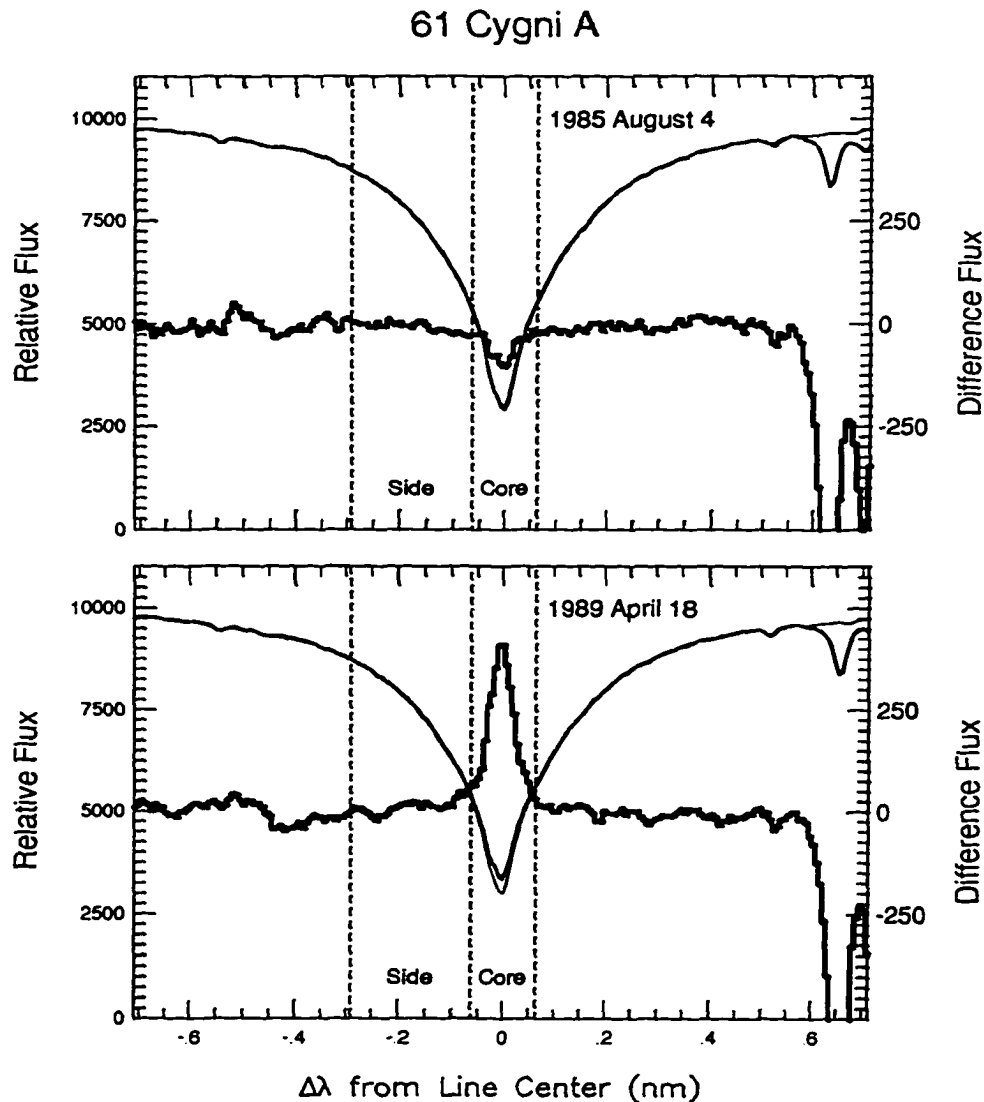


Figure 2.2: Difference spectra (heavy line) in the region of Ca II 866.2 nm line of 61 Cygni A. These spectra show a relative decrease in $\Delta EW_{866.2}$ on 1985 August 4 (JD 2446283.0371), and a relative increase on 1989 April 18 (JD 2447636.0688). The latter spectrum clearly shows a filling-in of the central core. Superposed on the difference spectra are the stellar + HF (medium line) and stellar-reference (light line) spectra.

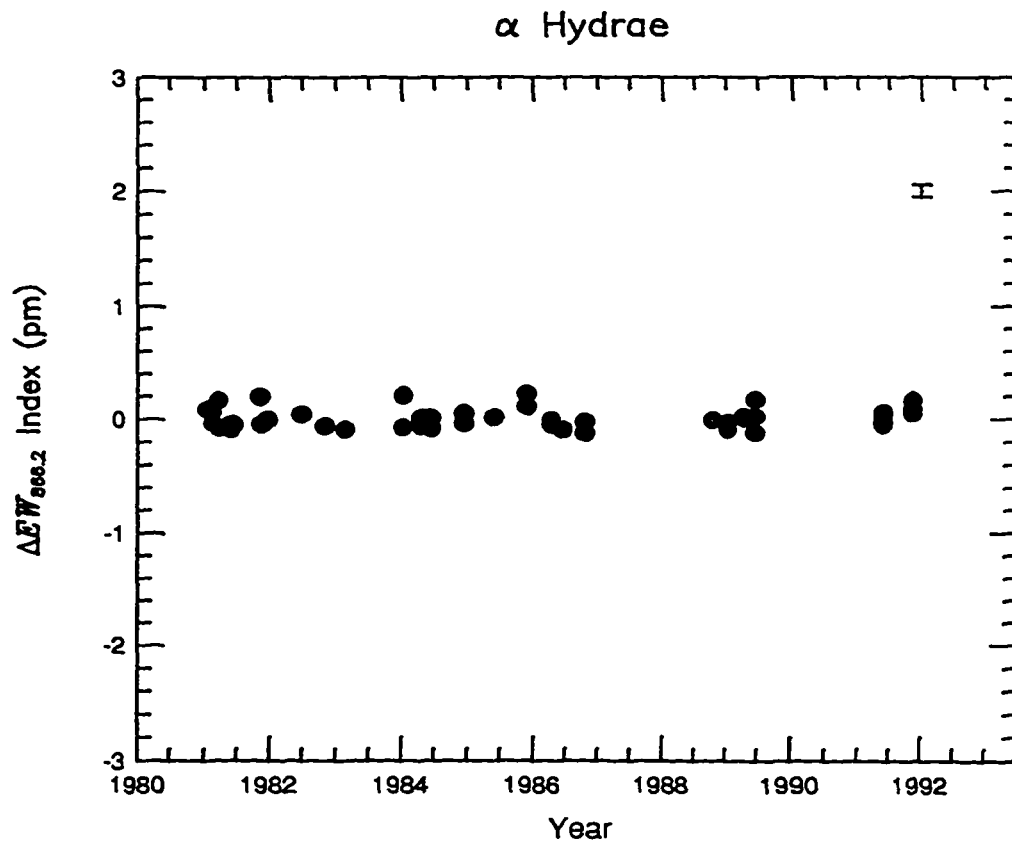


Figure 2.3: $\Delta EW_{866.2}$ vs. time for α Hydrae (HR 3748). This star is the most chromospherically quiet of the stars in our program with a standard deviation from the unweighted mean of 0.088 pm. The mean internal error of 0.053 pm is indicated by the error bar.

deviation of the difference spectrum pixel values in the sideband is multiplied by $\sqrt{1/N_s + 1/N_c}$ to give our estimate of the $\Delta EW_{866.2}$ internal error (in pm); N_s and N_c are the number of pixels in the sideband and core band.

We approximately correct $\Delta EW_{866.2}$ for variations in the instrumental profile. These variations are monitored by comparing a high-resolution HF spectrum with the HF spectra taken on the appropriate observing night. Before forming the difference spectrum used for the calculation of the $\Delta EW_{866.2}$ index, we convolve either the stellar reference spectrum or the stellar + HF spectrum with a Gaussian to ensure that both spectra have the same instrumental half-width.

Figure 2.3 shows our Ca II results for the most chromospherically quiet star in our sample, the K3 II-III star α Hydrae (HR 3748, $\alpha = 9^h 27^m 35^s .24$, $\delta = -8^\circ 39' 32'' .61$; J2000) (Hoffleit and Warren, 1991). The standard deviation from the unweighted mean of the Ca II index for this star is $\sigma_{\Delta EW_{866.2}} = 0.088$ pm. This external error (which might include intrinsic variations of the star) is only slightly larger than the mean internal error of 0.053 pm. This small difference suggests that our run-corrections procedure is valid.

2.2 Results and Discussion

2.2.1 The K Dwarfs

The HF program at the CFHT was optimized for the detection of long-term, low-amplitude variability indicative of the presence of sub-stellar-mass companions around nearby, solar-type stars. The 12 years of observations have been summarized in Walker et al. (1995). Because the data are sparse

and the target stars inadequately sampled over short time intervals, the data cannot constrain short period aliasing. True periods are often hidden in the noise. However, many of the program stars have been included in other studies including the long-term monitoring of the Ca II H and K lines at the Mount Wilson observatory. Where possible, I have interpreted the CFHT data in light of the additional information available.

This section discusses the results for the K dwarfs: 36 Ophiuchi A and B and 61 Cygni A and B. The periodograms for 36 Oph AB (not shown) reveal what has been humorously referred to in the literature as “insignificant grass”; that is, there are no outstanding peaks (stalks?) which warrant much further analysis. The analysis of the data for 61 Cygni A forms the basis of the quantification of our $\Delta EW_{866.2}$ index (Larson et al., 1993b), and the RV data are discussed in light of our detection of the star’s rotation period in the $\Delta EW_{866.2}$ index data. The periodograms for 61 Cygni B revealed no significant periods (confidence level $\geq 99\%$); they are shown with the discussion on this star as the periodogram for the $\Delta EW_{866.2}$ index showed some periods having a 95% confidence level. One goal of this discussion is to compare the two binary stars; although the stars in each pair are coeval and have similar spectral types, there are some obvious differences in the $\Delta EW_{866.2}$ index data.

The RV, $\Delta EW_{866.2}$ index, and $\Delta(R - I)$ index data are shown in the relevant figures in each section; however the data are not tabulated here. The radial velocity data are archived with NSSDC/ADC [the (United States) National Space Science Data Center/Astronomical Data Center]. Electronic

access to the NSSDC/ADC catalogs can be obtained from the URL:

<http://adc.gsfc.nasa.gov/>

The data for the $\Delta EW_{868.2}$ and $\Delta(R - I)$ indices will be the subject of a future summary paper (Larson and Irwin, et al., in progress) and will be provided at that time.

36 Ophiuchi

The “early” set of K dwarfs included in this analysis is the K0-K1 V pair, 36 Ophiuchi AB. These stars were included in the H and K survey conducted at Mount Wilson Observatory (Wilson, 1978; Baliunas and Vaughan, 1985; Baliunas et al., 1995). Although these stars are coeval and are essentially the same spectral type, they show different chromospheric behavior. For 36 Oph B, Table 1 of Baliunas et al. (1995) lists a period of $P_{cyc} = 5.7 \pm 0.1$ yr for the solar-type cycle. For 36 Oph A, they list the star as variable; that is, it shows significant variability (and cyclic behavior) but no definite periodicity.

The PRV data and $\Delta EW_{868.2}$ and $\Delta(R - I)$ index data versus time for 36 Oph A and B are plotted in Figs. 2.4 and 2.5. These data were obtained at the CFHT at a continuum signal-to-noise ratio of over 1100 per pixel for A and over 1000 per pixel for B, for a typical 40 – 45 minute exposure. The binary motion is seen through the opposite slopes in the radial velocity data. For 36 Oph B Irwin et al. (1996) discuss the apparent discrepancy between the orbit parameters estimated from 170 years of observations and the precise radial velocities. That is, the acceleration of 36 Oph B is a factor of 1.64

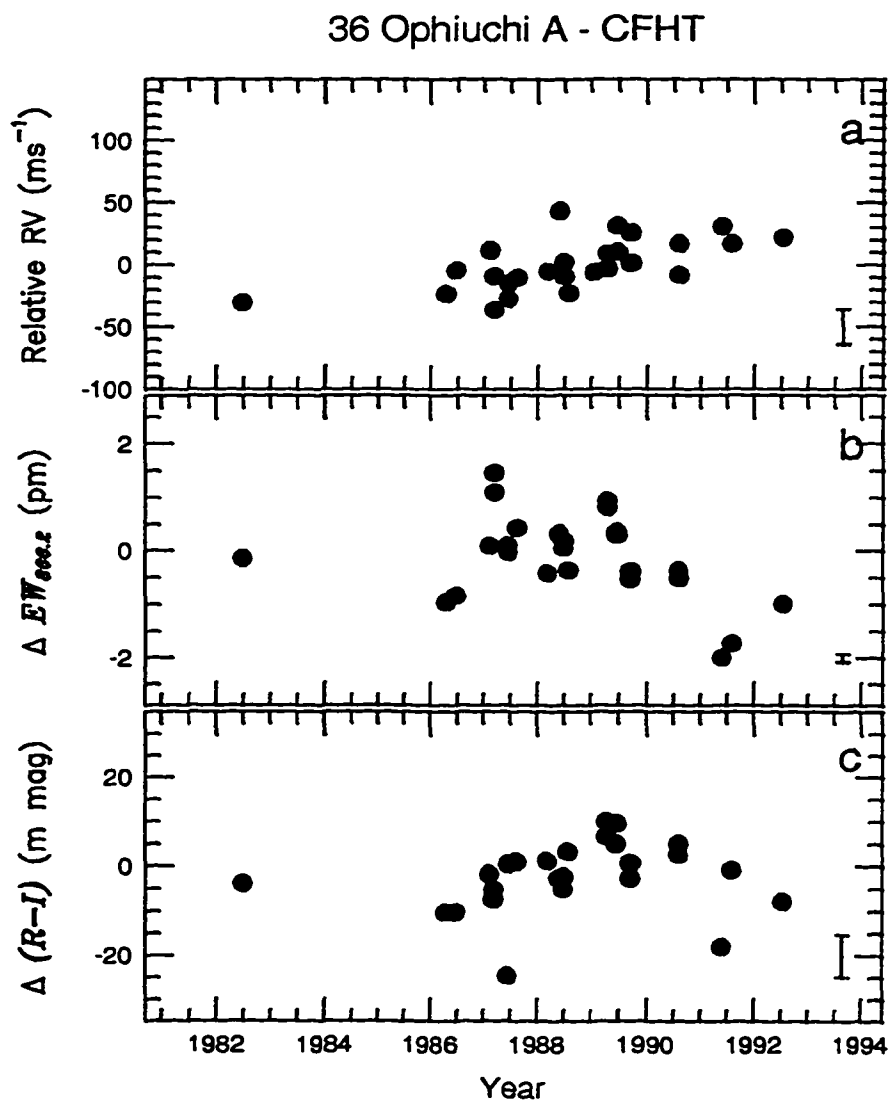


Figure 2.4: The CFHT data for 36 Ophiuchi A (HR 6402) vs. year. A weighted mean has been subtracted from each data set. The mean internal errors are given by the error bars.

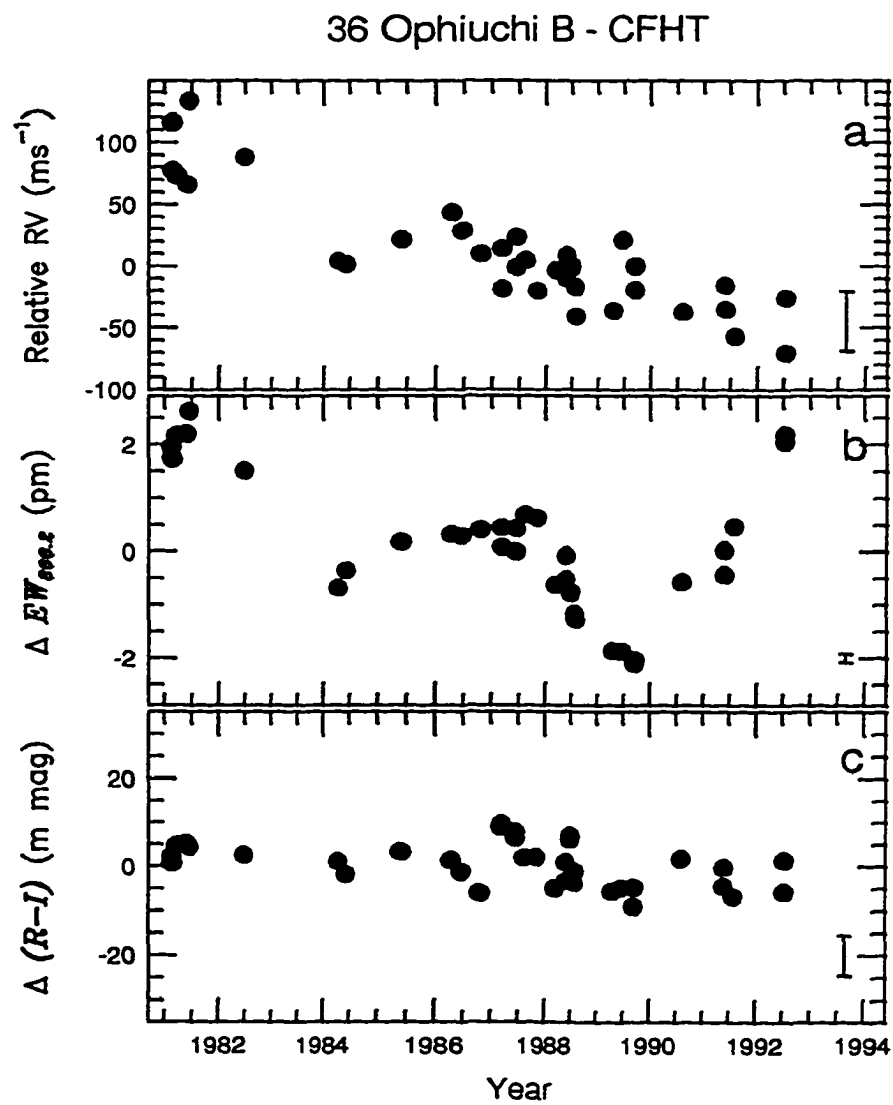


Figure 2.5: The CFHT data for 36 Ophiuchi B (HR 6401) vs. year. A weighted mean has been subtracted from each data set. The mean internal errors are given by the error bars.

larger than that predicted from the orbit, and no reasonable variation of the sums of masses, mass ratio, parallax, or orbital parameters can alleviate the discrepancy. Also, 36 Oph B has an apparent long-term, sawtooth-shaped, solar-type cycle in the $\Delta EW_{868.2}$ index, as Fig. 2.5 shows.

The $\Delta EW_{868.2}$ index can be directly compared with the Mount Wilson Observatory S index (see later discussion for 61 Cyg A). Figure 1f of Baliunas et al. (1995) shows the S -index data from 1967-1992 for these two stars. A comparison with our $\Delta EW_{868.2}$ index data, shown as part of Figs. 2.4 and 2.5, shows reasonable agreement for 36 Oph A and B for the overlapping time span. This binary was also part of the sample of 47 lower main-sequence stars observed extensively over a 3-4 month period in 1980 at Mount Wilson for the purpose of measuring rotation periods. Table 3 of Baliunas et al. (1983a) lists rotation periods of 22.9 and 20.3 days for B and A respectively. Periodogram analysis of the RV data and $\Delta EW_{868.2}$ and $\Delta(R - I)$ indices revealed no corresponding periods, nor any significant periods at all, in any of the data sets for $P \leq 40$ days. Our inability to detect the rotation periods is probably due to our more limited sampling of these two stars or to the possibility that the chromospheric activity of these two stars, while ongoing, is spatially coherent only over short time scales. The pathology of the long-term cycle of 36 Oph B prevents the calculation of an accurate parent function, at least for now, and thus may also contribute to the nondetection of a rotation period for this star.

The radial velocity data versus time are shown in Fig. 2 of Walker et al. (1995), we have included them here, along with the equivalent width indices, in Fig. 2.4 and Fig. 2.5 to maintain consistency with the other stars discussed

in this thesis.

61 Cygni A

The K5 V star 61 Cygni A is a Ca II variable star. It was included in the H and K survey conducted at Mount Wilson Observatory (Wilson, 1978; Baliunas and Vaughan, 1985; Baliunas et al., 1995). Our analysis⁵ of the $\Delta EW_{866.2}$ index for this star is described first in this section, followed by the analysis of the radial velocity data and $\Delta(R - I)$ index for periods less than 40 days.

The $\Delta EW_{866.2}$ index data for 61 Cyg A, which are listed in Table A.1 and plotted in Fig. 2.6b, were obtained at the CFHT at a continuum signal-to-noise ratio of over 1200 per pixel for a typical 20 – 30 minute exposure. The long-term, sawtooth-shaped, solar-type cycle is obvious. In addition, there is scatter from this long-term variation which is clearly larger than our external errors (see Fig. 2.3). As explained below, we modeled this scatter by a short-period sinusoid.

Periodogram analysis and non-linear least-squares results: The preliminary step in modeling the periodicities in the $\Delta EW_{866.2}$ index data was a least-squares fit to a constant plus sawtooth function (programmed by A. W. Irwin). The sawtooth function is defined as

$$\mathcal{W}(t_i, K, T, \Delta T, P) = K \left(\frac{[\phi(t_i) - \phi(T + \Delta T)] - [\phi(T) - \phi(t_i)]}{[\phi(T) - \phi(T + \Delta T)]} \right), \quad (2.2)$$

where t_i is the current epoch; K , the amplitude; T , the epoch of maximum relative core emission; $T + \Delta T$, the epoch of minimum relative core emission;

⁵Results have been published (Larson et al., 1993b)

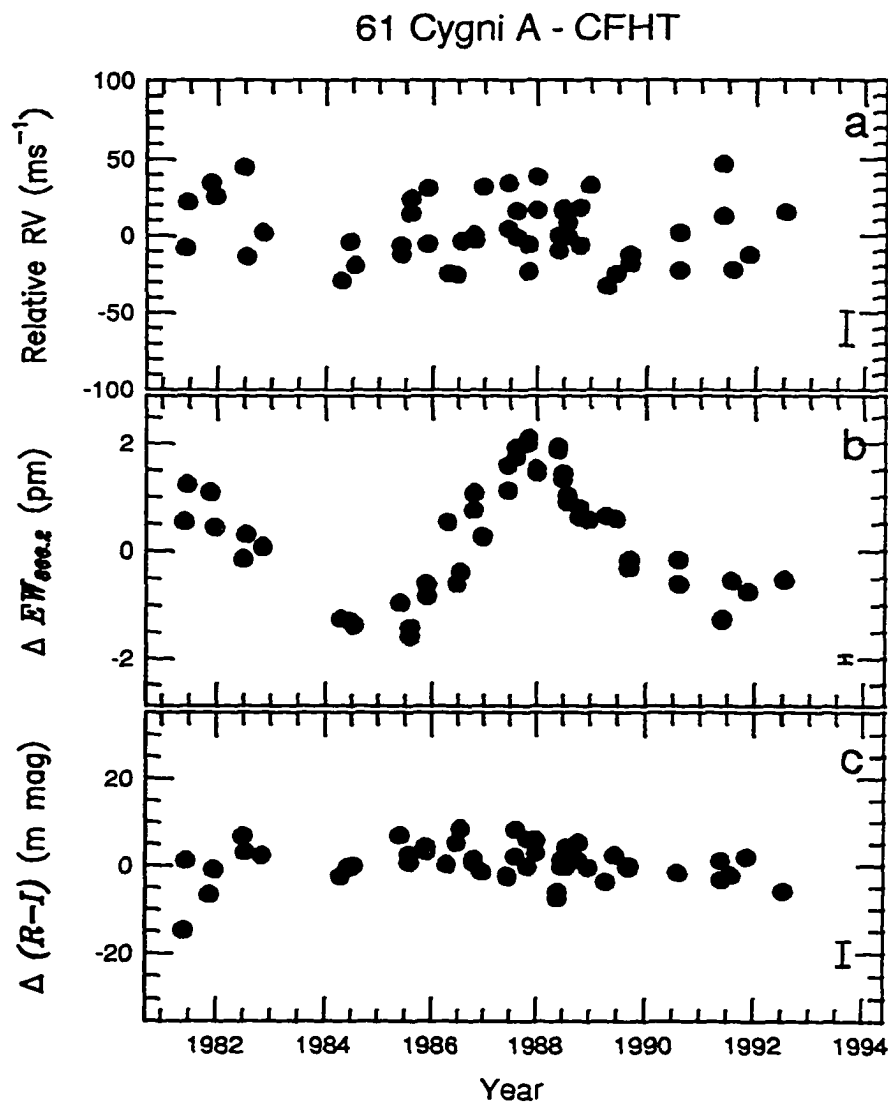


Figure 2.6: RV , $\Delta EW_{866.2}$, and $\Delta(R-I)$ vs. time for 61 Cyg A (HR 8085). The short-term rotation modulation has not been removed from the $\Delta EW_{866.2}$ long-term sawtooth cycle of 7.2 years. The mean internal errors are indicated by the error bars.

and P , the period. The phase is given by

$$\phi(t) = \frac{(t - T)}{P} \bmod 1. \quad (2.3)$$

With this definition the phase of maximum is

$$\phi(T) \equiv 0, \quad (2.4)$$

and the phase of minimum is

$$\phi(T + \Delta T) \equiv \frac{\Delta T}{P} \bmod 1. \quad (2.5)$$

The Marquardt technique we use for solving the weighted non-linear least-squares problem has been described elsewhere (Irwin et al., 1992; Press et al., 1986).

Based on previous H and K results (Baliunas et al., 1983a), we expect rotation modulation of $\Delta EW_{866.2}$ for 61 Cyg A. Therefore, we have adopted a final model fitting function given by

$$\begin{aligned} \mathcal{F}(t_i, \gamma, K_1, T_1, \Delta T, P_1, K_2, T_2, P_2) = \\ \gamma + \mathcal{W}(t_i, K_1, T_1, \Delta T, P_1) + \mathcal{S}(t_i, K_2, T_2, P_2), \end{aligned} \quad (2.6)$$

where the sinusoid function is given by

$$\mathcal{S}(t_i, K, T, P) = K \cos 2\pi(t_i - T)/P. \quad (2.7)$$

The weighted mean for the least squares solution is parameterized by γ . If we restrict the sinusoid period to be close to the rotation period found by Baliunas et al. (1983a), see discussion below, then the parameters of the best least squares solution are given in Table 2.1. Fig. 2.7 plots the residuals from

Table 2.1: 61 Cygni A: periodic solution for $\Delta EW_{866.2}$ (1981 - 1992)

parameter ^a	value	σ	units
γ	-0.26	0.051	pm
sawtooth parameters			
K_1	1.715	0.089	pm
ΔT	1775.00	97.00	dy
T_1	6998.00 ^b	39.00	dy
P_1	2637.00	76.00	dy
sinusoid parameters			
K_2	0.404	0.081	pm
T_2	6909.20 ^b	1.20	dy
P_2	36.212	0.041	dy

^a See Eqs. 2.2 and 2.6 for the definitions of the parameters^b JD - 2440000

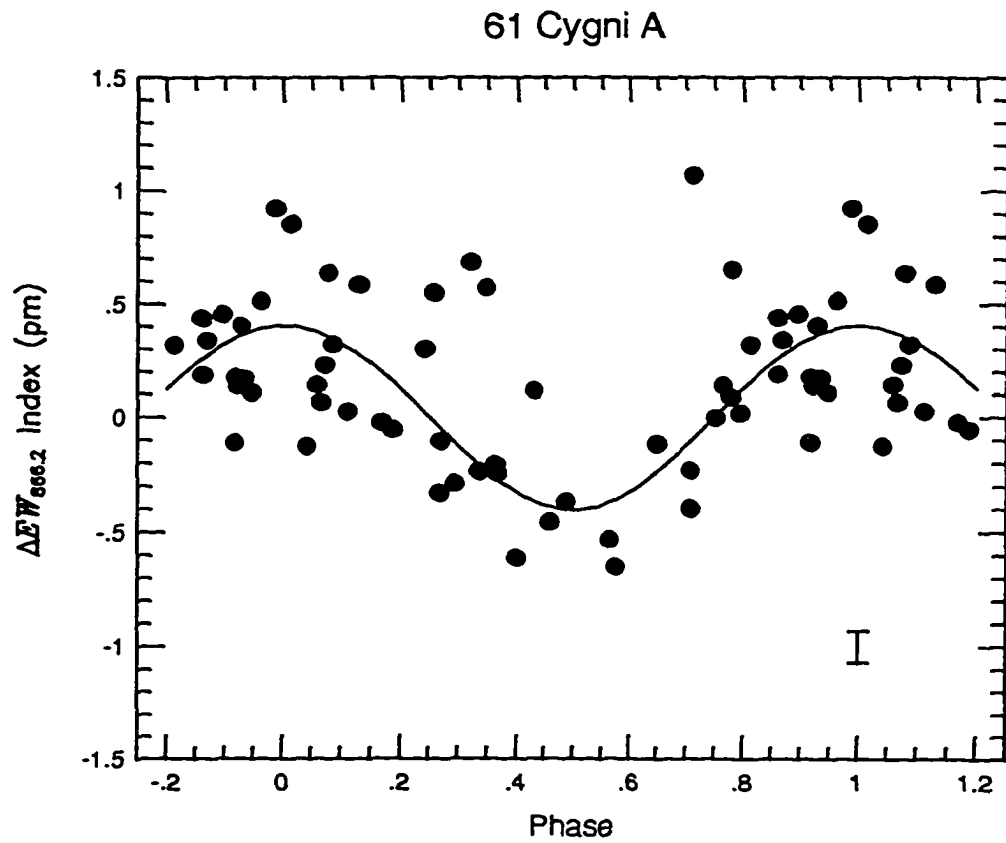


Figure 2.7: Phase diagram of the residuals of the $\Delta EW_{866.2}$ index from the constant plus sawtooth model for 61 Cygni A folded on the 36.212-dy rotation period. The mean internal error of 0.069 pm is indicated by the error bar. The large residuals compared to the mean internal error may be evidence of amplitude, frequency, and/or phase modulation.

the constant + long-term sawtooth folded on the 36.212-dy sinusoid period derived here.

The weighted normalized periodogram (Irwin et al., 1989, Eq. (5)) of the residuals from the constant plus sawtooth solution is shown in Fig. 2.8a, while the weighted normalized periodogram of the residuals from the complete model (Table 2.1) is shown in Fig. 2.8b. The 99% and 95% confidence levels (Irwin et al., 1989) are indicated on these figures. According to this analysis, the rotation peak near 36 days in Fig. 2.8a is judged significant because it would be the result of random noise less than 5 per cent of the time. The other significant peaks that occur near periods of 296, 190, and 47 days in Fig. 2.8a are aliases of the rotation peak; they become insignificant (Fig. 2.8b) when the complete model is subtracted from the data. The only significant peak left in Fig. 2.8b, with period near 147 days, may be an artifact of the sawtooth approximation used to model the solar-type cycle variation.

Comparison of the $\Delta EW_{866.2}$ and S indices for 61 Cygni A: We expect our $\Delta EW_{866.2}$ index to be related to the S index, which defines a measure of chromospheric activity using the H and K lines. The Ca II infrared triplet lines share the upper 4^2P° term of the H and K lines; the 866.2 nm line connects the $4^2P_{1/2}^\circ$ upper level of the H line with the metastable $3^2D_{3/2}$ level. The comparison of the observed H and 866.2 nm line profiles for three solar plage strengths is presented in Figs. 12 and 13 of Shine and Linsky (1974). Although the profiles differ in detail, the changes in the equivalent widths are correlated. At least in the Sun, higher intensity in the H line is reflected in a higher intensity for the 866.2 nm line. The S index described

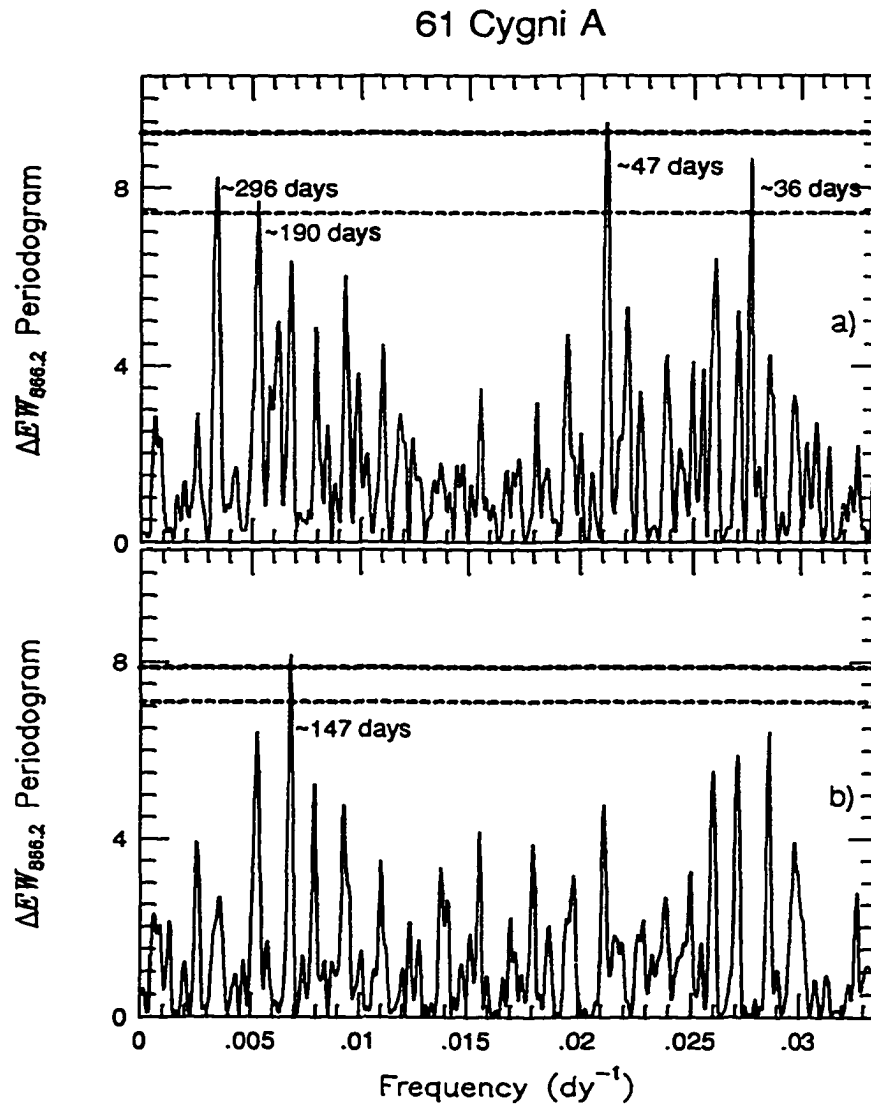


Figure 2.8: *a*) Weighted normalized periodogram of the $\Delta EW_{866.2}$ index of the residuals from the constant plus sawtooth model for 61 Cygni A. *b*) Weighted normalized periodogram of the residuals from the complete model given in Table 2.1. For both *a*) and *b*) the 99% (heavy dashed line) and 95% (light dashed line) confidence levels are indicated.

in Vaughan et al. (1978) and Duncan et al. (1991) measures the flux in 0.109 nm passbands centered on the H and K emission cores relative to 2.0 nm continuum passbands at 390 and 400 nm. The similarities of the two indices can be seen in the results for 61 Cyg A.

Monitoring of the H and K fluxes for 61 Cyg A started in 1967 (Wilson, 1978); the observations are plotted in Baliunas and Vaughan (1985), Fig. 9. Our approximate 12 years of monitoring of this star began in 1981. Unfortunately, direct comparisons of our data with the S index results during the overlap period (1981 - 1985) are difficult because the S -index data points are 30-day averages, whereas our data contain the full rotation scatter.

We fitted a constant plus sawtooth function to the yearly averages tabulated for 61 Cyg A in Wilson (1978). The results for the sawtooth function, given in Table 2.2, show a period that is 2.6σ different from $\Delta EW_{868.2}$ results (Table 2.1). This may be weak evidence that, as with the Sun, the cycle is not strictly periodic.

It is interesting to compare the internal errors of each index with the amplitude seen for the long-term periodicity in 61 Cyg A. Vaughan et al. (1978) give the mean standard deviation for a single observation for the Wilson survey as 1.7% and for their subsequent work with different instrumentation as 1.9%. Based on the mean of the $\langle S \rangle$ values for 61 Cyg A, this gives $\sigma_{\langle S \rangle} / K_{\langle S \rangle} \approx 0.08$. Using the mean internal error of 0.069 nm for 61 Cyg A (see Table A.1), $\sigma_{\Delta EW_{868.2}} / K_{\Delta EW_{868.2}} = 0.04$. Our $\Delta EW_{868.2}$ index seems more sensitive to changes in chromospheric activity, at least for this star.

The rotation period of the Sun can be detected in disk-integrated mea-

Table 2.2: 61 Cyg A: periodic solution for $\langle S \rangle$ index (1967 - 1977)^a

parameter	value	σ	units
γ	0.5442	0.0170	
sawtooth parameters			
K	0.1144	0.0280	
ΔT	911.0	260.0	dy
T	6546.0 ^b	370.0	dy
P	2278.0	140.0	dy

^a Wilson (1978)^b JD - 2440000

measurements of the S index (Baliunas et al., 1983b, Fig. 2). Based on the behavior of the solar plage regions, we would expect amplitude, frequency, and phase modulation of the rotation signal. In the short term, amplitude modulation will be caused by plages forming and dissipating over time scales of weeks to months. In the long term, amplitude modulation will be caused by variations in the number of plages through the course of the solar cycle and from cycle to cycle. Frequency modulation will be caused by differential rotation; the mean latitude of sunspots and their associated plage regions moves toward the equator during a solar cycle (Zirin, 1988, Fig. 10.2), (Harvey, 1992, Fig. 11), thus sampling different rotation rates. Erratic phase modulation will be caused by plage regions forming at different longitudes.

However, sunspot formation (and presumably the formation of the associated plages) is not a random process; Zirin (1988, p. 305) notes that formation of new sunspots is 10 times as probable near the site of old sunspots. This leaves some chance that rotation modulation will preserve phase coherence over relatively long time scales.

It appears the expected behavior of the rotation modulation can be generalized from the solar to the stellar case. For example, HD 190007 (Baliunas et al., 1983b, Fig. 1) seems to show amplitude modulation. Frequency modulation is certainly present; Baliunas et al. (1985) have found some stars exhibit 5 – 20 per cent changes in their measured rotation periods. However, significant phase changes were not detected for those stars measured over two different observing seasons (Baliunas et al., 1983b).

For 61 Cyg A, Baliunas et al. (1983b) established the rotation period as 37.9 ± 1.0 dy which agrees with our least-squares period of 36.21 days (Table 2.1) and the location of the corresponding significant peak in our periodogram (Fig. 2.8a). If our period of 36.21 days is interpreted as the mean rotation period, then the large residuals in Fig. 2.7, when compared to our internal errors (Table A.1), might be evidence that one or all of amplitude, frequency or phase modulation have been occurring. It is interesting that these modulations have not been sufficient to completely destroy the rotation signal of 61 Cyg A during the course of our 12 years of observations.

Radial velocity periodicity: The radial velocity data for 61 Cyg A are shown in Fig. 2 of Walker et al. (1995); they are included in Fig. 2.6 here along with the equivalent width indices for consistency. Figure 2.9 shows

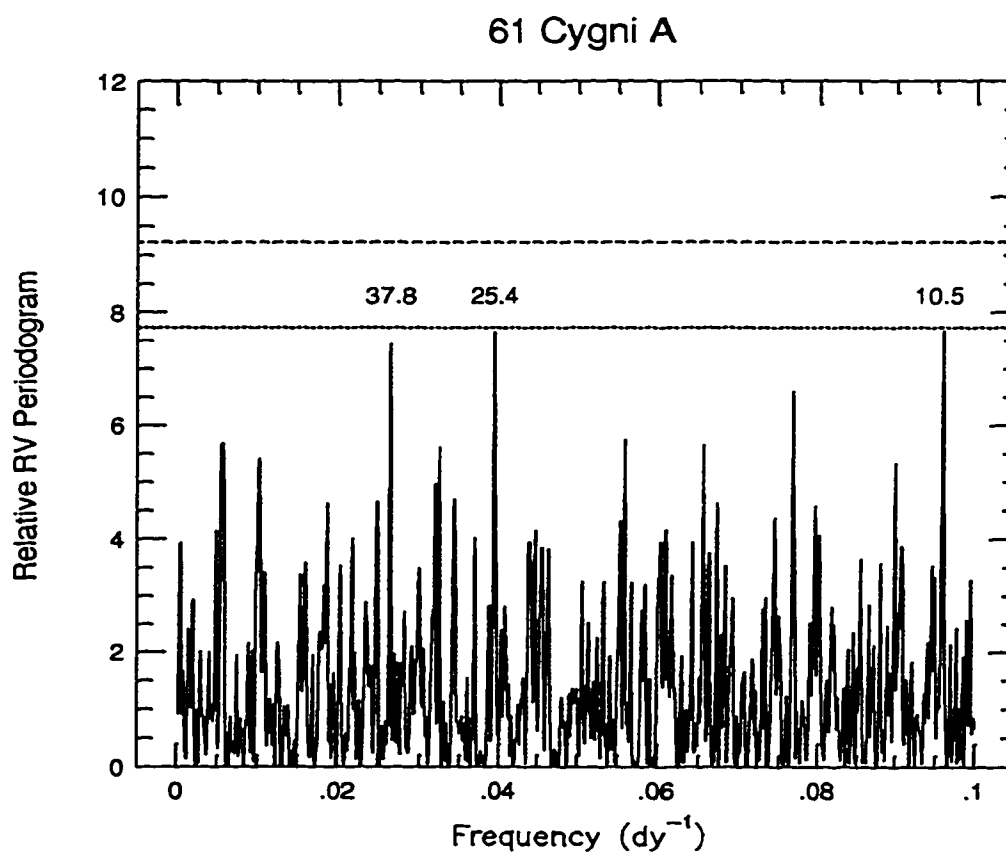


Figure 2.9: The weighted periodogram for the changes in the relative radial velocities of 61 Cygni A for $P \leq 40$ days. A linear term has been included in the parent function. The 99% (dashed line) and 95% (dotted line) confidence levels are indicated. The 37.8-dy period, at a 91% confidence level, corresponds to the rotation period for this star.

the weighted periodogram for RV periods less than 40 days; a linear term has been included in the parent function to model the long period, orbital motion. The three peaks are significant at only the 91% confidence level, but one of the peaks corresponds to the rotation period of 37.8 days. Since the radial velocity variations are derived from photospheric lines, this implies that the active regions maintain some coherence at lower levels in the stellar atmosphere. Further work will be needed to model more accurately the sawtooth function for the analysis of the $\Delta EW_{866.2}$ index. Note that the periodogram analysis of the $\Delta(R - I)$ index showed no significant periods.

61 Cygni B

The K7 V star 61 Cygni B was also included in the H and K survey conducted at Mount Wilson Observatory (Wilson, 1978; Baliunas and Vaughan, 1985; Baliunas et al., 1995). Table 1 of Baliunas et al. (1995) lists a period of $P_{\text{cyc}} = 11.7 \pm 0.4$ yr for the solar-type cycle. This cyclic behavior is apparent in their Fig. 1g for the years 1967-1992; however, the characteristics and perhaps the length of this cycle change after 1982.

The CFHT data versus time for 61 Cyg B are plotted in Fig. 2.10. The spectra have an average continuum signal-to-noise ratio of 1250 per pixel for an average 40-45 minute exposure. Our $\Delta EW_{866.2}$ index data from 1986-1993, shown in Fig. 2.10b, resemble the S index data from that same time period; i.e., there is scatter in the data but no overall trend. Whether this star is adjusting its cycle period or is entering a stage of low activity is unknown. The Sun has an approximate 80-yr fluctuation in its activity level in addition to the 11-yr cycle. 61 Cyg B may be entering such a fluctuation

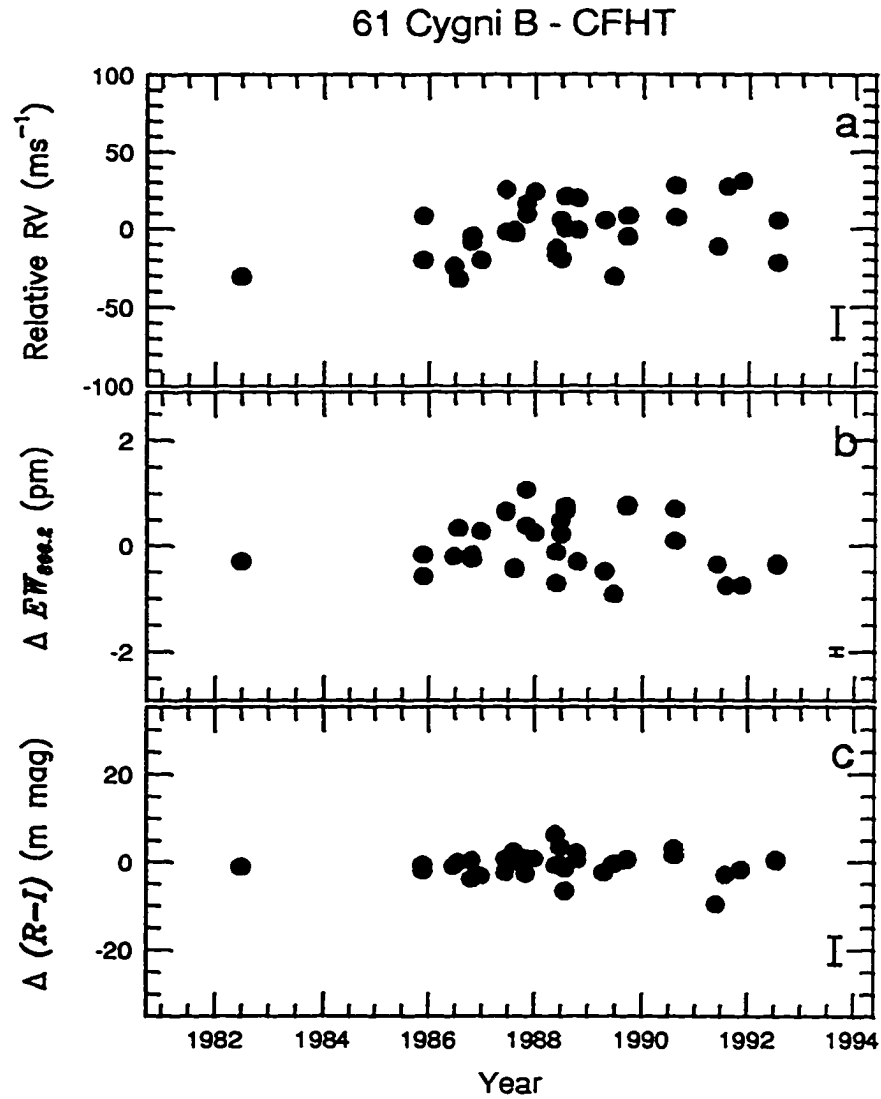


Figure 2.10: The radial velocity data, $\Delta EW_{866.2}$ index, and $\Delta(R - I)$ index vs. time for observations of 61 Cygni B (HR 8086) at the CFHT. A weighted mean has been subtracted from each data set. The mean internal errors are shown by the errorbars.

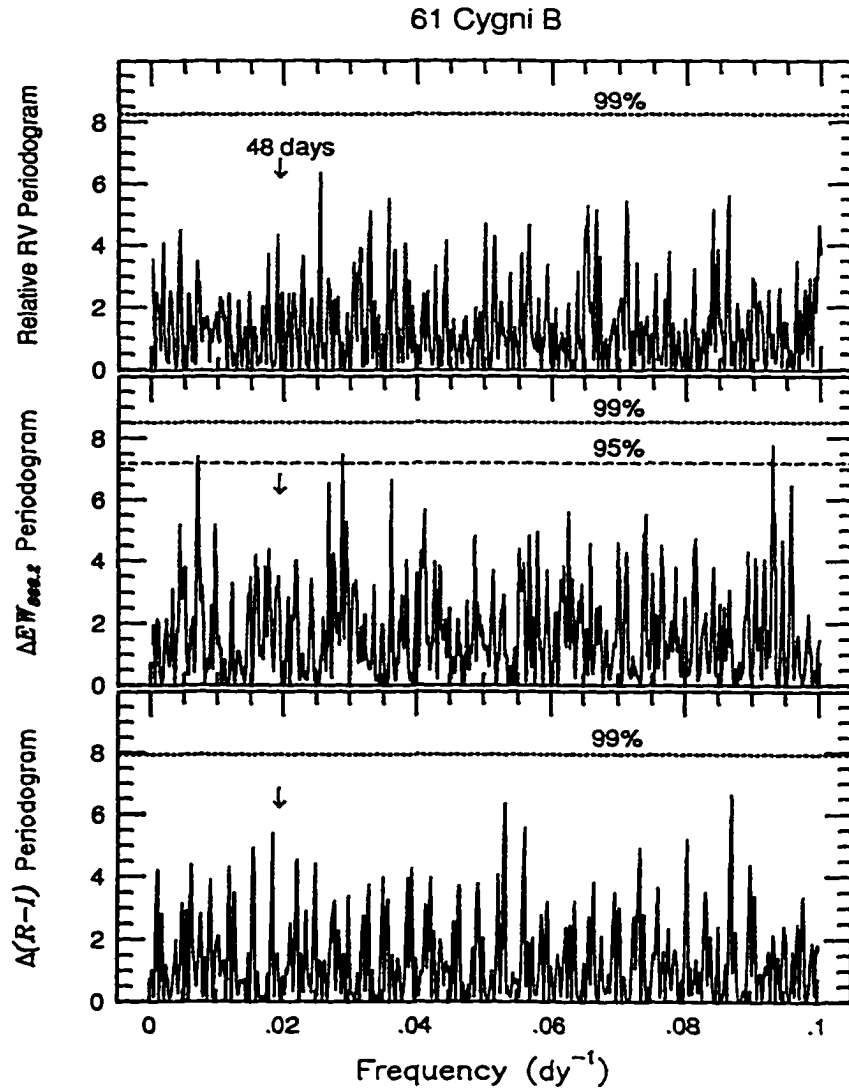


Figure 2.11: The weighted periodograms for the 61 Cygni B CFHT data. As indicated by the 99% confidence level (dotted lines), no significant periods are present in these data. Periodic signals are noted in the $\Delta EW_{866.2}$ index data, 95% confidence level; however, none correspond to the 48-dy rotation period of this star, noted by the arrows (Baliunas et al., 1983b).

which manifests itself differently than that of the Sun.

61 Cyg B star was included in the three months of intensive observations at the Mount Wilson Observatory for measuring rotation periods. Baliunas et al. (1983b) give a rotation period of 48 days (their Table 3). Our CFHT observations for 61 Cyg B are too limited to detect this period. The weighted periodograms for this star are shown in Fig. 2.11; a linear term was included with the parent function for the RV data to model the long-term orbital motion. One notes that there are a few significant peaks, 95% confidence level, present in the $\Delta EW_{866.2}$ index, but none of these correspond to the rotation period. There are no significant periods in either the RV data (although there is an extremely weak signal at approximately the rotation period) or $\Delta(R - I)$ index.

2.2.2 The K Giants

Observational evidence for low-amplitude ($30 \leq K \leq 600 \text{ m s}^{-1}$) variability in the differential velocities of K giants is continuing to grow. Long-term ($\geq 1 \text{ yr}$) periods have previously been verified for α Bootis, γ Cephei, β Geminorum, and α Tauri (Irwin et al., 1989; Walker et al., 1992; Larson et al., 1993a; Hatzes and Cochran, 1993). Other possible long-term variables include α Hydrae and α Arietis (Walker et al., 1989), and γ^2 Delphini. Of these stars, multiple, short-term (\approx few days) periods in the differential velocities have been confirmed for α Boo (Smith et al., 1987; Hatzes and Cochran, 1994a). Periods of less than one day have been claimed for β Gem (McMillan et al., 1994) and β Ophiuchi (Hatzes and Cochran, 1994b).

This thesis continues the discussion of the low-amplitude variability of K

giants. Our discovery of the long-term period for β Geminorum (Larson et al., 1993a) was made independent of the Hatzes and Cochran (1993, hereafter HC93) study and is discussed first in this section. Our detection of a similar, but weak, period in the $\Delta EW_{866.2}$ index lends support to the rotation hypothesis, but the derived rotation period then conflicts directly with the most reliable published value of the $v \sin i$ for β Gem. This thesis adds another K giant to the variable list: δ Sagittarii⁶. This comparatively little-studied star has 293- and 1.98-dy aliased periods in the differential radial velocities. δ Sgr also has a long-term trend in the radial velocities, $\Delta EW_{866.2}$ index, and $\Delta(R - I)$ index which may be related to active regions on the star. We review the long-term period detected in α Tau in the context of the lack of any corresponding periods in the $\Delta EW_{866.2}$ and $\Delta(R - I)$ indices. In addition, we discuss the new discovery of a 1.84-dy period in the relative radial velocities of α Tau; possible short-term periods in the radial velocities of this star were previously suggested by HC93. α Tau may exhibit variability on even shorter time scales, and the discussion of a possible ~ 30 -min period concludes this section.

β Geminorum

We obtained the observations for β Gem at the 3.6-m CFHT and at the 1.22-m telescope at DAO. Table A.2 lists the results from the CFHT observations. The average continuum signal-to-noise ratio of these spectra is 1400 per pixel. The average exposure time was 110 seconds. Table A.3 lists the RV results from the DAO observations. The DAO spectra have an average continuum

⁶This work has been submitted to the *Astronomical Journal*

signal-to-noise ratio of 720 per pixel. The average exposure time was 1760 seconds.

Periodogram analyses and non-linear least-squares results: The analysis program uses the peaks of the normalized weighted periodogram as starting approximations for non-linear, least-squares fits with one (or multiple) sinusoids (Irwin et al., 1989, Eqs. (5,13)). We limited our periodogram analyses to periods greater than 40 days, which roughly corresponds to the minimum rotation period expected from the $v \sin i$ for this star (see discussion below).

Figures 2.12 and 2.13 show the CFHT and DAO velocities with the best least-squares sinusoidal fit superimposed. Table 2.3 gives the parameters of this fit where the fitting function is

$$\mathcal{F}(\gamma_{\text{CFHT}}, \gamma_{\text{DAO}}, K, t_i, T, P) = (\gamma_{\text{CFHT}} \text{ or } \gamma_{\text{DAO}}) + \mathcal{S}(K, t_i, T, P), \quad (2.8)$$

and the sinusoid function is

$$\mathcal{S}(K, t_i, T, P) = K \cos\left[\frac{2\pi}{P}(t_i - T)\right]. \quad (2.9)$$

γ_{CFHT} and γ_{DAO} allow for the different velocity zero points. The least-squares solution is in satisfactory agreement with both the CFHT and DAO data. As mentioned, HC93 independently determined a similar RV periodicity.

We combined the CFHT and DAO radial-velocity data sets and calculated the normalized periodogram from the residuals of independently fitted, weighted means of these data. Figure 2.14a shows the periodogram for the frequency range 0.0–0.025 cycles per day. The power level which corresponds

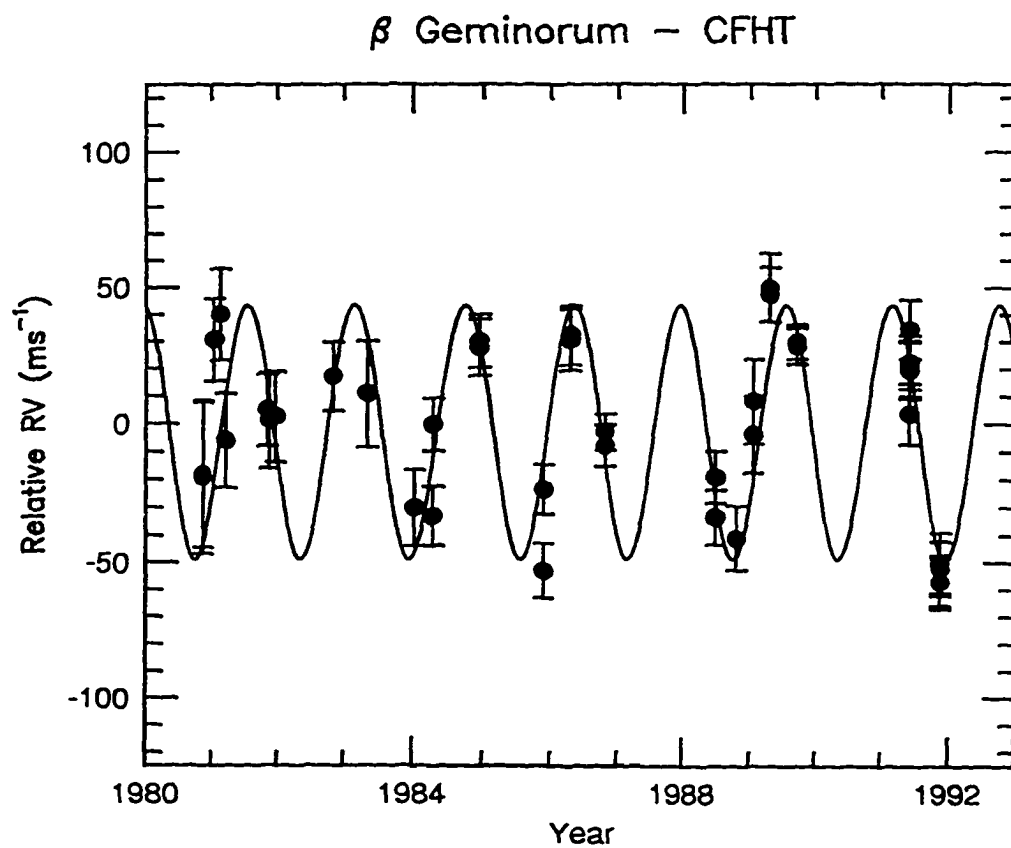


Figure 2.12: Relative radial velocity vs. time for the CFHT observations of β Geminorum (HR 2990). The best sinusoidal solution ($P = 584.65$ days, see Table 2.3) is shown superimposed.

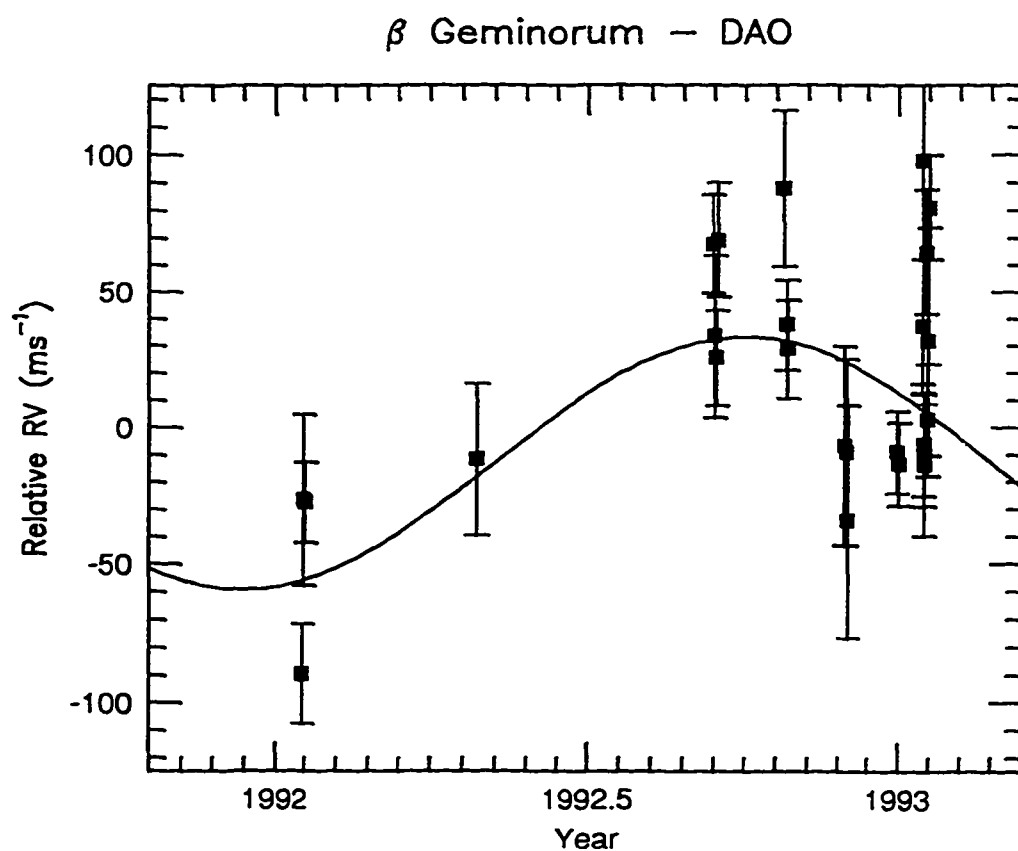


Figure 2.13: Relative radial velocities vs. time for the DAO observations of β Geminorum (HR 2990). For clarity, two early data points have been omitted. The best sinusoidal solution ($P = 584.65$ days, see Table 2.3) is shown superimposed.

Table 2.3: β Geminorum: periodic solution for relative radial velocities

parameter	value	σ	units
χ^2/ν	2.39		
γ_{CFRT}	-2.66	2.9	m s^{-1}
γ_{DAO}	-12.91	6.4	m s^{-1}
K	46.23	3.9	m s^{-1}
T^a	7142.92	6.9	dy
P	584.65	3.3	dy

^a JD - 2440000

to the 99% confidence level (Irwin et al., 1989) for this frequency range is also indicated.

Although the 585-dy period dominates the periodogram, a number of significant periods ($\geq 99\%$ confidence level) are also present which are aliases of this period; removal of the best solution dramatically reduces all other peaks (see Fig. 2.14b). For this frequency range, only one significant period at ~ 44 days remains, a period not present in the original periodogram. This 44-dy period may have a physical cause or may be an artifact of using an over-simplified sinusoidal model to represent the 585-dy periodicity.

The $\Delta EW_{866.2}$ index data (see Fig. 2.15a) show a long-term trend, which we fit with a quadratic. We add a sinusoid (Eq. 2.8) to model possible

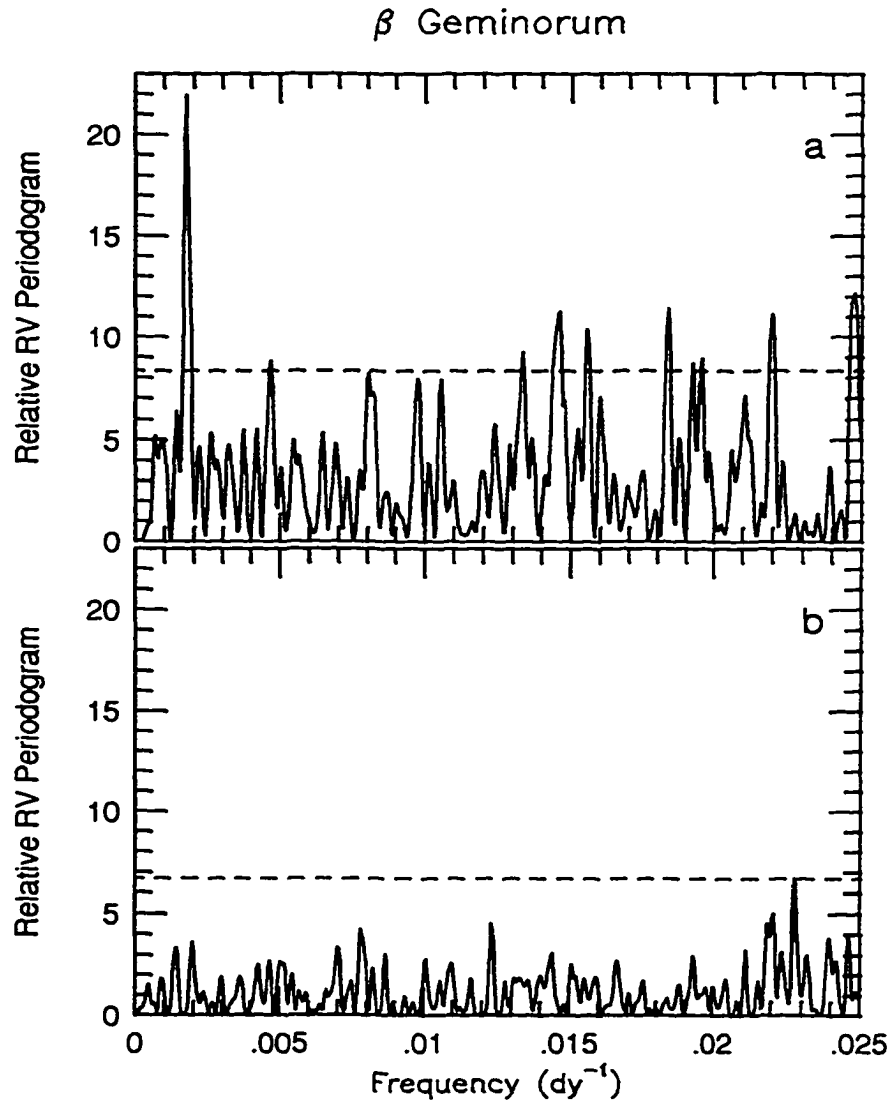


Figure 2.14: a) Weighted normalized periodogram of the residuals of the CFHT and DAO radial-velocity data from independently fitted, weighted means. b) Weighted normalized periodogram of the residuals of the CFHT and DAO radial-velocity data from the complete model given in Table 2.3. For both a) and b) the power level corresponding to the 99% confidence level (dashed line) is indicated.

Table 2.4: β Geminorum: quadratic plus periodic solution for $\Delta EW_{866.2}$

parameter	value	σ	units ^a
χ^2/ν	1.23		
a_0	1.19	0.19	pm
a_1	19.19	2.90	pm/JC
a_2	72.00	11.00	pm/(JC) ²
K	0.0583	0.019	pm
T	6506.3	21.0	dy
P	587.7	12.0	dy

^a JC \equiv Julian Century = 36525 days.

periodicity so that our final fitting function is

$$\mathcal{W}(t_i) = a_0 + a_1(t'_i) + a_2(t'_i)^2 + S(t_i, K, T, P), \quad (2.10)$$

where t_i is the epoch of observation (JD-2440000), and

$$t'_i = (t_i - 11545)/36525 \quad (2.11)$$

is the epoch of observation measured in Julian centuries since J2000. One of the best least-squares solutions for $\Delta EW_{866.2}$ has a period which coincides with that found in the radial velocities; Table 2.4 lists the parameters of the fitting function which contains this coincident period.

The quadratic trend shown in Table 2.4 is statistically significant, but could be the result of instrument instability. To explore this possibility,

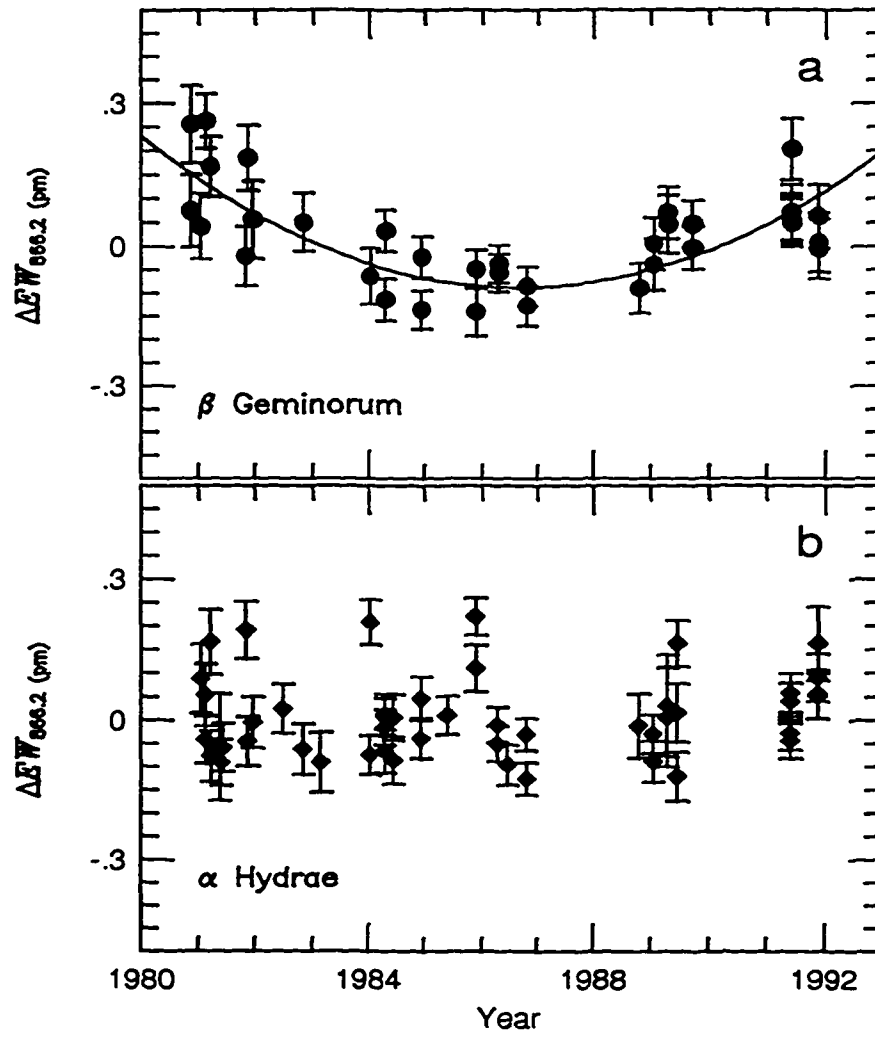


Figure 2.15: a) $\Delta EW_{866.2}$ vs. time for the CFHT observations of β Geminorum. The quadratic fit (Table 2.4) is shown superimposed. b) $\Delta EW_{866.2}$ versus time for the CFHT observations of α Hydrae.

we have compared the $\Delta EW_{866.2}$ results for β Gem with those of α Hydrae (HR 3748, K3 II-III), a star which was usually observed on the same nights under the same conditions. The lack of a long-term trend in these data (which might, however, show some intrinsic short-term variations, see Fig. 2.15b) supports the conclusion that we have detected actual long-term changes in the chromosphere of β Gem.

Although the $\Delta EW_{866.2}$ period of 588 days (Table 2.4) is one of the best solutions and is in good agreement with the period found in the RV data (Table 2.3), it has a very small amplitude, which is evident in the periodogram of the residuals from the quadratic trend (Fig. 2.16). Analysis of this periodogram indicates the peaks are aliases of each other; all peaks are reduced below the 2.5 power level by subtracting the 588-dy period. Furthermore, none of the periodogram peaks would be judged *on its own* to be significant at the 99% confidence level for a period search greater than 40 days. However, the calculation of this confidence level ignores the coincidence between the best peak in the velocity periodogram and the $\Delta EW_{866.2}$ peak at 588 days (compare Tables 2.3 and 2.4 and Figs. 2.14a and 2.16). It is well known that restricting the range of the period search reduces the confidence levels since there is less chance for the periodograms of randomized data sets to have large peaks in the more restricted period range. Of course, one cannot pick an arbitrary range around a favorite peak. However, in the present case where we have independent evidence of a well-defined period in the radial velocities, it is legitimate to ask the following question: what fraction of the periodograms of randomized data sets have higher levels than the observed $\Delta EW_{866.2}$ data in the range of the RV period, $\pm 3\sigma$ ($574.75 \leq P \leq 594.55$)?

When we investigate this question, we find that the agreement between the RV and $\Delta EW_{866.2}$ periods would occur by chance only 1 out of 100 times. Figure 2.17 shows the $\Delta EW_{866.2}$ residuals from the quadratic trend phased on the 588-dy period.

We emphasize that the $\Delta EW_{866.2}$ amplitude is so small that the 588-dy period is at the detection limit of our observation and reduction methods. For example, if we do not apply run corrections to $\Delta EW_{866.2}$, the peak is shifted out of coincidence with the RV peak (which is not significantly affected by the RV run corrections). However, we note that the similarity of the two periods in the run-corrected data cannot be due to the radial velocities influencing $\Delta EW_{866.2}$ measured from the same spectra. If that were the case, the large changes in the *apparent* radial velocity due to the Earth's orbital motion would result in a large peak in the $\Delta EW_{866.2}$ periodogram at one year. There is no such peak in the periodogram.

The periodogram analysis for the $\Delta(R - I)$ index shows no significant periodicities, even when we narrow the period range to $\pm 3\sigma$ from the RV period. In contrast to $\Delta EW_{866.2}$, no significant long-term trends were found in the $\Delta(R - I)$ data; these data are not shown here.

We ran numerical simulations to determine an approximate upper limit allowed by our data for the amplitude of a possible $\Delta(R - I)$ signal having the RV period. By adding sinusoids of varying amplitude but with phase and period identical to the RV solution given in Table 2.3, we determined that an amplitude of 0.002 in $\Delta(R - I)$ corresponds to a 99% confidence level for the narrow period range of $\pm 3\sigma$ from the RV period. We conclude that any $\Delta(R - I)$ variation at the RV period with an amplitude greater than 0.002

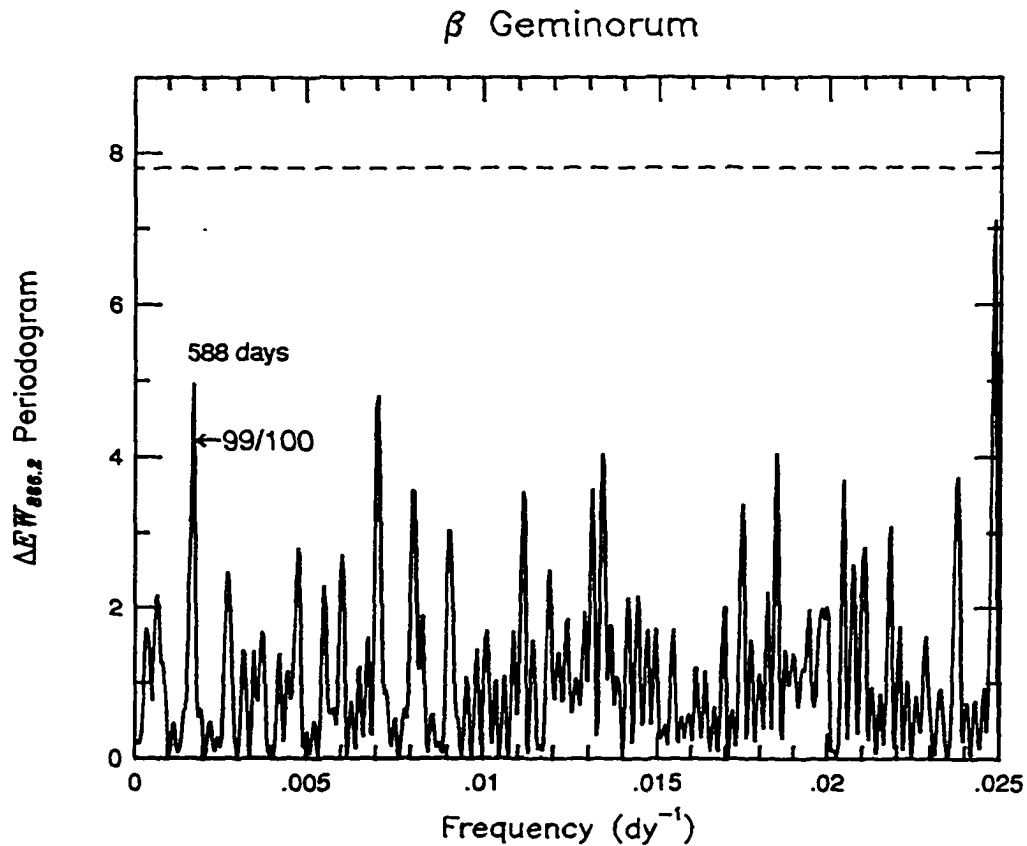


Figure 2.16: Weighted normalized periodogram of the residuals of the β Geminorum $\Delta EW_{868.2}$ data from the quadratic fit (Table 2.4). The power level corresponding to the 99% confidence level for the full period range has been shown by a dashed line. The power level corresponding to a 99% confidence level for the narrow period range, $574.85 \leq P \leq 594.55$, is indicated by the arrow.

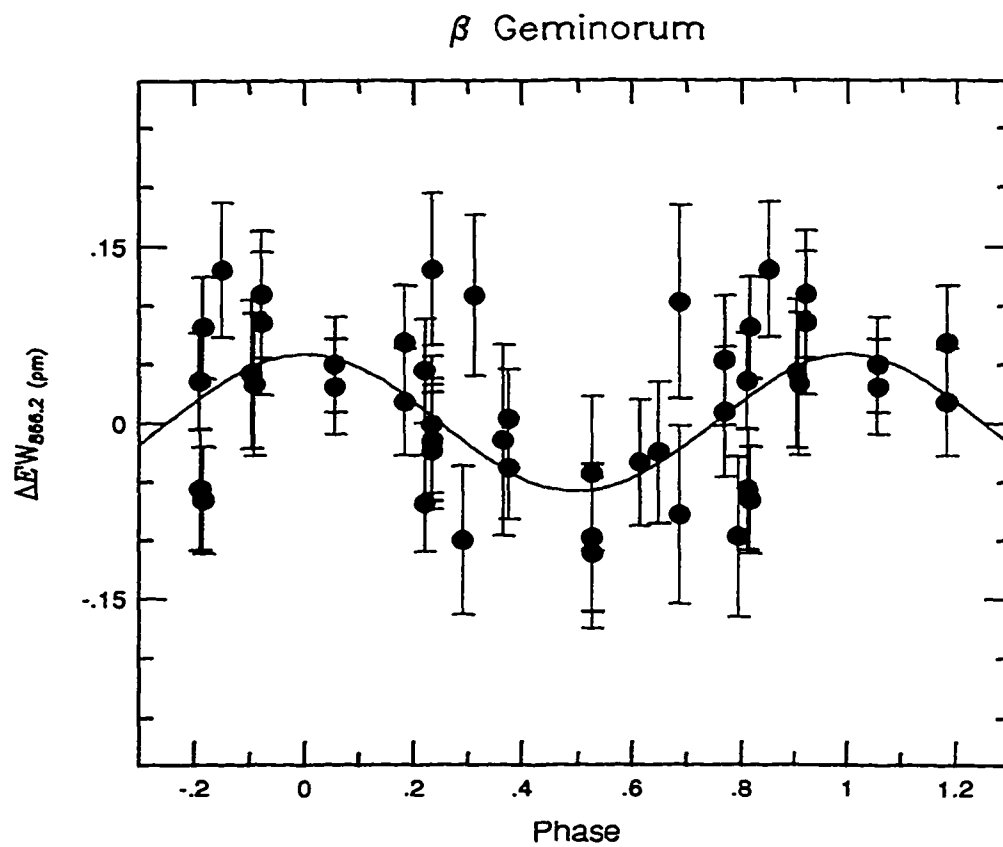


Figure 2.17: The residuals of $\Delta EW_{866.2}$ data of β Geminorum from the quadratic fit (Table 2.4) folded on the 588-dy period.

mag would probably have been detected by our technique.

Discussion: Is the quadratic trend in the $\Delta EW_{866.2}$ index due to a long-term chromospheric emission cycle? The time scale of the secular change in the chromospheric emission level of β Gem is consistent with the approximate 20-year magnetic cycle expected for giants (Hall, 1990, Table 2). Although the presence of solar-type cycles in the chromospheric emission level of dwarf stars has long been recognized (Baliunas and Vaughan, 1985), it has only been recently that these variations have been detected in higher luminosity classes. Dravins et al. (1993) studied the Mg II h and k emission in the G2 subgiant β Hydri (HR 98). The chromospheric variability in this star suggests the presence of a solar-type cycle with a periodicity in the range of 15-18 years. Preliminary evidence for long-term chromospheric emission cycles in giant stars (Baliunas et al., 1983a) was confirmed through a seven-year observational program of the four K0 Hyades giants (Saar and Baliunas, 1992, Fig. 20). In addition, Baliunas et al. (1991) have detected long-term variations in three of the giants in the Praesepe cluster. It will take at least another decade of observations to discover whether the long-term changes we see in the $\Delta EW_{866.2}$ index for β Gem are indeed cyclic.

Is the periodicity in the RV data and $\Delta EW_{866.2}$ index due to rotation modulation? We have used the parallax, angular diameter, and $v \sin i$ of β Gem to derive the stellar radius and the maximum predicted rotation period (Table 2.5). The stellar radius was obtained from the parallax (van Altena et al., 1991) and limb-darkened angular diameter (Di Benedetto and Rabbia, 1987). From $v \sin i = 2.5 \text{ km s}^{-1}$ (Gray, 1982), the upper limit of

Table 2.5: β Geminorum: stellar properties needed to derive rotation period

quantity	value	units	notes
π	0.0969 ± 0.0039	arcsec	1
ϕ	7.90 ± 0.31	mas	2
$v \sin i$	2.5	km s^{-1}	3
R/R_{\odot}	8.8 ± 0.5		4
P_{\max}	178	dy	5

¹⁾ van Altena et al. (1991)

²⁾ Di Benedetto and Rabbia (1987)

³⁾ Gray (1982); reliability of this value discussed in the text

⁴⁾ Derived from ϕ and π

⁵⁾ $P_{\max} = 2\pi R/(v \sin i)$; reliability of this value discussed in the text

the rotation period is

$$P_{\max} = 2\pi R/(v \sin i) = 178 \text{ dy.} \quad (2.12)$$

An approximate lower limit of

$$P_{\min} = P_{\max}/4.5 = 40 \text{ dy} \quad (2.13)$$

can be derived from probability arguments based on the distribution of randomly oriented inclinations; rotation periods less than 40 days should occur for only 2.5% of a random sample of stars with the β Gem radius and $v \sin i = 2.5 \text{ km s}^{-1}$.

If the 585-dy RV period and the similar $\Delta EW_{866.2}$ period are due to rotation modulation, then they are inconsistent with P_{\max} inferred from Gray's

(1982) value of $v \sin i$ for β Gem. (If the hypothesized surface phenomenon has a periodic pattern in longitude, then rotation modulation would lead to observed periods which are shorter than the actual rotation period; this would make the inconsistency with P_{max} and $v \sin i$ even worse.) The disagreement would be resolved if the actual $v \sin i$ value were less than 0.76 km s^{-1} . We note that Smith and Dominy (1979) have derived $v \sin i = 0.8 \pm 1.0 \text{ km s}^{-1}$ for β Gem, but we feel Gray's value is more reliable because his result is based on more lines in spectra with higher signal-to-noise ratios. In addition, the reliability of Gray's $v \sin i$ values has been confirmed for other stars. For example, Campbell and Garrison (1985, Table 1) have found good statistical agreement between rotation periods derived from $v \sin i$ values and those measured through rotation modulation of Ca II H and K emission. Furthermore, none of the inferred $\sin i$ values significantly exceed unity. These comparisons were for dwarf stars. Additional confirmation of the reliability of Gray's $v \sin i$ values has been obtained for two Hyades giants. Saar and Baliunas (1992) note an approximate S -index rotation period of 120 days for θ^1 Tauri (HR 1411) and γ Tauri (HR 1346). We used a Hyades distance modulus of 3.35 (Peterson and Solensky, 1988), and the Barnes-Evans relationships (Barnes et al., 1978; Di Benedetto and Rabbia, 1987) to derive radii and P_{max} values. From $v \sin i = 3.4 \text{ km s}^{-1}$ for θ^1 Tau and $v \sin i = 2.4 \text{ km s}^{-1}$ for γ Tau (Gray, 1982), we obtain $P_{max} \approx 175$ and 275 days, respectively. These values are consistent with the 120-dy rotation periods measured for these stars. Thus, there is no evidence that Gray has overestimated the $v \sin i$ values by the factor of three required to reconcile P_{max} with the 585-dy RV period and similar $\Delta EW_{866.2}$ period observed for β Gem.

Consideration of γ Cephei results provides only a slight additional constraint on the rotation modulation hypothesis. Because γ Cep has an even longer period than β Gem, explaining this period by rotation modulation demands that the $v \sin i$ must be less than 0.3 km s^{-1} (Walker et al., 1992). Unfortunately, only an upper limit of 0.8 km s^{-1} has been obtained for $v \sin i$ (Gray and Nagar, 1985) so we have no direct evidence ruling out the rotation modulation hypothesis for this star. The $\Delta EW_{866.2}$ index is sensitive to conditions in the chromosphere (see Sec. 2.1.2), while the radial velocities (which exclude the 866.2 nm line) are derived from much weaker lines which are sensitive to conditions closer to the photosphere. For γ Cep we find $K_{\Delta EW_{866.2}}/K_{RV} = 0.0034 \text{ pm/m s}^{-1}$ (Walker et al., 1992), while in the present work for β Gem, $K_{\Delta EW_{866.2}}/K_{RV} = 0.0013 \text{ pm/m s}^{-1}$. This difference would argue against one coherent mechanism to explain the periods observed in these two stars of similar spectral type. However, this does not argue strongly against the rotation modulation hypothesis; each star could have independent chromospheric and photospheric activity which is being modulated by rotation.

Rotation or revolution?: With our present data, the rotation versus revolution question cannot be resolved for β Gem. There are at least two possible interpretations of the periods discussed above. 1) If the observed $v \sin i$ value can be revised from 2.5 km s^{-1} (Gray, 1982) to less than 0.76 km s^{-1} , then the RV and $\Delta EW_{866.2}$ periods we find are probably best interpreted as rotation modulation of (possibly independent) photospheric and chromospheric phenomena. 2) Alternatively, if the currently observed $v \sin i$

is reliable, we could explain the RV period and amplitude as evidence that a low-mass companion ($M_2 \sin i = 2.5$ Jupiter masses, if we assume a circular orbit) is revolving around the β Gem primary (with an assumed mass of $1.6 M_\odot$) at a distance of 1.6 AU. However, in this case of a reliable $v \sin i$, we must find some non-rotation mechanism to explain the $\Delta EW_{866.2}$ period.

δ Sagittarii

Because of its southerly declination, δ Sagittarii has not been intensely studied. As far as we know, the radial velocity of δ Sgr has been monitored on a long-term basis only by our program⁷ and that of Murdoch et al. (1993, hereafter MHC93). Our CFHT observations for δ Sgr are listed in Table A.4 and shown in Fig. 2.18. The average exposure time for the CFHT observations was 360 seconds; the average continuum signal-to-noise ratio is 1355 per pixel. The 6-yr gap in the data is due to our temporarily dropping this star from our target list. After significant periodicity in the differential radial velocities of δ Sgr was discovered while we were examining the variability of all of the giants in the HF program (Larson et al., 1993c), the star was returned to the target list at the CFHT and observed over shorter time intervals there and at the DAO. The DAO observations for δ Sgr are listed in Table A.5 and shown in Fig. 2.19. The average exposure time for these observations was 2400 seconds; the spectra have an average continuum signal-to-noise ratio of 320 per pixel. The $\pm 1\sigma$ mean internal error for each data type is also shown in Figs. 2.18 and 2.19. In addition to the periodic variability found in the differential radial velocities of δ Sgr, the CFHT data also show sig-

⁷This work has been submitted to the *Astronomical Journal*

nificant, > 12 -yr linear trends in the radial velocity, the $\Delta EW_{866.2}$ index of the Ca II 866.2 nm core emission (described above) and the $\Delta(R - I)$ index (Bohlender et al., 1992). Note that we have arbitrarily shifted the linear trend derived from the RV data of CFHT to match the DAO data shown in Fig.2.19 for comparison purposes. We discuss the linear trends first.

Linear trends: There are distinct linear trends in the RV data and the $\Delta EW_{866.2}$ and $\Delta(R - I)$ indices from the CFHT observations. The slopes of these trends, shown by the dotted lines in Fig. 2.18, are quantified by the second column, S , in Table 2.6. Using Eq. (6.3.11) of Press et al. (1986), we calculated the false alarm probabilities, FAP, for the F statistic, comparing the sum of squares of the residuals for a model with no slope and one with a slope determined by a least-squares fit. The last column of Table 2.6 shows that all of the trends are significant, although marginally so for the $\Delta(R - I)$ index.

The source of these long term trends is unclear. The correlations may represent one coherent mechanism, or, indeed, each slope may have a different physical cause. In the next paragraphs, we discuss two scenarios which support a single mechanism, as well as the possibility for independent mechanisms.

One possibility which is consistent with all three trends is a general increase in the number and/or size of active regions, if, like very young stars, δ Sgr funnels this activity primarily into dark spots or spot groups rather than faculae or the brighter, more extensive plages (Radick et al., 1990, hereafter RLB90). The Sun changes luminosity during its activity cycle, becoming

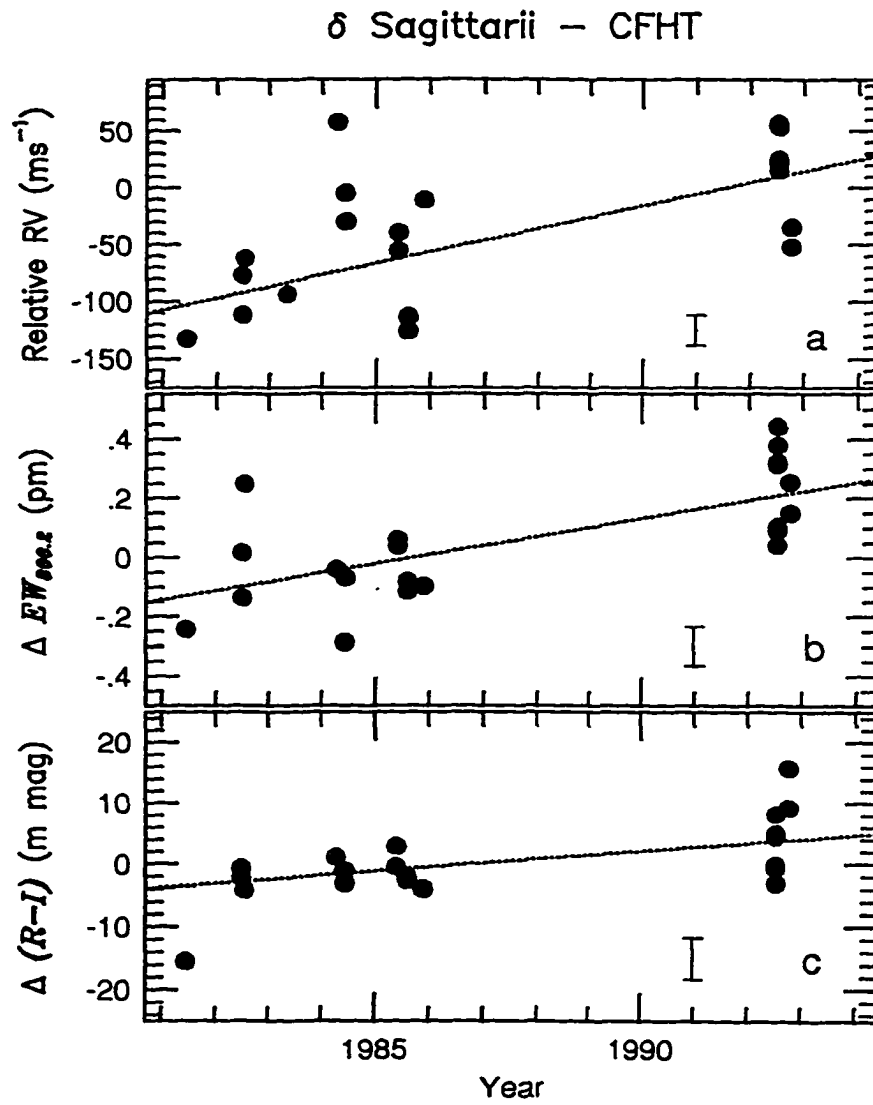


Figure 2.18: The data from CFHT observations vs. time for δ Sagittarii (HR 6859). The details of the linear trends, derived from a least-squares fit to each data set, are given in Table 2.6. The $\pm 1\sigma$ mean internal error is shown for each data type.

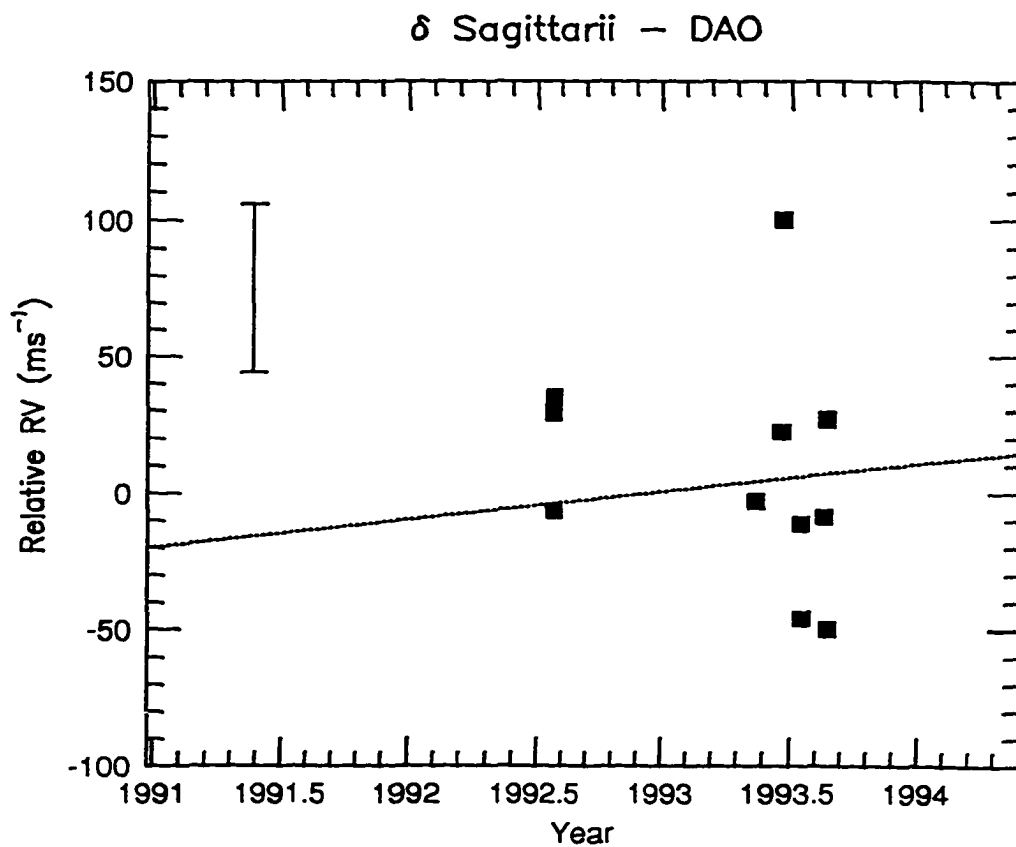


Figure 2.19: The data from DAO observations vs. time for δ Sagittarii (HR 6859). The linear trend is derived from the CFHT RV data and shifted to match the DAO data. The $\pm 1\sigma$ mean error is given by the error bar.

Table 2.6: δ Sagittarii: CFHT data linear trends and F -test results

data	S	units	ν	$F_{1,\nu}$	FAP ^a
RV	1016.2 ± 21.0	$\text{m s}^{-1}/\text{JC}^b$	21	23.26	0.0001
$\Delta EW_{866.2}$	3.043 ± 0.76	pm/JC	20	16.05	0.0008
$\Delta(R - I)$	65.26 ± 25.0	mmag/JC	20	6.80	0.0173

^a False alarm probability (Press et al., 1986)

^b JC \equiv Julian Century = 36525 days

brighter as activity increases. Like the Sun, other middle-aged dwarfs show a correlation between the increase in the chromospheric activity, luminosity, and effective temperature (Gray and Baliunas, 1995, and references therein). However, extensive monitoring of the Ca II H and K lines in young, active stars has shown that, unlike the solar-type stars, the young dwarfs become less luminous and cooler as their chromospheric activity increases (RLB90, Figs. 4 and 5). If we are observing growing regions of star spots on δ Sgr, our data imply that these regions have a lower temperature, thus a low plage-to-spot ratio. In general, we expect to see changes in the differential radial velocities due to the line asymmetries caused by large, dark spots as the absorption profile samples different depths and therefore different velocity fields. More long-term monitoring of the chromospheric activity in a much larger sample of K giants is needed for a better understanding of how the magnetic activity in these stars manifests itself.

Another possibility which argues for one, coherent mechanism is that we are detecting a decrease in the integrated convective blueshift and thus a corresponding decrease in temperature, with the $\Delta EW_{868.2}$ index responding, in step, to some nonradiative heating mechanism. The convective blueshift of a line profile reflects the fact that the rising convective elements are hot and the sinking elements are cool. Thus, even a small change in the temperature of the rising elements would look like a redshift in the differential radial velocities.

Observationally, there are ways to distinguish between these two scenarios. Spectrum synthesis may be used to model fractional coverage of the star as one searches for and measures features that would be produced only in star spots. For example, TiO bands can be used as a feature in the stars with $T_{eff} \geq 4325$ (Neff et al., 1995). We are examining this possibility for δ Sgr. One would expect, to first order, that the effects of the radial velocity fields of the large, dark spots are wavelength independent; on the other hand, the intensity contrast between the rising and falling elements of the convection granules would be greater in the blue. The MHC93 observations were centered around 520 nm; a plot of the data given in their Table 1 shows a steeper slope than our data, giving some support to the convective blueshift hypothesis (but see discussion below).

Alternatively, the slope in the the radial velocity may be due to a low mass companion, or unknown surface feature, and those in the $\Delta EW_{868.2}$ and $\Delta(R - I)$ indices to different, intrinsic features. Based on our review of other stars in our CFHT sample, we do not believe the slopes are due to instrumental drift (cf. Fig. 2.3). While we note a correlation between changes

in the radial velocity and the $\Delta EW_{866.2}$ index for γ Cep and the G5 dwarf κ^1 Ceti (Walker et al., 1992; Walker et al., 1995), other stars show no correlation. These results underscore the possibility that a number of different mechanisms may be contributing to the variability in these stars.

The slope in the data from the MHC93 observations of δ Sgr is significant (see their Table 3, column 6). We used the F test to compare the fit of their data constrained to our slope and a model having a slope derived from a least-squares fit to their data. The false alarm probability from this test was an inconclusive 0.045. Because of the limited number of observations (the MHC93 data span only 2 years) and the large scatter in their data, they list this star only as a “possible” variable. We have not used these data in the analysis which follows.

Periodogram and non-linear least-squares analyses: We combined the CFHT and DAO radial velocity data of δ Sgr and used the correlated periodogram (Walker et al., 1995, Appendix) to identify significant periods, defined as being $\geq 99\%$ confidence level, within the frequency range 0.9 days to 10 years. The parent function, the parameters of which are allowed to adjust under the correlated method, consisted of independent means for the CFHT and the DAO data plus a linear trend.

Although there are a number of periods in the data which satisfy our 99% confidence level criterion, we identify and discuss only the periods corresponding to the *two* strongest peaks in the periodogram, i.e., those at 1.98 and 293 days. We have marked these two periods in Fig. 2.20 where we show the correlated periodogram for frequencies $\leq 0.555 \text{ dy}^{-1}$. (Note that

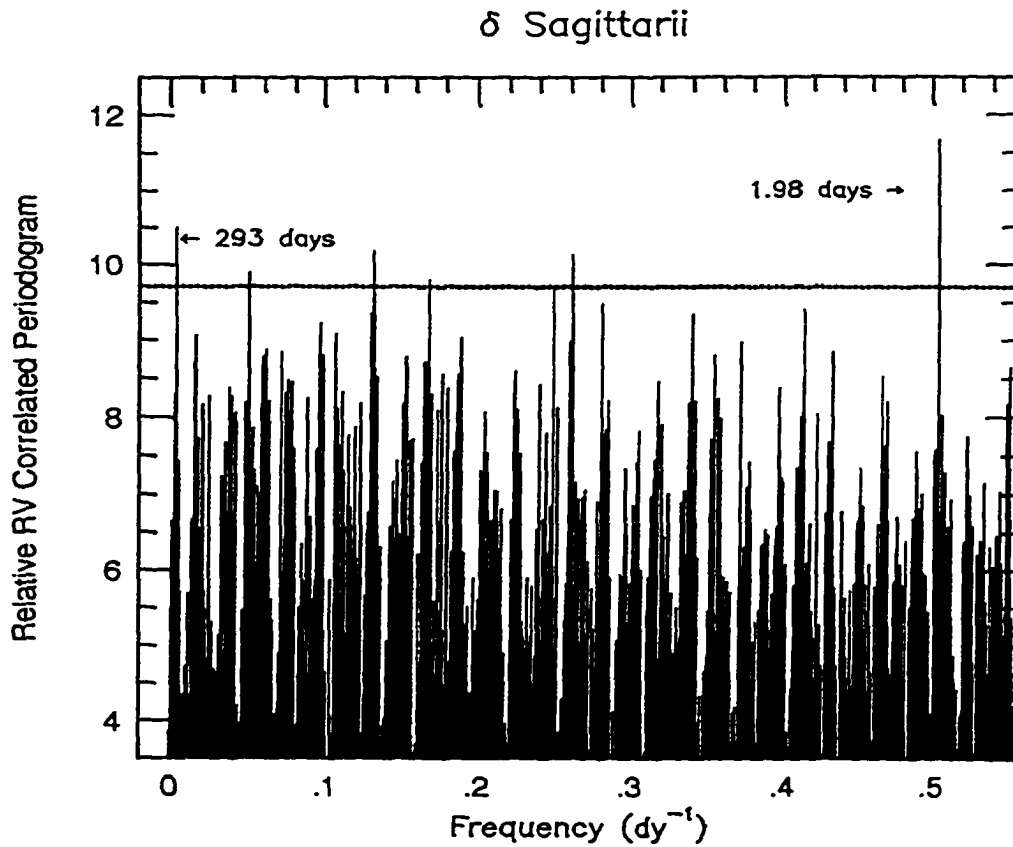


Figure 2.20: The correlated periodogram of the relative radial velocities for δ Sagittarii for periods between 10 years and 1.8 days. The two most significant periods greater than ~ 1 day are marked. The dotted line corresponds to the 99% confidence level. For display purposes, we have excluded values of the periodogram < 3.5 .

sidereal or synodic aliasing of our data produced two very significant peaks at frequencies of ~ 1 day, but there are no other peaks stronger than the 1.98- and 293-dy periods indicated in Fig. 2.20.) We have established that the 1.98- and 293-dy RV periods are aliases of each other: removing either period from the data significantly reduces the periodogram peak at the other period. Thus, based on this analysis alone, we cannot determine which is the true period; δ Sgr was not observed extensively enough over short time intervals to confirm or dismiss the 1.98-dy period.

Once we narrowed the period search under the periodogram analysis, we used a non-linear, least squares fit (Irwin et al., 1992, Eqs. (5, 13)), with a slope and a single sinusoid to model possible periodicity so that our final fitting function is

$$\mathcal{F}(\gamma, S, K, t_i, T, P) = (\gamma_{\text{CFHT}} \text{ or } \gamma_{\text{DAO}}) + S[(t_i - 11545)/36525] + K \cos \left[\frac{2\pi}{P}(t_i - T) \right], \quad (2.14)$$

where $t_i = \text{JD} - 2440000$. We list periodic solutions for both the 1.98- and 293-dy periods in Table 2.7 with the formal least-squares error for each quantity. Figure 2.21 shows the residuals folded on the exact 1.9838- and the 293.11-dy periods.

For two other K giants, γ Cephei (Walker et al., 1992) and β Geminorum (discussed above), we found similar periods in the RV and $\Delta EW_{866.2}$ data for each star, which lends support to rotation modulation of the radial velocities (although the case for β Gem is less certain). We cannot use these indices in the case of δ Sgr. Since there are fewer observations for δ Sgr, and the number of data for the $\Delta EW_{866.2}$ and $\Delta(R - I)$ indices is even smaller because of

Table 2.7: δ Sagittarii: relative radial velocity sinusoidal solutions^a

parameter	value	σ	units
χ^2/ν	2.34		
γ_{CFHT}	105.89	10.14	m s^{-1}
γ_{DAO}	84.79	13.36	m s^{-1}
S	1003.69	88.64	$\text{m s}^{-1}/\text{JC}^b$
K	82.07	9.09	m s^{-1}
T^c	7759.003	0.016	dy
P	1.983800	0.000021	dy
χ^2/ν	3.18		
γ_{CFHT}	83.88	27.51	m s^{-1}
γ_{DAO}	94.26	24.24	m s^{-1}
S	878.96	187.66	$\text{m s}^{-1}/\text{JC}^b$
K	68.75	9.80	m s^{-1}
T^c	7878.673	8.312	dy
P	293.11	1.01	dy

^a The periods are aliases of each other (see text)^b $\text{JC} \equiv \text{Julian Century} = 36525 \text{ days}$ ^c $\text{JD} - 2\,440\,000$

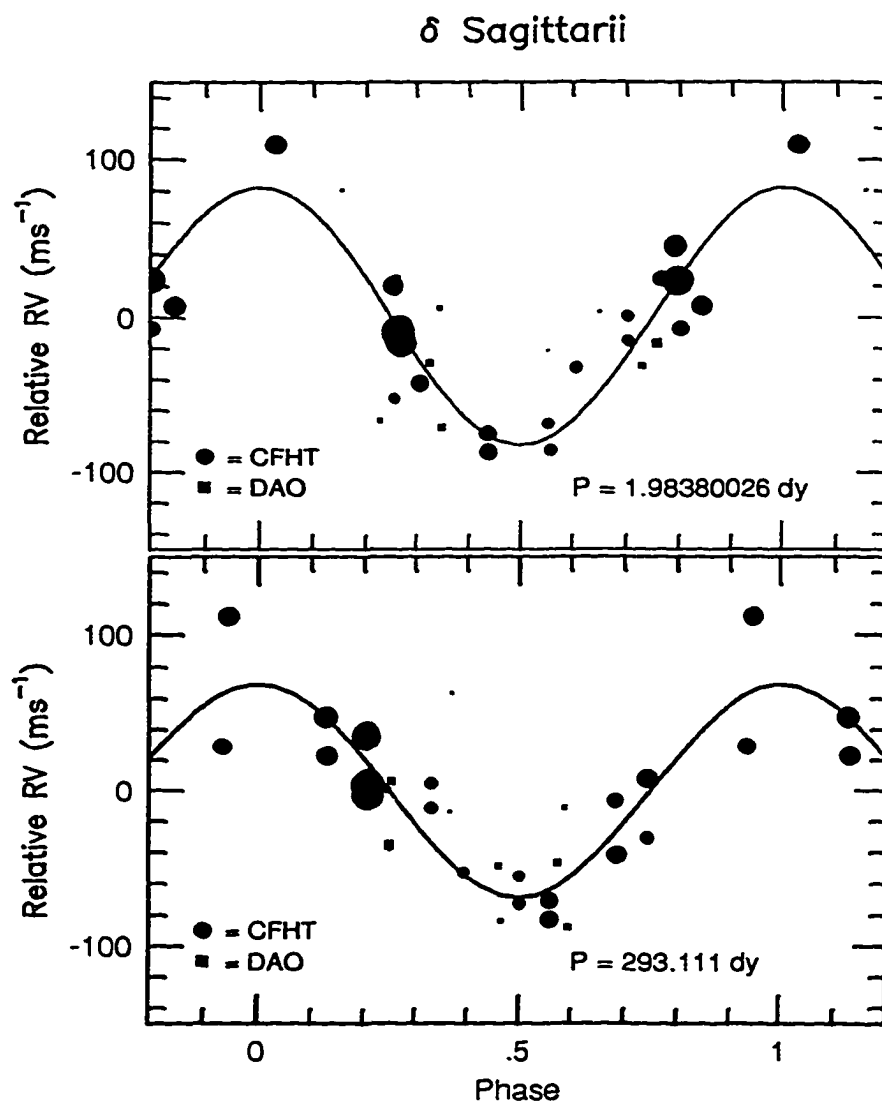


Figure 2.21: The CFHT and DAO data (individual weighted means subtracted) for δ Sagittarii folded on the best-fitting, short- and long-term, aliased periods (see Table 2.7).

the elimination of the DAO data due to fringing and fixed-pattern noise in the spectra, the aliasing of the data becomes more severe. We examined the periodograms for the $\Delta EW_{866.2}$ and $\Delta(R - I)$ indices specifically around the 1.98- and 293-dy aliases detected in the RV data, and did not find any coincident periods.

Period constraints based on stellar parameters: Can we constrain the aliased periods found in the differential velocities of δ Sgr based upon stellar parameters (Table 2.8)? The most uncertain, measureable quantity listed in Table 2.8 is the trigonometric parallax. The Catalogue of Stars within 25 Parsecs of the Sun (Woolley et al., 1970) lists the parallax as 0.045 (probable error 0.011); the on-line Yale University Observatory parallax catalogue (van Altena et al., 1991) gives a smaller value of 0.0189 (standard error 0.0075), a 1.6σ difference. The lower, more recent parallax value implies an absolute magnitude M_v of -0.9 , which we adopt. This is luminous for a K2.5 III giant [average $M_v = 0.4$ (Allen, 1973)], but not inconsistent with the bright giant (IIIa) luminosity classification for δ Sgr. Warner (1969) gives a value of $M_v = -0.9$ determined from measures of K-line emission widths. If we correct Wilson's (1976) $M_v(K)$ value to a Hyades distance modulus of 3.35 (Peterson and Solensky, 1988), we get $M_v = -1.45$, in fair agreement with our adopted value. We did not find a measured $v \sin i$ value for δ Sgr and thus extrapolated the relationship given in Eq. (17.6) of Gray (1992) to derive the equatorial velocity and rotation period. Given the uncertainties in the stellar parameters listed in Table 2.8, neither the 1.98- nor the 293-dy period may be favored over the other.

Table 2.8: δ Sagittarii: stellar properties needed to derive fundamental and rotation periods

parameter	value	units	uncertainty	reference
parallax	0.0189	arcsec	40%	1
T_{eff}	4140	K	2%	2
$\log L/L_{\odot}$	2.47		.35	3
M	2.25	M_{\odot}	50%	4
ϕ	6.24	mas	5%	5
R	35	R_{\odot}	40%	derived
$Q(M,R)$	0.05	dy	50%	6
Π_0	7.3	dy	80%	derived
$V_{equatorial}$	2.1	km s^{-1}	?	7
P_{rot}	850	dy	?	derived

¹van Altena et al. (1991)²Bohlender et al. (1992)³B.C. from Gustafsson and Bell (1979)⁴Judge and Stencel (1991), Fig. 1⁵Di Benedetto and Rabbia (1987)⁶Cox et al. (1972)⁷Gray (1992), see text

If the 1.98-dy period is the true period, then radial or nonradial [$\ell = 0, \ell > 0$ for the spherical harmonics $Y_\ell^m(\theta, \phi)$] acoustic pulsation could account for the periodicity. To derive the radial pulsation constant, we used the empirical relationships given in Cox, King and Stellingwerf (1972), formulae which are applicable only to stars with radiative envelopes. Table 2.8 lists the derived fundamental period of $\Pi_0 = 7.3$ days. Since the presence of convection will tend to increase the calculated periods, it is not likely that the 1.98-dy period is the fundamental mode, but the period could conceivably be a modest overtone. Hatzes and Cochran (1994b) discuss the large uncertainties which result from extrapolating the work of Ando (1976) for nonradial pulsations in late-type stars to values of $1 \leq \ell \leq 4$. Given the added uncertainty in the parallax for δ Sgr, we believe it is premature to do a similar extrapolation for this star.

If the 293-dy period is the true period, the periodicity might be due to nonradial g -modes, to rotation modulation of intrinsic features, or to a low-mass companion. In general, g -modes have periods which are much longer than the radial fundamental mode; the 293-dy period would correspond to the expected g -mode eigenfrequency of radial order $n \approx 40$, if the degree is low (i.e., $n \gg \ell$). We will be investigating instabilities against such high modes in red-giant stars. As mentioned above, for the case of γ Cep and more weakly for β Gem, similar periods in the RV data and $\Delta EW_{866.2}$ indices suggest rotation modulation of the radial velocity due to intrinsic features. We are not able to establish or eliminate rotation modulation for δ Sgr because aliasing in the equivalent width indices (due to the much smaller number of data) masks any significant periods. The lack of a measured $v \sin i$ value

also hinders our analysis here. As Table 2.8 shows, we have not estimated a formal error for the equatorial velocity or the rotation period. For giants between spectral type G3 and K2, Gray (1992) argues for a single-valued relationship between rotation and spectral type. The statistical fluctuations in this relationship are probably dominated by the $\sin i$ distribution, with errors also present in the $v \sin i$ measurements of the stars he used and in the spectral classifications. Thus, although we list 850 days as the rotation period, the 293-dy period may be the actual period or a fraction of it. Alternatively, the 293-dy period could also be explained by a low-mass companion with $M_2 \sin i = 4$ Jupiter masses (assuming a circular orbit) at a semi-major axis of ~ 1.1 AU's.

α Tauri

With over 500 references to this star in the SIMBAD database, α Tauri has been the target of numerous observational and theoretical programs. Although the Bright Star Catalogue (Hoffleit and Warren, 1991) lists it as a spectroscopic binary, there is no evidence of a stellar companion in the differential radial velocities. The low-amplitude RV variability of α Tau (which is much too small to have been detected before precise RV techniques were used) was first mentioned in Walker et al. (1989), and discussed subsequently by Hatzes and Cochran (1993, HC93). This star has been mentioned as an irregular photometric variable; however, Krisciunas (1992) found no evidence of this.

α Tau was observed at both the CFHT and the DAO. The CFHT observations are listed in Table A.6 and shown in Fig. 2.22; only a subsample of

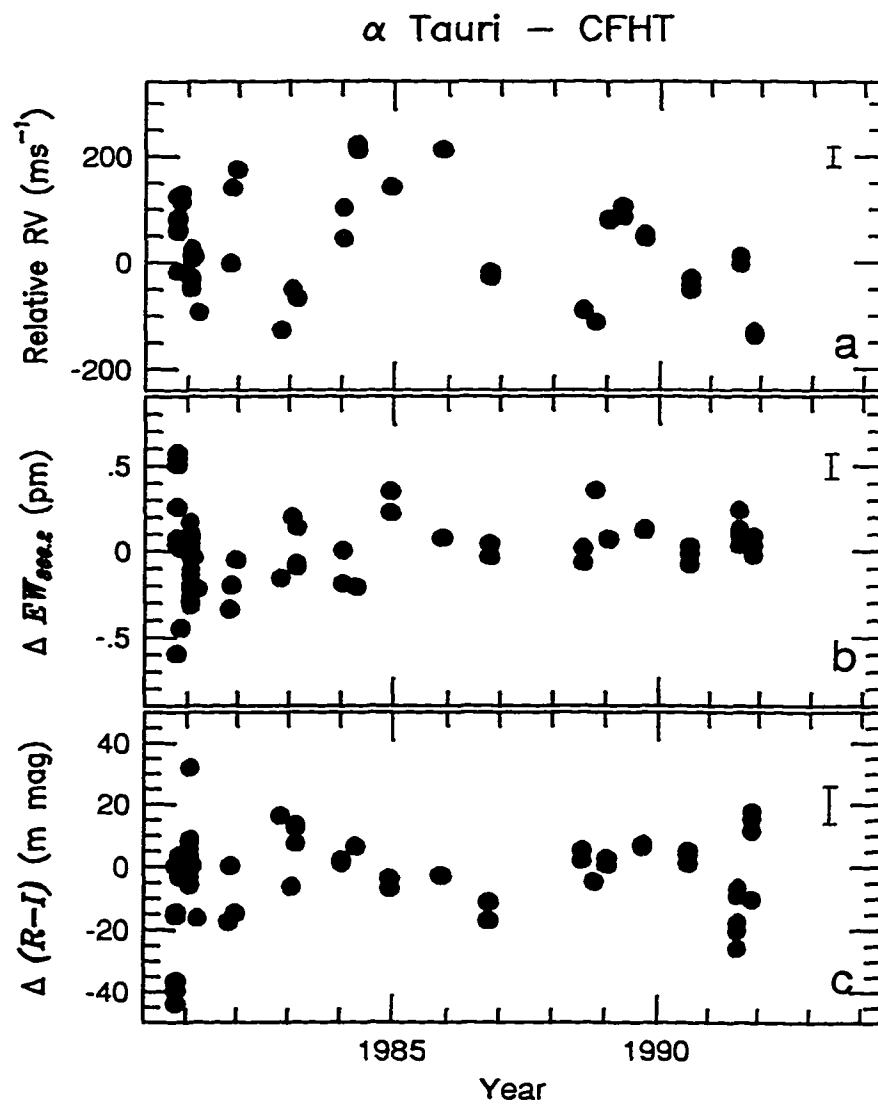


Figure 2.22: The CFHT data vs. time for α Tauri (HR 1475). The 1981 data include a subset of the time series observations. The mean internal errors are shown by the $\pm 1\sigma$ error bars.

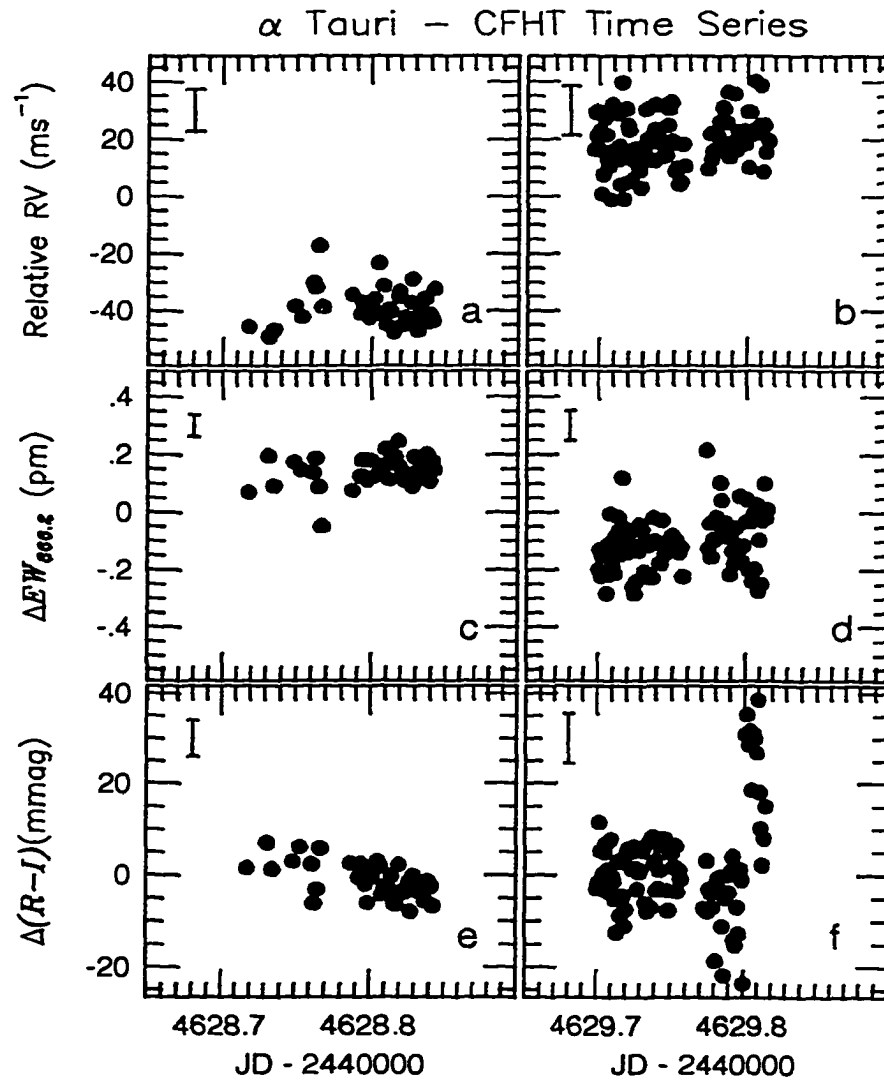


Figure 2.23: The 1981 CFHT time series data vs. time for the two nights of observations for α Tauri (HR 1475). The mean internal error is given by the $\pm 1\sigma$ errorbars. The abrupt change seen in the $\Delta(R - I)$ index on the second night is discussed in the text.

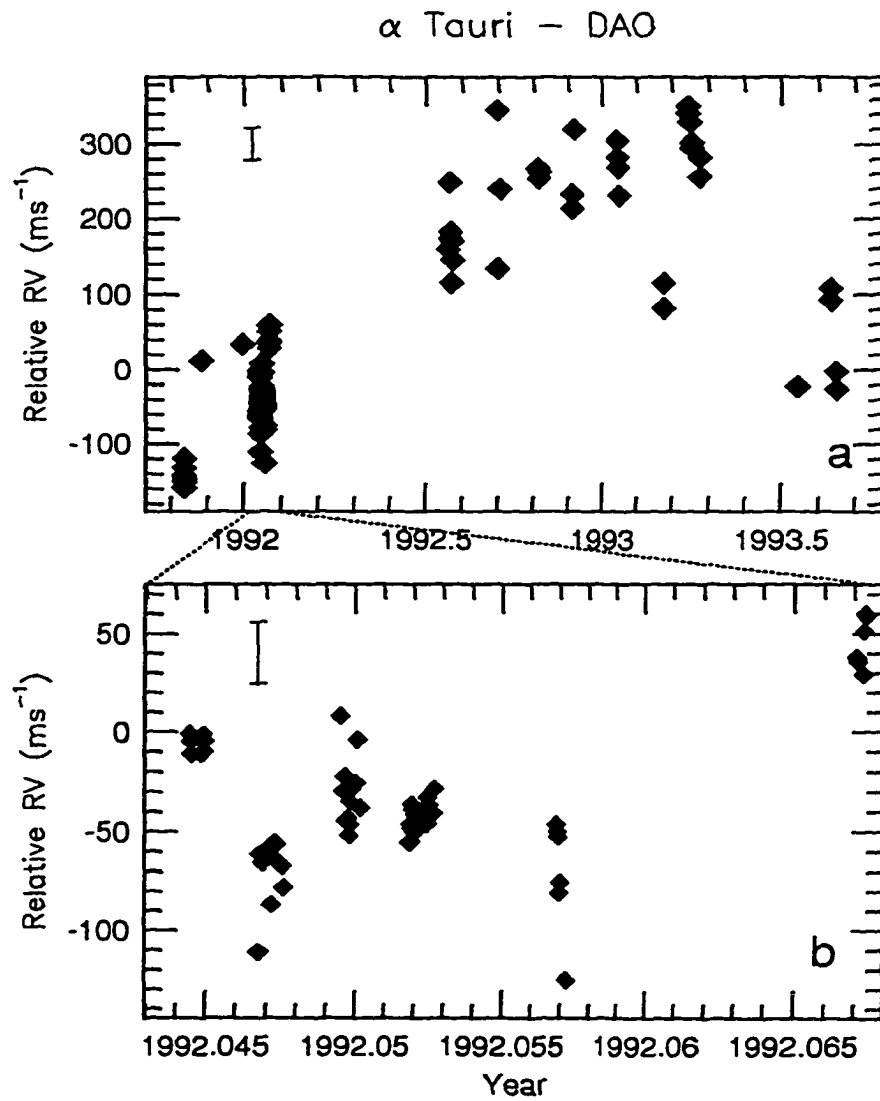


Figure 2.24: The DAO radial velocity data vs. time for α Tauri (HR 1475) for a) the complete data set and b) the time series from January 1992. The mean internal errors of a) 21.4 m s^{-1} and b) 15.6 m s^{-1} are shown by the respective $\pm 1\sigma$ error bars.

the time series from 1981 is given in Table A.6 and Fig. 2.22. The complete 1981 CFHT times series data are listed in Table A.7 and shown in Fig. 2.23. The typical exposure time for the CFHT observations is 1-2 minutes; the continuum signal-to-noise ratio is approximately 1400 per pixel. The DAO observations are listed in Table A.8, with nightly means given for the January, 1992 time series data. The 1992 time-series data are listed in Table A.9. Figure 2.24a shows all of the DAO data (Tables A.8 and A.9); Fig. 2.24b expands the DAO time series of January, 1992. The exposure times for the DAO observations range from 4 minutes to over 30 minutes; the continuum signal-to-noise ratio ranges from 150 to over 1600 per pixel. Tables A.6 and A.8 contain the data used in the periodogram analysis for periods greater than 100 days. In addition, for the long-term analysis, I included the HC93 data which were kindly provided by Dr. Hatzes. Tables A.7 and A.9 were used for the respective time-series periodograms.

α Tau shows RV variability on three levels: long-term ($10 \text{ yr} \geq P \geq 100 \text{ dy}$), short-term (\sim few days), and very short-term ($\ll 1 \text{ dy}$). The discussion in this section starts with analysis of the periodograms for the long-term period. This discussion is followed by the periodogram results of the DAO time-series observations from January, 1992, and an analysis of the CFHT time-series observations from January, 1981.

Long-term periodogram analysis and non-linear least-squares results: Figure 2.25 shows the weighted periodograms for the $\Delta EW_{866.2}$ and $\Delta(R - I)$ indices from the CFHT observations and the combined CFHT + DAO + HC93 radial velocity data. The parent functions are weighted means

for each data set. The dashed lines give the periodogram value corresponding to the 99% confidence level. Normally, one would not want to compare periodograms calculated using different data sets (i.e., CFHT $\Delta EW_{866.2}$ or $\Delta(R - I)$ index data versus CFHT + DAO + HC93 RV data) because aliasing will be different in each type of data. The periodogram for the CFHT RV data alone (not illustrated here) is similar to that of the combined set except that the periodogram value of the 648-dy period is reduced in the periodogram of the CFHT data to the same level as the next longest period. Combining the data reduces the aliasing and emphasizes the 648-dy period. The HC93 data were obtained using different instruments. The error in each measurement was quoted as being between 7 m s^{-1} and about 20 m s^{-1} ; I have assumed a mean internal error of 15 m s^{-1} for all HC93 observations as no individual errors were derived.

From Fig. 2.25 it is obvious that there are no coincident periods at 648 days in either the $\Delta EW_{866.2}$ or $\Delta(R - I)$ index. Except for a marginal signal at ~ 241 days in the $\Delta(R - I)$ index, there are *no* significant long-term periods (≥ 100 days) in these indices. The dotted line in Fig. 2.25 is the periodogram of the RV data after the 648-dy period was removed. Except for the peak corresponding to a period of ~ 1000 days, all other significant peaks are aliases of the 648-dy period. The 1000-dy period may be real or an artifact of the run-corrections; the period is not present in the HC93 data.

We followed the usual practice of using these periodogram results to search for sinusoidal solutions under a non-linear least-squares analysis. The best long-term RV periodic solution, derived from the combined RV data set, is given in Table 2.9; Fig. 2.26 shows these data phased on this solution. The

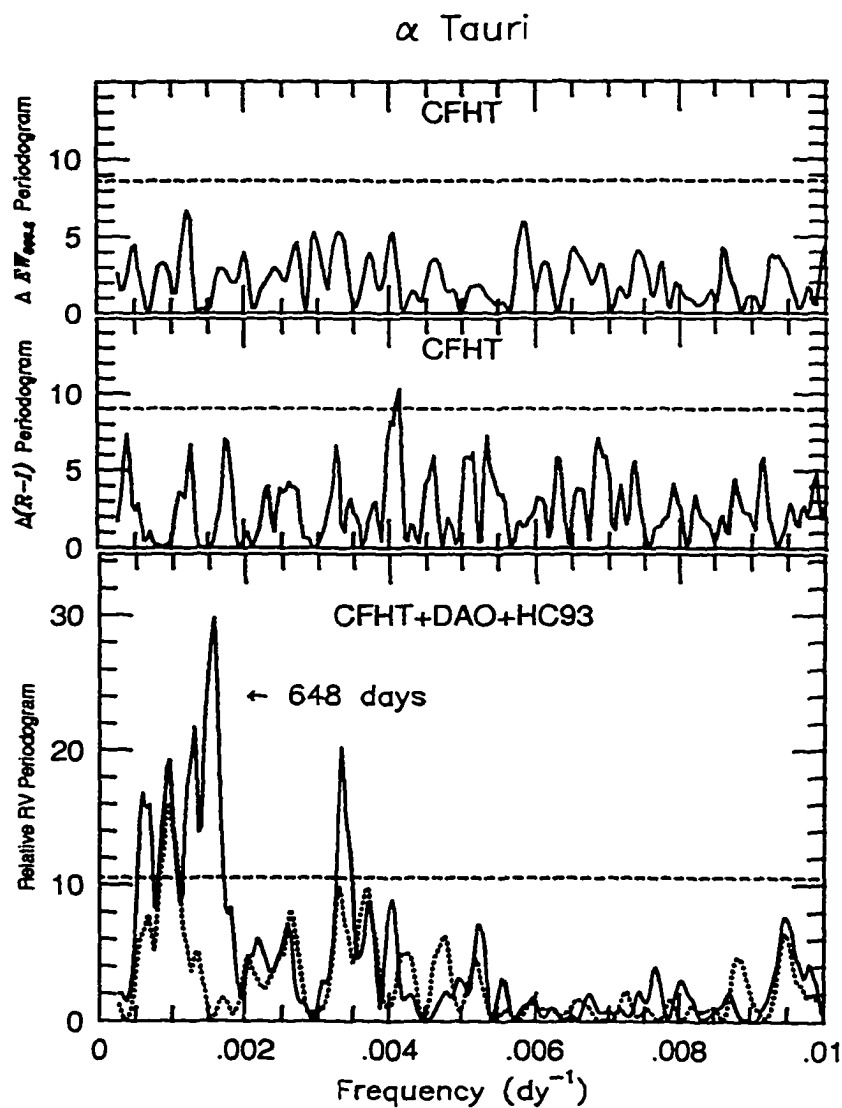


Figure 2.25: The weighted periodograms for α Tauri for $10 \text{ yr} \geq P \geq 100 \text{ dy}$. The dashed lines indicate the 99% confidence level. The dotted line in the RV periodogram represents the weighted periodogram after the 648-dy period was removed from the data and shows that all of the significant peaks are aliases of the 648-dy period except for one at ~ 1000 days.

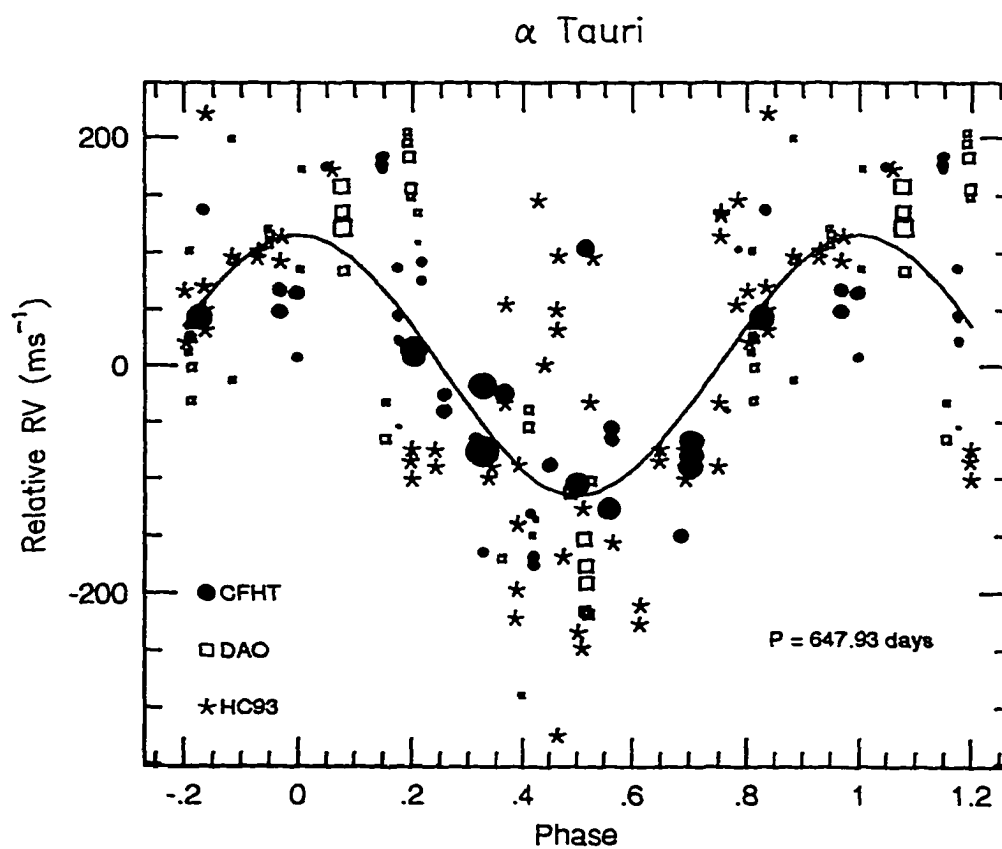


Figure 2.26: The relative radial velocities of α Tauri from observations obtained at the CFHT (filled circles), at the DAO (open squares) and by HC93 (stars) phased on a period of 647.93 days. For the CFHT and DAO data, the area of each data point is inversely proportional to the square of the internal error estimate for that point. Most of the scatter seen mid-phase in the HC93 data occurred over a short time period.

Table 2.9: α Tauri: long-term radial velocity periodic solution

parameter	value	σ	units
γ_{CFHT}	37.4	12.1	m s^{-1}
γ_{DAO}	146.5	17.2	m s^{-1}
γ_{HC93}	70.0	11.4	m s^{-1}
K	114.9	10.6	m s^{-1}
T^a	7658.29	9.17	dy
P	647.93	4.62	dy

^a JD -2 440 000

large scatter at mid-phase, which occurs mostly in the HC93 data (and over a short observation period), probably reflects a short-lived variability. This phase diagram exemplifies the difficulty of interpreting these data because short-term variability creates an added source of noise.

Table 2.10 lists the stellar properties needed to derive the periods for the fundamental pulsation and the rotation periods. This star has an accurate parallax and a measured angular diameter and $v \sin i$. The 648-dy period is well within the errors of the predicted rotation period and below the maximum rotation period of $P_{\max} = 2\pi R/(v \sin i) \approx 900$ days.

The underlying physical mechanism for the long-term period is not known, except that radial pulsation can be ruled out. If the radial velocities are being modulated by some surface phenomena, then these phenomena are such that either the chromosphere is not affected, or very weakly so, or any long-

Table 2.10: α Tauri: stellar properties needed to derive fundamental and rotation periods

quantity	value	σ	units	notes
π	0.0479	0.0035	arcsec	1
ϕ	20.21	0.30	mas	2
R	45	3	R_{\odot}	3
$v \sin i$	2.7	0.2	km s^{-1}	4
V_{eq}	3.4	1.2	km s^{-1}	5
P_{rot}	668	235	dy	3
\mathcal{M}	2.2	$+0.7$ -0.3	\mathcal{M}_{\odot}	6

¹ van Altena et al. (1991)² Di Benedetto and Rabbia (1987)³ derived⁴ Smith and Dominy (1979)⁵ $V_{eq} = (4/\pi) v \sin i$ ⁶ Judge and Stencel (1991)

term periodic signal which may be present escapes detection due to multiple phase shifts, dissipation of the radiative/nonradiative energy before the chromospheric layer is reached, or some other cause. The possibility for g -modes in giant stars was discussed with δ Sgr. The long-term solution for α Tau could be explained by an 11.4 Jupiter-mass planet at a distance of 2 AU from the star (HC93).

The 1.84-dy Period: Short-term radial velocity variations have been suspected for α Tau since the discussion in Walker et al. (1989); however, until the time-series observations at the DAO in 1992, there was not sufficient monitoring to determine if this variability was periodic. Figure 2.24b shows the observations from the six nights of observing in January 1992. Exposures for the time series were typically between 15 and 20 minutes; the average signal-to-noise in the continuum is 1320 per pixel. For two of the nights the observations spanned approximately 8 hours. This type of time coverage is ideal for finding periods of order 2-3 days, and as the weighted periodogram (Fig. 2.27) shows, a significant period of ≈ 1.84 days was detected, the only real period present in the data. The periods at 2.23 and 0.643 days are the sidereal aliases of this period; the 3.16-dy period results from the 4-dy gap in the observations. If I include all of the DAO data in the periodogram analysis, the results do not change significantly. Additional aliasing is created by the added gaps in the data when all of the DAO data are used, and the power in the 1.84-dy period is reduced, but the detection remains above the 99% confidence level. I used a mean as the parent function for the periodogram; note, however, that the parent function could be modeled by either a mean or a first- or second-order polynomial. The overall conclusions made here do not depend upon which function was chosen.

Figure 2.28 shows the data phased on the short-term period given in Table 2.11. The high data points at zero-phase reflect sporadic, short-term variability not unusual for this star. This increase in the RV could be analogous to a similar shift seen in the HC93 data (see Fig. 2.26).

The external errors of the DAO observations have been estimated as

Table 2.11: α Tauri: short-term radial velocity periodic solution

parameter	value	σ	units
γ_{DAO}	-36.1	2.7	m s^{-1}
K	32.0	5.0	m s^{-1}
T^a	8640.442	0.048	dy
P	1.8358	0.048	dy

^a JD -2 440 000

being $\sim 40 \text{ m s}^{-1}$, larger than the amplitude of 32 m s^{-1} for this period (see Table 2.11). However, we expect any systematic errors in the DAO data to be *much* smaller than 40 m s^{-1} during any single run where there are no instrument changes or realignment problems. There is no evidence that we have seriously underestimated our internal errors; the mean internal error for the time series data is 15.6 m s^{-1} compared to the mean internal error of 21.4 m s^{-1} for all of the DAO data. During this observing run, the observations of α Tau varied in length, the sampling in time differed, and the star was observed for two nights through a large change in air mass. Thus, especially given the significance of the detection, it seems unlikely that the 1.84-dy period is a spurious period. As discussed below, the analysis of the periodicities and scatter found in the relative radial velocities of this star is complicated by the fact that variability of order $30\text{-}40 \text{ m s}^{-1}$ (see Fig. 2.28 and 2.30) is observed over periods of less than one day.

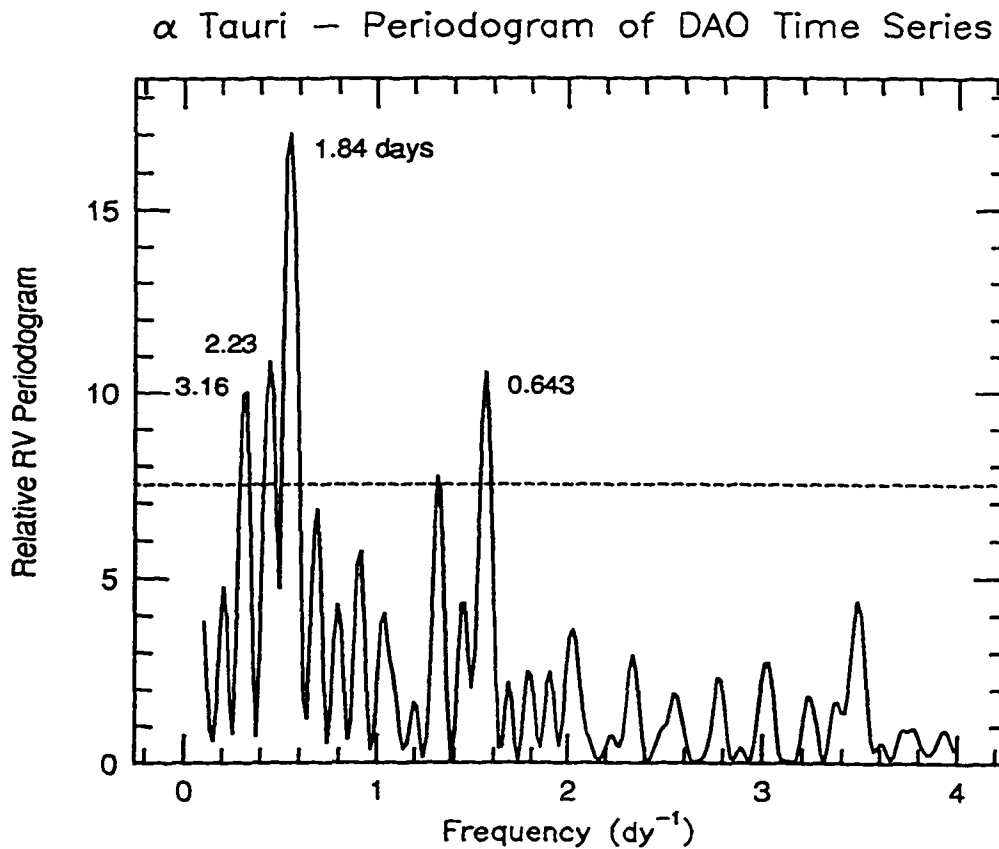


Figure 2.27: The weighted periodogram for the 1992 time series of the relative radial velocities of α Tauri for $10 \text{ dy} \geq P \geq 0.25 \text{ dy}$. The dashed line represents the 99% confidence level. The periods at 2.23 and 0.643 days are sidereal aliases of the 1.84-dy peak; the peak at 3.16-dy results from the 4-dy gap in the data.

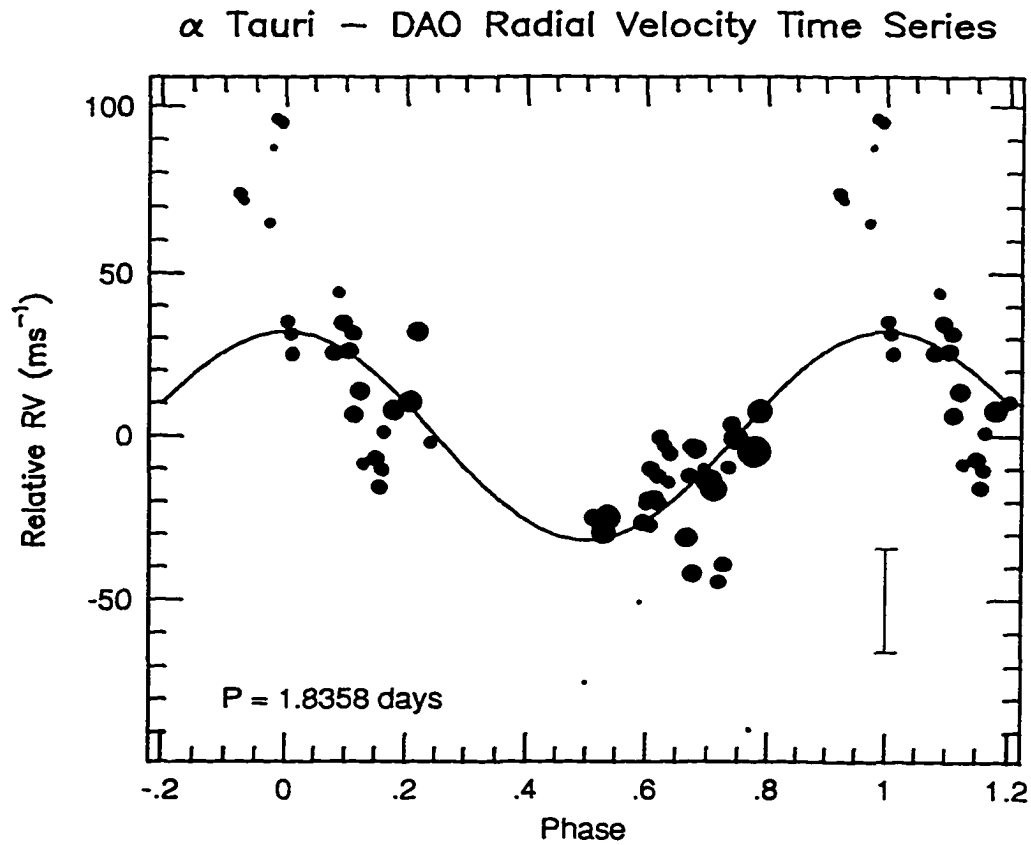


Figure 2.28: The DAO relative radial velocity time series data for α Tauri phased on the 1.8358-dy period. The mean internal error of $\pm 15.6 \text{ m s}^{-1}$ is shown by $\pm 1\sigma$ error bar. The area of each data point is inversely proportional to the square of the internal error estimate for that point.

There may be any number of driving mechanisms for the short-term period. The overall status of radial and nonradial pulsation in giants was covered in the discussion for δ Sgr. We discuss here the recent theoretical and empirical work on granulation-driven acoustic modes and the periods expected for the fundamental and overtone modes for the radial pulsation in α Tau.

Scaling Schwarzschild's (1975) work on convective elements of red giants, Judge and Cuntz (1993, hereafter JC93) predicted that α Tau should have about 500 surface granules. They combined this estimate with a fundamental treatment of convection theory and introduced perturbations having different wave properties (Table 2, JC93). Although their models were not particularly successful in reproducing the line profile of the C II] (semi-forbidden) line, they predicted, for optically thin lines, that if the chromosphere of α Tau were heated by granulation-driven acoustic waves then time series observations should show peak power at frequencies corresponding to periods of 2-3 days.

Carlsson and Stein (1992) investigated the vertical propagation of acoustic waves in a solar-type atmosphere and the role acoustic shocks play in profile changes of the Ca II K line. They find a steepening of small-amplitude waves, an increase in the velocity amplitude as the waves propagate upward, and eventually the formation of shocks. They predict that both short- and long-period waves may produce these shocks. The shocks will be separated by the acoustic cutoff period, $P_{ac} = 2c/\gamma g$, where c is the sound velocity, γ the ratio of the specific heats of gas, and g the gravitational acceleration (Unno et al., 1979, Eq. (9.4)). In the case of α Tau, this cutoff period is approximately four days at the top of the convection zone (JC93), of the

same order as the period we detect.

Additional theoretical work is needed to follow the granulation-driven acoustic modes as they propagate from the photosphere through the lower chromosphere. This work should specifically address the effect these acoustic modes will have on the core flux of the Ca II infrared triplet lines. The following hypotheses need to be examined for a red giant atmosphere. 1) Waves produced in the lower atmosphere layers undergo changes as they propagate outwards. Some waves may coalesce and form waves or shocks having different periods; thus periods detected from observations of photospheric lines (radial velocities) will differ from observations of chromospheric lines ($\Delta EW_{868.2}$ index). 2) Some waves survive and form shocks in the upper atmosphere; a phase shift will be detected which reflects the propagation time. 3) Some waves may undergo destructive interference and not propagate at all; periods will be detected in the radial velocities, but not in chromospheric lines. Extensive observations, over a number of runs of ~ 1 week each, of photospheric and chromospheric lines (preferably simultaneous observations) will help constrain the models and also give information concerning the time scales for coherence of these acoustic shocks. This work should begin as soon as possible.

The 1.84-dy RV period may reflect radial pulsation in α Tau. Although new calculations are needed for the pulsation constants for late-type giants, one can obtain a rough estimate of the period of the fundamental and first and second harmonics from the relationships given in Cox et al. (1972). These periods are shown in Fig. 2.29 for the mass and radius ranges applicable to α Tau. One notes from Fig. 2.29 that the fundamental mode should be of

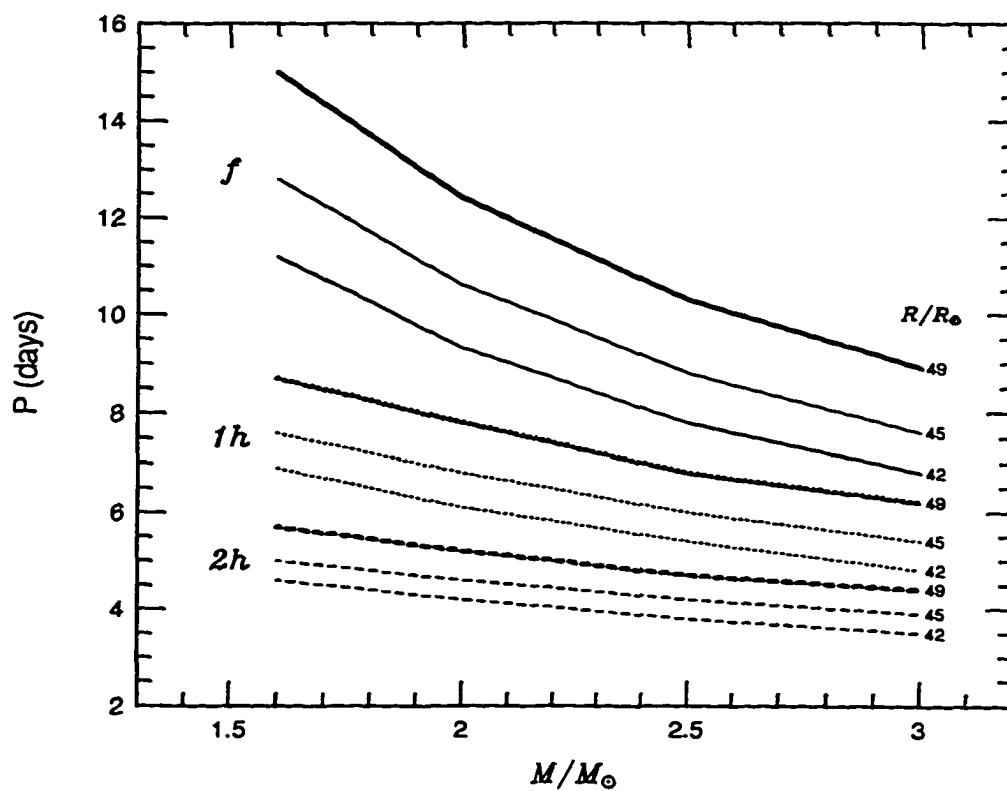


Figure 2.29: The fundamental and first two overtone theoretical pulsation periods for masses and radii applicable to α Tauri calculated from the fitting formulae of Cox et al. (1972).

order 10 days. The presence of convection will increase these periods; thus, it is also apparent from Fig. 2.29 that if the 1.84-dy period is radial pulsation, it must be one of the higher harmonics ($n \approx 4$).

The 30-minute period: The time series of α Tau from observations at the CFHT on January 23/24 and 24/25, 1981, are shown in Fig. 2.23 and listed in Table A.7. The exposure times for these data were 1-2 minutes; the average continuum signal-to-noise is 1360 per pixel.

Some interesting variability is seen in the data even over this short time interval. Besides the night-to-night variation in the radial velocities of ≈ 60 m s^{-1} , which may be related to granulation or overtone pulsation discussed above, the RV data for α Tau show a range of approximately 30-40 m s^{-1} on shorter time scales. Also, the $\Delta EW_{868.2}$ index shows an anticorrelation (which may correspond to a phase shift, see discussion below) with the radial velocity between the two nights. The $\Delta(R - I)$ index shows a considerable excursion around RJD 4629.8; the change of 60 mmag in the $\Delta(R - I)$ index corresponds to a decrease in the effective temperature of ~ 200 K in less than an hour. This sudden drop is then followed by a monotonic increase in the effective temperature. The internal errors for these data are approximately 7-10 mmag, compared to 3-6 mmag for the rest of the data for the second night. We have no explanation for this event.

Figure 2.30 shows the CFHT time-series data with a 1.8358-dy sinusoidal model superimposed. The amplitude and period of the RV model was that derived from the DAO time series, but the phase and mean were allowed to float to fit the data. Only the period was fixed for the $\Delta EW_{868.2}$ index

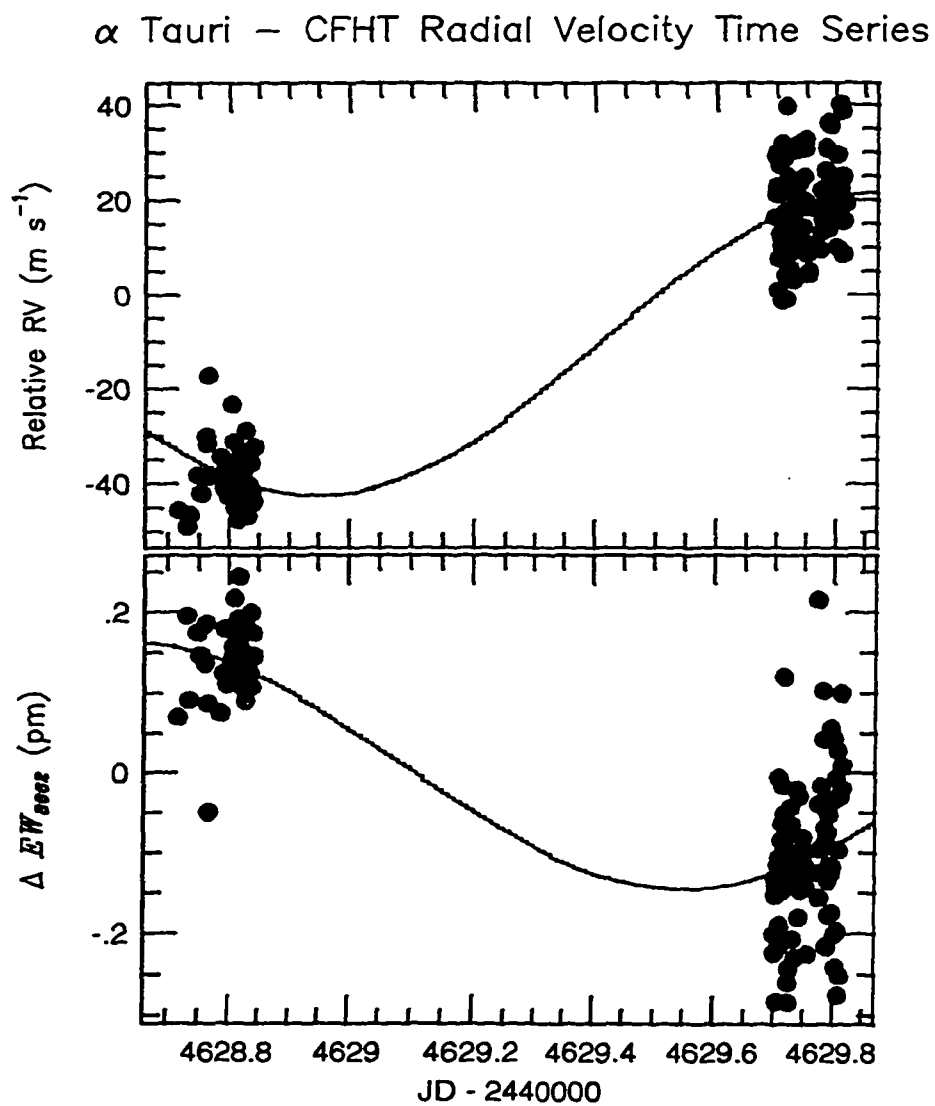


Figure 2.30: The CFHT radial velocity and $\Delta EW_{866.2}$ time series data for α Tauri with the 1.8358-dy model derived from the DAO radial velocity data superimposed. See text for fitting procedure.

data; the amplitude, phase, and mean were allowed to float to fit the data. This plot shows that the CFHT time series data are not inconsistent with the period detected in the DAO time series data.

The periodogram analyses of these two nights are shown in Fig. 2.31. The strongest peak at about 30 minutes for the RV data of the first night is barely significant (confidence level of 93%). A similar period of 24 minutes in the $\Delta EW_{868.2}$ index data is even less significant (confidence level of 84%). If there was no basis for comparison with other data, these periodograms would probably be viewed as fine analysis of noise. However, the variability in the Ca II H and K lines of α Tau has been known since 1978 (Baliunas et al., 1981). In their analysis of the power spectrum of the changes of the emission cores of the H and K lines relative to the sidebands, Baliunas et al. (1981) report a broad peak between 25 and 30 minutes in the November 5, 1978, $\text{mag}(\tau_K)$ data (an index similar to their S index discussed in Sec. 2.2.1 above). If, as suggested by Baliunas et al. (1981), these variations come from small, coherent active regions, then additional simultaneous RV and chromospheric activity observations over a number of nights should give valuable information concerning the photospheric-chromospheric connection in this red giant.

Other comments: Besides the overall need for additional observations, the above analysis can be improved by additional statistical testing. For example, we can run numerical simulations which test the amplitudes needed in the $\Delta EW_{868.2}$ and $\Delta(R - I)$ indices, at the period and phase of the 648-day RV period, for a specified confidence level detection (similar to those performed in the $\Delta(R - I)$ index for β Gem). The window function for

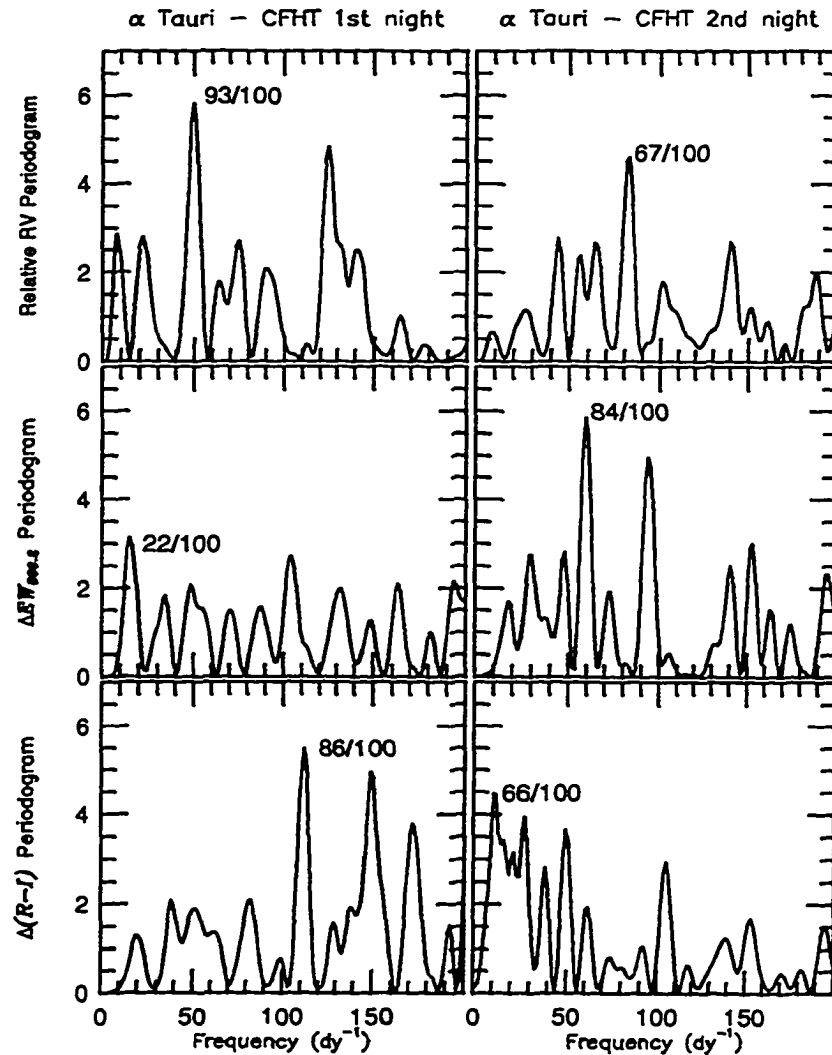


Figure 2.31: The weighted periodograms for the RV data and $\Delta EW_{866.2}$ and $\Delta(R - I)$ index data for α Tauri from the CFHT 1981 time series. With the marginal exception of the peak at ~ 30 minutes in the RV data from the first night, no significant periodicities exist in these data. However, the RV period of 30 min and the peak at approximately 24 min in the $\Delta EW_{866.2}$ data of the second night are similar to periods found by Baliunas et al. (1981) in Ca II H and K data (see text).

the 1.84-dy period could be tested. A window function is calculated by substituting constant velocities, having the same sampling pathology and error distribution as the original data, for the observations. The periodogram is recalculated using the artificial data. Hatzes and Cochran (1994b) discuss other algorithms and simulations to eliminate spurious signals from the data. These may be considered in the future.

2.2.3 The K Supergiant

ϵ Pegasi

The supergiant, ϵ Pegasi, was the only supergiant extensively monitored in the original CFHT program (α Orionis was observed for a few nights). The CFHT data are shown in Fig. 2.32 and listed in Table A.10. The CFHT spectra have an average signal-to-noise ratio in the continuum of over 1450 per pixel for a typical 3-min exposure. This star is one of the few in the PRV observations where the variability can be measured in km s^{-1} rather than m s^{-1} . It is a suitable radial velocity standard only for those measurements requiring precision of no less than 1 km s^{-1} . The limited number of DAO observations are shown in Fig. 2.33 and listed in Table A.11. The DAO spectra have an average signal-to-noise ratio in the continuum of 820 per pixel for a typical 24-min exposure. The DAO data have not been included in the periodogram analysis. This omission does not change the results discussed here.

Periodogram and non-linear least-squares analyses: The weighted periodograms for the CFHT data are shown in Fig. 2.34, $10 \text{ yr} \geq P \geq 20 \text{ dy}$,

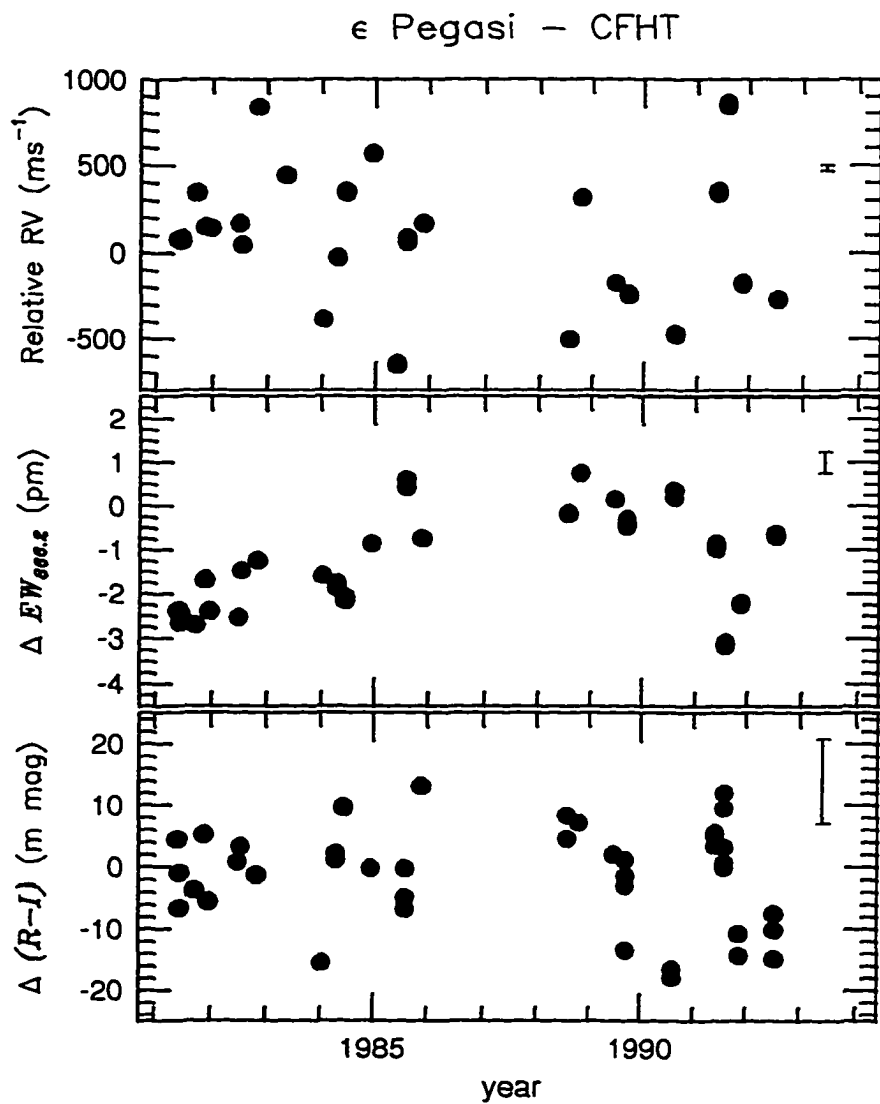


Figure 2.32: The data from CFHT observations vs. time for ϵ Pegasi (HR 8308). The $\pm 1\sigma$ mean internal error is shown for each data type.

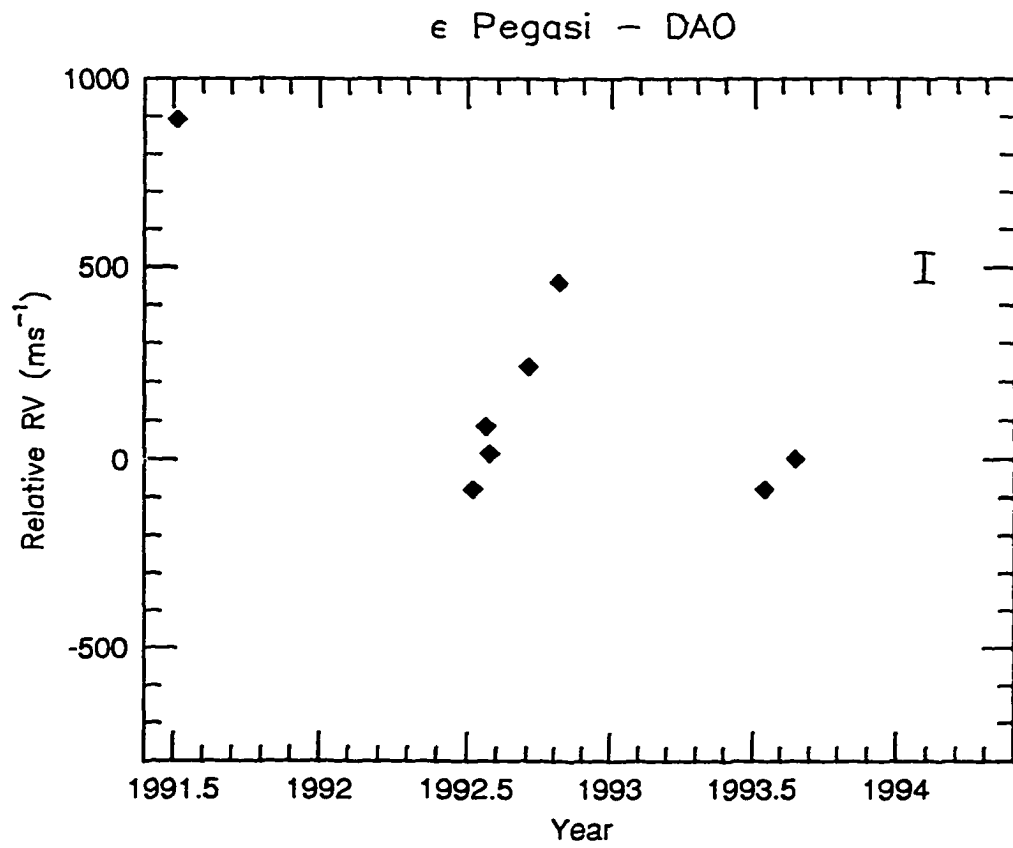


Figure 2.33: The relative radial velocity data from DAO observations vs. time for ϵ Pegasi (HR 8308). The $\pm 1\sigma$ mean error is given by the error bar.

and Fig. 2.35, $20 \text{ dy} \geq P \geq 10 \text{ dy}$. The dashed lines represent the 99% confidence level. Some of the most significant peaks in each periodogram are noted with the respective periods in days. Nearly coincidental periods are seen in the RV data and $\Delta(R - I)$ index: at ~ 260 days, ~ 65 days, ~ 63 days, ~ 47 days, and ~ 10.4 days. Of these periods, the $\Delta EW_{866.2}$ index shows much less significant peaks at ~ 260 and ~ 65 days. Both the RV and $\Delta EW_{866.2}$ data show a significant period at ~ 10.7 days; all three types of data show a periodicity at ~ 10.4 days, although the period is less significant in the RV and $\Delta EW_{866.2}$ index data. Note that there are other, less significant periods which also are present in each periodogram; the aliasing of the data is discussed below. The parent function for the RV and $\Delta(R - I)$ periodograms was a weighted mean. The parent function for the $\Delta EW_{866.2}$ index included a second-order term because of the apparent parabolic trend; this trend indicates a long-term change in the core emission of the 866.2 nm line.

The aliasing of the RV data was tested by using the best-fit model at a given period as the parent function and recomputing the periodogram. This procedure was followed for the 65.2-, 46.3-, and 10.7-dy periods, selected because they are the strongest three RV periods which have coincidental periods in the $\Delta(R - I)$ index and/or $\Delta EW_{866.2}$ index. The details of the individual parent functions are given in Table 2.12; these parameters would adjust if the three periods were simultaneously used as the parent. This procedure will introduce spurious signals in the residuals if the parent model is not accurate, and thus one must use caution to avoid over-interpreting the results. However, the periodograms of the residuals (not shown here) indicated, preliminarily, that ϵ Peg has RV periods of approximately 65, 46

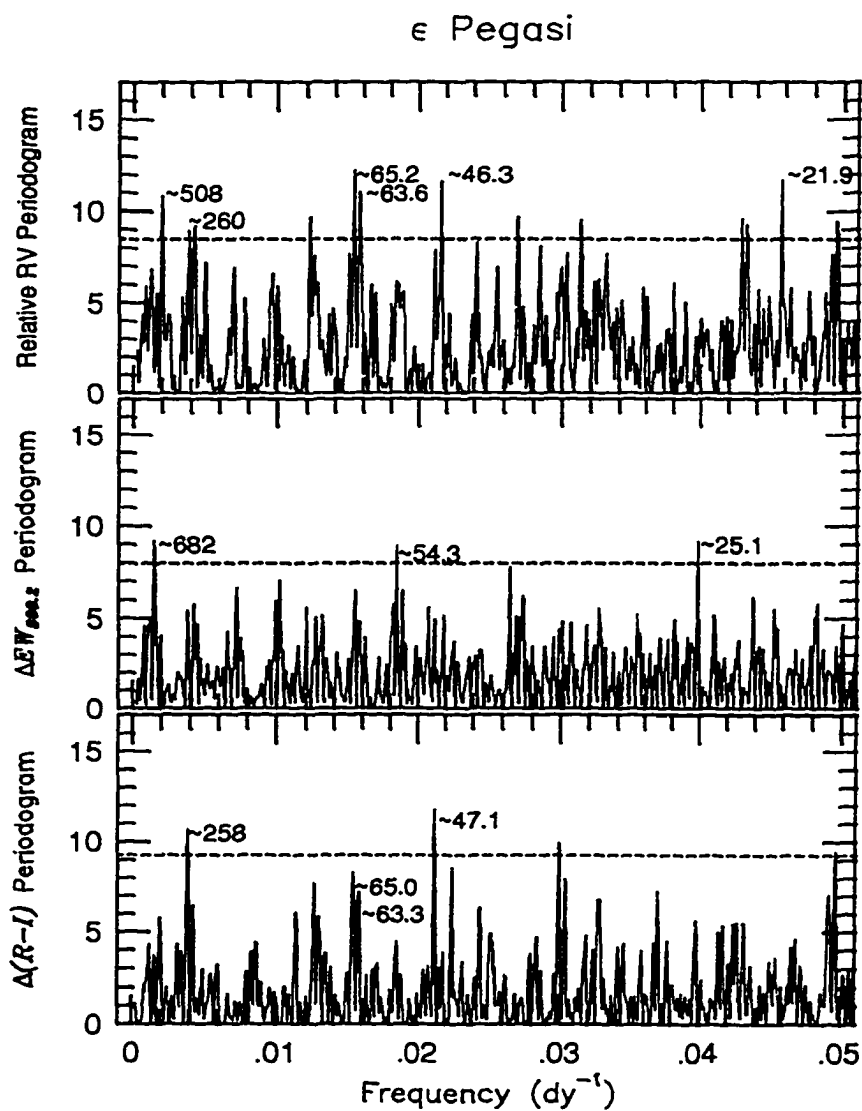


Figure 2.34: The weighted periodograms of the relative radial velocities and $\Delta EW_{888.2}$ and $\Delta(R-I)$ indices for ϵ Pegasi for $10 \text{ yr} \geq P \geq 20 \text{ dy}$. The most significant peaks and/or those corresponding to coincident periods are marked. The dashed line corresponds to the 99% confidence level.

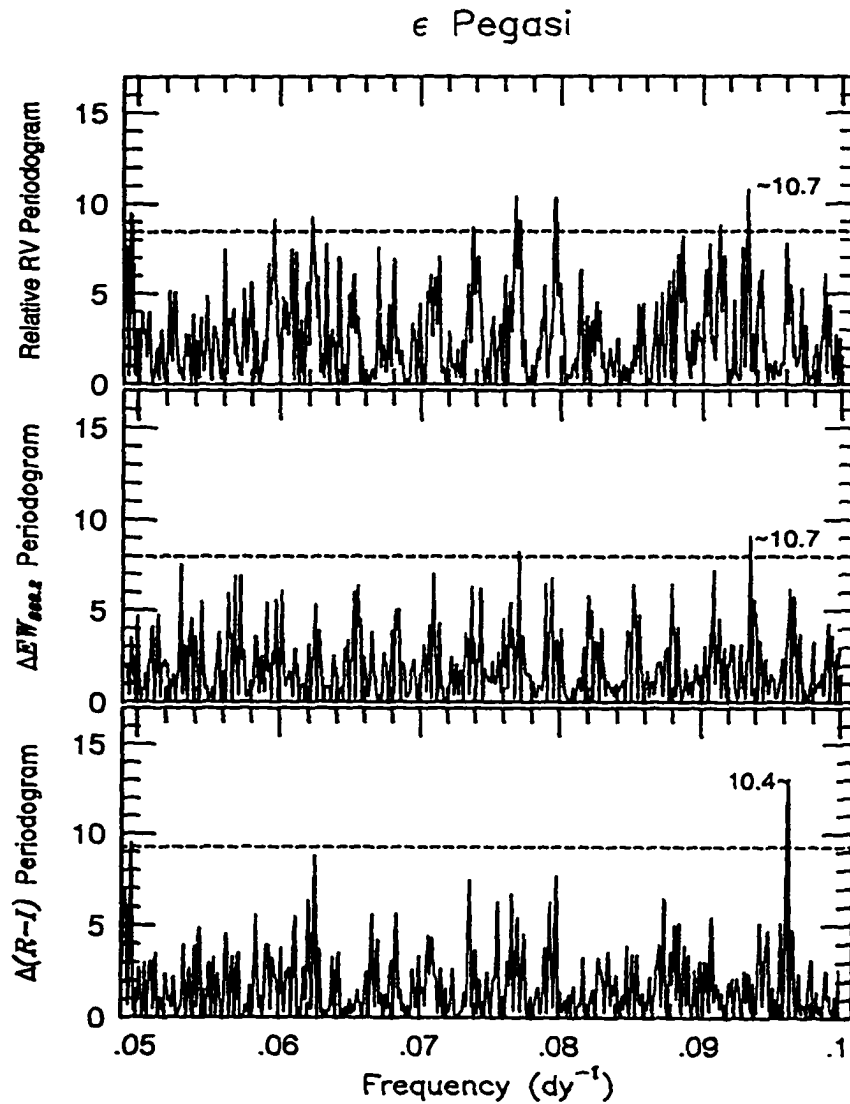


Figure 2.35: The weighted periodograms of the relative radial velocities and $\Delta EW_{868.2}$ and $\Delta(R-I)$ indices for ϵ Pegasi for $20 \text{ dy} \geq P \geq 10 \text{ dy}$. The coincidental $\sim 10 - 11$ -dy period is indicated. The dashed line corresponds to the 99% confidence level.

and 10-11 days. The periodograms of the residuals from the parent functions showed that these periods are not aliases of each other as the other two periods remained in the data when one of the periods was removed.

Discussion: As is the case with δ Sagittarii, the large uncertainty in the parallax for ϵ Peg, 0.0077 ± 0.0085 (s.e.) (van Altena et al., 1991) makes a meaningful prediction of the pulsation periods and rotation period difficult. Table 2.13 lists the stellar properties needed to derive the rotation period and the fundamental period for ϵ Peg. The distance derived from the parallax differs by 170 parsecs from that derived from the luminosity (Kovács, 1983, from the Wilson-Bappu absolute magnitude), but the distance derived from the luminosity is consistent within the errors quoted for the parallax value. I adopted the average of the two stellar radii derived from the angular diameter, measured by Michelson interferometry (Kovács, 1983), and the two distances. The effective temperature of this star is slightly higher and its luminosity slightly lower than the supergiant or AGB (asymptotic giant branch) models given in Fox and Wood (1982); however, the periods found in the CFHT RV data show good agreement with the Fox and Wood theoretical pulsation periods. Using their formula for Galactic supergiant variables in the interval $1 - 25M_{\odot}$, $\log P_0 = -2.59 + 2.2 \log R/R_{\odot} - 0.83 \log M/M_{\odot}$ (and ignoring the weak dependency on fractional helium and heavier elemental abundances) and the stellar mass and radius shown in Table 2.13, I find $P_0 \approx 53$ days. Unfortunately, this value is not constrained; the uncertainties in the values listed in Table 2.13 allow for a fundamental period range of 7 – 260 days. The ratio of the two periods, $65.2/46.3 \approx 1.4$, indicates this

Table 2.12: ϵ Pegasi: radial velocity multi-periodic solutions

parameter	value	σ	units
γ	50.7	40.0	m s^{-1}
K	415.8	59.0	m s^{-1}
T^a	7097.43	1.5	dy
P	65.2232	0.065	dy
γ	179.9	38.0	m s^{-1}
K	559.08	57.0	m s^{-1}
T^a	7122.6667	0.59	dy
P	46.28565	0.019	dy
γ	-73.29	51.0	m s^{-1}
K	410.34	66.0	m s^{-1}
T^a	7131.3492	0.26	dy
P	10.721524	0.0022	dy

^a JD -2 440 000

star may be pulsating in overtone frequencies. According to Fox and Wood, a period ratio $P_0/P_1 \approx 2$ corresponds to stars with low masses (~ 1 solar) unless the star is an overtone pulsator. With an accurate parallax and more observations (and more applicable theoretical models), one may be able to determine the mass of ϵ Peg based on the periods found.

Table 2.13 predicts a very long rotation period; the 682-dy period seen in the $\Delta EW_{868.2}$ index may represent one-half of the rotation period. However, periodograms of the residuals including this period in the parent function and separately the 10.7-dy period showed that these two periods are aliases of each other. Since there are similar 10-dy periods in the RV and $\Delta(R - I)$ data, the 10.7-dy period is most likely the real one.

The peaks at 10.4 and 10.7 days in the periodograms may be related to activity thought to cause variations in the He I chromospheric line at 1083 nm. O'Brien and Lambert (1986) observed the He I 1083 nm line in eight K stars of luminosity classes I and II, including ϵ Peg. Of those observed more than once, all were variable. For ϵ Peg, the equivalent width of the 1083 nm line changed from 7.5 pm in emission to 31.3 pm in absorption, and the line experienced a total velocity shift of 66 km s^{-1} (see their Table 5). These variations sometimes occurred on timescales of less than two weeks, and resemble changes seen in solar spicules (jets). In these spicules, mass is transferred to the corona, but since $v < v_{esc}$, the matter falls back to the chromosphere. The 1083 nm data suggest that their occurrence and disappearance may be a frequent event in ϵ Peg. If the $\sim 10 - 11$ -dy periods are related to the He I variability, our detection of a similar period over 12-yr of data suggests that this is the case. O'Brien and Lambert (1986)

Table 2.13: ϵ Pegasi: stellar properties needed to derive fundamental and rotation periods

quantity	value	uncertainty	units	notes
π	0.0077	0.0057	arcsec	1
d_{π}	130	75%	pc	
$\log L/L_{\odot}$	3.90	40%		2
d_L	300	40%	pc	2
\mathcal{M}	7	$^{+13}_{-4}$	\mathcal{M}_{\odot}	2
ϕ	8	10%	mas	2
R	190	50%	R_{\odot}	3
$v \sin i$	6.5	1.6	km s^{-1}	4
V_{eq}	8.3	2.8	km s^{-1}	5
P_{rot}	1180	60%	dy	

¹ van Altena et al. (1991)² Kovács (1983, and references therein); luminosity derived from Wilson-Bappu absolute magnitude; error in ϕ estimated.³ The radius is a mean value derived from the two distances and ϕ ⁴ Gray and Toner (1986)⁵ $V_{eq} = (4/\pi)v \sin i$

describe the blueshift/redshift characteristics of the 1083 nm line along with the emission/absorption features. A similar comparison of the changes in the profile of the 866.2 nm line over time would be very interesting.

Chapter 3

Spectrum Synthesis

spectrum - *n*, a series of colors formed when a beam of white light is dispersed ...so that its parts are arranged in the order of their wavelengths
synthesis - *n*, the combination of parts or elements into a whole

--The New Merriam-Webster Dictionary (1989)

3.1 Introduction to Spectrum Synthesis

3.1.1 Historical overview

The purpose of a spectrum synthesis is to determine the properties of the atmosphere of a star; i.e., the effective temperature, surface gravity, metallicity, microturbulence, and abundances of individual elements. One of the earliest examples of spectrum synthesis comes from the University of Victoria. In the early 1960's, Dr. John L. Climenhaga, then associate professor of Victoria College, studied the abundance ratio of C^{12}/C^{13} through the use of the semi-empirical equation:

$$1/R(\lambda) = 1/R_c + 1/\tau(\lambda) , \quad (3.1)$$

where $R(\lambda)$ is the line depth at the wavelength λ , R_c is the limiting central depth of a line for $\tau \gg 1$, and the optical thickness $\tau(\lambda)$ is the number of molecules in the line of sight involved in the transition times the line absorption coefficient per molecule (Climenthaga, 1963). His results from this straightforward approach were amazingly good. Individual efforts such as this became more widespread and eventually formed the foundation for the extensive computer programs developed by Kurucz (Kurucz and Avrett, 1981) and other programs in use today. Efforts to calculate synthetic spectra were stymied in the 1970's and 1980's due to the lack of comprehensive line lists. Kurucz and his associates vigorously attacked the problem of incomplete linelists by beginning a project in the early 1970's to include statistically millions of lines in their models (Kurucz, 1991a). These efforts brought about an immediate improvement in the model atmospheres and in the comparisons with observed spectra. In the early 1980's, Kurucz focused on extending and updating the old line lists. He worked on the data for diatomic molecules and included lines between known levels as well as lines with predicted wavelengths. The predicted work proved adequate for statistical opacities only, not for direct line-by-line comparisons. Comparisons with the solar spectrum showed that Kurucz's models still did not have enough opacity (Kurucz, 1991a), and a concerted effort was made to calculate energies and wavelengths for the iron group atomic lines. The product of his efforts is now available on a series of CD-ROM's, where he has recorded all of his model atmosphere programs, his spectrum synthesis programs, the grids of atmospheres, colors, fluxes, the line lists, the opacity distribution functions (ODFs) used to calculate the line opacities, and other information.

Additional line data are also becoming available from the group at Niels Bohr Institute, Copenhagen. Jørgensen (1994a) is computing line data for several diatomic molecules, and, more importantly, for several polyatomic molecules such as H_2O . The polyatomic data are not yet available, due in part to delays in calculating their model atmospheres and to inadequate storage and distribution facilities. These line lists are crucial if we hope to compute accurate spectra for stars with effective temperatures less than 3500 K.

3.1.2 A general description of spectrum synthesis

The spectrum synthesis process builds upon the model atmosphere, the equation of state, the continuum and line opacities, the calculation of the source function, and the solution to the equation of transfer. Once the surface intensity or flux is determined, each spectrum must be transformed to account for the broadening effects of stellar rotation, stellar macroturbulence, and the instrumental profile. More accurate treatments will include a disk-integrated rotation profile and limb darkening.

The model atmospheres are fundamental to the whole process and describe the temperature and the pressure structure of the surface layers of the star. The models by Kurucz (1993a) are computed under standard assumptions: the atmosphere is in hydrostatic equilibrium; the convective and radiative flux is constant with depth; the atmosphere is homogeneous except in the normal direction; the layers are considered plane parallel; and the atmosphere is in local thermodynamic equilibrium (LTE). In addition, all atomic abundances are specified and constant throughout; convection is

treated under a local mixing-length theory; and the atmospheres are line blanketed. These atmospheres are often referred to here as the “grid.” For most of the atmospheres, Kurucz has provided grid points for every 250 K, starting with an effective temperature of 3500 K. The grid points for $\log g^1$ are every 0.5 dex, $0 \leq \log g \leq 5$. Atmospheres used here are those computed for $[M/H] = 0.0, -0.1, -0.2, -0.3, -0.5$, and microturbulence $\xi = 2.0 \text{ km s}^{-1}$. We also use the Kurucz solar atmosphere ($T_{eff} = 5777 \text{ K}$, $\log g = 4.4377$, $\xi = 1.5 \text{ km s}^{-1}$).

The equation of state specifies the number densities and the degree of ionization and dissociation of the atoms and molecules. Here the solutions come via the assumptions that the atmosphere is a perfect gas, particles are conserved, charge is conserved, and the Saha-Boltzmann equation applies. The partition functions must also be calculated for each species. The product of this particular step is usually expressed as N/Q , or the number density over the partition function for each species.

The continuum and line opacities must be calculated during the synthesis. The continuum opacity (Kurucz, 1970) is calculated from the bound-free and/or the free-free transitions of H I, H_2^+ , H^- , He I, He II, He^- , low temperature absorbers (C I, Mg I, Si I, Al I), intermediate-temperature absorbers (Si II, Mg II, Ca II, N I, O I), high-temperature absorbers (C II-IV, N II-V, O II-VI, Ne I-VI); the H I + He I + H_2 Rayleigh scattering and electron scat-

¹Throughout this thesis, the surface gravity, g , is expressed in cm s^{-2} and will *always* be noted as $\log g$, if not spelled out. This notation should not be confused with the symbol for the statistical weight of an atomic or molecular transition, which is also g but which will *always* be accompanied by the symbol for the oscillator strength, f , as in “ gf value” or “ $\log gf$.”

tering; and the bound-bound transitions of H I lines. For a single transition, the line absorption coefficient is expressed as

$$l_\nu = \frac{\pi^{1/2} e^2 N gf H(a, \nu)}{m_e c Q \rho \Delta\nu_D} [e^{-\chi/kT}] [1 - e^{-h\nu/kT}] , \quad (3.2)$$

where e is the electron charge, m_e is the electron mass, ρ is the density of the atmosphere layer, gf is the statistical weight of the transition times the oscillator strength, $\Delta\nu_D$ is the Doppler broadening, χ is the excitation energy of the level being considered, k is the Boltzmann constant, T is the temperature of the atmosphere layer, and $(1 - e^{-h\nu/kT})$ is the correction for stimulated emission. $H(a, \nu)$ is the Voigt function, with the standard notation: $a \equiv (\Gamma/4\pi\Delta\nu_D)$, $\nu \equiv (\nu - \nu_0)/\Delta\nu_D$; Γ is the total broadening factor, $(\nu - \nu_0)$, the difference between the frequency being considered and that of the line center.

The source function and the equation of transfer can be expressed in various different ways. From Mihalas (1978, Eqs. (2-39), (2-36)) we note one form of the source function:

$$S_\nu = \frac{(\kappa_\nu B_\nu + \sigma_\nu J_\nu)}{(\kappa_\nu + \sigma_\nu)} , \quad (3.3)$$

and the standard transfer equation:

$$\mu \left(\frac{\partial I_\nu}{\partial \tau_\nu} \right) = I_\nu - S_\nu , \quad (3.4)$$

where κ_ν includes continuum and line opacity, B_ν is the Planck function, σ_ν is the scattering term, J_ν is the mean specific intensity, I_ν is the specific intensity, and μ is the cosine of the polar angle of the pencil of radiation. Under strict LTE, $S_\nu = B_\nu$. The optical depth is defined as:

$$d\tau_\nu \equiv -(\sum \kappa_c + \sum l_\nu + \sum \sigma_\nu) \rho dz , \quad (3.5)$$

$\sum \kappa_c$ = total continuum opacity, $\sum \ell_\nu$ = total line opacity, and $\sum \sigma_\nu$ = the total of all scattering processes.

3.1.3 A description of SSynth

SSynth², our spectrum synthesis code, was initially developed by Irwin (1978). SSynth calculates the equation of state using a Newton-Raphson iteration procedure which is equivalent to Helmholtz free-energy minimization (Irwin, in preparation). The partition functions are from Irwin (1981; 1987; 1988) and Sauval and Tatum (1984). The relative energy, i.e., ionization potentials, electron affinities, or dissociation or atomization energies, of each species is taken from Moore (1970); Huber and Herzberg (1979); Hotop and Lineberger (1985); Martin, Zalubas, and Musgrove (1985, and references therein); Moore (1985, and references therein); Sugar and Corliss (1985); and Irwin (1988). While SSynth can be used to predict ab initio atmospheres, at the present time we use an input temperature and pressure grid from a given Kurucz model atmosphere, calculate the corresponding opacity and optical depth, and calculate a scaled atmosphere. The program uses a modified Feautrier-Auer method (Auer, 1976; Mihalas, 1978, A76, M78) to solve the equation of transfer.

I have adopted the SSynth programs as developed by Irwin. I made a number of minor modifications which were necessary because of the trans-

²For purposes of discussion here, SSynth will refer to that part of the total analysis package which includes the calculation of the equation of state, the scaled atmosphere, and the synthetic spectrum. The preprocessing of the line lists and the post-modification of each spectrum to account for instrumental and stellar broadening are discussed separately below.

fer of the code from the VAX VMS operating system (VAX FORTRAN, mostly single precision code) to the Unix operating system (FORTRAN 77, all double precision code). This process took over a year to accomplish as full testing was done at each step. A few of the programs were in a transitory state and had to be made consistent with the rest of the code. Some parts of the code (e.g., convection, grey- and diffusion-predicted atmospheres) have not yet been tested. Since the SSynth programs have been described elsewhere (Irwin, 1978), I will discuss here those details specifically relevant to this thesis. Many of the options available in these programs are outlined in the manual pages, a sample of which is included in Appendix D. More specifically, the information in the manual pages describing *scale.cnt*, *ssynth.cnt*, *tabulate.cnt*, and *tabulate.csh* was gathered from the programs written by Irwin.

The H^- continuum opacity is the dominant source of continuum opacity for the stars in this study. I modified the program made available by Kurucz (1993c) for use in SSynth. This program, which is based on published values of the bound-free and free-free absorption cross sections, interpolates tables to determine the total continuous absorption coefficient as a function of wavelength and temperature. This algorithm should determine the coefficients more accurately than the fitting formulae of John (1988), and thus should attain an accuracy to better than 1%.

Irwin (1985) describes the methods used to predict the stellar atmospheres from known atmospheres, and discusses in depth the errors which arise using the predicted methods (see his figures 3, 4, and 5). We used scaled atmospheres for this work; scaling an atmosphere is the simplest method to

use to calculate an atmosphere, but it is also the least accurate. Figure 3.1 shows the deviations in the $T - \tau$ relationship from the grid values for an atmosphere scaled to $T_{eff} = 4500$ K from $T_{eff} = 4250$ K and from $T_{eff} = 4750$ K; note, since the grids of the Kurucz atmospheres are separated by 250 K, the actual difference in T_{eff} would be ≤ 125 K and thus the errors would be less than shown in Fig. 3.1. Large errors in temperature occur in the shallow layers above $\log \tau = -4$ when the scaling is made from lower effective temperatures. Errors also occur below $\log \tau = 0$ because convection is ignored.

For most lines, these discrepancies do not matter; however, tests showed that the strong lines in this spectral region are affected by the errors in the scaled temperatures and pressures of the atmospheric layers. At $T_{eff} = 4500$ K ($\log g = 4.5$, $[M/H] = 0.0$), for example, the errors in scaling to a mid-grid atmosphere result in a substantial change in the line depth of the temperature sensitive Ti I line at 867.537 nm. This change would wrongly be interpreted as a ~ 250 K difference (500 K difference scaling from 4250 K to 4500 K) in the effective temperature, or equivalently, an erroneous determination of the titanium abundance. In addition, at $\log g = 4.5$, the wings of the Ca II line also proved sensitive to these errors in precisely the same region which was used to determine the surface gravity. To mid-grid ($\Delta T_{eff} = 125$ K), the scaling errors would be interpreted as a decrease in $\log g$ of 0.35 dex; thus, one would need to increase the model's $\log g$ to compensate.

The errors in temperature at small optical depths arise because our calculated Rosseland mean opacities do not match those of Kurucz; we are including fewer opacity sources at low pressures and temperatures and thus

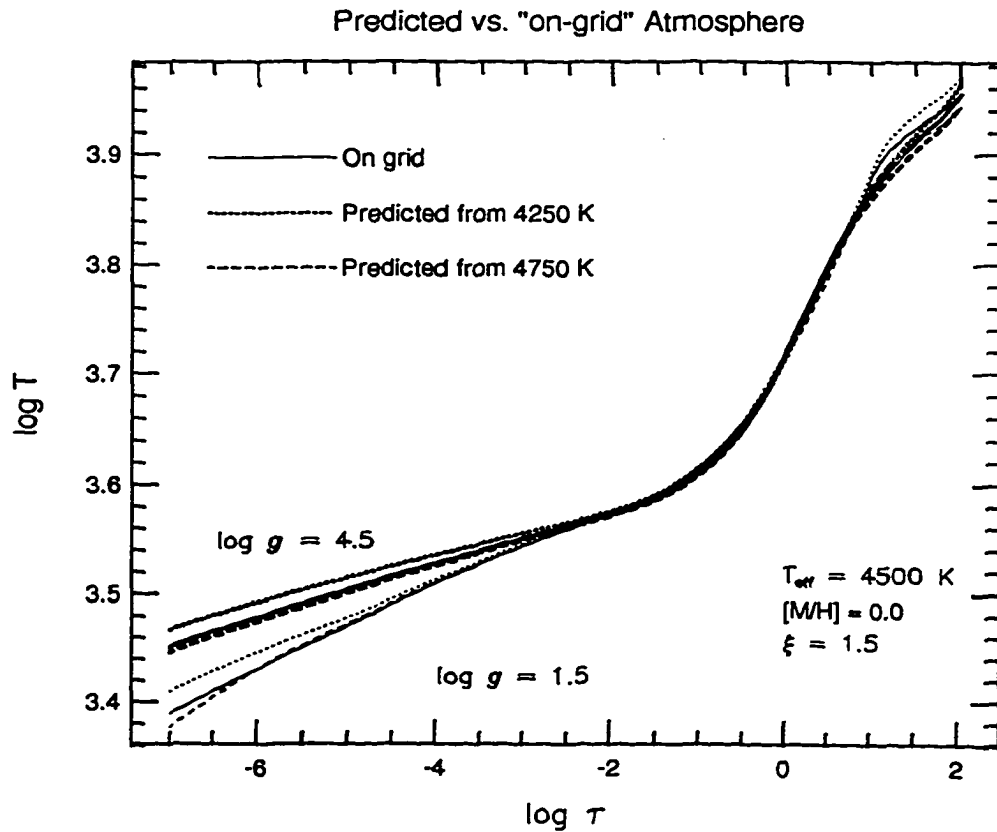


Figure 3.1: The scaled vs. "on-grid" T - τ relationship for atmospheres scaled to $T_{\text{eff}} = 4500 \text{ K}$ from 4250 K (dotted line) and from 4750 K (dashed line), for $[M/H] = 0.0$, $\log g = 4.5, 1.5$. The differences are due to missing opacities in the calculated Rosseland mean and to not including convection.

must go to a deeper atmospheric layer and higher temperature to reach the same optical depth. In addition, Kurucz uses photospheric abundances in his calculations whereas we use the meteoritic abundances; this difference affects primarily the number of electron donors. There are additional and updated continuum opacities given in Kurucz (1993c), such as He I and Fe I, which were not installed in SSynth. These opacities and the ODFs from Kurucz will be added to our Rosseland mean opacities in the future. As mentioned in Irwin (1985), efforts will also need be made to incorporate a more sophisticated treatment of convection, the source of the discrepancies seen in Fig. 3.1 at depth. To minimize the scaling errors, I consistently scaled from higher to lower effective temperatures. As Fig. 3.1 shows, scaling in this direction will reduce the scaling errors to 1% or less.

3.2 Procedures

This section describes the principal contributions I made to the spectrum synthesis process and the programs available at the University of Victoria. The discussion starts with an overview of the processing of the raw line lists. This discussion is then followed by the description of the method we developed to eliminate the ultraweak lines from the line lists, ultraweak lines are defined as those which have no cumulative effect on the SSynth results. This “pre-SSynth” discussion is followed by a descriptive outline of the “post-SSynth” steps that are critical for any meaningful comparison of the synthetic spectra with observed spectra.

3.2.1 Pre-SSynth line list processing: description of the work

The past decade has seen a revival in the use of spectrum synthesis in stellar analyses primarily due to the efforts of Kurucz in gathering line information from various sources and in calculating predicted energies and wavelengths where line data were missing. Prior to the efforts of Kurucz and his collaborators as well as other groups, the atmospheres were inaccurate for some spectral regions due to the omission of line-blanketing effects, the underestimate of the pseudocontinuum, and many unidentified features. However, now one must contend with the "bookkeeping" for over 20,000 lines per nm in the near infrared; perhaps over 30,000 lines per nm in the blue spectral region. Our method (discussed in Sec. 3.2.2) of eliminating the ultraweak lines from the line database ensures that SSynth does not have to deal with this density of lines; however, one must ensure that the line list entering the line-elimination step is as accurate and as complete as possible. Although the work was time-consuming and a bit tedious, the development and streamlining of the pre-SSynth programs is unquestionably the cornerstone of our analysis.

One of our goals is to make the SSynth analysis available to outside users. Although technically anyone could put together an independent line list in the proper format for subsequent use by SSynth, I invested a substantial amount of time in writing and testing the programs which read, modify, and combine the line lists of R. L. Kurucz and those of U. G. Jørgensen. All of the steps I created and the algorithm that I and future users will

use are summarized as Unix-based manual pages. The manual page which includes a brief outline of all of the pre-SSynth procedures is included as an appendix to this dissertation (see Appendix D). A copy of the complete manual is located in the physics reading room (University of Victoria, Elliott 105) and is available via anonymous FTP: *coho.phys.uvic.ca* in the directory */pub/larson/ssynthman*. Some of the programs used were adapted from those provided by Kurucz or by earlier versions of SSynth. Since the manual pages are comprehensive and complete, no further description will be made here. One should note, however, that these programs are dynamic. Our eventual goal is to make the process invisible to the user once s/he has specified the desired wavelength region to be synthesized, at least up to the step where the ultraweak lines are eliminated. There are also a number of parameters in the various control files which can be hidden, since they are rarely modified and may confuse the novice.

3.2.2 Pre-SSynth line list processing: treatment of the line haze

Researchers who synthesize stellar spectra have seen the accuracy of their work increase dramatically with the recent improvements in atomic and molecular line data. Data for approximately 58 million atomic and molecular lines are available from the compilations of Kurucz (1993b; 1993c) (K93b, K93c) and 70 million molecular lines from Jørgensen (1994a, hereafter J94a). (CN, CH, and TiO data overlap in these compilations.)

We need these extensive line lists not only for the accurate calculation of the strong lines but also for the calculation of the line haze. As is well

known, the line haze is formed by the en masse veiling of the continuum by lines which individually are too weak to be visible. However, some lines are too weak to have even a cumulative effect on the line haze. These lines are normally eliminated in synthetic spectrum computations because it takes substantial computer resources to calculate opacity profiles. Typical line rejection criteria, which usually depend on the ratio of line to continuum opacity, introduce the possibility that the computations will cost an excessive amount of computer time (rejection level set too low) or will underestimate the line haze (rejection level set too high).

SSynth calculates the line haze in a consistent manner; that is, the result has the correct integrated equivalent width over the whole spectral interval. Rather than ignore all lines below some fraction (typically 0.0001) of the continuum opacity, all parts of the Voigt profile [calculated using a modified version of the routine given by Drayson (1976)] below this fraction are "smeared" (or averaged) and added to the continuum opacity. This process can be made reasonably efficient since, for weak lines, the program uses mean broadening coefficients and shifts the line centers to the nearest frequency sample points. For each depth and species we can then precompute the Voigt profile as a function of sample point from line center. This minimizes the computer costs for each line. However, if the line list includes large numbers of lines which contribute negligibly to the smeared line opacity and resulting line haze, these costs can rapidly and unjustifiably increase. We call these lines "ultraweak" to distinguish them from the "weak" lines which *do* contribute appreciably to the line haze.

In this section we describe an algorithm that rapidly eliminates the ul-

traweak lines from a line list and thus improves the efficiency of the subsequent synthetic spectrum computations without compromising the line haze calculation³.

Methods

Our method for eliminating ultraweak lines proceeds in four steps: 1) For a given model atmosphere and wavelength central to the region of interest, we calculate the equivalent width coefficients, $W'_0(\chi)$ [defined by Eq. (3.8)], for a number of excitation potentials, χ , using a short artificial line list for every species in the line list. We collect these values of $W'_0(\chi)$ in a table as a function of species and χ . 2) We rapidly interpolate this table in χ and combine the derived value of $W'_0(\chi)$ with the gf value of each line to calculate the equivalent widths of all lines in the region [see Eq. (3.9)]. 3) We calculate the cumulative line blocking as a function of equivalent width [see Eq. (3.10)]. 4) We use this function to eliminate all lines which contribute negligibly to the line haze (demonstrated below with the discussion of the results).

We start with the standard definition for the equivalent width of a line

$$W = \int_0^\infty A_\lambda d\lambda = \int_0^\infty \left(1 - \frac{H_\lambda}{H_\lambda^c}\right) d\lambda, \quad (3.6)$$

where A_λ is the absorption depth of the line, H_λ is the flux we observe at a given wavelength, λ , and H_λ^c is the associated continuum flux. For weak lines, $A_\lambda \propto gf$, independent of the details of the depth-dependent opacity profiles. We expand Eq. (3.6) from $gf = 0$ in a first-order Taylor series to

³This work has been published (Larson and Irwin, 1996)

obtain

$$W = gf \int_0^\infty \frac{\partial A_\lambda}{\partial gf} d\lambda. \quad (3.7)$$

For each species, the tabulated equivalent width coefficients are defined by

$$\lim_{gf \rightarrow 0} \frac{W}{gf} \equiv W'_0(\chi) = -\frac{1}{H_\lambda^c} \int_0^\infty \frac{\partial H_\lambda}{\partial gf} d\lambda. \quad (3.8)$$

The $W'_0(\chi)$ coefficients could be tabulated as a function of wavelength. However, in our application, we use just the central wavelength; the $W'_0(\chi)$ coefficients are essentially independent of wavelength within the narrow spectral interval 864–878 nm. We assume a boxcar opacity profile and use the chain rule to follow the line opacity perturbation through the equation of transfer. We differentiate the appropriate Feautrier-Auer equations and the line opacity (see Appendix B) such that $W = W'_0(\chi) gf$ is consistent with the equivalent width SSynth would calculate for isolated weak lines.

Once we have tabulated the coefficients, we calculate W_l , the equivalent width of the l^{th} line in the wavelength interval:

$$W_l = W'_0(\chi)_l (gf)_l. \quad (3.9)$$

Since this approach is applicable only to weak lines, the calculated equivalent widths of the stronger lines will be overstated. On the other hand, this method extends the calculation of equivalent widths to lines so weak that other methods fail due to numerical significance loss.

We define the cumulative blocking coefficient as

$$\epsilon_\lambda(W) \equiv 1 - \left[\frac{\int H_{\lambda'} d\lambda'}{\int H_\lambda^c d\lambda'} \right] = \frac{\sum_l W_l}{2 \Delta \lambda}, \quad (3.10)$$

where the right-hand term follows from the assumption that H_{λ}^c is constant over the integration range $\lambda \pm \Delta\lambda$. We take the sum over all l such that $W_l \leq W$ to calculate the cumulative line blocking as a function of W (see Fig. 3.2).

Results

We demonstrate our line-elimination method using the 864–878 nm region of late-type stellar spectra. The atmospheres were taken from the grid provided by Kurucz (1993a) for effective temperatures from 4000 to 6000 K, $\log g$ from 1.5 to 4.5, solar abundances, and a microturbulence value of 2.0 km s⁻¹. Our line list has approximately 320 000 lines in the 864–878 nm wavelength region. The atomic data and most of the diatomic data in our line list are taken from Kurucz (K93b, K93c). We supplemented Kurucz's CN data with Jørgensen data [J94a, see also Jørgensen & Larsson (1990)], which extend to higher J values and nearly to the dissociation limit. The TiO data are from J94a and Jørgensen (1994b). Under the conditions examined here, CN and TiO dominate the diatomic line blocking; other diatomics either have no lines in this wavelength region or have a negligible effect. We adopted a CN dissociation energy of 7.9 eV and a TiO dissociation energy of 6.87 eV.

Figure 3.2 shows the cumulative line blocking error as a function of equivalent width for $T_{eff} = 6000$ K, 5000 K, and 4000 K and $\log g = 4.5$ and 1.5. The heavy, solid line of each graph represents the cumulative line blocking for all of the species which have equivalent widths on the linear part of the curve of growth; the upper limit of the abscissas corresponds to $\log(W/\lambda) \leq -5.5$. The lighter lines represent the isolated cumulative line blocking of TiO (dot-

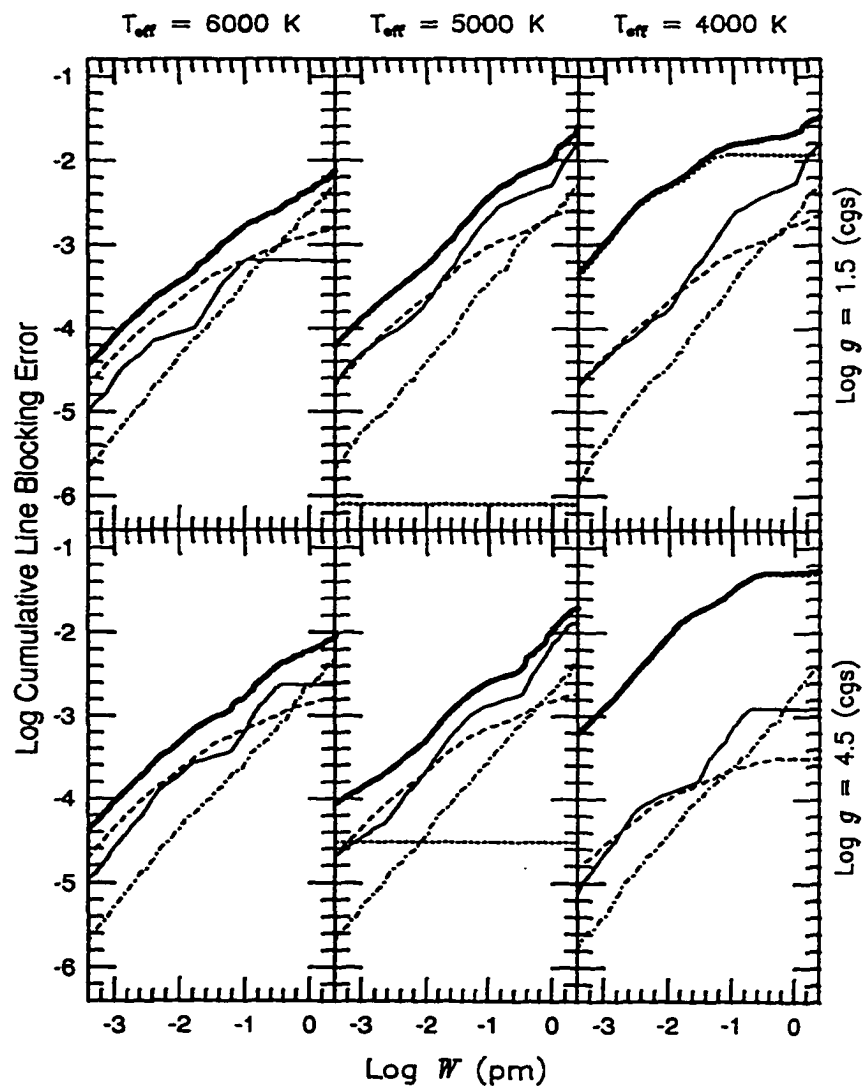


Figure 3.2: The cumulative line blocking error as a function of equivalent width for optically thin lines. The heavy solid line represents all atomic and molecular lines; the dotted line, TiO; the light solid line, CN; the dashed line, atomic lines with predicted energy levels (see text); the dot-dashed line, atomic lines with measured energy levels (see text). At 6000 K, the total blocking for the TiO lines falls below the lower limit.

ted), CN (solid) and two atomic line lists (described below).

Some well-known molecular behavior is immediately apparent in Fig. 3.2. First, the cumulative line blocking for TiO shows a strong temperature dependence; TiO provides nearly all of the cumulative blocking at $T_{eff} = 4000$ K, but provides essentially no blocking at 6000 K. Second, the TiO blocking decreases with decreasing surface gravity. Since the temperature classification of cool stars is defined by TiO, a giant must be cooler than a dwarf of identical spectral type. Third, the cumulative line blocking for CN increases with decreasing surface gravity at 4000 K, but the effect weakens at 5000 K and slightly reverses at 6000 K. This result agrees qualitatively with the *calculated* results of Bell and Tripicco (1991, Fig. 7) for CN in the blue region of the spectrum. (These authors conclude that an additional mechanism, e.g. nitrogen enhancement and carbon depletion, is required to explain the *observed* CN luminosity effect in the stars having $T_{eff} > 4500$ K.)

The cumulative line-blocking function can also be used for examining the effect of the incompleteness of the line lists. For example, we separated the atomic line data into two sets. The “predicted set” (dashed line of Fig. 3.2) contains only those lines with predicted energies and wavelengths from the file “lowlines.dat” from CD-ROM 1 (K93b). The “measured set” (dot-dashed line of Fig. 3.2) contains lines from CD-ROM 18 (K93c), which have measured energies and wavelengths (Kurucz, 1991a). While any effective temperature/gravity dependence for the cumulative line blocking of the individual atomic species is masked by the grouping used here, one notes from Fig. 3.2 that, although the cumulative line blocking is dominated by the predicted set at small equivalent widths, the total cumulative blocking

for the predicted set never exceeds -2.5 dex.

The weakness of the predicted lines is probably the result of a selection effect; Kurucz's predicted lines are unobserved in laboratory spectra and thus tend to be weak not only in laboratory but also stellar spectra. The weakness of the predicted lines for the effective temperatures and gravities considered here suggests the predicted line data may be ignored for our wavelength region. This is a reassuring result; it is precisely for these predicted lines that the model Hamiltonian used in Kurucz's semi-empirical analysis tends to have its largest uncertainties.

Our primary use for the cumulative line-blocking function shown in Fig. 3.2 is to eliminate the ultraweak lines. We choose an acceptable line-blocking error and retain only those lines whose equivalent widths are greater than the corresponding value. The fraction of lines retained (see Figure 3.3) will change as a function of the accuracy desired and as a function of the stellar parameters. For $\log g = 4.5$, one notes, for example, that the fraction of lines retained at a line-blocking error of 0.1% falls from about 0.15 at $T_{eff} = 4000$ K to about 0.001 at $T_{eff} = 6000$ K.

Table 3.1 shows the execution times, in minutes, for each of the major sections of our synthetic spectrum computations for $T_{eff} = 5000$ K, $\log g = 4.5$, and five separate line lists. All timing was done on a workstation with a capacity of 3.5 megaflops (3.5 million floating point operations per sec), and the only difference between the computations was the fraction of lines retained in the line lists, as given in the table. For each computation the criterion for the line smearing (or the averaging of the unused portions of each Voigt profile) was set at 0.0001 of the continuum opacity. The equation

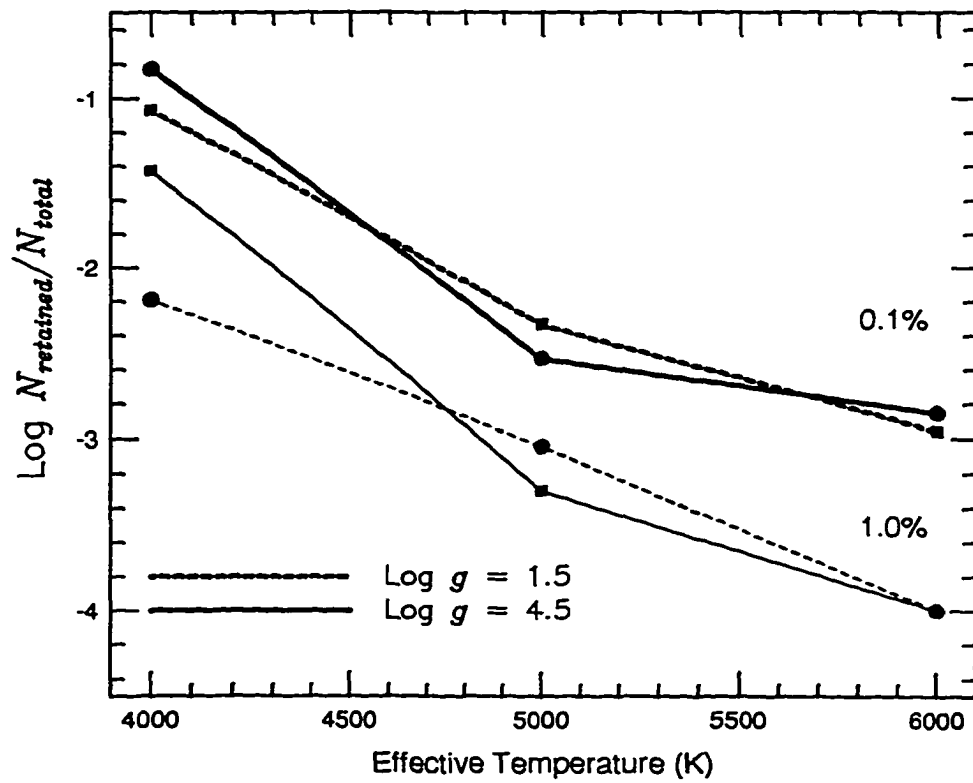


Figure 3.3: The fraction of lines which would be retained under a 0.1% and a 1% line-blocking error for a range of effective temperatures and surface gravity values.

of transfer was solved with three quadrature angles and 5400 wavelength points, and the continuum scattering was treated as ordinary absorption without stimulated emission (see Appendix B).

By separating the execution times attributable to the equation of state (EOS), pre-SSynth (where we process the line lists) and SSynth routines, we highlight those areas where the greatest time savings will occur. We show the calculation of the EOS separately as this calculation is needed only once per model atmosphere. Our pre-SSynth procedure includes the line-elimination method described above (except, obviously, where we have included all lines at a line-blocking error of 0.0% for demonstration purposes). It also includes a modified Heapsort (Press et al., 1992) algorithm which sorts the selected line data into manageable wavelength intervals and by species within each wavelength interval. This sorting step greatly facilitates the line opacity and equation of transfer calculations. To make a fair comparison, one should note that the pre-SSynth step would only need to be done once per wavelength region for the 0.0% line-blocking error. However, for non-zero line-blocking errors, the selected line list may be used for a range of stellar models; thus, depending on the tolerable line-blocking error and the range of atmospheric parameters being tested, the pre-SSynth steps may need to be done only infrequently.

The execution time for our SSynth routines, shown in the last line of Table 3.1, is dominated by the calculation of the line opacity profiles and the solution to the equation of transfer. At the 1% blocking error, the execution time reaches the overhead presented by the solution to the equation of transfer. It is readily apparent from subtracting this overhead that the execution

Table 3.1: Approximate execution times for the programs associated with a spectrum synthesis

Line-Blocking Error ^a	0.0%	0.0001%	0.01%	0.1%	1.0%
Log N_r/N_t^b	0.0	-0.68	-1.96	-2.55	-3.34
	Execution Time (minutes)				
EOS ^c	4.4	4.4	4.4	4.4	4.4
Pre-SSynth:					
LEM ^d	N/A	9.7	5.1	4.8	4.8
Sort ^e	26.5	4.6	0.2	<< 1	<< 1
SSynth ^f	22.6	7.0	2.7	2.2	2.0

All calculations were done on a workstation having a capacity of 3.5 megaflops; $T_{eff} = 5000$ K, $\log g = 4.5$.

^a Systematic error in pseudocontinuum resulting from the elimination of the ultraweak lines from the line list

^b $N_r \equiv$ number of lines retained, $N_t \equiv$ number of lines total

^c Equation of State (average)

^d Line-Elimination Method (see text)

^e Sort uses a modified Heapsort algorithm from Press et al. (1992)

^f Time is dominated by the calculation of the line opacity profiles and the solution to the equation of transfer

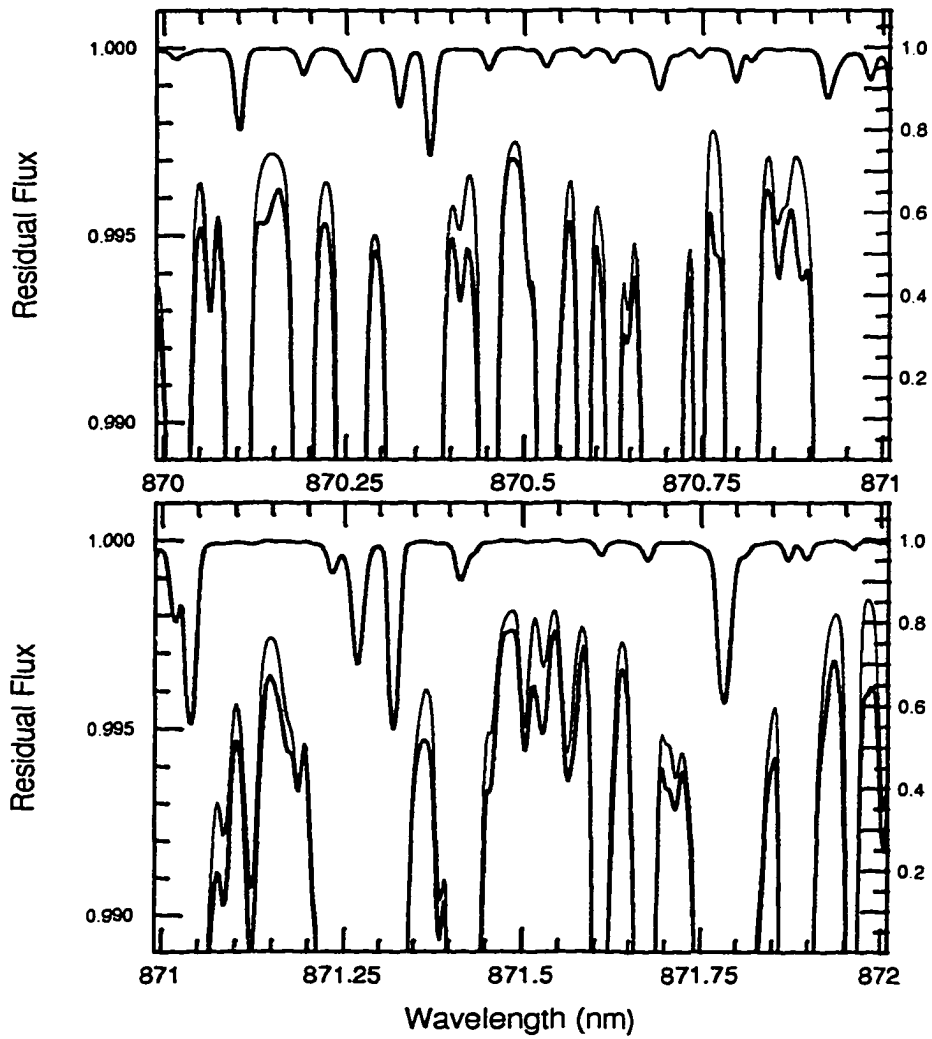


Figure 3.4: A portion of the wavelength region for $T_{eff} = 5000$ K, $\log g = 4.5$. The spectrum calculated using all line data is indicated by the heavy line; the spectrum calculated using 0.0028 of the line data (selected using a 0.1% line-blocking error), by the light line. The expanded scale shows that the errors in the pseudocontinuum are approximately 0.1%, as expected.

time for the calculation of the line opacity profiles is roughly proportional to the number of lines used. The order-of-magnitude difference between the time for a 0.0% line-blocking error and that for a $\geq 0.1\%$ line-blocking error emphasizes the efficiency of our line-elimination method. In spectral regions having a higher density of lines than the present case, the overhead presented by the solution to the equation of transfer will be a smaller proportion of the execution time and the potential time savings may be greater. The exact savings will depend on the shape of the cumulative line-blocking function. However, our line-elimination method clearly should be considered for all wavelength regions.

Figure 3.4 superimposes the synthetic spectrum where the line list included all of the lines, 0.0% line-blocking error, and the synthetic spectrum where the line list included 0.0028 of the lines, 0.1% line-blocking error, over a selected subregion. A line-blocking error of 0.1% was chosen for comparison as this value optimizes the efficiency of our method, as Table 3.1 shows. The differences between the spectrum computed using all of the lines and the spectrum computed using the abbreviated line list are indiscernible on a normal scale, as shown in the upper spectra (right hand ordinate) of both the top and bottom plots shown in Fig. 3.4. The lower spectra in both the upper and lower plots in Fig. 3.4 are shown on an expanded scale (left hand ordinate) and emphasize the continuum region. As expected, the errors are of order 0.1% in the pseudocontinuum and less in the lines. From a practical standpoint, if one were using lines having a line depth of 0.05 for abundance analysis one would expect relative errors, in this case, on the order of 2% in the calculated line depth.

3.2.3 Post-SSynth: solar comparison

If the laboratory oscillator strengths and wavelengths of the lines were accurate enough and extensive enough, there would be no need to use the Sun as a laboratory source. Unfortunately, the laboratory data are insufficient even for this relatively narrow, low-density spectral region. Thus, the very first step taken for any wavelength region is to compare the synthetic solar intensity spectrum with an observed central disk spectrum and derive empirical oscillator strengths and broadening coefficients and adjust wavelengths to optimize the match.

Before a synthetic spectrum can be compared to an observed spectrum, the synthetic spectrum must be transformed. This subsequent processing of the synthetic spectra must include the telescope imperfections (the scattering of light in the spectrograph, the resolution) and properties intrinsic to the star (macroturbulence, rotation). For the Sun, the intrinsic properties are fairly well known. Thus, we can compare our estimate of the scattered light and our treatment of the instrumental profile in the synthetic spectrum with the high resolution solar flux atlas and with spectra of the Sun taken at both the CFHT and the DAO.

Note that no manual pages have been written yet for the post-SSynth steps.

Solar central intensity comparison

The use of the Sun as a high-temperature “laboratory” to derive oscillator strengths, broadening factors, and wavelengths has been debated extensively

in the literature [Kostik et al. (1996) give an excellent and somewhat humorous historical summary]. Although annual conferences between laboratory and stellar spectroscopists are held and methods exist for exchanging up-to-date needs and databases (Martin, 1992), the availability of accurate, measured line data still fall far below the needs of stellar spectroscopists. Unfortunately, the “laboratory” conditions of the Sun cannot be controlled. Many of its intrinsic properties – e.g., microturbulence, non-LTE conditions, and inhomogeneities – enter the derivation of oscillator strengths and broadening factors as free parameters, perhaps even as a function of depth and/or the model atmosphere used.

Even where accurate laboratory data exist, different elemental solar abundances are derived based upon the methods used to measure equivalent widths or calculate broadening interaction constants and based upon which lines are used. The problem is exacerbated by the fact that the derived meteoritic abundances of many elements are different from the solar abundances. The ongoing search for the “true” solar iron abundance is nicely summarized in Kostik et al. (1996), who also note the convergence of the elemental abundances to the meteoritic values.

Thus, the first step in synthesis work is to adopt either the solar- or meteoritic-derived set of abundances (Grevesse and Anders, 1991). Having done this, and having chosen the solar atmosphere model to be used and the appropriate microturbulence value, one proceeds to “adjust” the individual oscillator strengths (in practice, the $\log gf$ value) and/or broadening coefficients of the strong lines and wavelengths of the atomic lines (or adjust all the molecular lines of a given electronic transition for a change in oscil-

lator strength or bandhead frequency) so that the synthetic and observed solar spectra match. The following paragraphs discuss the choice of the free parameters used in this process, the programs which were developed for use with SSynth, the results of the match for Fe I lines and other lines of interest, and the process used to obtain the gf value and broadening coefficients for the Ca II line.

For this discussion, the free parameters are those which, when adjusted, generally affect lines across the entire spectral region. These are the microturbulence value, any enhancement factor for the broadening coefficients, which, for the Sun, are dominated by collisions with hydrogen, and the macroturbulence of the Sun. Since I have not adjusted any broadening coefficients other than those for the Ca II line (discussed below), I will ignore any discussion of the use of a broadening enhancement factor.

Because the determinations of the solar abundances are converging to the meteoritic values, we have chosen these abundances for this work. All subsequent stellar abundance determinations are made relative to the adopted solar abundances.

Since there are a number of solar model atmospheres available, one is free to choose the "best" one. Since we are using the extensive stellar grids provided by Kurucz, we have chosen the Kurucz solar atmosphere. Typically, the model photosphere of the Holweger-Müller solar atmosphere (1974, hereafter HMS), which has been called the "ubiquitous choice of abundance determiners" (Kostik et al., 1996), is used. The HMS atmosphere was used by Smith and Drake (1988, hereafter SD88, see discussion below) to derive the hydrogen damping coefficients for the Ca II infrared triplet lines.

Microturbulence, ξ , which represents small-scale velocity fields, enters the equation of transfer through its affect on the atomic absorption coefficient. The intermediate strength lines, those on the flat part of the curve of growth, are most affected by the choice of ξ (Gray, 1992, Fig. 14.4) (Kostik et al., 1996, Fig. 1). The Kurucz solar atmosphere uses a depth-independent microturbulence value of $\xi = 1.5 \text{ km s}^{-1}$, which is larger than the $\xi = 0.9 \text{ km s}^{-1}$ used by Kostik et al. (1996) with the HMS atmosphere, and with the generally accepted value of 1 km s^{-1} . At the present, I have retained Kurucz's value for consistency since all abundances will be determined in a relative sense.

Macroturbulence, ζ , represents large-scale velocity fields and does not affect the equivalent widths of the lines. Weak lines are similarly affected by microturbulence *and* macroturbulence in that the profiles of the lines are changed but not the equivalent widths. Intermediate strength lines become broader and shallower as the macroturbulence value is increased. In practice, one should be able to use a combination of weak and intermediate-strength lines to optimize the choice of ξ and ζ , assuming there are lines for which the laboratory oscillator strengths and broadening coefficients are accurate.

Once the values of the microturbulence and the macroturbulence for the Sun are chosen, the gf values, broadening coefficients, and wavelengths of the lines are adjusted until a good match is achieved with the high-resolution solar central intensity spectrum. The spectrum used here was observed by J. W. Brault using the Fourier Transform Spectrograph (FTS) at Kitt Peak and reduced and made available in digital form by Kurucz (1991b). This atlas has a resolution of approximately 522,000 and a signal-to-noise ratio

of between 2000 and 9000. I developed all of the programs used in the process of empirically adjusting the gf values, broadening coefficients, and wavelengths and incorporated them with IRAF⁴ tasks within an IRAF script. The code integrates Lick Mongo 1991⁵ and superposes the real and synthetic spectra on the computer screen in small wavelength intervals along with the wavelengths and identifications of each of the *visible* (equivalent width ~ 0.1 pm) lines.

This process is necessarily iterative. Once the initial spectrum is calculated from the “presynth4” step (see Appendix D), the spectrum is convolved with a Gaussian with $\sigma = \zeta$; the instrumental profile of the Kitt Peak solar intensity spectrum is assumed to be negligible. The user then uses a “chi-by-eye” method to compare each line in the synthetic spectrum with the corresponding line in the solar spectrum and to adjust the corresponding wavelength, gf value, and/or hydrogen broadening coefficient in the selected line listing. The synthetic spectrum is recalculated, reconvolved, and the comparison and adjustment process repeated. Once a satisfactory match is achieved, the master line list is edited.

As noted above, while the strength of the weak lines is directly proportional to their oscillator strengths, for the strong lines (line depth greater than 0.5-0.6) the depth of the wings is proportional to the product of the oscillator strength and the hydrogen broadening parameter: $f\gamma_H$. If there is an obvious disagreement between the synthetic spectrum computed from the

⁴Image Reduction and Analysis Facility, developed by the National Optical Astronomy Observatories for use by the astronomical community

⁵An Interactive Graphics Program, Revised by S. Allen and R. Pogge; Lick Observatory Edition, 1995

given Kurucz values (or other source as in the case of the Ca II line here) and the central intensity atlas, the gf value and/or the hydrogen broadening coefficient will need to be adjusted. In practice, one also needs to be aware of and preferably use any laboratory determination of either of these parameters for the individual lines.

Since this thesis is concerned with the match of the 864.7 - 867.7 nm region, I have adjusted, where necessary, the wavelengths and gf values for all atomic lines within ± 1.5 nm of the Ca II line (the Ca II line is discussed separately below). The wavelengths and gf values for the Fe I lines have been adjusted, where needed, for the full 14 nm. Except for subtracting 0.02 nm from some of the CN wavelengths, no adjustments have been made to any of the molecular lines. Future work will include adjusting the gf values, strong-line broadening coefficients, and wavelengths for the full 14 nm (see Figs. C.1 - C.7).

Since results for various lines over the entire spectral region are of interest for future reference and work, these results will be discussed briefly here as well. Figures C.1 - C.7 compare the synthetic central intensity spectrum and the solar central intensity spectrum for the full 14 nm, in 1 nm segments, in vacuum wavelengths. Each visible line, defined as having a calculated equivalent width greater than 0.1 pm, having a corresponding identification in the Kurucz line list, is marked. Those lines marked with an "⊙" were listed as solar (but unidentified) by Swensson et al. (1970). Note that hyperfine structure, which is evident in some of the lines (e.g., Mn I), is not considered here. Kurucz has calculated the hyperfine splitting for some of the lines; these calculations will be included in future line lists.

Note that all of the comparisons at this stage in the SSynth analysis are done using vacuum wavelengths, and thus vacuum wavelengths are quoted in this section. The wavelengths in all other sections, i.e., those which compare the solar and stellar flux spectra with the synthetic flux spectra, are expressed as air wavelengths.

The Fe I lines: Figure 3.5 compares the Fe I $\log gf$ values derived from this work, for the 14 nm spectral interval, with those given in the Kurucz line list. The scatter about the line of equality is random. The standard deviation of the difference in the gf values between Kurucz and this work is 0.28 dex. The standard deviation of the difference in the gf values between this work and the laboratory values compiled by Nave et al. (1994) is 0.08 dex (7 values); between Kurucz and Nave et al. (1994), 0.19 dex (same 7 values); and between Kurucz and an empirical matching exercise by Erdelyi-Mendes and Barbuy (1989), 0.80 dex (19 values). The last work epitomizes the disparate results which can be obtained when deriving solar gf values. Erroneous results are especially likely for lines on the flat part of the curve of growth as, by implication, large changes can be made in the gf value of the line with little change in the line strength. An exhaustive discussion of the complications in determining solar gf values and damping constants is given in Peterson et al. (1990). However, since there are so few laboratory-determined values for the Fe I lines in the spectral region examined here, we have no other choice but to use the Sun as our "furnace."

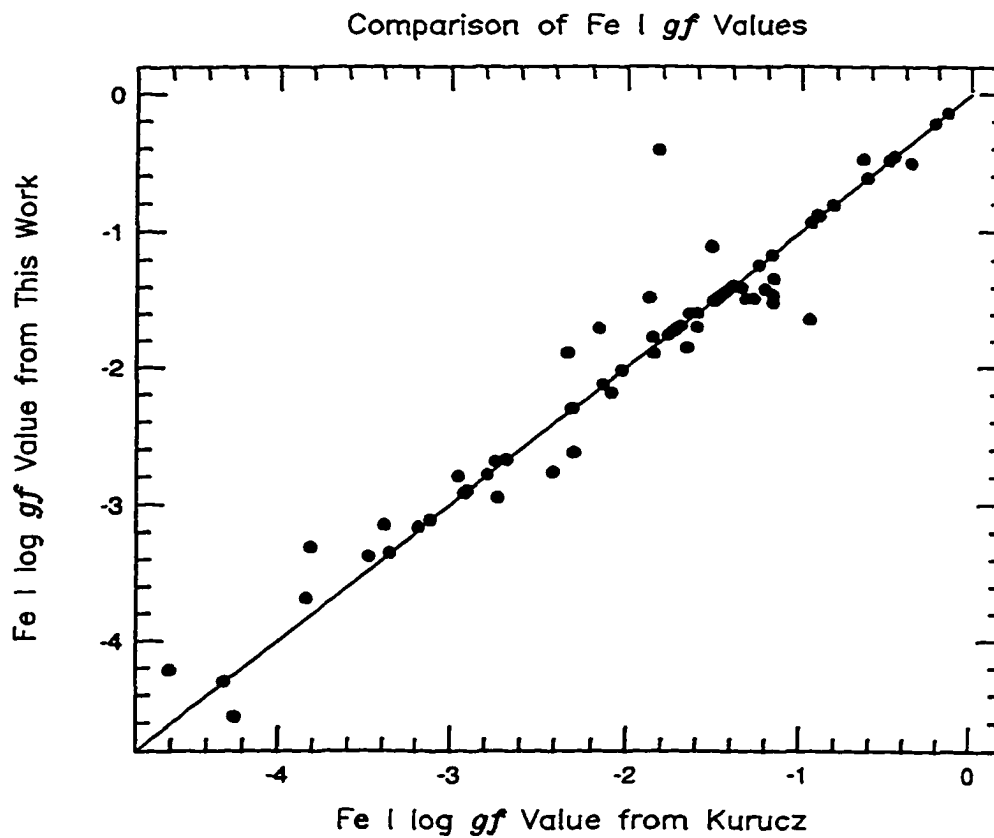


Figure 3.5: A comparison of the gf values for Fe I derived from this work and those given in the line list from Kurucz. Equality is indicated by the solid line.

Other lines: There are a number of other interesting comparisons to be made in Figs. C.1 - C.7. Note first that the continuum window at ~ 869.9 nm (99% level) shows an approximate 0.25% error between the synthetic and solar spectrum; no rectification of the solar to the synthetic spectrum was done before this comparison (note, however, that the spectra shown in Fig. 3.6, air wavelengths, have been rectified).

Where one can find unblended CN lines, the overall strength of the synthetic lines is approximately correct. This shows that the CN dissociation energy of 7.77 eV (Costes et al., 1990) adopted for these calculations is close to the true value. (This value is lower than the 7.9 eV used in the line haze description given in Sec. 3.2.2 above). There are a number of CN lines which are systematically too red by about 0.02 nm, and further work will be needed to identify the transition(s). In early comparisons of the Kurucz CN lines and the Jørgensen CN lines, it was noted that the Jørgensen lines were systematically bluer. For the line list used in these calculations, the Kurucz data were accepted by default for duplicate CN lines. The Jørgensen line list has not yet been tested against observations, but will be in the future.

In general, the gf values and/or broadening parameters for the stronger Si I lines are too small, as is evident in the multiplets at 873.04, 873.10, and 873.17 nm; and 874.48, 875.36, and 875.44 nm. (The gf values for the Si I multiplet at 864.87, 865.08 and 868.87 nm were adjusted to fit.) Since the branching ratios seem to be accurate, the absolute strength of these lines, or the broadening coefficients, has been underestimated and an overall correction can be used. The lines of Mn I show obvious hyperfine splitting; hyperfine splitting will need to be included before any abundance analysis is

possible for this element. The Paschen 15 and 14 lines at 866.740 and 875.29 nm are calculated accurately. The Al I multiplet at 877.53 and 877.63 nm also match well. As a final comment, there are a number of blends of lines of equal strength (for example, Ni I and S I blended with CN) which will make abundance analysis difficult for these elements. The blending between the Na I lines and CN lines between 865.2 and 865.4 nm is particularly relevant for the SSynth calculations for the stars in the sample as it was difficult to get a good match between the synthetic and observed spectra around these lines.

The Ca II line: Figure 3.6 shows the comparison between the synthetic spectrum (using a conservative -6 dex line-blocking error) and the solar central intensity spectrum for the wavelength interval (866.214 ± 1.5 nm, air wavelengths) which forms the foundation for the derivation of the surface gravity, metallicity, microturbulence, and individual elemental abundances of the stars in this study. Adjustments were made to most of the lines in this interval, where necessary, to achieve the match given in Fig. 3.6 (see Figs. C.1 and C.2 for more line identifications at vacuum wavelengths). The continuum windows (98% level) at ~ 865.15 and 867.65 nm were matched for this comparison.

I used a process similar to that given in SD88 to determine the broadening coefficient from collisions by hydrogen. SD88 obtained the gf value and the coefficients for broadening by helium and electrons from other research and then derived the hydrogen broadening coefficient based upon the Ca II profile alone calculated using the Holweger-Müller atmosphere.

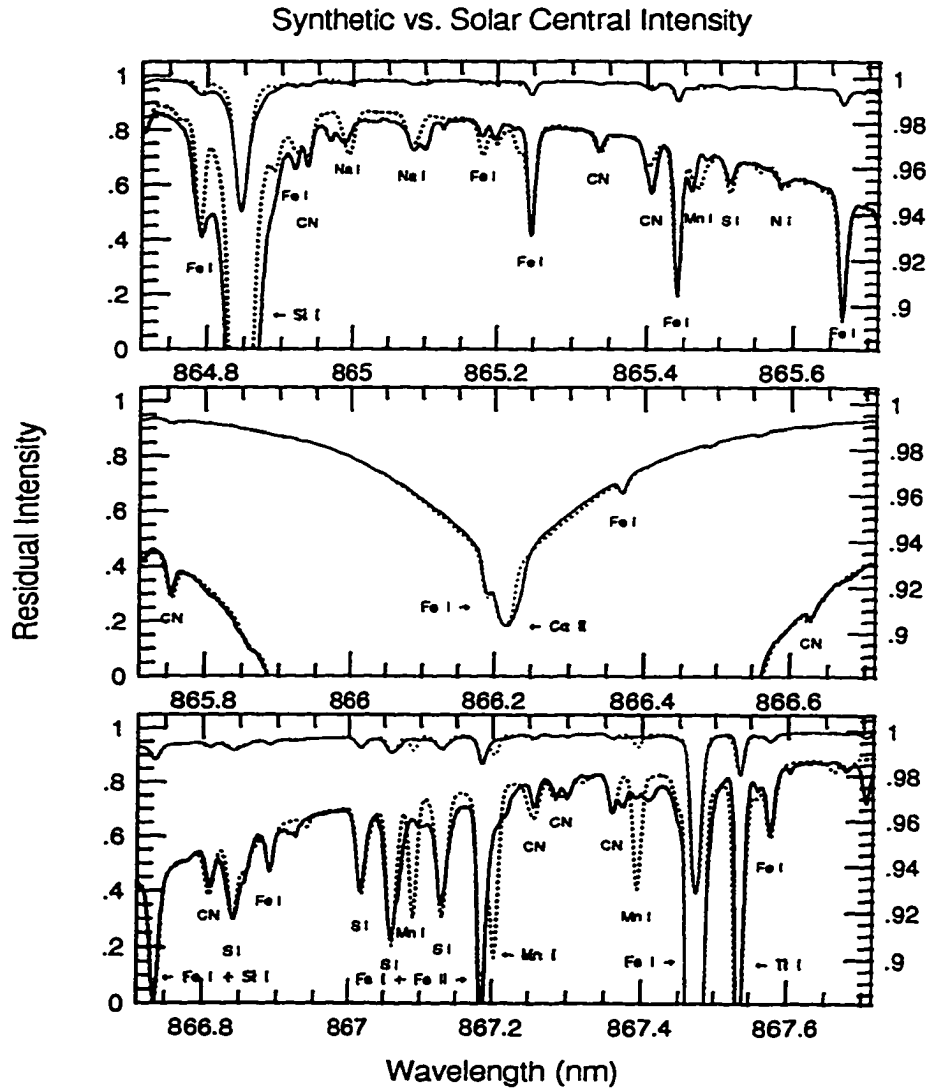


Figure 3.6: A comparison between the Kitt Peak solar central intensity spectrum (solid line, see text) and the synthetic intensity spectrum (dotted line), calculated with a -6 dex blocking error, for the region around the Ca II line at 866.214 nm, air wavelengths, ± 1.5 nm. The comparison is shown both on a normal (left axis) and an expanded (right axis, heavier weighted lines) scale.

My calculations differed in that I adopted the slightly larger $\log gf$ values from Kurucz and Peytremann (1975) for the Ca II triplet lines, included all of the lines in the wavelength interval (i.e., those not eliminated under a -6 dex line-blocking error), and used the Kurucz solar atmosphere. Using $\log gf = -0.73$ for the 866.214 nm line, I derived a hydrogen broadening coefficient of $\log \gamma_H/N_H = -9.28$, 0.1 dex lower than that derived by SD88.

I adopted the other broadening coefficients and temperature dependence as given by SD88 with some minor adjustments. The coefficients for broadening by hydrogen, helium and electrons have been rescaled from 5000 K to adjust for the temperature dependence and are quoted here at full-width. (Note that SD88 had scaled the helium coefficient from 655 K.) Since the lower, $3d$ level of the Ca II line is metastable, the radiative broadening has been determined from the lifetime of the upper, $4p$ levels. According to SD88, this lifetime is precisely known. The hydrogen and helium parameters are assumed to vary as $T^{0.4}$ and the Stark parameter as $T^{0.17}$ throughout the atmosphere. The broadening parameters (quoted for full width half maximum) are as follows:

$$\log \gamma_H/N_H = -9.28 \text{ rad s}^{-1} \text{cm}^3 \quad (3.11)$$

$$\log \gamma_{He}/N_{He} = -9.7 \text{ rad s}^{-1} \text{cm}^3 \quad (3.12)$$

$$\log \gamma_S/N_e = -6.15 \text{ rad s}^{-1} \text{cm}^3 \quad (3.13)$$

$$\log \gamma_R = 8.18 \text{ rad s}^{-1} . \quad (3.14)$$

The total broadening is thus:

$$\Gamma = \gamma_H T^{0.4} + \gamma_{He} T^{0.4} + \gamma_S T^{0.17} + \gamma_R . \quad (3.15)$$

The Ca II infrared triplet line lies on the square-root or damping part of the curve of growth. Any change in the line parameters changes the depth of the wings (Mihalas, 1978, Fig. 10-1). If the gf -value or the calcium abundance adopted here are found to be in error, the hydrogen broadening coefficient must be adjusted to maintain consistency with the $A_{Ca} gf \gamma_H / N_H$ (A_{Ca} being the abundance of calcium) value for the solar spectrum.

Figs. 3.6 shows a much better fit to the entire Ca II line than that achieved by SD88, even to within ± 0.1 nm of the line core where non-LTE effects should prevail. Figure 3.6 also shows the well-known asymmetry of the line core, due perhaps to large-scale motions in the lower chromosphere (SD88).

Solar flux comparison

After the adjustment of the line-specific parameters, the next step is to calculate the stellar flux spectra, convolve the spectra with the appropriate rotation-macroturbulence of the star, and then with the estimated instrumental profile. The uncertainty in this step is determining *the* instrumental profile. I proceeded with this analysis under the assumption the instrumental profiles of the CFHT and DAO telescopes would be similar due to the similarity of the spectrographs. Booth et al. (1989) analyzed the instrumental profile of the DAO 1.22-m coudé spectrograph using the same Reticon detector and Richardson image slicer used in our observations. Figure 7 of their report shows the broad, extensive wings of the profile indicative of a rather high level of instrumental scattered light: of order 10% at 632 nm.

For this analysis, I modeled the instrumental profile by adding a constant

(and renormalizing) for the instrumental scattered light and convolving each spectrum with a Gaussian for the instrumental resolution. The accuracy of this approximation can be tested because, fortunately, we have DAO and CFHT solar flux spectra observed with the same instrumental set up as the other spectra. These observed spectra can be compared with the digitized, high-quality Solar Flux Atlas (Kurucz et al., 1984), which was also observed with the Kitt Peak FTS. This spectrum has a resolving power of 522,000 in the infrared and a signal-to-noise ratio of between 2,000 and 9,000. Since all spectra contain the macroturbulence and rotation broadening from the Sun, the only difference should be the instrumental profiles contained in the DAO and CFHT spectra.

The algorithm adopted for the correction for the instrumental scattered light is discussed in detail by Gray (1992). We modified his Eq. (12.16) to derive the observed spectrum rather than the “true” spectrum:

$$\frac{F_\lambda}{F_\lambda^c} = \frac{F_{0\lambda}/F_{0\lambda}^c + s}{1 + s}, \quad (3.16)$$

where F_λ is the observed flux, c denotes the continuum, F_0 is the true flux in the absence of instrumental scattering (i.e., that calculated by SSynth), and s is the scattering fraction. This simplified formula will not work in a crowded spectral region nor where only a few strong lines dominate (e.g., the spectrum of an A0 V star). This formula also does not correct the inverse-square wings of the Ca II 866.2 nm line as accurately as would a more detailed treatment of the instrumental profile.

Stephenson Yang obtained the DAO solar spectrum on 6 January 1989 by observing the reflection off the inside of the dome of the 1.22-m telescope.

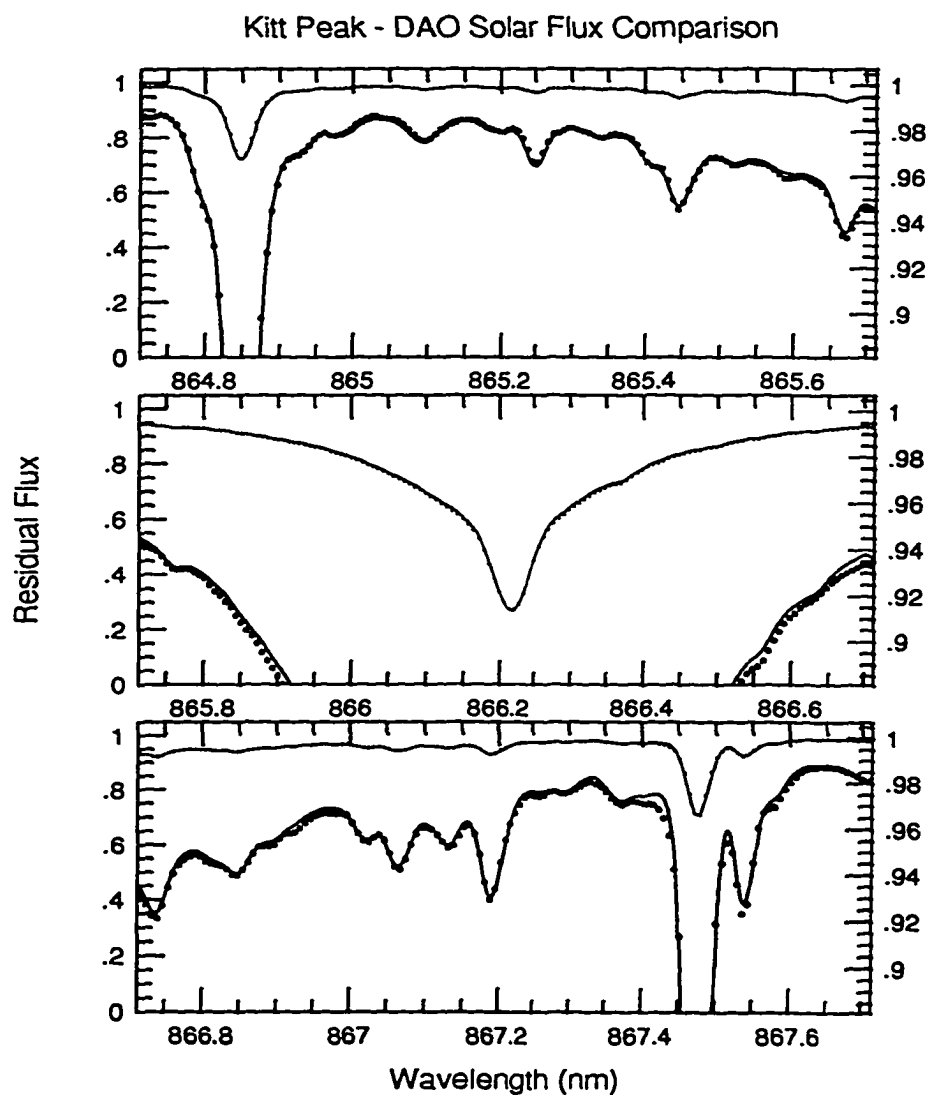


Figure 3.7: A comparison of the DAO solar flux spectrum (dotted line) with the Kitt Peak FTS solar flux spectrum (solid line) corrected for 5% light scattering and convolved with a Gaussian having $\sigma = 4.2 \text{ km s}^{-1}$. The spectra are shown both on a normal scale (left axis) and expanded scale (right axis).

The signal-to-noise ratio is over 2500 per pixel in the continuum. Figure 3.7 compares this DAO spectrum with the Kitt Peak flux spectrum corrected for 5% scattering and convolved with a Gaussian with $\sigma = 4.2 \text{ km s}^{-1}$. The DAO spectrum was rectified to the Kitt Peak spectrum. The figure shows that the approximation for the instrumental profile of the 1.22-m telescope gives differences between these two spectra of typically less than 0.25% for this spectral interval. The scattering level is about half that estimated by Booth et al. (1989), implying that the scattered light is less in the near infrared.

The spectral purity, $\delta\lambda$, can be calculated by:

$$\delta\lambda = Pw' , \quad (3.17)$$

where P is the reciprocal linear dispersion and w' is the projected slit width (Schroeder, 1987, Eq. (12.2.2)). The projected slit width⁶ for the Richardson IS32R image slicer is given as $36 \mu\text{m}$. At a reciprocal dispersion of 0.48 nm mm^{-1} , $\delta\lambda = 0.0173 \text{ nm}$. The FWHM of the convolved Gaussian is 2.354σ or 9.89 km s^{-1} . This corresponds to $\delta\lambda = 0.0286 \text{ nm}$ and an effective projected slit width at the Ca II line of $\sim 60\mu\text{m}$. The larger effective slit width is due to a combination of factors: 1) there is some spherical aberration in the spectrograph (Booth et al., 1989); 2) electrons excited by lower-energy photons tend to diffuse between pixels more than those excited by higher-energy photons; 3) the four gratings of the mosaic are not perfectly aligned; and most importantly, 4) the focal plane is curved at the Reticon and thus the spectrum is not in focus.

⁶Given in the on-line instrument manuals for the 1.2-m telescope at:

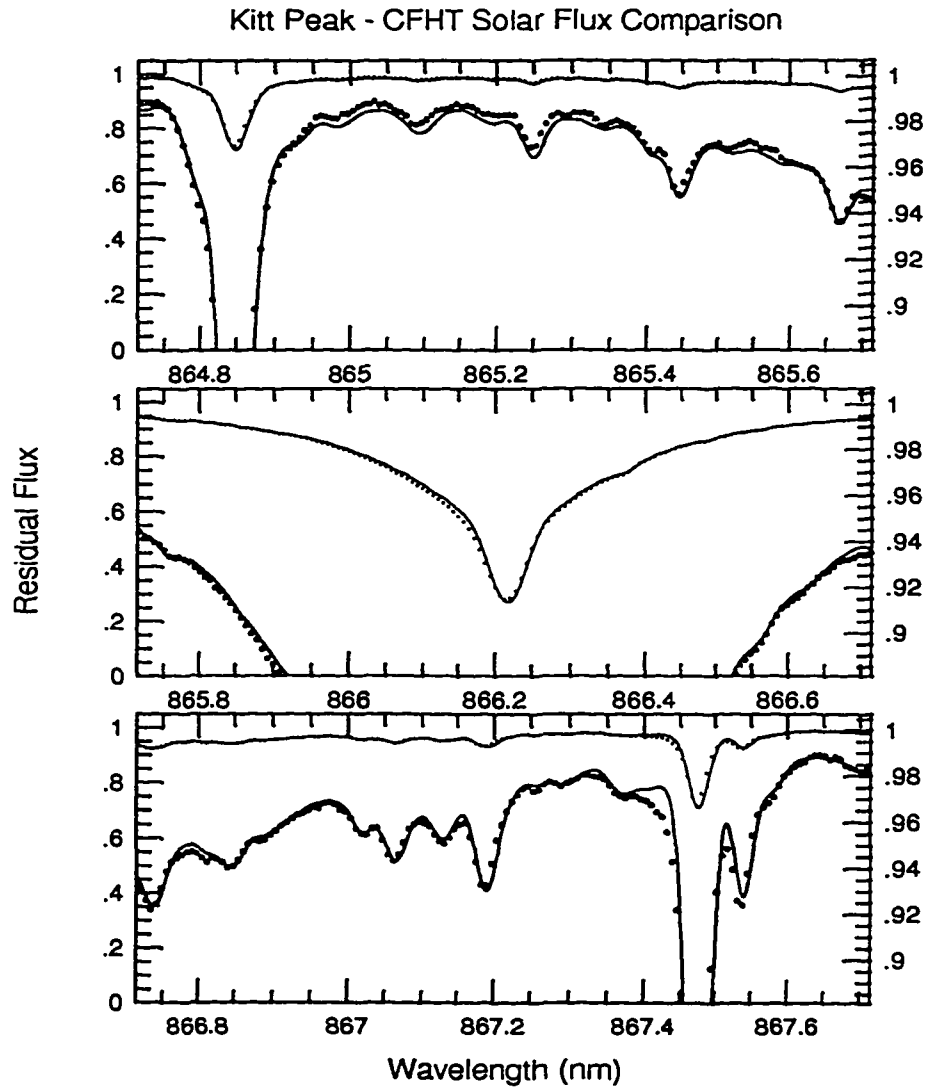


Figure 3.8: A comparison of the CFHT solar flux spectrum (dotted line) with the Kitt Peak FTS solar flux spectrum (solid line) corrected for 5% light scattering and convolved with a Gaussian having $\sigma = 4.2 \text{ km s}^{-1}$ (see text). The spectra are shown both on a normal scale (left axis) and expanded scale (right axis).

The spectrum of the Sun was obtained at the CFHT on 12 December 1984 through observations of the 20-day old moon. The signal-to-noise ratio is approximately 1200 per pixel in the continuum. Figure 3.8 compares the CFHT spectrum with the Kitt Peak spectrum again corrected for 5% scattered light and convolved with a Gaussian having $\sigma = 4.2 \text{ km s}^{-1}$. The approximation for the instrumental profile of the 3.6-m telescope gives differences between these two spectra of typically less than 0.5% for this spectral interval. Close examination of the expanded spectra of Fig. 3.8 reveals that the actual resolution of the CFHT spectrum is higher than that implied by the Gaussian used. A Gaussian with $\sigma \approx 3.8 \text{ km s}^{-1}$ better matched the resolution, but then there was no constant which could be added to correct for the scattered light which would simultaneously create a match with the line cores of the strongest lines and the wings of the Ca II line. The DAO values were then simply adopted. The projected slit width⁷ of the Richardson CF4Red image slicer used at the CFHT is $34 \mu\text{m}$. Since the reciprocal linear dispersion was also $\sim 0.48 \text{ nm mm}^{-1}$, $\delta\lambda = 0.0163 \text{ nm}$. The FWHM corresponding to the Gaussian with $\sigma = 3.8 \text{ km s}^{-1}$ is 0.0258 nm , or, since the dispersion is $0.00712 \text{ nm pixel}^{-1}$, a projected slit width of $54 \mu\text{m}$. The spectra observed at the DAO are slightly better sampled than those at the CFHT.

As mentioned, the comparison between the Kitt Peak and CFHT solar flux spectra shows that the use of the DAO instrumental profile results in

<http://www.dao.nrc.ca/DAO/TELESCOPE/telescope.1-2m.html>

⁷Previously given in the on-line manuals for the CFHT instruments at: <http://cadwww.dao.nrc.ca/cfht/cfht.html>. This information has now been removed from the instrument manuals as the image slicer is no longer used

differences which are typically less than 0.5%. Future work will involve a more robust model of the instrumental profile for both telescopes. We have records of the arc lamps taken with each grating and may be able use these to model the time dependent instrumental profile with a Gaussian for the line core, a Lorentzian between 25 and 90 pixels from line center, and a pseudo-Lorentzian with a power of 1.6 beyond 90 pixels, as was done in Booth et al. (1989). One should note, however, that our approximation to the instrumental profile qualitatively compares just as well, for many more lines, with the Solar Flux Atlas as the spectra shown in Fig. 8 of Booth et al. (1989).

Figure 3.9 compares the spectrum of β Geminorum taken at the CFHT with that taken at the DAO. The top figure shows the ratio of the two spectra; the standard deviation of the residuals for the complete spectrum is 0.0118. The bottom figure overplots the CFHT spectrum (solid line) on the DAO spectrum (dotted line), and shows in a slightly different manner the difference in the scattered light and resolution for each spectrograph. The cores of the stronger lines are shallower in the CFHT spectrum, up to 10% in some cases. The differences between the spectra will have a systematic effect on the value of ξ , and to a lesser extent on the abundances, derived from the spectra from each observatory in the sense that the DAO values will be larger. Even so, this comparison gives an indication that our results are reproducible between observatories at an approximate 1% level. This comparison can be extended to other stars where we have duplicate spectra between observatories or where we have multiple reference spectra for individual stars at each observatory. At the present time, the systematic errors in the line data are much greater than those arising from the reproducibility of our results between observatories.

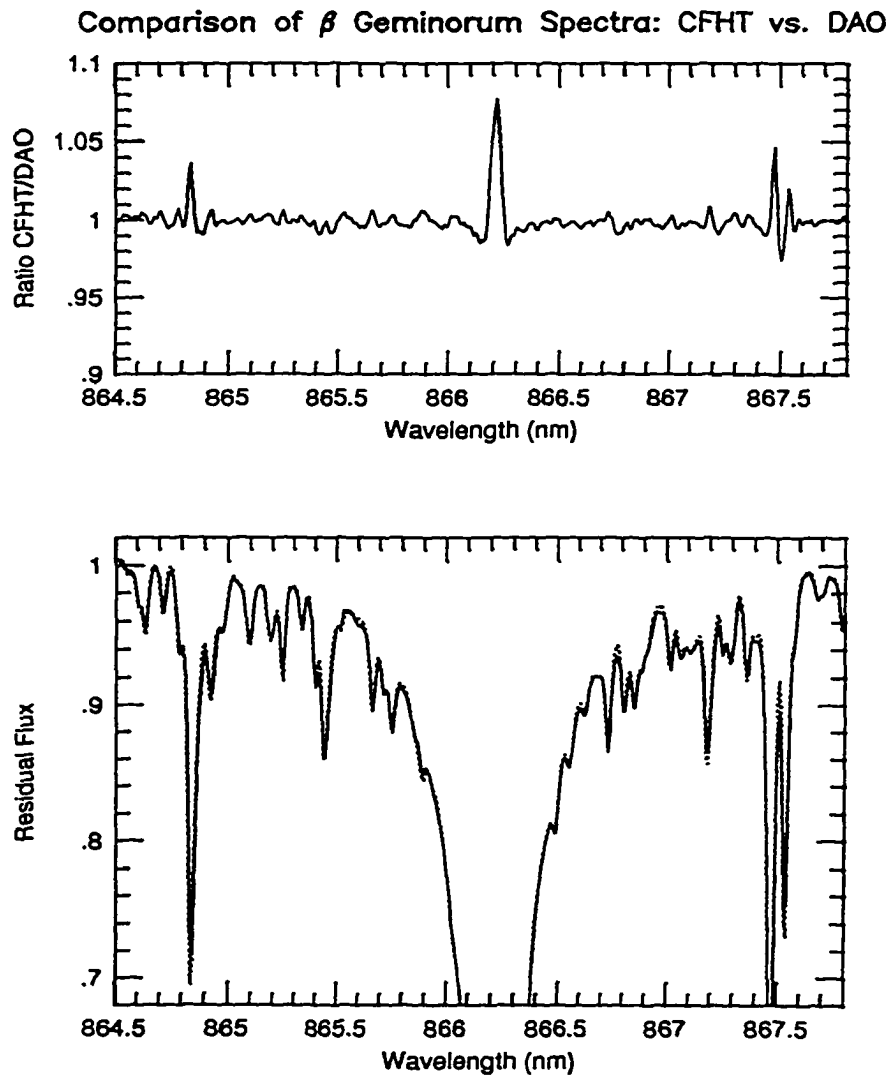


Figure 3.9: A comparison of spectra of β Geminorum observed both at the CFHT and the DAO for the region 864.7-867.7 nm. The top figure shows the ratio of the CFHT and DAO spectra; the standard deviation for the full ~ 14 nm is 0.0118. The largest difference is in the amount of scattered light in each spectrograph; the scattered light is greater in the CFHT spectrum.

Figure 3.10 and 3.11 compare the corrected synthetic flux spectrum with the DAO and CFHT spectra. In addition to the instrumental profile, the synthetic solar flux spectrum must also be convolved with the rotation and macroturbulence profiles of the Sun. The Sun rotates differentially with respect to latitude, with periods ranging from 25 to 30 days, the maximum $v \sin i$ being about 2 km s^{-1} . Since the Doppler shift also varies across the disk of the Sun, the largest shift will occur at the limb at the equator. Gray (1992, Fig. 17.5), gives an example of a disk-integrated rotation profile, and shows that it is non-Gaussian. The macroturbulence of the Sun is estimated to be about $1.0\text{-}1.2 \text{ km s}^{-1}$. A consideration of the anisotropy of macroturbulence and the integration across the disk leads to the macroturbulence function, also non-Gaussian, shown in Gray (1992, Fig. 18.4). I reproduced these rotation and macroturbulence profiles and convolved them; the resulting profile is nearly Gaussian. Thus, in the solar case where the rotation and macroturbulence broadening are nearly equal, we will consider each profile as Gaussian and add the standard deviations quadratically to obtain a Gaussian with $\sigma = 2.236 \text{ km s}^{-1}$. The exact shape of the rotation and macroturbulence profiles is not important as the line profiles for the Sun are dominated by the instrumental profile; thus the convolution which includes resolution, rotation, and macroturbulence is with a Gaussian having $\sigma = 4.758 \text{ km s}^{-1}$.

3.2.4 Post-SSynth: stellar comparisons

Section 3.2.3 discussed the steps taken to adjust each synthetic spectrum for the rotation and macroturbulence of the Sun and for the light scattering in the spectrograph and instrumental profile of the telescope; similar adjust-

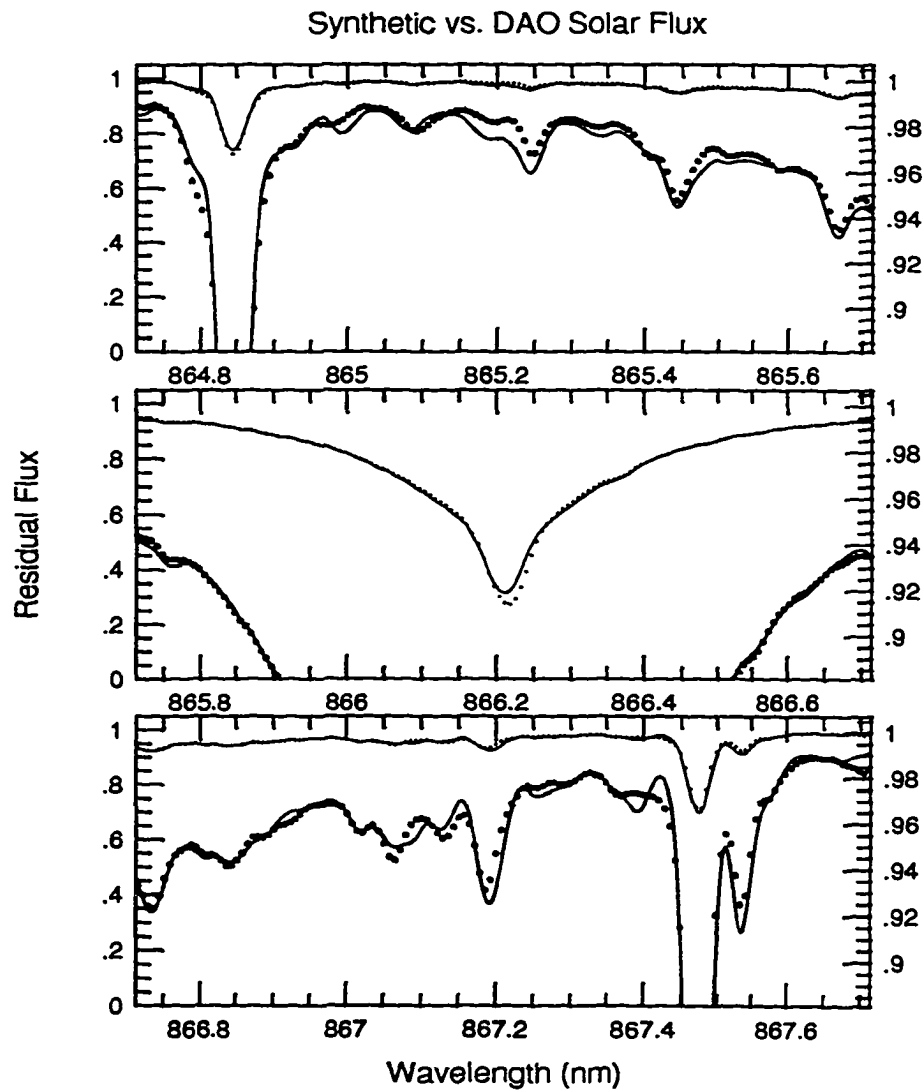


Figure 3.10: A comparison of the DAO solar spectrum (dotted line) with the synthetic flux spectrum (solid line) corrected for 5% light scattering and convolved with a Gaussian with $\sigma = 4.758 \text{ km s}^{-1}$ for rotation-macroturbulence and instrumental broadening. The spectra are shown on both a normal (left axis) and expanded (heavy lines, right axis) scale.

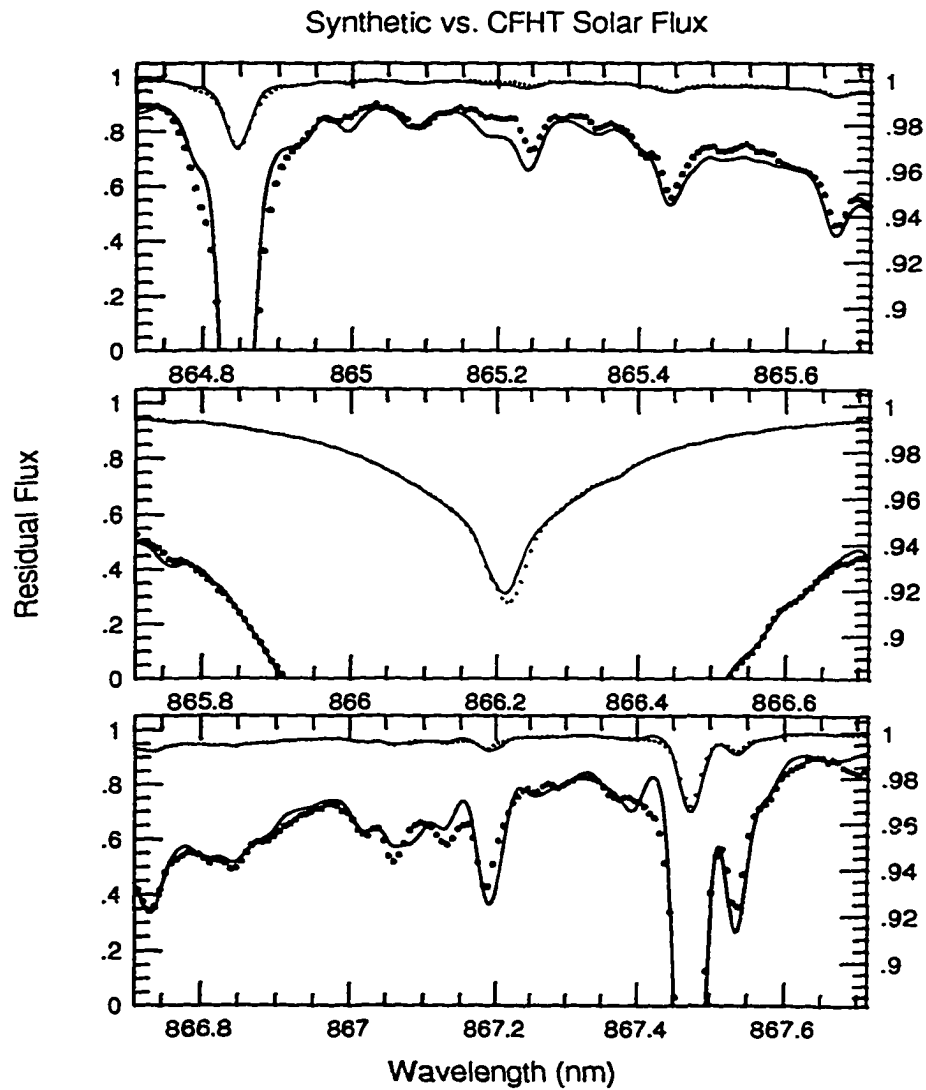


Figure 3.11: A comparison of the CFHT solar spectrum (dotted line) with the synthetic flux spectrum (solid line) corrected for 5% light scattering and convolved with a Gaussian with $\sigma = 4.758 \text{ km s}^{-1}$ for rotation-macroturbulence and instrumental broadening. The spectra are shown on both a normal (left axis) and expanded (heavy lines, right axis) scale.

ments are made for the other stars. In addition, two more adjustments must be made before one can compare the synthetic and observed spectra for the other stars. First, the observed spectrum must be corrected for the relative line-of-sight motion of the observer and the star. Second, the observed and synthetic spectra must be rectified. IRAF is used for both of these tasks.

The IRAF task *rvcorrect* is used to correct the observation to the barycenter of the solar system. The task corrects for the diurnal, lunar, annual, and solar velocities relative to some specified standard of rest. IRAF scripts have been written to do this automatically, with information concerning the right ascension and declination of the star, observatory, date of observation, etc., provided by the user. The program requires an estimate of the true radial velocity of the star. This task returns the radial velocity of the star with respect to the local standard of rest; the task *dopcorrect* is then used to actually shift the observed spectrum. This particular task is used subsequently if fine adjustments to the Doppler shift are needed.

The observed spectra must be rectified to the synthetic because the observed spectra retain the influence of any variation of instrumental response not removed by flat fielding (discussed in Sec. 2.1.1) plus, possibly, a normalized residual flux level (introduced in the reduction process) which is different from the synthetic one. The synthetic spectrum reproduces the stellar flux divided by the continuum: $SS = F(\lambda)/F_c(\lambda)$. The rectified stellar spectrum, S_{rect} is formed through

$$S_{rect} = \frac{S'}{S'_{fit}} \times SS_{fit} \quad (3.18)$$

where S' is the flat-fielded observed spectrum, S'_{fit} is a linear least-squares

fit to this spectrum, and SS_{fit} is a linear least-squares fit to the synthetic spectrum.

3.3 Gauging the Atmospheric Parameters

The model atmosphere for a star is described by four global parameters: the effective temperature, the surface gravity, the metallicity, and the microturbulence. Ideally, one would use a large number of lines to constrain each parameter. Because a limited spectral region is examined here, I found only a few lines which are suitable for estimating these parameters: the relative strength of the Ti I 867.537 nm line to Fe I 867.474 nm for the effective temperature; the wings of the Ca II 866.214 nm line for the surface gravity; and the Fe I lines at 865.247, 865.440, and 865.667 nm for $[Fe/H]$ (and thus $[M/H]$ assuming all elements scale with iron). The usual practice of demanding that the abundances derived from weak lines (here, the Fe I lines at 865.247, 865.440, and 865.667 nm) match those derived from saturated lines (here, the Fe I line at 867.474 nm) was used for estimating the microturbulence.

The use of line-depth ratios is an accurate means of determining *relative* effective temperatures for cool stars, often to less than 10 K (Gray, 1994). Bohlender et al. (1992) used the equivalent widths of certain temperature sensitive lines in the HF spectral region to derive the relative changes used in the $\Delta(R - I)$ index. These methods are not as accurate in determining absolute effective temperatures as one must be concerned with accurate continuum placement, blending of lines at the continuum, and blending in the

cores of the lines used.

Spectrum synthesis should prove to be a reliable method of determining the *absolute* value of the effective temperature of a star because of the comprehensive way the synthesis calculates the continuum and includes all (known) blended lines. There are two lines in the 864.7-867.7 nm region which were used to estimate the effective temperatures of the stars: the Fe I line at 867.474 nm (multiplet No. 339, excitation energy of $40491.274 \text{ cm}^{-1}$) and the Ti I line at 867.537 nm (multiplet No. 69, excitation energy of 8602.34 cm^{-1}). Figure 3.12 shows the unprocessed SSynth spectra of these two lines for two metallicities and surface gravities. One notes that for $\log g = 4.5$ and low T_{eff} both lines are saturated and are largely insensitive to temperature; the Ti I line is affected as the calculations go to higher effective temperatures. The line depth ratios (line depth defined at the minimum of the line profile) are not strongly affected by changes in surface gravity. Figure 3.13 shows the line-depth ratio of Ti I to Fe I as a function of effective temperature over the same range of metallicity and surface gravity and emphasizes the temperature sensitivity of the Ti I line, especially at lower metallicities. However, this temperature sensitivity also makes the Ti I line susceptible to any errors in the $T - \tau$ relationship of the atmospheres. Based upon the fits to the stellar spectra, I estimate an uncertainty of $\pm 50 \text{ K}$ for the effective temperatures derived here. This estimate assumes $[\text{Ti}/\text{Fe}] = 0$. Since there is only one strong Ti I line in the spectral region examined here, the use of this line as a temperature indicator precludes any independent determination of the titanium abundance. Alternatively, I could have adopted an effective temperature, perhaps one derived from the infrared-flux method,

and determined the titanium abundance for each star. These limitations will be eliminated once the full spectral region of 14 nm is examined.

A fit to the wings of the Ca II infrared triplet line at 866.214 nm was used to derive the surface gravity for each star. The top graph of Fig. 3.14 shows the fraction of the total line depth, at $\lambda = 865.8$ nm, contributed by each of the individual broadening mechanisms for the Ca II line for an atmosphere with $T_{eff} = 4500$ K, $\xi = 2.0$ km s⁻¹, $[M/H] = 0.0$, and a range of $\log g$ values. Broadening by collisions with helium and the electrons contribute negligibly. The cross-over for collisional broadening by hydrogen and radiative broadening occurs at $\log g \approx 2.5$. The bottom plot of Fig. 3.14 shows the 866.2 nm line in isolation for three $\log g$ values, for the same T_{eff} , ξ , and $[M/H]$. This figure shows the sensitivity of the wings to changes in surface gravity between 0.2 and 1.0 nm from line center.

For the stars considered here, Ca II is the dominant ionic stage of calcium and H⁻ opacity is the dominant source of continuum opacity. Because of this, one expects the Ca II lines to strengthen as pressure decreases for these stars (due to the decrease in electron pressure, P_e) where radiative broadening dominates and to strengthen as pressure increases where pressure broadening dominates. This can easily be shown analytically. Where H⁻ dominates, the continuum opacity $\kappa_\nu \propto n_e \propto P_e$. The line opacity, $l_\nu \propto \Gamma$, where $\Gamma \propto P_{gas} + P_e + constant$, Γ being the total broadening from hydrogen, helium, and electrons, and the radiative contribution, and P_{gas} is the gas pressure. Thus,

$$W_\nu \propto \frac{l_\nu}{\kappa_\nu} \propto \frac{\Gamma}{P_e}. \quad (3.19)$$

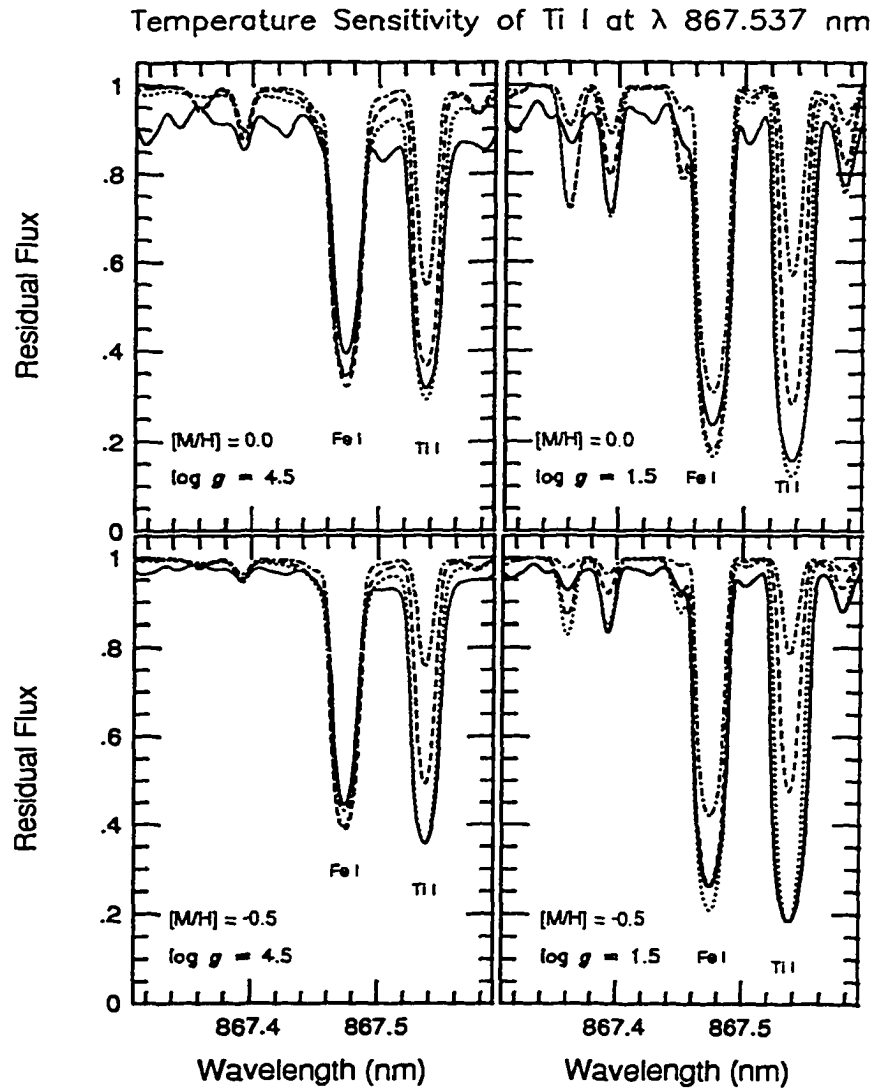


Figure 3.12: The T_{eff} sensitivity of the low-excitation Ti I line at 867.537 nm, relative to the Fe I line at 867.474 nm is shown as a function of $[M/H] = 0.0$ and -0.5 , $\log g = 4.5$ and 1.5 , $\xi = 2.0$ and $T_{eff} = 3750$ K (solid line), 4250 K (dotted line), 4750 K (dashed line), and 5250 K (dash-dot line). These spectra have not been convolved with any additional broadening.

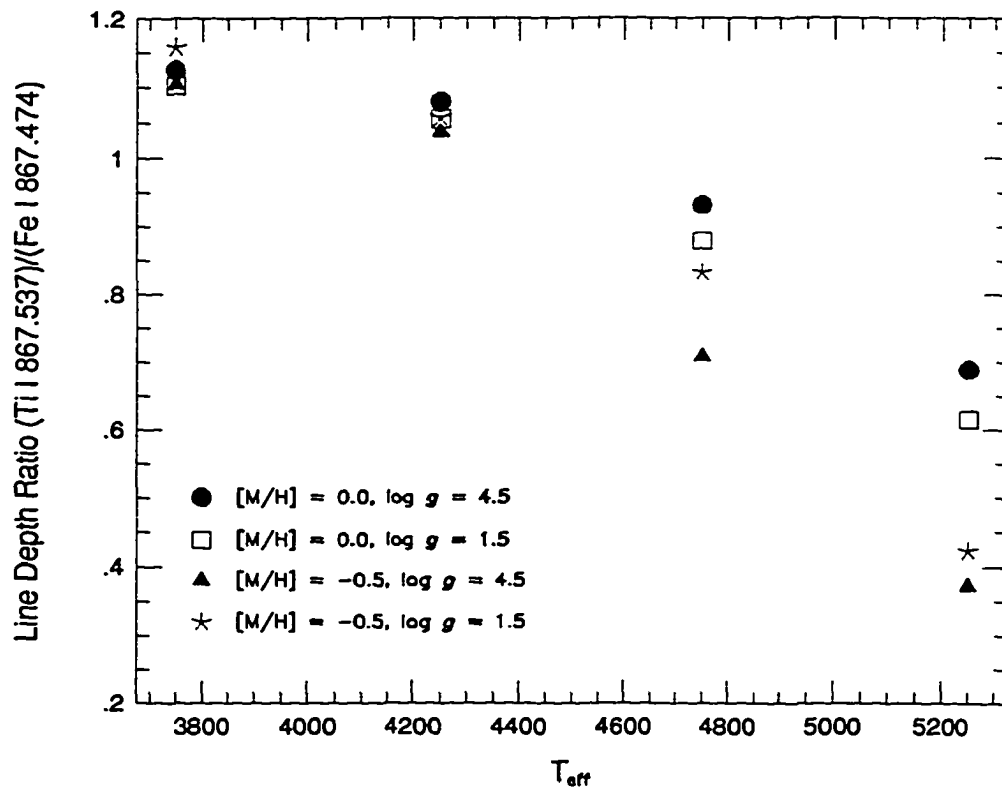


Figure 3.13: The line-depth ratio (line depth defined at the minimum point of the line profile) of the temperature-sensitive, low-excitation Ti I line at 867.537 nm to the Fe I line at 867.474 nm for two $[M/H]$ and $\log g$ values. The Ti I line is most sensitive to changes above 4200 K at lower metallicities.

Ignoring the negligible contribution from helium and Stark broadening and any temperature dependence, we find:

$$\frac{\Gamma}{P_e} \propto \left(\frac{P_{gas}}{P_e} \right) \quad (3.20)$$

for large values of $\log g$, and

$$\frac{\Gamma}{P_e} \propto \left(\frac{1}{P_e} \right) \quad (3.21)$$

for small values of $\log g$.

Figure 3.15 shows a more quantitative measurement of the change in the equivalent width of the Ca II line as a function of surface gravity and two metallicities for $T_{eff} = 4500$ K and $\xi = 2.0$ km s⁻¹. For $[M/H] = 0.0$ and $\log g \geq 3$, $W_\lambda \propto g^{1/30}$. For $[M/H] = 0.0$ and $\log g \leq 1$ (where radiative broadening truly dominates), $W_\lambda \propto g^{-1/2}$. These relationships steepen and flatten respectively for the $[M/H] = -0.5$ value due to increasing gas pressure at lower metallicities. The dependence of W_λ on surface gravity differs from similar arguments given by Jørgensen et al. (1992) and the qualitative relationship given by their Eq. (4),

$$W(g) = c_w g^{1/3} + c_s + c_n g^{-1/3} \quad (3.22)$$

where c_w , c_s , and c_n are fitting constants. However, we predict the same overall behavior of the equivalent width of the Ca II line as Jørgensen et al. (1992), as a comparison of our Fig. 3.15 and their Fig. 1b-c shows.

The exact parametric behavior of the Ca II infrared triplet lines has been the topic of active discussion since the mid-1980's. Jørgensen et al. (1992) summarize the different approaches taken and the respective conclusions.

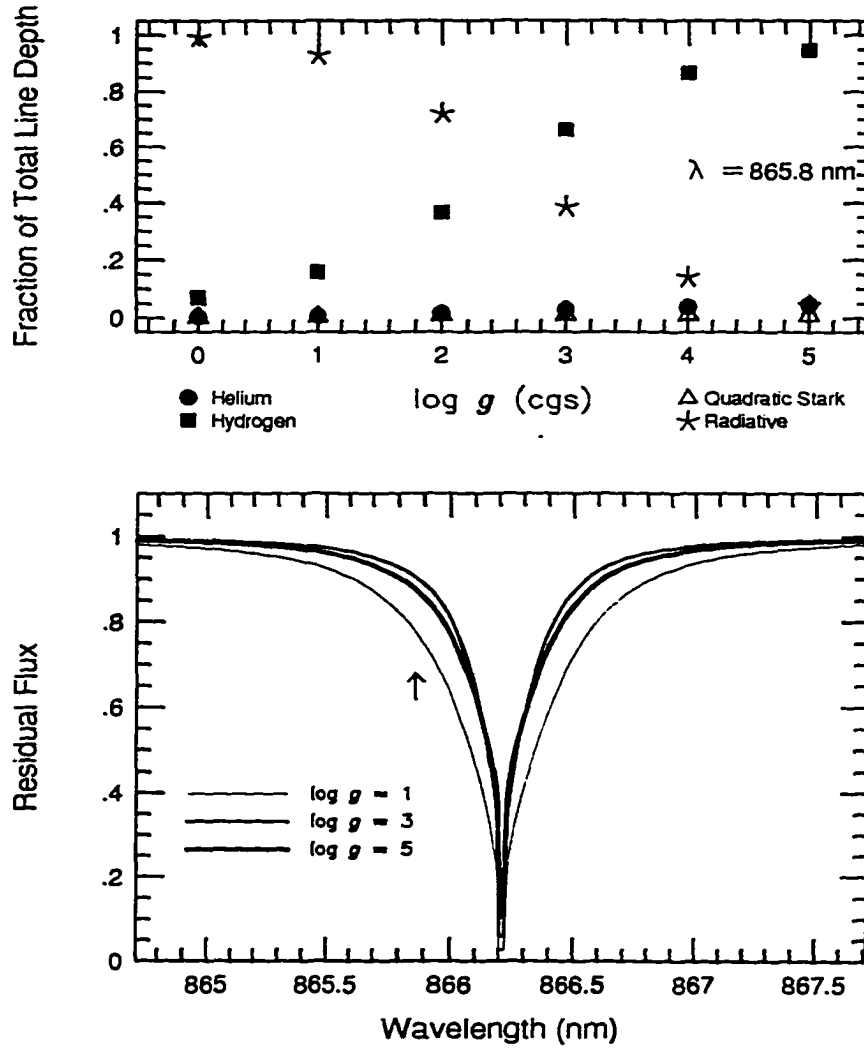


Figure 3.14: Top: the relative contribution of the four broadening mechanisms to the total line depth of the Ca II 866.2 nm line at $\lambda = 865.8$ nm. Bottom: the line profile of Ca II 866.2 nm as a function of surface gravity. Note particularly the sensitivity of the wings between 0.2 and 1.0 nm from line center. These calculations were for $[M/H] = 0.0$, $T_{eff} = 4500$ K, $\xi = 2.0$ km s⁻¹.

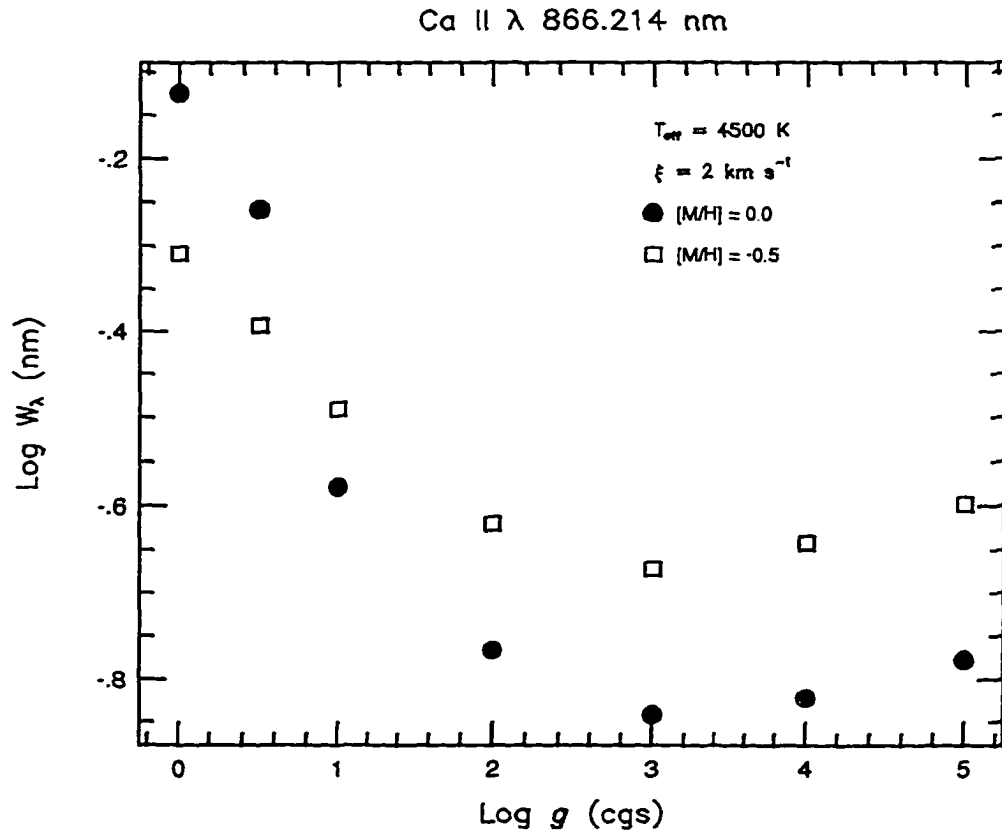


Figure 3.15: The equivalent width, W_λ , of the Ca II 866.2 nm line vs. surface gravity for $T_{\text{eff}} = 4500 \text{ K}$, $\xi = 2.0 \text{ km s}^{-1}$, and $[M/H] = 0.0$ and -0.5 . The equivalent width is particularly sensitive to decreasing surface gravity below $\log g \approx 2.0$ where radiative broadening begins to dominate.

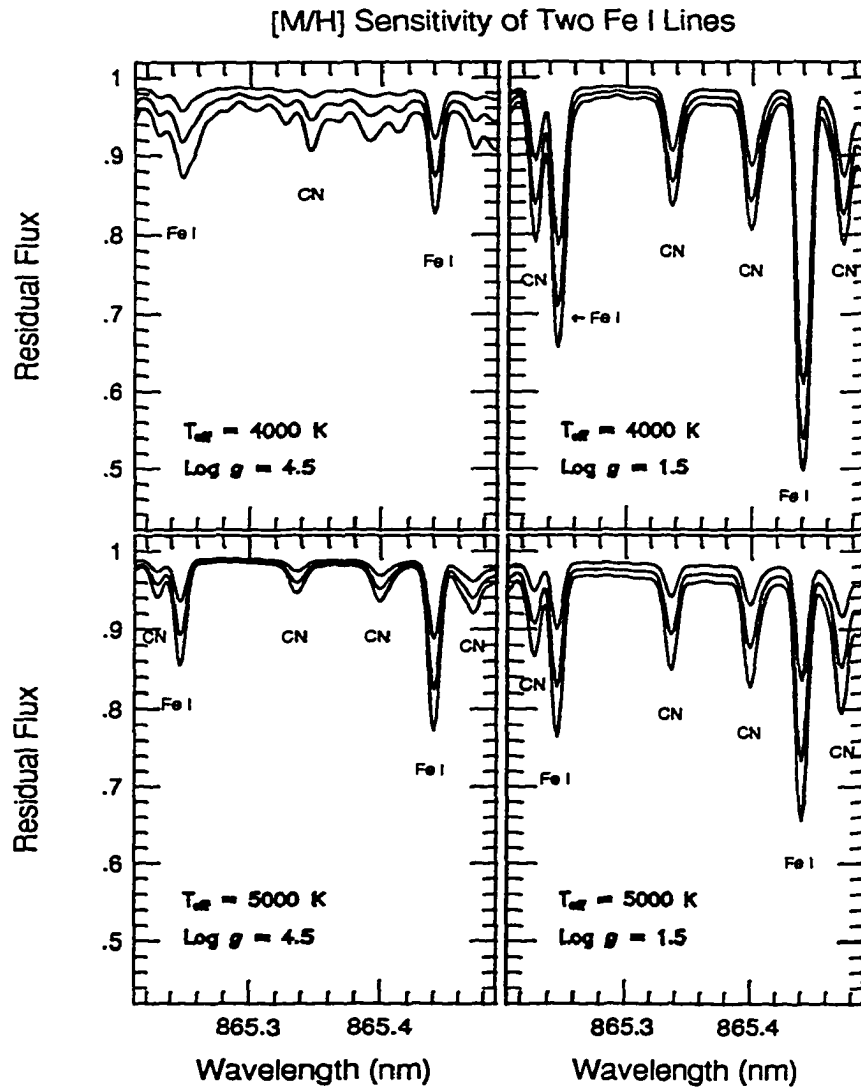


Figure 3.16: The change in two Fe I lines as a function of abundances, $[M/H] = -0.5, -0.2,$ and $0.0,$ for $T_{eff} = 4000$ and 5000 K, and $\log g = 4.5$ and $1.5.$ The $[M/H]$ value for the stars was derived from profile fits to the Fe I lines at $865.247, 865.440,$ and 865.667 (not shown) nm.

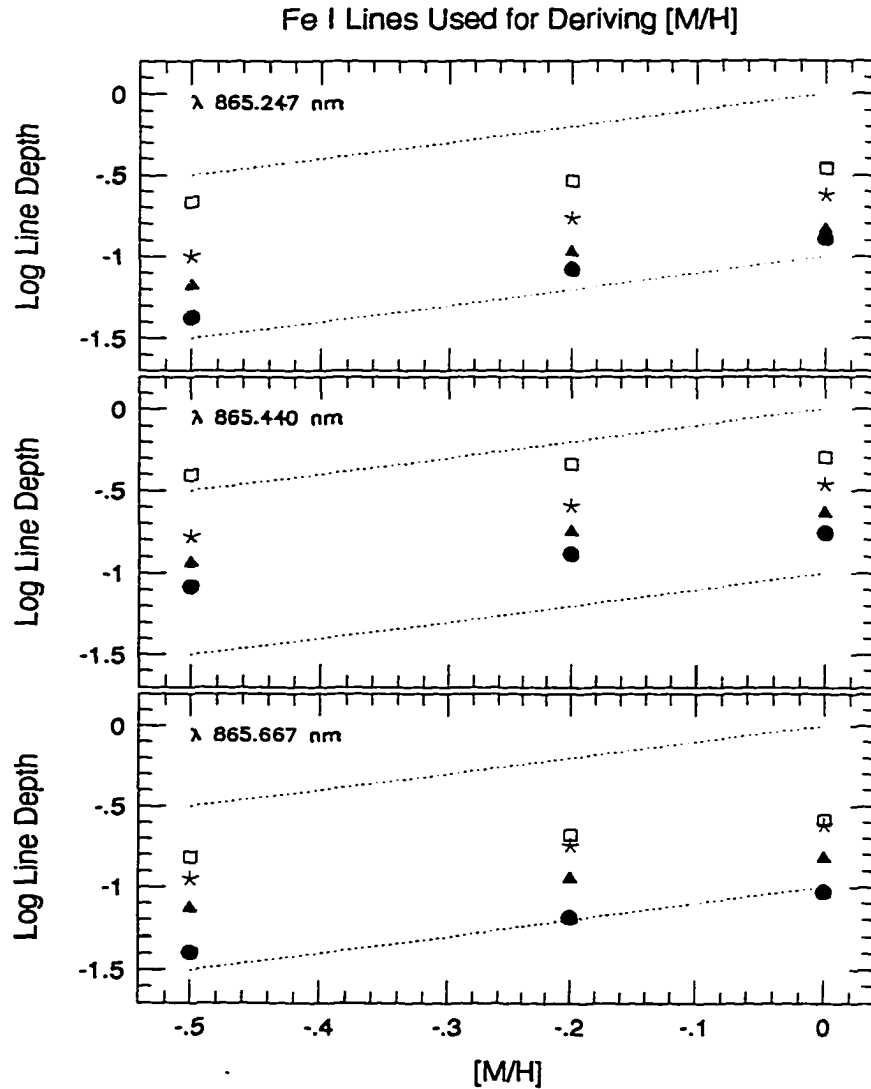


Figure 3.17: The line depth as a function of metallicity, [M/H], for the Fe I lines at 865.247, 865.440, and 865.667 nm for $T_{eff} = 4000$ K, $\log g = 4.5$ (filled circles); $T_{eff} = 4000$ K, $\log g = 1.5$ (open squares); $T_{eff} = 5000$ K, $\log g = 4.5$ (filled triangles); and $T_{eff} = 5000$ K, $\log g = 1.5$ (stars). Blending with CN lines flattens the correlation at low T_{eff} and $\log g$. The dotted lines represent the slope weak lines would have in this comparison.

The consensus now is that the strength of the Ca II infrared triplet lines depends on T_{eff} , $\log g$, and $[M/H]$. Stars with lower abundances tend to have an overabundance of the α elements. Thus, the relative abundance of Ca II is a function of $[M/H]$. Since the Ca II 866.214 nm line is on the square-root part of the curve of growth, one also expects $W_\lambda \propto \sqrt{N_{Ca}}$. The equivalent width of the Ca II lines is also affected by the relative increase in the abundance of the electron donors, principally Si and Mg. The Ca II lines cannot be dependably used as a surface gravity indicator unless an independent measure is made of the T_{eff} (accomplished here through the Fe I and Ti I lines) and $[M/H]$ of each star (derived here from the Fe I lines). For an assumed $[Ca/Fe]$ value, I estimate the uncertainty in the $\log g$ values derived here to be ± 0.05 for the dwarfs and ± 0.2 for the giants. These uncertainties are based on the quality of the fits to the spectra, and are higher for the giants because the fits are harder to judge. That is, even though the wings of the Ca II line are more sensitive to changes in $\log g$ at small $\log g$, the wings are "contaminated" by line blending and the profile is fit at only a few points (compare Figs. 3.20 and 3.24).

The $[M/H]$ value for the stars in this study was derived primarily through the synthetic fit to three Fe I lines at 865.247, 865.440, and 865.667 nm (multiplet Nos. 1050, 623, and 1269). The metallicity sensitivity of the first two lines only (for clarity) is shown in Fig. 3.16 for $[M/H] = 0.0, -0.2,$ and -0.5 , and $T_{eff} = 4000$ and 5000 K, $\log g = 4.5$, and 1.5 . Figure 3.17 shows a synthetic (unconvolved) comparison of the line depth (defined at the minimum of the line profile) of each line for the three values of $[M/H]$, and two values of T_{eff} and $\log g$. The dotted lines indicate the slope that

weak lines would have in this comparison. All three lines are on or near the linear part of the curve of growth. The smaller growth in line strength with metallicity for $T_{eff} = 4000$ K and $\log g = 1.5$ (open squares) is due to strong blending with CN lines, lines which appear to be on a different part of their curve of growth. Again, based upon the spectra fits, I estimate the uncertainty in $[M/H]$ is ± 0.2 dex (assuming $[M/H]$ follows $[Fe/H]$).

Once the $[M/H]$ value was determined for the star and once the relative line depths of the Ti I and Fe I lines was calculated approximately, the microturbulence value was adjusted until the line strengths of these two lines matched those in the observed spectrum. These lines were particularly sensitive to the choice of ξ , and thus I estimate the uncertainty in the derived value of ξ to be ± 0.2 km s⁻¹.

Since the $v \sin i$ and macroturbulence values are represented by a single convolved Gaussian, I can determine only the standard deviation of the final Gaussian: $\Upsilon = \sqrt{(v \sin i)^2 + \zeta^2}$. Since the equivalent widths of the lines are not affected by changes in these parameters, with experience, one can judge whether or not a change in Υ will improve the match between the spectra. Most of the $v \sin i$ and macroturbulence values listed in Table 1.3 are from the work of D. F. Gray. The profiles used here to transform the synthetic spectra for the effects of $v \sin i$ and macroturbulence are defined differently than those given in Gray (1992). For the dwarfs in this sample where $v \sin i$ and macroturbulence are comparable, the different treatments do not matter, as a later comparison of Tables 1.3 and 3.2 will show. Figure 18.9 of Gray (1992) shows that for bright giants and supergiants, mean values of the macroturbulence range from 5-10 km s⁻¹, and thus, since $v \sin i$ is typically

less than $1\text{-}2 \text{ km s}^{-1}$ for these stars, macroturbulence will be the dominant broadening mechanism. Gray (1992) uses a much more complicated formula for deriving his ζ_{RT} values [see his Eq. (18.9)]. His values are given as the most probable velocity, $\sqrt{2}$ larger than an rms velocity. For our calculations, we consider the macroturbulence as strictly isotropic and will quote the Gaussian dispersion.

3.4 Results and Discussion

As I alluded to earlier, because of the interdependence of the line profiles and line strengths on the stellar parameters, there is more than one approach which may be taken when calculating synthetic spectra. One may determine all parameters simultaneously (and recognize that the solution may not be unique), or one may choose to independently constrain one or more of the parameters and derive the remaining parameters. Examples would be to adopt an effective temperature derived from the infrared flux method and/or a surface gravity value from theoretical interior models. One would then be free, for example, to change the overall metallicity of the star and individual elemental abundances. To avoid any systematic errors present in the other research, I chose to derive *all* of the global parameters based on SSynth results alone and calculated a number of synthetic spectra for each star starting with the values given in Table 1.3. A line-blocking error of 0.1% was used in the stellar calculations.

As shown in Table 1.2, there is a large range of published values for $[\text{Fe}/\text{H}]$ for the dwarfs in this sample, and for T_{eff} , $\log g$, and $[\text{Fe}/\text{H}]$ for the evolved

stars. The uncertainty in ξ values for most of the stars is approximately 50%. The values of the global parameters will depend upon the initial solar model, the stellar model atmospheres, the completeness and accuracy of the equation of state calculations, the quality of the observed spectra, plus other factors. The comparison between the SSynth results and those of the compilation of Cayrel de Strobel et al. (1992), McWilliam (1990, hereafter McW90), and others given in Table 1.3 is discussed below.

After following each step listed in Sec. 3.2.4, I found that in some cases the observed spectrum needed to be multiplied by an additional constant to match the synthetic pseudocontinuum points at 864.75 and 867.23 nm. This is because the rectification was made using the entire 14 nm where the overall line strengths and thus the means of the spectra can be disparate because of unadjusted solar gf values. In addition, there was an excess of flux at the blue edge of each observed spectrum for the dwarfs, especially for 61 Cygni A. I empirically determined the wavelength at which the excess flux seemed to disappear, fit a linear function between the blue edge and this wavelength, and ratioed the region of excess flux with the fitting function. This procedure is not ideal, does not address the reason for the excess flux (unknown at this time), and may lead to asymmetric profiles for the Ca II wings and erroneous abundances for the Si I line in the region. These possible shortcomings will be diminished or will become insignificant once the full 14 nm region is explored. Once the pseudocontinuum match was made at the two wavelengths, I made a visual line-by-line comparison and then computed a new spectrum with individual or multiple parameter changes and repeated the process.

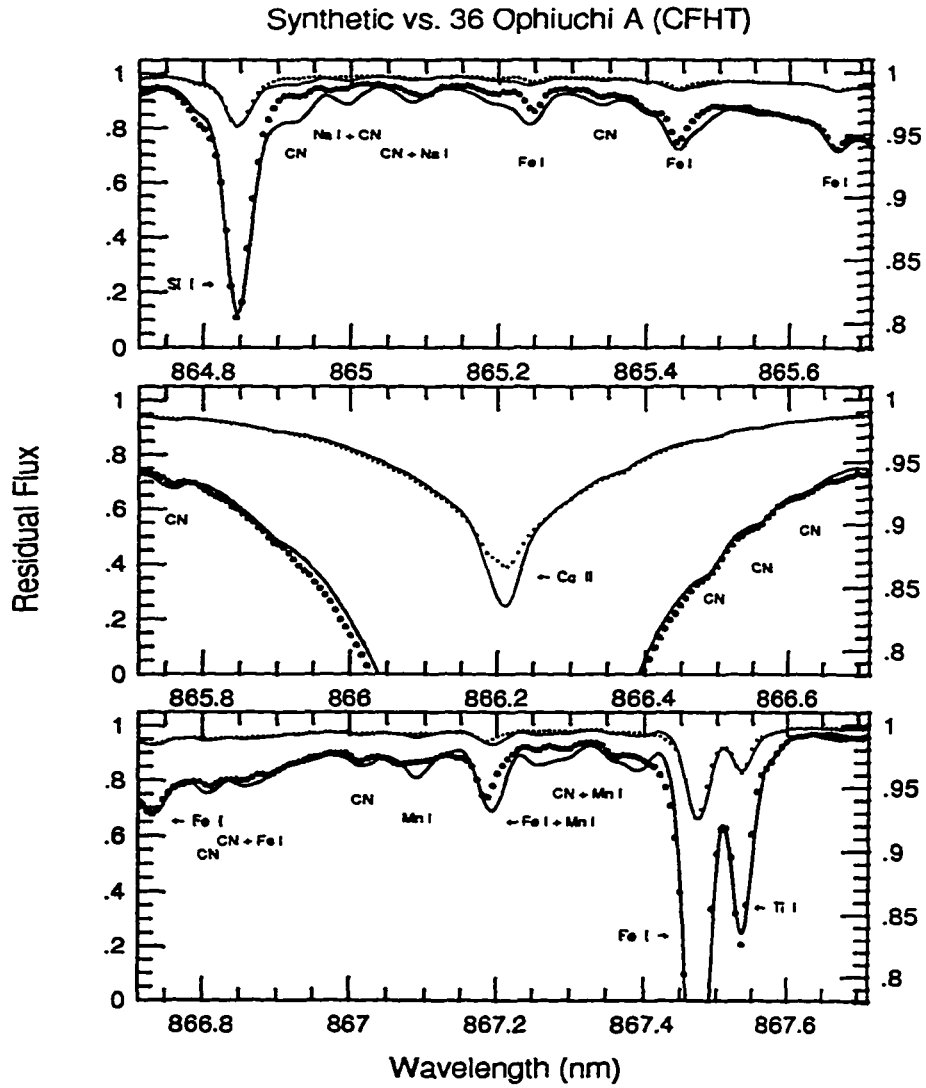


Figure 3.18: The calculated synthetic spectrum (solid line) vs. the observed stellar spectrum for 36 Ophiuchi A. The synthetic spectrum was calculated using $T_{eff} = 5125$ K, $\log g = 4.67$, $[M/H] = -0.25$, and $\xi = 1.4$ km s⁻¹. $\Upsilon = 2.34$ km s⁻¹ (see Table 3.2). No abundance anomalies were assumed.

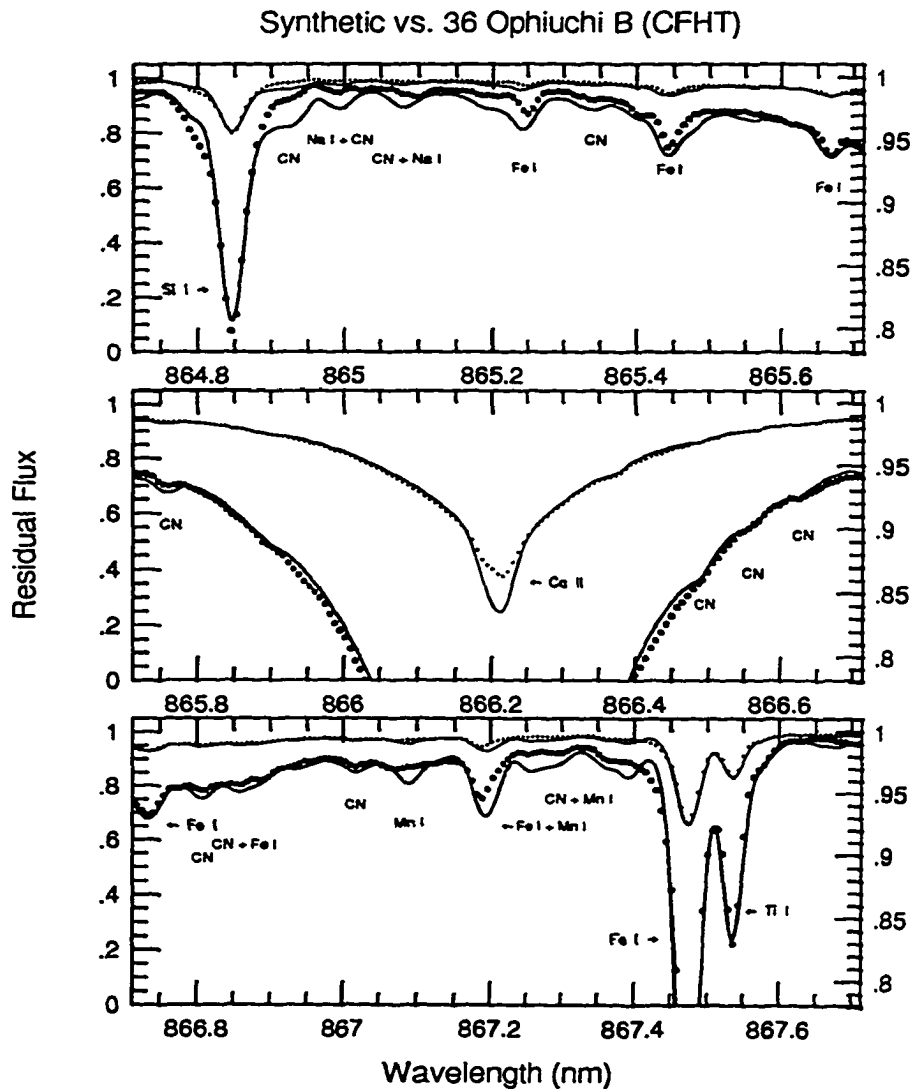


Figure 3.19: The calculated synthetic spectrum (solid line) vs. the observed stellar spectrum for 36 Ophiuchi B. The synthetic spectrum was calculated using $T_{eff} = 5125$ K, $\log g = 4.67$, $[M/H] = -0.25$, and $\xi = 1.4$ km s⁻¹. $\Upsilon = 2.06$ km s⁻¹ (see Table 3.2). No abundance anomalies were assumed.

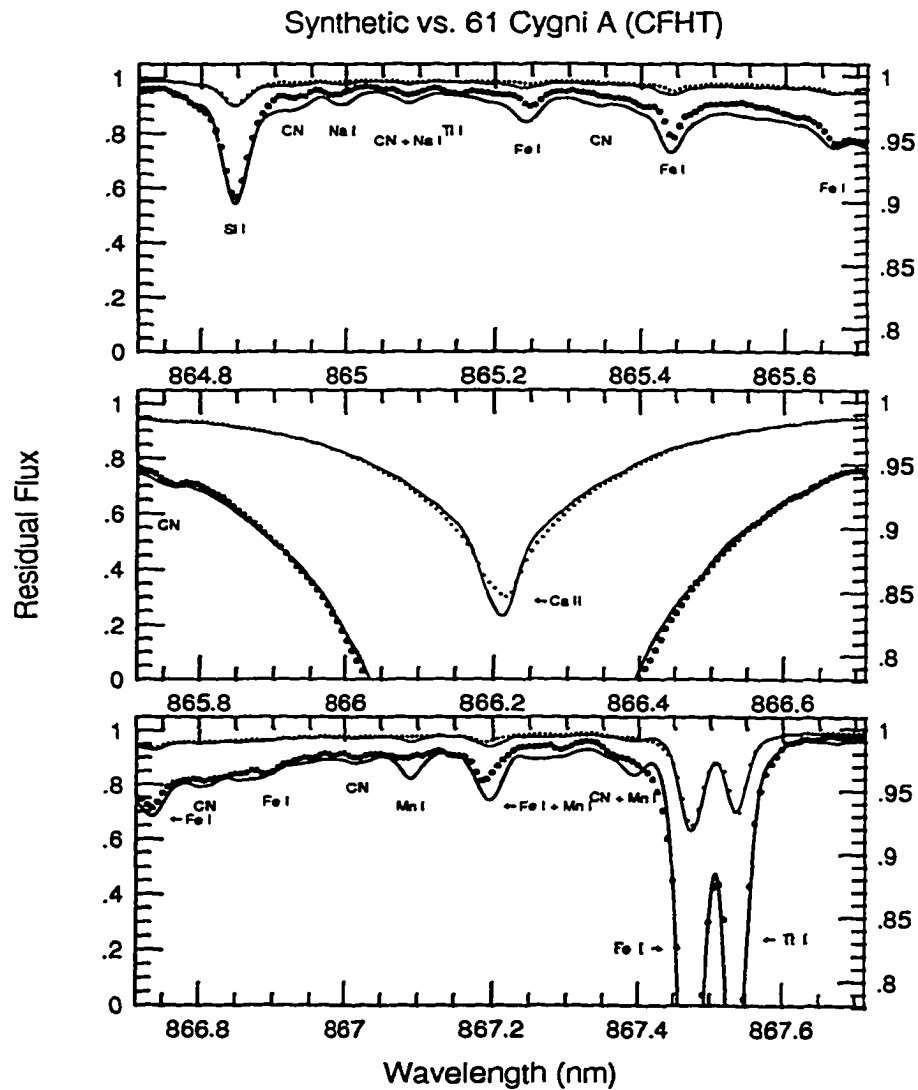


Figure 3.20: The calculated synthetic spectrum (solid line) vs. the observed stellar spectrum for 61 Cygni A. The synthetic spectrum was calculated using $T_{eff} = 4545$ K, $\log g = 4.55$, $[M/H] = -0.40$, and $\xi = 1.5$ km s $^{-1}$. $\Upsilon = 1.8$ km s $^{-1}$ (see Table 3.2). No abundance anomalies were assumed.

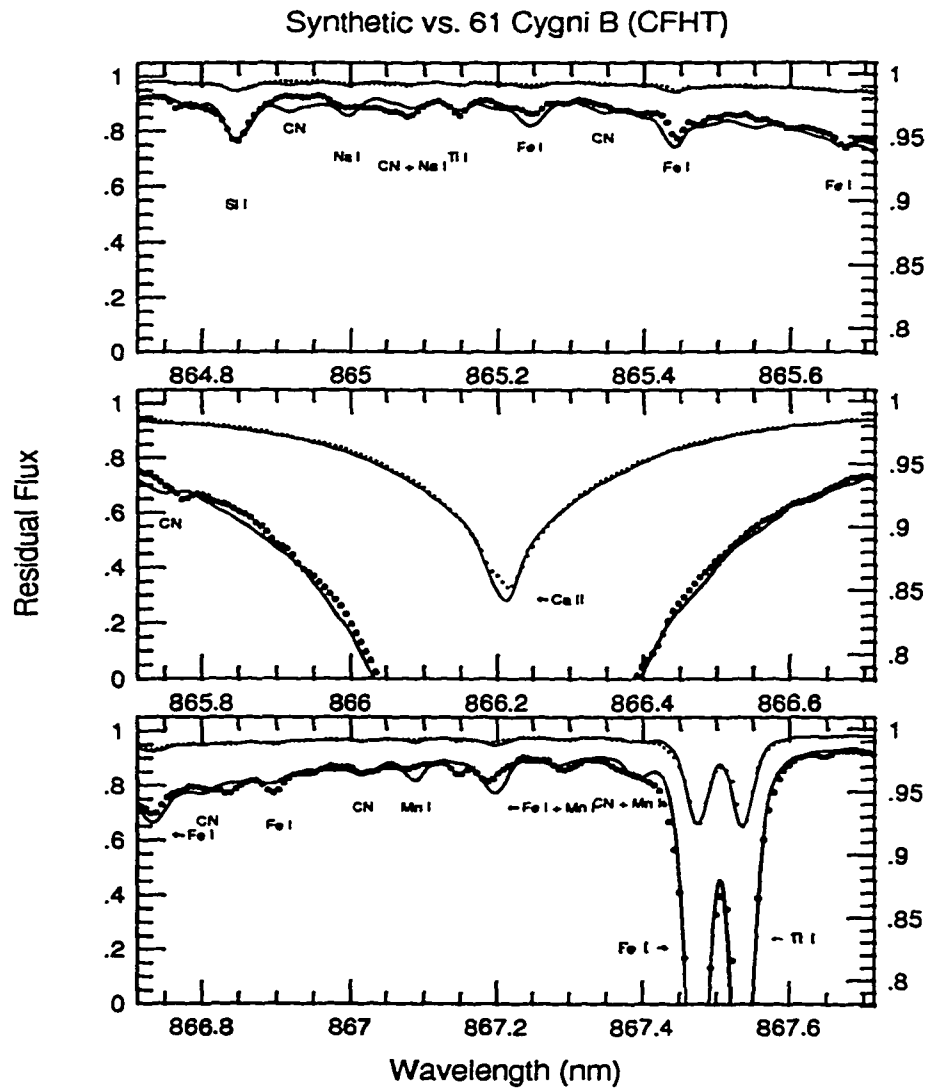


Figure 3.21: The calculated synthetic spectrum (solid line) vs. the observed stellar spectrum for 61 Cygni B. The synthetic spectrum was calculated using $T_{eff} = 4150$ K, $\log g = 4.55$, $[M/H] = -0.40$, and $\xi = 0.7$ km s $^{-1}$. $\Upsilon = 0.1$ km s $^{-1}$ (see Table 3.2). No abundance anomalies were assumed.

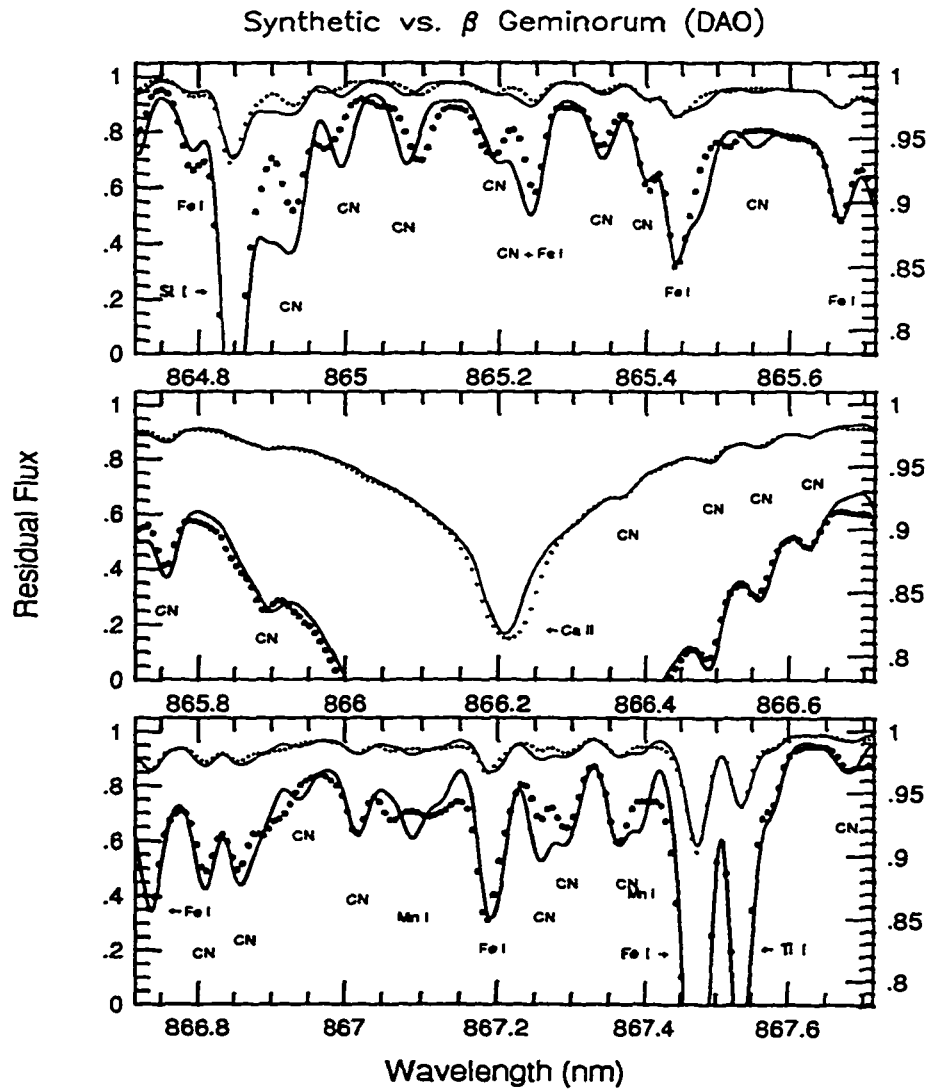


Figure 3.22: The calculated synthetic spectrum (solid line) vs. the observed stellar spectrum for β Geminorum. The synthetic spectrum was calculated using $T_{\text{eff}} = 4850$ K, $\log g = 2.5$, $[M/H] = 0.0$, and $\xi = 1.5$ km s $^{-1}$. $\Upsilon = 1.8$ km s $^{-1}$ (see Table 3.2). No abundance anomalies were assumed.

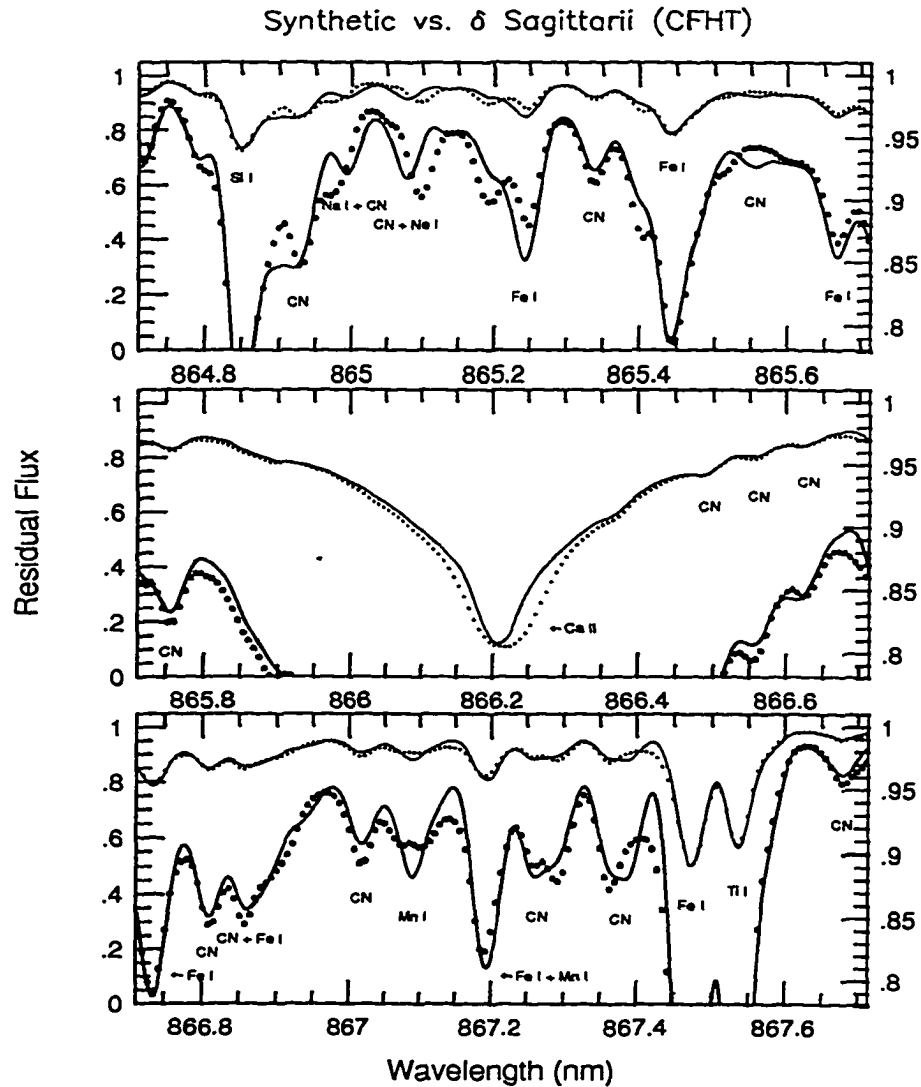


Figure 3.23: The calculated synthetic spectrum (solid line) vs. the observed stellar spectrum for δ Sagittarii. The synthetic spectrum was calculated using $T_{eff} = 4350$ K, $\log g = 1.3$, $[M/H] = -0.15$, and $\xi = 1.7$ km s⁻¹. $\Upsilon = 3.2$ km s⁻¹ (see Table 3.2). Abundance changes: $[C/Fe] = -0.15$, $[Si/Fe] = -0.15$, $^{12}C/^{13}C = 9$.

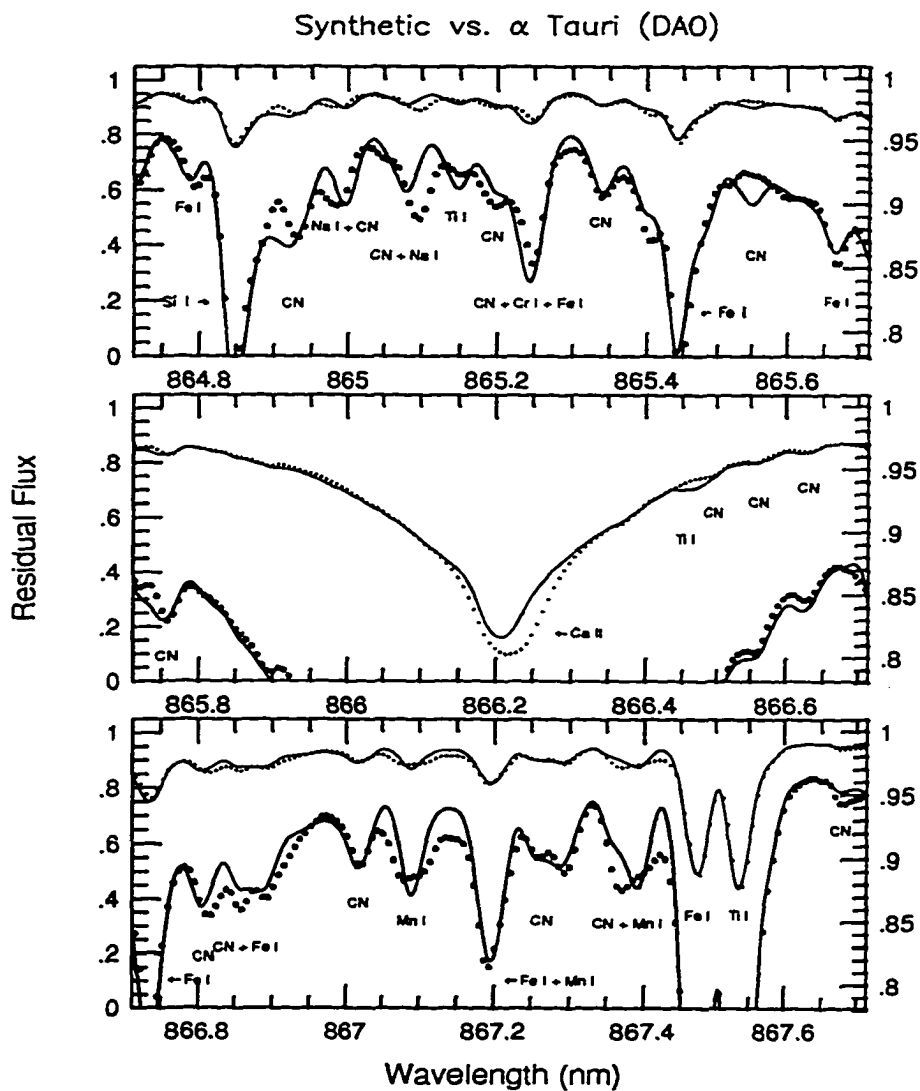


Figure 3.24: The calculated synthetic spectrum (solid line) vs. the observed stellar spectrum for α Tauri. The synthetic spectrum was calculated using $T_{eff} = 3850$ K, $\log g = 0.9$, $[M/H] = -0.15$, and $\xi = 2.0$ km s⁻¹. $\Upsilon = 2.12$ km s⁻¹ (see Table 3.2). Abundance changes: $[Ca/Fe] = +0.2$, $[Si/Fe] = +0.7$, $^{12}C/^{13}C = 25$.

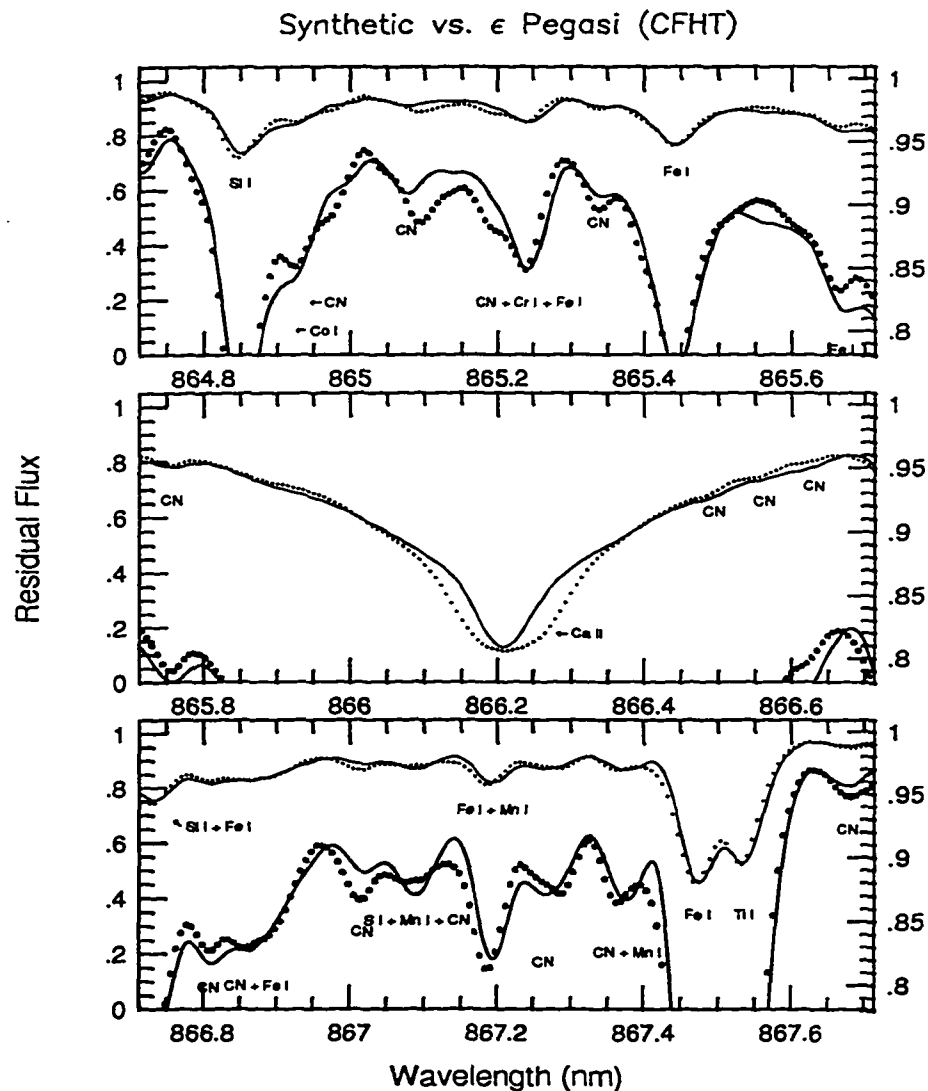


Figure 3.25: The calculated synthetic spectrum (solid line) vs. the observed stellar spectrum for ϵ Pegasi. The synthetic spectrum was calculated using $T_{eff} = 4350$ K, $\log g = 0.85$, $[M/H] = -0.20$, and $\xi = 3.0$ km s $^{-1}$. $\Upsilon = 5.66$ km s $^{-1}$ (see Table 3.2). Abundance changes: $[Ca/Fe] = +0.2$, $[Si/Fe] = -0.1$, $[C/Fe] = -0.2$, $^{12}C/^{13}C = 5$.

Figures 3.18 through 3.25 show the results of the “chi-by-eye” iteration. The iterations were generally stopped when an overall match of better than $\sim 1\%$ was achieved. As mentioned earlier, in theory one should be able to use the particular sensitivity of each line or sets of lines to derive the corresponding parameter. In practice, each line or sets of lines has a dependence on other global parameters making manual adjustment of the parameters complicated and somewhat intractable. This procedure will become even more onerous when the full 14 nm is analyzed. I discuss the need for a least-squares fitting program for this process in Chapter 4.

In spite of the shortcomings of the visual fitting process, the overall agreement with each spectrum is encouraging, as Figs. 3.18 through 3.25 show. The parameters from the fits are summarized in Table 3.2; the direct comparison between published and derived atmospheric parameters are summarized in Tables 3.3 and 3.4. One should continue to keep in mind that, at most, three lines were used to determine each parameter. Following is a brief discussion of the results for each star: from the dwarfs to the supergiant, and from hotter to cooler stars in each luminosity class.

3.4.1 The K Dwarfs

36 Ophiuchi AB: The stars in this binary system are nearly identical twins. The same SSynth calculation was used for both stars, with the small differences in the $v \sin i$ values noted in Table 1.3 considered in the Υ value. The difference in the core of the 866.2 nm line is explained by 36 Oph A’s more chromospherically active status. The derived global parameters are: $T_{eff} = 5125$ K, $\log g = 4.67$, $[M/H] = -0.25$, $\xi = 1.4$ km s $^{-1}$ (see Table 3.2).

Table 3.2: Derived global parameters for the stellar sample

Name	T_{eff} (K)	$\log g$ (cgs units)	[M/H]	ξ (km s ⁻¹)	Υ † (km s ⁻¹)	[A/Fe]
DWARFS						
36 Oph B	5125	4.67	-0.25	1.4	2.06	1
36 Oph A	5125	4.67	-0.25	1.4	2.34	1
61 Cyg A	4545	4.55	-0.40	1.5	1.80	1
61 Cyg B	4150	4.55	-0.40	0.7	0.10	1
GIANTS						
β Gem	4850	2.50	0.0	1.5	1.80	1
δ Sgr	4350	1.30	-0.15	1.7	3.20	2
α Tau	3850	0.90	-0.15	2.0	2.12	3
SUPERGIANT						
ϵ Peg	4350	0.85	-0.2	3.0	5.66	4

$$\dagger \Upsilon^2 = (v \sin i)^2 + \zeta^2$$

¹ No abundance anomalies used, $^{12}\text{C}/^{13}\text{C} = 90$

² [Si/Fe] = -0.15, [C/Fe] = -0.15, $^{12}\text{C}/^{13}\text{C} = 9$

³ [Ca/Fe] = +0.2, [Si/Fe] = +0.7, $^{12}\text{C}/^{13}\text{C} = 25$

⁴ [Ca/Fe] = +0.2, [Si/Fe] = -0.1, [C/Fe] = -0.2, $^{12}\text{C}/^{13}\text{C} = 5$

Note: No quantitative measure was made of the uncertainties. Based upon the flexibility in each parameter giving similar “best” fits to a single spectrum, I estimate uncertainties of ± 50 K in T_{eff} (assuming [Ti/Fe] = 0); ± 0.05 dex in $\log g$ for the dwarfs, ± 0.2 dex in $\log g$ for the giants (assuming a given [Ca/Fe], see text); ± 0.2 in [M/H]; ± 0.2 km s⁻¹ in ξ ; and ± 1 km s⁻¹ in Υ .

Table 3.3: Published vs. derived effective temperature and surface gravity values

Name	$T_{eff\dagger}$ (K)	T_{eff*} (K)	ΔT_{eff} (K)
36 Oph B	5100	5125	+25
36 Oph A	5125	5125	0
61 Cyg A	4543	4545	+2
61 Cyg B	4332	4150	-182
β Gem	4850	4850	0
δ Sgr	4180	4350	+170
α Tau	3910	3850	-60
ϵ Peg	4350	4350	0
	$\log g\dagger$ (cm s ⁻²)	$\log g^*$ (cm s ⁻²)	$\Delta \log g$ (cm s ⁻²)
36 Oph B	4.60	4.67	+0.07
36 Oph A	4.60	4.67	+0.07
61 Cyg A	4.50	4.55	+0.05
61 Cyg B	4.60	4.55	-0.05
β Gem	2.96	2.50	-0.46
δ Sgr	2.23	1.30	-0.93
α Tau	1.59	0.90	-0.69
ϵ Peg	1.00	0.85	-0.15

† Published values from Table 1.3

* Values derived from this work; see Table 3.2 for estimates of the uncertainties.

Table 3.4: Published vs. derived metallicity and microturbulence values

Name	[Fe/H] ‡	[M/H]*	Δ [Fe/H]
36 Oph B	-0.16	-0.25	-0.09
36 Oph A	-0.15	-0.25	-0.10
61 Cyg A	-0.05	-0.40	-0.35
61 Cyg B	-0.19	-0.40	-0.21
β Gem	-0.12	0.0	+0.12
δ Sgr	-0.01	-0.15	-0.14
α Tau	-0.11	-0.15	-0.04
ϵ Peg	-0.07	-0.20	-0.13
	ξ ‡ (km s ⁻¹)	ξ^* (km s ⁻¹)	$\Delta\xi$ (km s ⁻¹)
36 Oph B	1.0	1.4	+0.4
36 Oph A	1.0	1.4	+0.4
61 Cyg A	1.0	1.5	+0.5
61 Cyg B	1.0	0.7	-0.3
β Gem	1.9	1.5	-0.4
δ Sgr	2.7	1.7	-1.0
α Tau	2.1	2.0	-0.1
ϵ Peg	2.5	3.0	+0.5

‡ Published values from Table 1.3

* Values derived from this work.

Note: [M/H] assumed \equiv [Fe/H].

I used the $v \sin i$ and macroturbulence values given in Table 1.3 for each star. Within the estimated errors for T_{eff} (± 50 K), $[M/H]$ (± 0.2 dex), and $\log g$ (± 0.05 dex) the derived global parameters agree with the published values (see Tables 3.3 and 3.4).

It is interesting to compare these observational results with the theoretical models. The Bright Star Catalog (Hoffleit and Warren, 1991) lists the visual magnitudes as 5.07 and 5.11 for A and B respectively. The parallax (van Altena et al., 1991) is 0.1874 ± 0.0093 . Assuming a bolometric correction of -0.27 , [interpolated from the grids given in Vandenberg (1985)], the range of bolometric magnitudes, within the 99% confidence interval for the parallax, is $5.87 \leq M_{bol} \leq 6.43$ for A, and $5.91 \leq M_{bol} \leq 6.47$ for B. Figure 3.26a shows that the effective temperature and bolometric magnitude of these two stars places them on an evolutionary track for a star with $0.7 \leq M/M_{\odot} \leq 0.8$. The $\log g$ values derived from SSynth calculations are consistent with these evolutionary tracks.

61 Cygni AB: As shown in Table 3.2, the global stellar parameters for the “best fit” SSynth calculations for 61 Cygni are $T_{eff} = 4545$ K, $\log g = 4.55$, $[M/H] = -0.4$, and $\xi = 1.5$ km s $^{-1}$ for A; and $T_{eff} = 4150$ K, $\log g = 4.55$, $[M/H] = -0.4$, and $\xi = 0.7$ km s $^{-1}$ for B. The $v \sin i$ and macroturbulence parameter, Υ , is 1.8 km s $^{-1}$ for A, and 0.1 km s $^{-1}$ for B. For 61 Cyg B, Υ is much smaller than 1.6 km s $^{-1}$ calculated from the $v \sin i$ and macroturbulence values given in Table 1.3. The effective temperatures derived for these two stars indicate that component A is approximately 400 K hotter than B. Even with a line-blocking error of 0.1% ($\sim 92\%$ of the lines eliminated), the

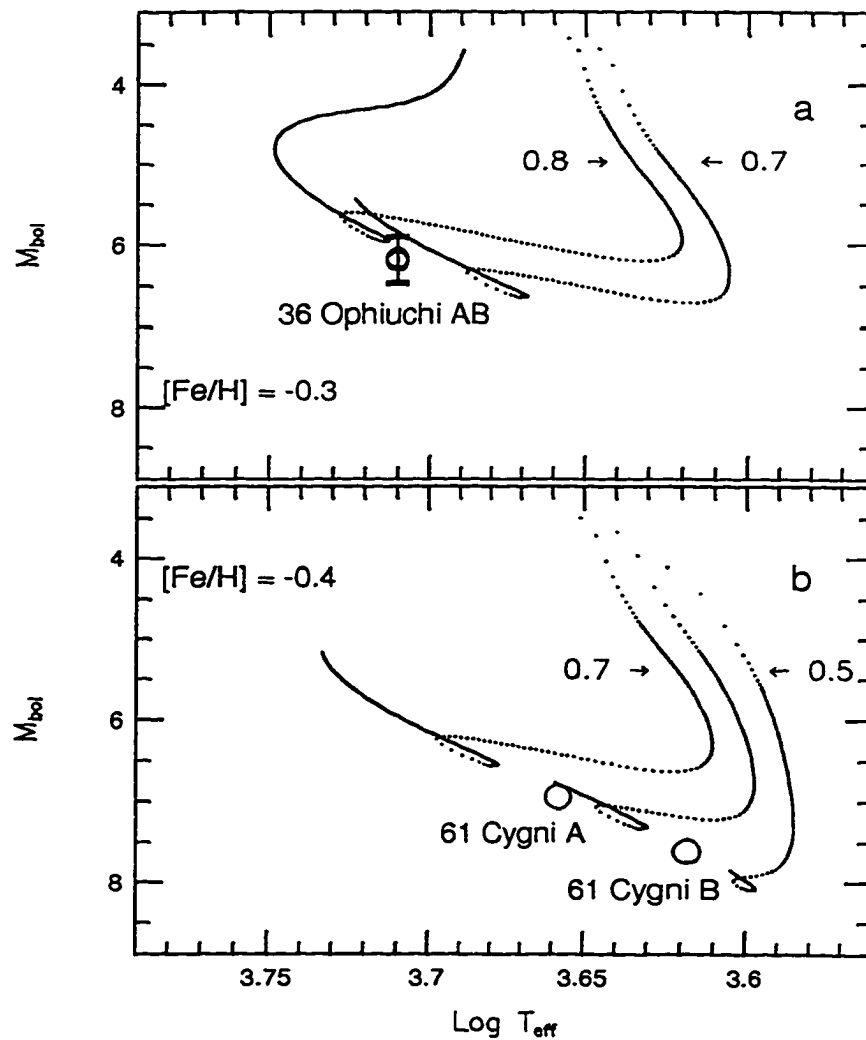


Figure 3.26: a: VandenBerg evolutionary tracks for $[\text{Fe}/\text{H}] = -0.3$, $M/M_{\odot} = 0.7$ and 0.8 . The error bars represent the 99% confidence interval based on the parallax for these stars (van Altena et al., 1991). b: VandenBerg evolutionary tracks for $[\text{Fe}/\text{H}] = -0.4$, $M/M_{\odot} = 0.5$, 0.6 , and 0.7 . The uncertainties in the bolometric magnitudes, based upon the measured parallax, are contained within the point sizes.

pseudocontinuum of the synthetic spectrum of 61 Cyg B, shown in Fig. 3.21, is inundated with hundreds of TiO lines, approximately 200 per nm.

Fig. 3.26b compares these two stars with the Vandenberg evolutionary tracks for $[\text{Fe}/\text{H}] = -0.4$, $\mathcal{M}/\mathcal{M}_\odot = 0.5, 0.6, \text{ and } 0.7$. The Bright Star Catalog (Hoffleit and Warren, 1991) lists the visual magnitudes as 5.21 and 6.03 for A and B respectively. The parallax (van Altena et al., 1991) is accurately known: 0.2870 ± 0.0009 . The bolometric corrections of -0.56 and -0.71 for A and B respectively are from Vandenberg and Bell (1985), with the bolometric correction for 61 Cyg B extrapolated from relations given in Table 1 of Vandenberg and Bell. Given the small uncertainty in the parallax value, the 99% confidence interval is within the point size shown in Fig. 3.26b. Figure 3.26b shows that the effective temperatures derived here and the bolometric magnitudes of these two stars place 61 Cyg A on an evolutionary track for a star with $0.6 \leq \mathcal{M}/\mathcal{M}_\odot \leq 0.7$ and 61 Cyg B on an evolutionary track for a star with $0.5 \leq \mathcal{M}/\mathcal{M}_\odot \leq 0.6$. The values of $\log g$ at the zero-age-main-sequence (ZAMS) are 4.48, 4.38, and 4.30 for $\mathcal{M}/\mathcal{M}_\odot = 0.5, 0.6, \text{ and } 0.7$ respectively. The maximum $\log g$ values beyond the ZAMS are 4.84, 4.74, and 4.70, respectively. The $\log g$ values derived using SSynth are consistent within these ranges.

The ZAMS establishes $\Delta M_{\text{bol}}/\Delta \log T_{\text{eff}}$. A previously published value of $\Delta T_{\text{eff}} \approx 200$ K, derived from the infrared flux method (see Table 1.3), cannot be correct. A difference of 200 K between these two stars would have a sizeable ΔM_{bol} discrepancy independent of the parallax. Our derived effective temperatures of 4545 and 4150 K are in excellent agreement with the values of 4501 and 4143 K derived by Gray and Johanson (1991), who

used the line-depth ratio of V I at 625.183 nm and Fe I at 625.257 nm.

3.4.2 The K Giants

The giant stars in the sample will be discussed with a slightly different approach. Whereas the masses of K dwarfs can be determined to within a few hundreds of a solar mass, the uncertainty in the masses of K giants can be as large as 2-3 solar masses. As Tsuji (1986) states, "Empirical determination of the surface gravity is most difficult in red giant stars." In addition, while there are a large number of studies of K giants which use equivalent width analysis and low-dispersion spectra, only a minority of K giants have more than one published high-dispersion analysis (Taylor, 1991). The surface gravities in Table 1.3, which were taken from McWilliam (1990, McW90), were derived from mass estimates made from evolutionary tracks and have quoted uncertainties of only 0.1 - 0.4 dex. Given the errors in bolometric magnitudes and underlying stellar interior models, I believe these uncertainties are understated. The metallicity and microturbulence values quoted by McW90 were derived simultaneously by demanding that the iron abundance derived from weak lines agrees with that derived from saturated lines; 20 Fe I lines were used. The estimated errors are 0.14 dex in $[\text{Fe}/\text{H}]$ (mean), and 0.1 km s^{-1} in ξ . For other studies, the range in values for $\log g$ is sometimes as high as 1.0 dex; that of $[\text{Fe}/\text{H}]$, 0.5 dex; that of ξ , 0.5 km s^{-1} . Fortunately, the infrared-flux method has reduced the uncertainty in effective temperatures, often to below 25 K.

The values of Υ given in Table 3.2 are consistently about one-half of that implied by the $v \sin i$ and macroturbulence values given in Table 1.3. This

is due to the different definitions, and probably normalization, used for the macroturbulence, the dominant broadening mechanism in evolved stars.

β Geminorum: Figure 3.22 shows the comparison between the synthetic spectrum and the β Gem spectrum obtained at the DAO. The derived global parameters are $T_{eff} = 4850$ K, $\log g = 2.5$, $[M/H] = 0.0$, $\xi = 1.5$ km s⁻¹ (see Table 3.2). Table 3.3 shows the values for the effective temperature and metallicity are consistent with those given by McW90. The derived value of ξ is smaller by 0.4 km s⁻¹; the value given in McW90, $\xi = 1.9$ km s⁻¹, may be more correct since many more lines were used in its determination. The $\log g$ value derived here is 0.46 dex smaller than that given in McW90; however, it agrees with the mean value of $\log g = 2.53$ given in the compilation of Cayrel de Strobel et al. (1992). McW90 derived $[Si/Fe] = +0.18$, $[Ca/Fe] = +0.01$, $[Ti/Fe] = -0.04$ (assuming photospheric abundances instead of meteoritic); no similar element enhancements were needed here. β Gem has an estimated ¹²C/¹³C ratio of 25 (Cottrell and Sneden, 1986), a ratio of 90 was used in the SSynth calculations.

δ Sagittarii: Figure 3.23 shows the comparison between the synthetic spectrum and the δ Sgr spectrum obtained at the CFHT. The derived global parameters are $T_{eff} = 4350$ K, $\log g = 1.3$, $[M/H] = -0.15$, $\xi = 1.7$ km s⁻¹ (see Table 3.2). Table 3.3 shows that the effective temperature derived for δ Sgr is 170 K hotter than that given by McW90; the $\log g$ value is ~ 0.9 dex smaller. Although the uncertainty is large, the $\log g = 1.7$ value implied by the mass and radius given in Table 2.8 is intermediate between the spectro-

scopic value derived here and that given by McW90. Table 3.4 shows that the $[M/H]$ values differ by -0.14 dex; the ξ values, by -1.0 km s $^{-1}$. Overall, the SSynth calculations using the McW90 global parameter values were a very poor match to the CFHT spectrum.

δ Sgr has been noted as being a very strong lined star, a characteristic not noted in the wavelength region examined here. As Table 3.2 shows, the calculations included an underabundance of carbon, $[C/Fe] = -0.15$, and silicon, $[Si/Fe] = -0.15$, and the isotopic ratio $^{12}C/^{13}C = 9$. Rather than choose a carbon underabundance, I could have chosen an oxygen overabundance to reduce the strength of the CN lines as the formation of CO controls the availability of carbon in stars with effective temperatures similar to that of δ Sgr. For this star, McW90 finds $[Si/Fe] = +0.47$, $[Ca/Fe] = -0.29$, $[Ti/Fe] = -0.57$ (assuming photospheric abundances instead of meteoritic), results which are inconsistent with our analysis. Note, however, that we assumed $[Ti/Fe] = 0$. Calculations which included an underabundance of titanium would need a corresponding decrease in the effective temperature to maintain the same Ti I line depth in the CFHT δ Sgr spectrum. To compensate for an underabundance of calcium, the SSynth calculations would have to use a smaller $\log g$ value, making the discrepancy between the derived $\log g$ values even worse.

The analysis of the full 14 nm of the CFHT spectrum should give more definitive abundance ratios for this star. One expects non-LTE effects to become more obvious in higher luminosity stars; the core of the Ca II line definitely shows substantial additional broadening.

α Tauri: Figure 3.24 shows the comparison between the synthetic spectrum and the α Tau spectrum obtained at the DAO. The derived global parameters are $T_{eff} = 3850$ K, $\log g = 0.9$, $[M/H] = -0.15$, $\xi = 2.0$ km s⁻¹ (see Table 3.2). As Figs. 3.12 and 3.13 show, at temperatures below about 4200 K, the Fe I and Ti I lines used as temperature indicators here lose their sensitivity; thus the derived effective temperature for α Tau is uncertain to within ± 100 K. Tables 3.3 and 3.4 show fair agreement with the McW90 values, except for the $\log g$ value. The compilation by Cayrel de Strobel et al. (1992) gives $\log g = 1.22$ for α Tau, in better agreement with the value derived here. All of the global parameters derived here are in good agreement with those derived spectroscopically by Luck and Challener (1995): $T_{eff} = 3875$ K, $\log g = 0.55$, $[Fe/H] = -0.16$, and $\xi = 2.2$ km s⁻¹.

One should keep in mind that the pseudocontinuum of the α Tau spectrum is dominated by TiO lines: over 3600 lines per nm even with a line-blocking error of 0.1%. If the overall strength of these TiO lines is in error, the strength of the Ca II line will be either under- or over-estimated and the derived $\log g$ value will also be in error. Calibrating the accuracy of the TiO line list is difficult as the TiO lines are not visible in the solar spectrum. Future work may include calculating the spectrum for α Bootis and comparing the SSynth results with the Griffin Arcturus Atlas (Griffin, 1968)

Table 3.2 lists $[Ca/Fe] = +0.2$, $[Si/Fe] = +0.7$, and $^{12}C/^{13}C = 25$. In this case, I allowed a calcium overabundance for this star based on the fact that a substantial silicon overabundance was required. McW90 derived $[Si/Fe] = +0.73$, $[Ca/Fe] = +0.2$, and $[Ti/Fe] = -0.22$. As was the case with δ Sgr, substantial extra broadening is apparent in the core of the Ca II line.

For the giants, Table 3.3 shows that the derived $\log g$ values are all lower than the published values of McW90. As mentioned, McW90 determined the stellar masses from evolutionary tracks and then derived the $\log g$ values from estimates of the stellar radii. We do the opposite by deriving the stellar masses from the $\log g$ values and radii:

$$\mathcal{M}_* = \frac{R_*^2 g_*}{R_\odot^2 g_\odot} \mathcal{M}_\odot . \quad (3.23)$$

From the spectroscopic surface gravities derived here and the radii listed in Tables 2.5, 2.8, and 2.10, and the corresponding uncertainties, I calculated a mass range of $0.5 \leq \mathcal{M}_*/\mathcal{M}_\odot \leq 1.6$ for β Gem, $0.2 \leq \mathcal{M}_*/\mathcal{M}_\odot \leq 2.8$ for δ Sgr, and $0.3 \leq \mathcal{M}_*/\mathcal{M}_\odot \leq 1.1$ for α Tau. Since the progenitors of these K giants are most likely A-G dwarfs, the lower masses stated here imply significant, and probably unphysical, mass loss. Stellar evolution theory favors the more massive end of the uncertainties.

Under any spectrum synthesis analysis, the spectroscopic surface gravities derived for the giants depend explicitly on the gf value adopted for, in this case, the Ca II line. Recall, one only knows $gf\gamma_H/N_H$ for the Sun, and thus increasing the gf value would mean decreasing γ_H and vice versa. Figure 3.14 shows that radiative broadening dominates at small surface gravities. Where radiative broadening dominates, then, a larger gf value would make the calculated 866.214 nm line stronger, allowing for an increase in the surface gravity (to weaken the Ca II wings) and therefore the mass derived for each star. For stars with a surface gravity ≤ 2.0 , an approximate 0.1 dex increase in the $\log gf$ value would result in an approximate 0.2 dex increase in the surface gravity value. Based upon the research for measuring the life-

time of the $4p$ levels and the branching ratios of the Ca II infrared triplet lines summarized in Smith and Drake (1988), I see no justification at this time for increasing the $\log gf$ value used here. However, there is additional observational evidence (Rutledge et al., 1996), based upon globular cluster work where the masses of the stars are more easily determined, that the gf values for the Ca II lines are larger (e.g., those given in Column 5 of Table 1 of SD88) than those adopted for this study. Since the gf values are intimately related to the measured lifetime through the Einstein A coefficient, the observations suggest that the lifetime of the $4p$ levels and/or the branching ratios need to be remeasured. Note that the change in gf and γ_H will cancel for the dwarfs, and will not affect the results discussed above for the K dwarfs.

3.4.3 The K Supergiant

ϵ Pegasi: Considering the fact that we are using a plane-parallel, homogeneous atmosphere under LTE considerations to describe a supergiant, the agreement between the synthetic and observed spectra for ϵ Peg shown in Fig. 3.25 is remarkable, especially for the far wings of the Ca II line. ϵ Peg is the only star in this sample where interstellar reddening becomes significant. This reddening will lead to an understatement of the effective temperature if derived from the colors of this star, but should have no effect on the methods used here.

Table 3.2 lists the derived global parameters for this star of $T_{eff} = 4350$ K, $\log g = 0.85$, $[M/H] = -0.2$, and $\xi = 3.0$ km s $^{-1}$. Table 3.2 also lists an underabundance of carbon and silicon, $[C/Fe] = -0.2$ and $[Si/Fe] = -0.1$;

an overabundance of calcium, $[\text{Ca}/\text{Fe}] = +0.2$; and a low isotopic ratio for carbon, $^{12}\text{C}/^{13}\text{C} = 5$. The derived temperature agrees with that given by Smith and Lambert (1987). Smith and Lambert (1987) derived $[\text{Si}/\text{Fe}] = +0.08$, $[\text{Ca}/\text{Fe}] = +0.25$, $[\text{Ti}/\text{Fe}] = -0.01$, for $[\text{Fe}/\text{H}] = -0.03$. The low $^{12}\text{C}/^{13}\text{C} = 5$ isotopic ratio used here was based on figures given in Dearborn, Eggleton, and Schramm (1976).

Chapter 4

Summary and Future Directions

4.1 The K Dwarfs

We have confirmed that the core of the 866.2 nm Ca II infrared triplet line can be used to measure changes in the chromospheric activity of a star. The $\Delta EW_{866.2}$ index, determined as an additional step in our reduction of the stellar precise radial velocities, effectively defines the differential changes taking place in the central 0.135 nm core relative to a 0.227 nm sideband. This index is qualitatively related to the variations in the Ca II H and K flux as measured by the S index. Our analysis of the long-term solar-type cycle and rotation period in 61 Cygni A strengthens period results obtained from the S index alone. In particular, the stability of the ~ 36 -dy rotation period over the 12 years of our observations suggests that the regions of chromospheric activity are long-lived or grow and decay within a limited longitudinal range. The detection of the rotation period in the RV data for this star implies that the active regions maintain some coherence in the

photosphere as well.

Since the radial velocity data have been previously discussed (Walker et al., 1995), I will mention some open questions concerning the chromospheric activity of these stars. For the 36 Ophiuchi system: Are we simply viewing these two stars at different stages in similar long-term activity cycles? Is there a fundamental difference in their magnetic structure? For 36 Oph B, will we detect the rotation period in the $\Delta EW_{866.2}$ index once the parent function is perfected, such as is seen in the $\Delta EW_{866.2}$ index for 61 Cygni A, which has a similar long-term cyclic behavior? Our observations of the activity of 61 Cyg A quantified the viability of our $\Delta EW_{866.2}$ index to monitor changes in chromospheric activity. Once the programs are in place to model sawtooth-like cycles, the search for rotation periods in the $\Delta EW_{866.2}$ indices, and corresponding periods in the radial velocity data, should continue for all of the dwarfs.

The excellent agreement between the synthetic and observed spectra for the dwarfs provides a solid foundation for future work. The agreement between the parameters derived from the observed spectra and those predicted by stellar interior models is especially interesting. The bolometric magnitudes and derived effective temperatures for both sets of binary stars places them on evolutionary tracks for stars with $[\text{Fe}/\text{H}]$ similar to that prescribed by the observations. The $\log g$ values derived spectroscopically are also consistent with the interior models.

4.2 The K Giants and Supergiant

With our present data, the rotation versus revolution question cannot be resolved for β Gem. There are at least two possible interpretations of the periods discussed above. 1) If the observed $v \sin i$ value can be revised from 2.5 km s^{-1} (Gray, 1982) to less than 0.76 km s^{-1} , then the RV and $\Delta EW_{866.2}$ periods we find are probably best interpreted as rotation modulation of (possibly independent) photospheric and chromospheric phenomena. 2) Alternatively, if the currently observed $v \sin i$ is reliable, we could explain the RV period and amplitude as evidence that a low-mass companion ($M_2 \sin i = 2.5$ Jupiter masses, if we assume a circular orbit) is revolving around the β Gem primary (with an assumed mass of $1.6 M_\odot$) at a distance of 1.6 AU. However, in this case of a reliable $v \sin i$, we must find some non-rotation mechanism to explain the $\Delta EW_{866.2}$ period. There are two initial observations that will help distinguish whether the radial velocity period of β Gem is due to rotation or revolution. It is important to redetermine the $v \sin i$ value of β Gem using the highest possible accuracy. Additional measures of chromospheric emission are needed to confirm the 588-dy $\Delta EW_{866.2}$ period (see discussion below).

δ Sagittarii is an interesting example of a giant having intriguing long-term, linear trends in the differential radial velocities, chromospheric emission, and $(R - I)$ color. These long-term trends may indicate an increasing number in the sizes and/or numbers of spots with a small faculae/spot ratio, or they may each have a different physical cause.

The changes in the relative radial velocities of δ Sgr show significant

periodicities at 1.98 and 293 days, periods which are aliases of each other. Because of our limited number of observations of this star and the uncertainties in its basic stellar data, we cannot determine which of the 1.98- or 293-dy radial velocity periods is the likely true period. This dichotomy may be resolved in the near future. We recently received data from Bill Cochran and Artie Hatzes for δ Sgr. These data, as yet unanalyzed, more than double the number of observations we have for this star (which may preclude the use of the correlated periodogram) and include a large number of observations over a four-day time period.

Our analysis of the enigmatic star α Tauri exemplifies the complexity not only of the variability in these stars but also in interpreting this variability. The long-term period represents one of the most significant found in any of the giants; yet, unlike γ Cephei and, to a lesser extent, β Gem, we detect no corresponding period in the $\Delta EW_{868.2}$ index. Unlike δ Sgr, α Tau was observed extensively. The discovery of the short-term, 1.84-dy period should spark additional observations by other radial velocity groups. Does α Tau show mode switching similar to that observed for α Boo? What additional observations will be needed to confirm granulation-driven acoustic modes?

Our analysis of ϵ Peg suggests this supergiant should be classified as a low-amplitude, semi-regular variable. Observations of additional luminosity class II K giants and class I K supergiants, such as α Hydrae and ζ Cephei, should prove interesting as we search for a continuous progression of variability between the class III K giants and the supergiants. The synthesis of the spectrum of this supergiant indicates that SSynth has a solid LTE basis on which to add non-LTE calculations.

I have recently observed a number of K-M giants using the 4096×200 pixel² UBC-1 thick chip on the 1.22-m DAO telescope. The extra-long size of this chip means that the wavelength coverage is 29 nm rather than 14 nm, centered at 860 nm, at the same resolution as previous observations. All three Ca II infrared triplet lines are included. I am working on the feasibility of using these spectra to continue the monitoring of the chromospheric activity in K-M giants. Since the 849.8 nm and 854.2 nm Ca II lines are contaminated by a number of telluric lines, I am also including observations of early (spectral type B and A), rapidly rotating stars to isolate and monitor the changes in the telluric lines. Initial results look promising, even though the signal-to-noise ratio of each spectrum is reduced to approximately 600. Two K giants discussed in this study, β Gem and α Tau, will be among the first stars to be observed extensively to confirm the $\Delta EW_{868.2}$ period discussed for β Gem and to search for a 1.84-dy period in chromospheric activity for α Tau.

Table 4.1 places the work presented here in the context of that done by other groups and that still in progress, and represents the primary sample of a growing list of K giants with long-term and/or short-term radial velocity periodicity. The results presented in this thesis comprise one-third of the stars on this list, and thus have contributed substantially to the knowledge that low-amplitude variability may be a ubiquitous characteristic of K giants. Note that I have included HR 152 in this table. This star was the subject of a recent International Astronomical Union Circular (Noyes et al., 1996) where the radial velocity variability was cited as evidence of a multiple planetary system. The claim has since been tempered by the notification that virtually

Table 4.1: Summary of K giant radial velocity data and detected periods

Star	SpT	Long Period (dy)	Short Period (dy)	σ_{RV} m s^{-1}	M_{bol}
* γ Cep	K0 III	913	?	29	1.60
γ^2 Del	K0 III	530	?	13	0.90
* β Gem	K0 IIIb	585	?	33	0.55
α Boo	K1.5 III	233	2-4	148	-0.78
† β Oph	K2 III	14	0.26	20	-0.55
◊ α Ari	K2 IIIab	?	?	31	-0.03
δ Sgr	K2.5 IIIa	293*	1.98*	64	-1.46
α Tau	K5 III	648	1.84	87	-1.75
◊ α Hya	K3 II-III	?	?	115	-1.96
◊HR 152	K5-M0 III	650	~ 14	170	-1.55
◊ Peg	K2 Ib	†	10.7	424	-4.90

* Coincident period in $\Delta EW_{888.2}$ index; Walker et al. (1992), and this work

† Hatzes and Cochran (1994b)

◊ Not analyzed yet

* Periods are aliases, see Sec. 2.2.2

◊ Noyes et al. (1996)

† Multiperiodic: 63.5 and 46.3 days

every K giant seems to be variable on timescales of this order. Because of our expertise in the field of variable K giants, we received high-quality radial velocity data from Geoff Marcy for HR 152 and will be including this star in a future summary paper on the radial velocity variability of K giants.

The short-term periods detected in these stars may be due to radial pulsations; the long-term periods (if not aliases) may be attributed to rotation or the presence of a small $M_2 \sin i$ companion. Nonradial pulsations may underlie either the short-term or the long-term periods. To help distinguish between orbital and rotation effects, two improvements can be made for future radial velocity measurements, the most sensitive indicator of periodicity. If the radial velocity periodicity is the result of rotation modulation, then we should be able to detect amplitude and phase shifts as the surface features being modulated by rotation grow and decay at various longitudes and as they are eclipsed by the rotation. In order to determine this kind of detail, we need to sample the radial velocities more often and with higher accuracy. For bright stars such as the giants considered here, we note that reducing the random radial velocity errors to $\sim 2 \text{ m s}^{-1}$ is entirely feasible (Butler et al., 1996). The real challenge will be to maintain instrumental stability at this level for several years. Since the HF technique is no longer in use, we are currently discussing these requirements with other precise radial velocity groups.

There has been recent, renewed interest in the possibility that the long-term periods are caused by r -modes. Noted in observations of the Sun, the r -modes are small-amplitude oscillations with motions dominated by the Coriolis force and with periods typically longer than the rotation pe-

riod (Wolff, 1996). The r -modes are thought to occur where the convective timescale becomes comparable to or longer than the rotation period. The Sun may have gravity modes, or g -modes, excited deep in its interior. It is thought that g -modes are quickly damped in convective regions and thus will never be observed in giant stars, but the possibility should be explored that g -modes may be excited or trapped in the hydrogen or helium burning shell (J. Matthews, private communication). Interestingly enough, Wolff (1996) mentions that g -modes may possibly excite large-scale convective flows in the Sun. Theoretical calculations are needed here to extend the solar models to giant stars.

We reemphasize the request made by Hatzes and Cochran (1994b) for more rigorous theoretical calculations. This theoretical work should include the possibility of giant gaseous planets forming close to the early-type progenitors of K giant stars. As more is learned about these stars, we gain one more step in our observational and theoretical understanding of the low-level variability seen in almost all of the K giants. From the present and future work, we hope to learn more about mass loss, internal structure, evolution, convection, mass, and perhaps planetary systems in K giants.

The comparisons between the synthetic and the observed spectra for the giants are encouraging. The work presented in this thesis has shown that once we have adjusted the oscillator strengths, wavelengths, and broadening coefficients for all lines in the full 14-nm spectral interval, we will be able to derive more accurately the effective temperatures, surface gravities, metallicities, and microturbulence values for the full sample of K giants. Our work provides more consistent results than those of a similar study by McWilliam

(1990) in that the surface gravity of each giant is derived simultaneously with the other parameters.

4.3 Spectrum Synthesis

Through our treatment of the line haze as a perturbation to the continuum opacity, we have developed an efficient and automatic method of calculating the cumulative line blocking as a function of equivalent width. We use this function along with a specified line-blocking error to eliminate the large number of ultraweak lines, that is, those lines which contribute negligibly to the line haze. This method substantially reduces the line list used in the synthetic spectrum computation without compromising the calculated pseudocontinuum. By reducing the number of lines used, we realize an order-of-magnitude savings in the time needed for computing an individual spectrum. As a result, we will be able to more efficiently synthesize a greater number of stellar spectra.

While the primary use of the cumulative line-blocking function is to improve the efficiency of our synthetic spectrum computations, there are also a number of secondary uses. For example, we will be able to use these results to evaluate line list incompleteness and to explore the effect line haze has in stellar population studies. To insure that the cumulative line-blocking function is correct, it is absolutely essential that the calculated line lists are made as complete as possible. However, once that is done, individuals who generate these line lists should be able to use a criterion based on the cumulative line-blocking function to reduce the number of lines they need to

distribute for synthetic spectrum purposes.

Based upon my work in deriving the line-specific parameters versus the global stellar parameters, I suggest that the next step in improving the efficiency of the SSynth calculations should be the installation of a least-squares algorithm for determining the *global* stellar parameters. Although this means taking the derivatives of each parameter – temperature, surface gravity, abundances, microturbulence – through the equation of state calculations as well as the equation of transfer, the quality of our spectra and the frailties of human endurance demand it.

Bibliography

- Allen, C. W. 1973, *Astrophysical Quantities*, 2nd ed., (The Athlone Press, London)
- Ando, H. 1976, *Publications of the Astronomical Society of Japan* 28, 517
- Auer, L. 1976, *Journal of Quantitative Spectroscopic and Radiative Transfer* 16, 931, (A76)
- Baliunas, S. L., Donahue, R. A., Soon, W. H., Horne, J. H., Frazer, J., Woodard-Eklund, L., Bradford, M., Rao, L. M., Wilson, O. C., Zhang, Q., Bennett, W., Briggs, J., Carroll, S. M., Duncan, D. K., Figueroa, D., Lanning, H. H., Misch, A., Mueller, J., Noyes, R. W., Poppe, D., Porter, A. C., Robinson, C. R., Russell, J., Shelton, J. C., Soyumer, T., Vaughan, A. H., and Whitney, J. H. 1995, *Astrophysical Journal* 438, 269
- Baliunas, S. L., Hartmann, L., and Dupree, A. K. 1983a, *Astrophysical Journal* 271, 672
- Baliunas, S. L., Hartmann, L., Vaughan, A. H., Liller, W., and Dupree, A. K. 1981, *Astrophysical Journal* 246, 473
- Baliunas, S. L., Horne, J. H., Porter, A., Duncan, D. K., Frazer, J., Lanning, H., Misch, A., Mueller, J., Noyes, R. W., Soyumer, D., Vaughan, A. H., and Woodard, L. 1985, *Astrophysical Journal* 294, 310

- Baliunas, S. L., Rao, L., Frazer, J., Robinson, C., and Woodard, L. 1991, *Bulletin of the American Astronomical Society* **22**, 1199
- Baliunas, S. L. and Vaughan, A. H. 1985, *Annual Review of Astronomy and Astrophysics* **23**, 379
- Baliunas, S. L., Vaughan, A. H., Hartmann, L., Middelkoop, F., Mihalas, D., Noyes, R. W., Preston, G. W., Frazer, J., and Lanning, H. 1983b, *Astrophysical Journal* **275**, 752
- Barnes, T. G., Evans, D. S., and Moffett, T. J. 1978, *Monthly Notices of the Royal Astronomical Society* **183**, 285
- Bell, R. A. and Tripicco, M. J. 1991, *Astronomical Journal* **102**, 777
- Bohlender, D. A., Irwin, A. W., Yang, S. L. S., and Walker, G. A. H. 1992, *Publications of the Astronomical Society of the Pacific* **104**, 1152
- Booth, A. J., Blackwell, D. E., and Fletcher, J. M. 1989, *Publications of the Dominion Astrophysical Observatory* **18**, 1
- Butler, R. P., Marcy, G. W., Williams, E., McCarthy, C., Dosanjh, P., and Vogt, S. S. 1996, *Publications of the Astronomical Society of the Pacific* **108**, 500
- Campbell, B. and Garrison, R. F. 1985, *Publications of the Astronomical Society of the Pacific* **97**, 180
- Campbell, B. and Walker, G. A. H. 1979, *Publications of the Astronomical Society of the Pacific* **91**, 540
- Campbell, B. and Walker, G. A. H. 1985, in A. G. D. Philip and D. W. Latham (eds.), *IAU Colloquium 88, Stellar Radial Velocities*, p. 5, (L. Davis Press, Schenectady)
- Campbell, B., Walker, G. A. H., Pritchett, C., and Long, B. 1986, in M. C.

- Kafatos, R. S. Harrington, and S. P. Maran (eds.), *Astrophysics of Brown Dwarfs*, p. 37, (Cambridge University Press, Cambridge)
- Campbell, B., Walker, G. A. H., and Yang, S. L. S. 1988, *Astrophysical Journal* **331**, 902
- Carlsson, M. and Stein, R. F. 1992, *Astrophysical Journal* **397**, L59
- Cayrel de Strobel, G., Hauck, B., François, P., Thévenin, F., Friel, E., Mermiliod, M., and Borde, S. 1992, *Astronomy & Astrophysics Supplement Series* **95**, 273
- Cayrel de Strobel, G., Perrin, M.-N., and Lebreton, Y. 1989, *Astronomy & Astrophysics* **225**, 369
- Climenhaga, J. L. 1963, *Publications of the Dominion Astrophysical Observatory* **11**, 307
- Costes, M., Naulin, C., and Dorthe, G. 1990, *Astronomy & Astrophysics* **232**, 270
- Cottrell, P. L. and Sneden, C. 1986, *Astronomy & Astrophysics* **161**, 314
- Cox, J. P., King, D. S., and Stellingwerf, R. F. 1972, *Astrophysical Journal* **171**, 93
- Dearborn, D. S. P., Eggleton, P. P., and Scramm, D. N. 1976, *Astrophysical Journal* **203**, 455
- Di Benedetto, G. P. and Rabbia, Y. 1987, *Astronomy & Astrophysics* **188**, 114
- Dravins, D., Linde, P., Fredga, K., and Gahm, G. F. 1993, *Astrophysical Journal* **403**, 396
- Drayson, S. R. 1976, *Journal of Quantitative Spectroscopic and Radiative Transfer* **16**, 611

- Duncan, D. K., Vaughan, A. H., Wilson, O. C., Preston, G. W., Frazer, J., Lanning, H., Misch, A., Mueller, J., Soyumer, D., Woodard, L., Baliunas, S. L., Noyes, R. W., Hartmann, L. W., Porter, A., Zwaan, C., Middelkoop, F., Rutten, R. G. M., and Mihalas, D. 1991, *Astrophysical Journal Supplement* 76, 383
- Edmonds, P. D. and Gilliland, R. L. 1996, *Astrophysical Journal* 464, L157
- Erdely-Mendes, M. and Barbuy, B. 1989, *Astronomy & Astrophysics Supplement Series* 80, 229
- Fahlman, G. G. and Glaspey, J. W. 1973, in J. W. Glaspey and G. A. H. Walker (eds.), *Astronomical Observations with Television-Type Sensors*, p. 347, (University of British Columbia, Vancouver)
- Fox, M. W. and Wood, P. R. 1982, *Astrophysical Journal* 259, 198
- Garrison, R. F. and Beattie, B. 1992, in R. L. Bishop (ed.), *The Royal Astronomical Society of Canada Observer's Handbook 1993*, p. 181, (University of Toronto Press, Toronto)
- Gray, D. F. 1982, *Astrophysical Journal* 262, 682
- Gray, D. F. 1992, *The Observation and Analysis of Stellar Photospheres*, 2nd ed., (Cambridge University Press, Cambridge)
- Gray, D. F. 1994, *Publications of the Astronomical Society of the Pacific* 106, 1248
- Gray, D. F. and Baliunas, S. L. 1995, *Astrophysical Journal* 441, 436
- Gray, D. F. and Johanson, H. L. 1991, *Publications of the Astronomical Society of the Pacific* 103, 439
- Gray, D. F. and Nagar, P. 1985, *Astrophysical Journal* 298, 756
- Gray, D. F. and Toner, C. G. 1986, *Publications of the Astronomical Society*

- of the Pacific* **98**, 499
- Grevesse, N. and Anders, E. 1991, in A. N. Cox, W. C. Livingston, and M. S. Matthews (eds.), *Solar Interior and Atmosphere*, p. 1227, (The University of Arizona Press, Tucson)
- Griffin, R. F. 1968, *A Photometric Atlas of the Spectrum of Arcturus*, (Cambridge University Press, Cambridge)
- Gustafsson, B. and Bell, R. A. 1979, *Astronomy & Astrophysics* **74**, 313
- Hall, D. S. 1990, in C. Ibanoglu (ed.), *Active Close Binaries*, p. 112, (Kluwer Academic Publishers, Netherlands)
- Harvey, K. L. 1992, in K. L. Harvey (ed.), *The Solar Cycle*, p. 335, (ASP Conference Series, 27)
- Hatzes, A. P. and Cochran, W. D. 1993, *Astrophysical Journal* **413**, 339, (HC93)
- Hatzes, A. P. and Cochran, W. D. 1994a, *Astrophysical Journal* **422**, 369
- Hatzes, A. P. and Cochran, W. D. 1994b, *Astrophysical Journal* **432**, 763
- Hoffleit, E. D. and Warren, W. 1991, *The Bright Star Catalogue, 5th ed.*, NASA, Goddard Space Flight Center (ST Systems Corp.), machine-readable version
- Holweger, H. and Müller, E. A. 1974, *Solar Physics* **39**, 19, (HMS)
- Hotop, H. and Lineberger, W. C. 1985, *Journal of Physical and Chemical Reference Data* **14**, 731
- Huber, K. P. and Herzberg, G. 1979, *Molecular Spectra and Molecular Structure IV. Constants of Diatomic Molecules*, (Van Nostrand Reinhold Company, New York)
- Irwin, A. W. 1978, *Ph.D. thesis*, University of Toronto

- Irwin, A. W. 1981, *Astrophysical Journal Supplement* 45, 621
- Irwin, A. W. 1985, *Astronomy & Astrophysics* 146, 282
- Irwin, A. W. 1987, *Astronomy & Astrophysics* 182, 348
- Irwin, A. W. 1988, *Astronomy & Astrophysics Supplement Series* 74, 145
- Irwin, A. W., Campbell, B., Morbey, C. L., Walker, G. A. H., and Yang, S. L. S. 1989, *Publications of the Astronomical Society of the Pacific* 101, 147
- Irwin, A. W., Fletcher, J. M., Yang, S. L. S., Walker, G. A. H., and Goodenough, C. 1992, *Publications of the Astronomical Society of the Pacific* 104, 489
- Irwin, A. W., Yang, S. L. S., and Walker, G. A. H. 1996, *Publications of the Astronomical Society of the Pacific* 108, 580
- John, T. L. 1988, *Astronomy & Astrophysics* 193, 189
- Jørgensen, U. G. 1994a, *SCAN molecular data base*, (J94a)
- Jørgensen, U. G. 1994b, *Astronomy & Astrophysics* 284, 179, (J94b)
- Jørgensen, U. G., Carlsson, M., and Johnson, H. R. 1992, *Astronomy & Astrophysics* 254, 258
- Jørgensen, U. G. and Larsson, M. 1990, *Astronomy & Astrophysics* 238, 424
- Judge, P. G. and Cuntz, M. 1993, *Astrophysical Journal* 409, 776, (JC93)
- Judge, P. G. and Stencel, R. E. 1991, *Astrophysical Journal* 371, 357
- Kostik, R. I., Shchukina, N. G., and Rutten, R. 1996, *Astronomy & Astrophysics* 305, 325
- Kováks, N. 1983, *Astronomy & Astrophysics* 120, 21
- Krisciunas, K. 1992, *Commissions 27 and 42 of the IAU Information Bulletin on Variable Stars*, No. 3729

- Kunasz, P. B. and Hummer, D. G. 1974, *Monthly Notices of the Royal Astronomical Society* 166, 19
- Kurucz, R. L. 1970, *ATLAS: A Computer Program for Calculating Model Stellar Atmospheres*, Technical Report 309, Smithsonian Astrophysical Observatory
- Kurucz, R. L. 1991a, in L. Crivallari, I. Hubeny, and D. G. Hummer (eds.), *Stellar Atmospheres: Beyond Classical Models*, p. 441, (Kluwer Academic Publishers, Netherlands)
- Kurucz, R. L. 1991b, in A. N. Cox, W. C. Livingston, and M. S. Matthews (eds.), *Solar Interior and Atmosphere*, p. 666, (The University of Arizona Press, Tucson)
- Kurucz, R. L. 1993a, *ATLAS9 Stellar Atmosphere Programs and 2 km s⁻¹ Grid*, (CD-ROM No. 13)
- Kurucz, R. L. 1993b, *Atomic Data for Opacity Calculations*, (CD-ROM No. 1)
- Kurucz, R. L. 1993c, *SYNTHE Spectrum Synthesis Programs and Line Data*, (CD-ROM No. 18)
- Kurucz, R. L. and Avrett, E. H. 1981, *Smithsonian Astrophysical Observatory Special Report No. 391*, Technical Report 391, Smithsonian Astrophysical Observatory
- Kurucz, R. L., Furenlid, I., Brault, J., and Testerman, L. 1984, *Solar Flux Atlas from 296 to 1300 nm*, (National Solar Observatory, Sunspot, New Mexico)
- Kurucz, R. L. and Peytremann, E. 1975, *A Table of Semiempirical gf Values*, Technical Report 362, Smithsonian Astrophysical Observatory

- Larson, A. M. and Irwin, A. W. 1996, *Astronomy & Astrophysics Supplement Series* 117, 189
- Larson, A. M., Irwin, A. W., Yang, S. L. S., Goodenough, C., Walker, G. A. H., Bohlender, D. A., and Walker, A. R. 1993c, in J. M. Nemec and J. M. Matthews (eds.), *New Perspectives on Stellar Pulsation and Pulsating Variable Stars*, p. 384, Proceedings of IAU Colloquium 139
- Larson, A. M., Irwin, A. W., Yang, S. L. S., Goodenough, C., Walker, G. A. H., Walker, A. R., and Bohlender, D. A. 1993a, *Publications of the Astronomical Society of the Pacific* 105, 825
- Larson, A. M., Irwin, A. W., Yang, S. L. S., Goodenough, C., Walker, G. A. H., Walker, A. R., and Bohlender, D. A. 1993b, *Publications of the Astronomical Society of the Pacific* 105, 332
- Larson, A. M., Irwin, A. W., Yang, S. L. S., Walker, G. A. H., and Walker, A. R. 1996, *Intriguing Variability in the Radial Velocity, Chromospheric Emission, and R - I of δ Sagittarii*, submitted
- Linsky, J. L., Hunten, D. M., Sowell, R., Glackin, D. L., and Kelch, W. L.: 1979, *Astrophysical Journal Supplement* 41, 481
- Luck, R. E. and Challener, S. L. 1995, *Astronomical Journal* 110, 2968
- Martin, W. C. 1992, in P. L. Smith and W. L. Wiese (eds.), *Atomic and Molecular Data for Space Astronomy: Needs, Analysis, and Availability*, p. 121
- Martin, W. C., Zalubas, R., and Musgrove, A. 1985, *Journal of Physical and Chemical Reference Data* 14, 751
- McMillan, R. S., Moore, T. L., Perry, M. L., and Smith, P. M. 1994, *Astrophysics and Space Science* 212, 271

- McWilliam, A. 1990, *Astrophysical Journal Supplement* 74, 1075, (McW90)
- Mihalas, D. 1978, *Stellar Atmospheres*, (W. H. Freeman and Company, San Francisco), (M78)
- Mish, F. C. (ed.) 1989, *The New Merriam-Webster Dictionary*, (Merriam-Webster, Inc., Springfield)
- Moore, C. E. 1970, in *NSRDS - NBS 34*, (U.S. Government Printing Office, Washington, D.C.)
- Moore, C. E. 1985, *Selected Tables of Atomic Spectra, NSRDS - NBS 3, Section 11*, (U.S. Government Printing Office, Washington, D.C.)
- Moore, C. E., Minnaert, M. G. J., and Houtgast, J. 1966, in *National Bureau of Standards Monograph 61*, (U.S. Government Printing Office, Washington, D.C.)
- Murdoch, K. A., Hearnshaw, J. B., and Clark, M. 1993, *Astrophysical Journal* 413, 349, (MHC93)
- Nave, G., Johansson, S., Learner, R. C. M., Thorne, A. P., and Brault, J. W.: 1994, *Astrophysical Journal Supplement* 94, 221
- Neff, J. E., O'Neal, D., and Saar, S. H. 1995, *Astrophysical Journal* 452, 879
- Noyes, R., Korzennik, S., Nisenson, P., Jha, S., and Krockenberger, M. 1996, *International Astronomical Union Circular No. 6316*
- O'Brien, G. T. J. and Lambert, D. L. 1986, *Astrophysical Journal Supplement* 62, 899
- Payne-Gaposchkin, C. and Gaposchkin, S. 1938, *Harvard Monographs* 5, 359
- Peterson, D. M. and Solensky, R. 1988, *Astrophysical Journal* 333, 256
- Peterson, R. C., Kurucz, R. L., and Carney, B. W. 1990, *Astrophysical Journal* 350, 173

- Press, W. H., Flannery, B. P., Teukolsky, S. A., and Vetterling, W. T. 1986, *Numerical Recipes*, (Cambridge University Press, Cambridge)
- Press, W. H., Teukolsky, S. A., Vetterling, W. T., and Flannery, B. P. 1992, *Numerical Recipes*, (Cambridge University Press, Cambridge)
- Radick, R. R., Lockwood, G. W., and Baliunas, S. L. 1990, *Science* **247**, 39, (RLB90)
- Richardson, E. H., Brealey, G. A., and Dancey, R. 1970, *Publications of the Dominion Astrophysical Observatory* **14**, 1
- Rutledge, G., Hesser, J. E., Irwin, A. W., and Larson, A. M. 1996, in preparation
- Saar, S. H. and Baliunas, S. L. 1992, in K. L. Harvey (ed.), *The Solar Cycle*, p. 150, (ASP Conference Series, 27)
- Sauval, A. J. and Tatum, J. B. 1984, *Astrophysical Journal Supplement* **56**, 193
- Schroeder, D. J. 1987, *Astronomical Optics*, (Academic Press, Inc., New York)
- Schwarzschild, M. 1975, *Astrophysical Journal* **195**, 137
- Shine, R. A. and Linsky, J. L. 1972, *Solar Physics* **25**, 357
- Shine, R. A. and Linsky, J. L. 1974, *Solar Physics* **39**, 49
- Smith, G. and Drake, J. J. 1988, *Monthly Notices of the Royal Astronomical Society* **231**, 115, (SD88)
- Smith, M. A. and Dominy, J. F. 1979, *Astrophysical Journal* **231**, 477
- Smith, P. H., McMillan, R. S., and Merline, W. J. 1987, *Astrophysical Journal* **317**, L79
- Smith, V. V. and Lambert, D. L. 1987, *Monthly Notices of the Royal Astro-*

- nomical Society* 226, 563
- Sugar, J. and Corliss, C. 1985, *Journal of Physical and Chemical Reference Data* 14, Suppl. 2
- Swensson, J. W., Benedict, W. S., Delbouille, L., and Roland, G. 1970, *The Solar Spectrum from λ 7498 to λ 12016: A Table of Measures and Identifications*, (Mémoires de la Société Royale des Sciences de Liège, No. 5)
- Tanner, R. W. 1948, *The Journal of the Royal Astronomical Society of Canada* 42, 177
- Taylor, B. J. 1991, *Astrophysical Journal Supplement* 76, 715
- Topka, K. P. and Title, A. M. 1991, in A. N. Cox, W. C. Livingston, and M. S. Matthews (eds.), *Solar Interior and Atmosphere*, p. 727, (The University of Arizona Press, Tucson)
- Tsuji, T. 1986, *Astronomy & Astrophysics* 156, 8
- Unno, W., Osaki, Y., Ando, H., and Shibahashi, H. 1979, *Nonradial Oscillations of Stars*, (University of Tokyo Press, Tokyo)
- van Altena, W. F., Lee, J. T., and Hoffleit, E. D. 1991, *General Catalogue of Trigonometric Stellar Parallaxes*, [NASA, Goddard Space Flight Center (ST Systems Corp.)], (on-line version)
- VandenBerg, D. A. 1985, *Astrophysical Journal Supplement* 58, 711
- VandenBerg, D. A. and Bell, R. A. 1985, *Astrophysical Journal Supplement* 58, 561
- Vaughan, A. H., Preston, G. W., and Wilson, O. C. 1978, *Publications of the Astronomical Society of the Pacific* 90, 267
- Vaughan, A. R., Baliunas, S. L., Middelkoop, F., Hartmann, L. W., Mihalas,

- D., Noyes, R. W., and Preston, G. W. 1981, *Astrophysical Journal* 250, 276
- Walker, G. A. H. 1987, *Astronomical Observations: An Optical Perspective*, (Cambridge University Press, Cambridge)
- Walker, G. A. H., Bohlender, D. A., Walker, A. R., Irwin, A. W., Yang, S. L. S., and Larson, A. M. 1992, *Astrophysical Journal* 396, L91
- Walker, G. A. H., Walker, A. R., Irwin, A. W., Larson, A. M., Yang, S. L. S., and Richardson, D. 1995, *Icarus* 116, 359
- Walker, G. A. H., Yang, S., Campbell, B., and Irwin, A. W. 1989, *Astrophysical Journal* 343, L21
- Warner, B. 1969, *Monthly Notices of the Royal Astronomical Society* 144, 333
- Wilson, O. C. 1976, *Astrophysical Journal* 205, 823
- Wilson, O. C. 1978, *Astrophysical Journal* 226, 379
- Wolff, C. L. 1996, *Astrophysical Journal* 459, L106
- Woolley, R., Epps, E. A., Penston, M. J., and Pocock, S. B. 1970, *Catalogue of Stars within Twenty-Five Parsecs of the Sun*, Roy. Obs. Ann., No. 5, (on-line version compiled by Warren, W. H. Jr., 1982)
- Yang, S. L. S., Larson, A. M., Irwin, A. W., Goodenough, C., Walker, G. A. H., Walker, A., and Bohlender, D. A. 1993, in J. M. Nemeč and J. M. Matthews (eds.), *New Perspectives on Pulsation and Pulsating Variable Stars*, p. 383, IAU Colloquium No. 139
- Zirin, H. 1988, *Astrophysics of the Sun*, (Cambridge University Press, Cambridge)

Appendix A

Tables of Data

This appendix includes the $\Delta EW_{868.2}$ index data from the CFHT observations of 61 Cygni A; and the radial velocity and $\Delta EW_{868.2}$ and $\Delta(R - I)$ index data from the CFHT observations, and the radial velocity data from the DAO observations for β Geminorum, δ Sagittarii, α Tauri, and ϵ Pegasi. The radial velocity data for the dwarf stars are archived with NSSDC/ADC [the (United States) National Space Science Data Center/Astronomical Data Center]. Electronic access to the NSSDC/ADC catalogs can be obtained from URL = <http://adc.gsfc.nasa.gov/>. The data for the $\Delta EW_{868.2}$ and $\Delta(R - I)$ indices for the dwarf stars will be the subject of a future paper (Larson, Irwin et al., in progress) and will be provided at that time.

All values of the CFHT data have observing run corrections subtracted (Campbell et al., 1988, Table 2). For example, the systematic offsets in the collective radial velocities are shown as Fig. 1 in Walker et al. (1995). The current run corrections were calculated by A. W. Irwin; the following is a brief description of the least-squares method used. For each star the radial velocities are fitted with low-order polynomial trends as a function of time,

and the residuals from these polynomials are calculated. The run correction is the weighted mean of the residuals of all stars observed during a particular observing run (typically 10-15 stars); stars with the smallest residuals from their polynomial trends are assigned the highest weight. The residuals for different stars should not correlate, so the run corrections, which are usually less than 20 m s^{-1} with statistical errors less than 5 m s^{-1} , should reflect systematic instrumental errors in the radial velocities. Similar results (run corrections typically twice the internal errors) were obtained for $\Delta EW_{868.2}$ and $\Delta(R - I)$. After the run corrections are applied, the zero points of the final data are adjusted such that the weighted means of the data for each star is zero.

Certain $\Delta EW_{868.2}$ and $\Delta(R - I)$ data from the CFHT observations are deemed unreliable due to the use of a substitute detector or have potential twilight contamination (solar zenith angle was less than 96 degrees). These data have been excluded from all data tables included here. Results from other stars show that the radial-velocity data are not in fact significantly affected by the instrument change or twilight contamination.

The arbitrary zero points of the DAO velocities, which is independent of the CFHT velocity zero points, have been adjusted so that the weighted mean is zero. The current DAO spectra contain low-level fringing and fixed-pattern noise which increase the internal errors of the velocities and make the equivalent-width indices, $\Delta EW_{868.2}$ and $\Delta(R - I)$, unreliable.

The DAO observations have been limited to evolved stars. When compared to the dwarfs in the full CFHT program, these evolved stars have a relatively large velocity variability which generates a large statistical error in

the run corrections. We have not applied these corrections because they are not significantly different from zero. However, the 95% confidence intervals calculated from these corrections and their statistical errors imply typical upper limits of 40 m s^{-1} on possible systematic errors in the DAO velocities.

Table A.1: 61 Cygni A: $\Delta EW_{866.2}$ index data

JD ^a (dy) 2440000+	$\Delta EW_{866.2}$ (pm)		JD ^a (dy) 2440000+	$\Delta EW_{866.2}$ (pm)	
	value	σ^b		value	σ^b
4754.0988	0.56	0.09			
4770.0901	1.30	0.09	7101.8139	2.17	0.08
4926.8162	1.15	0.08	7102.8188	2.06	0.09
4957.7797	0.56	0.08	7159.7147	1.55	0.08
5148.0464	0.08	0.08	7160.7423	1.48	0.10
5165.9964	0.32	0.07	7307.0670	2.01	0.09
5276.8280	0.05	0.06	7308.0397	1.94	0.09
5810.1330	-1.23	0.05	7338.9849	1.37	0.08
5865.0868	-1.24	0.05	7339.9520	1.48	0.09
5901.9986	1.34	0.05	7370.9605	0.97	0.06
6216.1146	-0.98	0.05	7371.9333	1.05	0.07
6283.0108	-1.55	0.05	7453.8908	0.68	0.10
6283.0371	-1.39	0.06	7454.7670	0.87	0.09
6393.7482	-0.58	0.04	7521.7893	0.57	0.07
6394.7700	-0.69	0.06	7636.0688	0.69	0.07
6539.1235	0.52	0.05	7699.0728	0.65	0.07
6604.0742	-0.53	0.04	7787.9450	-0.17	0.04
6633.9551	-0.37	0.07	7788.8675	-0.13	0.04
6725.7772	0.78	0.06	8112.9215	-0.17	0.04
6726.8043	1.12	0.06	8113.9375	-0.57	0.05
6784.7854	0.31	0.08	8406.0358	-1.27	0.07
6961.0224	1.66	0.07	8407.0375	-1.24	0.07
6962.0288	1.09	0.08	8471.0024	-0.57	0.05
7019.9720	1.79	0.07	8577.7964	-0.73	0.05
7020.9444	1.96	0.08	8818.0045	-0.50	0.13

^a Corrected for the light travel time to the barycenter of the solar system

^b See text for the derivation of the standard deviation

Table A.2: β Geminorum: CFHT radial velocity and equivalent width data

JD ^a (dy) 2440000+	RV (m s ⁻¹)		$\Delta EW_{866.2}$ (pm)		$\Delta(R - I)$ (mmag)	
	value	σ	value	σ	value	σ
4559.1000	-19.2	27.6	0.075	0.076	-4.9	2.0
4559.1013	-18.2	26.2	0.256	0.082	10.5	4.9
4621.9479	30.8	15.3	0.042	0.068	-2.4	3.7
4654.8936	40.1	17.0	0.262	0.057	-2.0	2.8
4686.8244	-6.0	17.0	0.167	0.063	-2.4	1.3
4914.0784	5.1	12.9	-0.021	0.063	2.7	3.7
4927.0017	1.3	17.3	0.185	0.068	-22.8	6.6
4958.0555	2.6	16.4	0.056	0.081	21.8	8.5
5277.1158	17.2	12.6	0.050	0.061	-4.9	1.3
5458.7584	10.8	19.3				
5711.9672	-30.2	13.7	-0.064	0.060	-13.6	5.3
5809.7564	-0.3	9.5	0.033	0.043	0.2	0.9
5809.7575	-33.2	10.6	-0.114	0.046	-0.9	1.1
6048.0665	27.9	10.4	-0.136	0.041	0.7	1.2
6048.0688	30.2	9.7	-0.023	0.044	-3.8	1.7
6394.0062	-53.1	10.1	-0.049	0.041	3.8	1.4
6395.0229	-23.6	8.9	-0.141	0.052	0.7	1.1
6538.8582	30.8	11.4	-0.057	0.040	1.7	1.0
6538.8607	32.5	11.0	-0.038	0.040	0.4	0.7
6727.0528	-2.9	6.5	-0.085	0.042	16.7	5.1
6727.0542	-7.8	7.5	-0.127	0.044	18.0	5.5
7338.7281	-33.6	9.8				
7339.7281	-19.2	9.3				

(continued)

β Geminorum: CFHT radial velocity and equivalent width data (continued)

JD ^a (dy) 2440000+	RV (m s ⁻¹)		$\Delta EW_{866.2}$ (pm)		$\Delta(R - I)$ (mmag)	
	value	σ	value	σ	value	σ
7455.0840	-41.2	11.6	-0.090	0.054	6.5	2.7
7545.8791	-3.8	13.9	0.005	0.055	0.9	1.8
7545.8817	8.2	15.3	-0.039	0.055	1.0	1.8
7635.8502	47.4	10.1	0.070	0.054	-1.8	0.9
7635.8518	50.1	12.6	0.046	0.061	-3.0	1.3
7789.1208	28.4	6.6	0.046	0.049	3.1	1.8
7789.1224	29.9	6.3	-0.004	0.046	8.2	3.1
8406.7398	20.2	10.3	0.203	0.064	0.6	1.0
8406.7430	34.5	10.9	0.056	0.049	0.7	1.0
8406.7450	22.4	9.8	0.071	0.058	3.1	1.4
8406.7467	19.5	10.4	0.049	0.050	-1.3	0.9
8406.7501	3.5	11.0	0.058	0.052	3.0	1.3
8578.1033	-50.1	11.1	0.008	0.063	0.0	1.2
8578.1043	-52.2	10.1	0.008	0.063	2.4	1.5
8578.1053	-57.1	8.9	-0.005	0.064	-3.0	1.6
8578.1063	-57.2	10.0	0.063	0.066	-3.7	1.8

^a Corrected for the light travel time to the barycenter of the solar system

Table A.3: β Geminorum: DAO radial velocity data

JD ^a (dy) 2440000+	RV (ms ⁻¹)		JD ^a (dy) 2440000+	RV (ms ⁻¹)	
	value	σ		value	σ
6170.7075	-47.0	58.4	8957.1254	-9.1	34.2
7533.7309	-72.0	10.8	8957.7661	-34.4	42.4
8639.7923	-89.6	18.1	8987.7036	-9.0	15.1
8640.8359	-26.5	31.3	8988.7718	-13.5	15.2
8641.9457	-27.3	14.8	9002.8665	97.9	81.7
8740.7071	-11.8	27.8	9003.0223	37.3	24.9
8878.0085	67.7	18.1	9003.6991	-6.2	19.0
8878.9952	33.7	30.0	9003.8999	-10.1	18.8
8880.0133	25.7	17.5	9004.0441	-13.7	26.0
8880.9961	69.2	20.9	9004.7772	64.7	22.9
8919.0519	87.7	28.2	9005.7660	2.8	20.6
8920.9053	37.7	16.7	9006.0598	31.9	42.1
8921.9146	28.7	18.1	9006.7878	81.0	18.9
8955.7702	-6.8	36.6			

^a Corrected for the light travel time to the barycenter of the solar system.

Table A.4: δ Sagittarii: CFHT radial velocity and equivalent width data

JD ^a (dy) 2440000+	RV (m s ⁻¹)		$\Delta EW_{866.2}$ (pm)		$\Delta(R - I)$ (mmag)	
	value	σ	value	σ	value	σ
4769.9257	-132.5	21.6	-0.244	0.060	-15.5	6.0
5147.9305	-77.2	14.8	0.016	0.056	-0.7	2.2
5148.9305	-112.0	13.0	-0.137	0.055	-2.3	1.6
5165.8650	-62.3	11.8	0.248	0.073	-4.1	1.8
5458.9974	-93.7	18.1				
5810.9685	57.5	11.9	-0.040	0.040	1.1	0.7
5864.0613	-5.1	10.8	-0.288	0.050	-3.1	2.3
5864.9787	-30.1	11.9	-0.068	0.052	-1.2	1.3
6217.0004	-40.0	19.7	0.061	0.060	2.8	1.3
6217.0055	-55.9	18.8	0.039	0.057	-0.5	1.5
6283.9214	-113.7	13.8	-0.082	0.053	-2.1	2.5
6283.9262	-125.7	12.9	-0.114	0.047	-2.6	1.9
6393.6849	-11.2	13.7	-0.098	0.055	-4.0	2.8
8817.9444	56.1	9.7	0.313	0.085	-3.1	4.9
8817.9479	53.3	8.6	0.378	0.084	-0.7	4.8
8817.9522	54.3	8.7	0.441	0.088	8.1	5.0
8817.9564	54.6	8.8	0.320	0.083	-0.2	4.6
8818.8774	21.5	7.1	0.090	0.066	4.4	5.0
8818.8817	24.2	8.6	0.042	0.063	5.0	4.8
8818.8862	15.1	7.5	0.103	0.061	4.9	4.7
8904.7526	-35.1	21.5	0.148	0.089	15.7	5.2
8904.7625	-52.3	18.6	0.253	0.087	9.2	4.7

^a Corrected for the light travel time to the barycenter of the solar system

Table A.5: δ Sagittarii: DAO radial velocity data

JD ^a (dy) 2440000+	RV (m s ⁻¹)		JD ^a (dy) 2440000+	RV (m s ⁻¹)	
	value	σ		value	σ
8830.7673	29.0	23.9	9186.8048	-11.6	22.2
8831.7598	-6.7	17.6	9187.7937	-46.2	30.7
8832.7583	34.6	21.5	9219.7257	-8.9	21.8
9124.9526	-3.1	61.4	9223.7315	26.6	28.9
9158.8747	22.3	43.5	9225.7244	-49.9	22.1
9159.8715	99.8	46.1			

^a Corrected for the light travel time to the barycenter of the solar system

Table A.6: α Tauri: CFHT radial velocity and equivalent width data

JD ^a (dy) 2440000+	RV (m s ⁻¹)		$\Delta EW_{866.2}$ (pm)		$\Delta(R - I)$ (mmag)	
	value	σ	value	σ	value	σ
4531.0741	123.9	25.2	-0.594	0.136	0.3	3.5
4532.0915	60.8	29.5	0.573	0.108	-15.6	8.8
4532.1014	60.7	39.4	0.041	0.167	-39.5	14.1
4532.1088	58.3	34.6	0.508	0.132	-43.8	12.3
4532.1128	79.5	35.9	0.258	0.152	-14.5	9.4
4532.1261	-17.2	55.1	0.077	0.218	-36.8	12.1
4532.1292	82.5	23.4	0.540	0.137	-36.3	9.5
4559.0091	112.8	26.9	0.013	0.083	3.5	7.4
4559.0102	129.3	23.1	-0.446	0.093	-3.2	7.8
4621.8398	-28.2	18.4	0.170	0.081	-0.9	4.2
4628.7183	-43.0	12.8	-0.015	0.052	2.3	3.5
4628.7491	-35.3	12.7	0.089	0.056	3.8	3.1
4628.7634	-28.3	11.7	0.101	0.059	-5.3	3.4
4628.7940	-36.4	11.7	0.094	0.055	3.3	3.9
4628.7988	-42.8	13.0	0.095	0.058	-5.2	3.2
4628.8054	-26.9	12.9	0.050	0.052	3.7	5.2
4628.8151	-49.1	12.0	0.083	0.058	0.6	3.9
4628.8248	-40.5	12.2	0.049	0.051	-2.3	5.4
4628.8346	-42.7	12.7	0.062	0.055	-2.5	3.8
4628.8396	-44.0	11.3	0.024	0.051	-0.5	4.1
4628.8428	-35.2	11.3	0.060	0.054	-5.8	4.9
4629.6966	12.1	21.3				
4629.7014	12.7	16.5	-0.217	0.073	-0.7	6.0
4629.7069	7.5	15.6	-0.200	0.064	7.6	3.8
4629.7114	14.1	13.2	-0.299	0.065	0.5	4.0
4629.7177	5.2	18.6	-0.137	0.070	3.7	5.0

(continued)

α Tauri: CFHT radial velocity and equivalent width data (continued)

JD ^a (dy) 2440000+	RV (m s ⁻¹)		$\Delta EW_{866.2}$ (pm)		$\Delta(R - I)$ (mmag)	
	value	σ	value	σ	value	σ
4629.7296	11.1	14.6	-0.201	0.066	1.4	3.8
4629.7366	11.2	15.1	-0.313	0.071	8.1	4.8
4629.7445	13.1	12.7	-0.198	0.061	5.7	3.8
4629.7512	6.3	16.2	-0.210	0.066	5.7	3.6
4629.7776	16.4	14.5	-0.179	0.060	-3.0	5.6
4629.7832	21.1	18.4	-0.042	0.060	-2.2	7.0
4629.7911	26.3	14.9	-0.220	0.066	1.7	6.2
4629.7979	17.8	17.5	-0.260	0.070	2.0	5.3
4629.8069	13.5	14.7	-0.282	0.056	31.9	8.8
4629.8147	10.8	15.1	-0.104	0.070	8.9	6.6
4653.9219	12.7	11.9	-0.034	0.067	0.3	4.1
4686.7930	-93.4	24.2	-0.215	0.068	-16.3	6.2
4914.0600	-2.1	38.6	-0.338	0.072	-17.5	9.5
4926.9848	140.3	35.7	-0.199	0.055	0.3	5.7
4958.0171	174.7	21.9	-0.052	0.051	-14.7	7.7
5277.0689	-126.9	25.4	-0.155	0.057	16.2	8.3
5357.7746	-50.6	16.2	0.200	0.127	-6.3	12.1
5390.8418	-67.7	10.1	-0.075	0.070	13.5	8.3
5390.8440	-68.2	10.0	0.141	0.066	7.5	4.4
5390.8461	-66.8	10.8	-0.093	0.076	12.4	8.5
5711.8903	101.7	16.7	0.003	0.053	2.2	7.0
5712.9192	44.7	24.1	-0.189	0.050	1.2	4.5
5809.7127	220.3	22.1				
5809.7141	213.8	22.4	-0.210	0.049	6.4	8.9
5810.7056	221.3	25.2				
5810.7064	210.6	25.4				

(continued)

α Tauri: CFHT radial velocity and equivalent width data (continued)

JD ^a (dy) 2440000+	RV (m s ⁻¹)		$\Delta EW_{866.2}$ (pm)		$\Delta(R - I)$ (mmag)	
	value	σ	value	σ	value	σ
6048.0372	140.6	13.2	0.352	0.044	-3.7	3.0
6048.0388	141.5	13.8	0.226	0.042	-6.7	3.6
6393.9709	212.1	25.8	0.075	0.041	-2.9	8.9
6726.9928	-18.4	15.7	-0.033	0.055	-17.0	3.4
6726.9961	-28.2	17.0	0.043	0.050	-11.2	2.9
7372.0961	-89.2	10.3	-0.066	0.056	2.1	3.0
7372.0976	-91.7	15.2	0.018	0.065	5.2	4.3
7455.0482	-112.8	16.8	0.358	0.054	-4.7	3.7
7545.8314	81.7	10.2	0.073	0.047	2.6	3.6
7545.8327	78.3	10.1	0.067	0.049	0.6	2.6
7636.7033	85.7	16.5				
7636.7048	104.7	17.6				
7789.0912	45.8	10.6	0.122	0.043	7.2	3.8
7789.0927	52.0	9.0	0.133	0.040	6.4	3.1
8113.1188	-52.8	10.7	-0.077	0.055	1.2	3.1
8114.1137	-30.0	10.7	0.027	0.057	3.9	1.7
8114.1153	-43.0	10.5	-0.017	0.057	5.1	2.5
8472.1375	11.6	18.2	0.104	0.076	-9.1	5.1
8472.1382	-3.1	16.6	0.035	0.079	-25.8	10.0
8472.1388	11.2	20.6	0.134	0.077	-20.2	9.0
8472.1394	-3.1	16.3	0.105	0.077	-6.7	5.3
8472.1402	11.4	21.7	0.241	0.072	-17.6	6.8
8578.0475	-131.4	20.4	0.033	0.068	11.4	8.0
8578.0481	-130.5	21.8	0.088	0.072	-10.3	11.7
8578.0487	-137.1	22.9	0.034	0.072	15.3	8.8
8578.0493	-137.5	20.1	-0.024	0.075	17.6	8.3

^a Corrected for the light travel time to the barycenter of the solar system.
 JD 4628.5 and 4629.5 contain a random sample of the data.

Table A.7: α Tauri: CFHT 1981 time series radial velocity and equivalent width data

JD ^a (dy) 2440000+	RV (m s ⁻¹)		$\Delta EW_{866.2}$ (pm)		$\Delta(R - I)$ (mmag)	
	value	σ	value	σ	value	σ
4628.7183	-45.6	7.7	0.070	0.034	1.5	3.4
4628.7317	-48.9	8.5	0.195	0.052	7.0	2.9
4628.7353	-46.6	6.1	0.091	0.041	1.2	2.5
4628.7491	-38.3	8.3	0.174	0.040	2.9	3.0
4628.7537	-42.1	5.9	0.146	0.047	6.0	3.4
4628.7618	-30.2	5.8	0.136	0.040	2.3	3.2
4628.7634	-31.7	7.1	0.185	0.043	-6.2	3.3
4628.7650	-17.3	8.3	0.087	0.036	-3.2	2.6
4628.7672	-38.7	6.7	-0.050	0.035	5.7	4.5
4628.7873	-34.5	9.4	0.075	0.039	2.4	4.5
4628.7923	-41.2	7.4	0.124	0.036	-0.6	3.1
4628.7940	-37.1	7.4	0.179	0.038	2.4	3.9
4628.7956	-37.2	7.1	0.123	0.032	0.3	3.7
4628.7972	-38.7	6.4	0.110	0.036	-2.1	3.2
4628.7988	-42.6	6.2	0.180	0.042	-6.1	3.2
4628.8005	-38.6	5.9	0.178	0.036	1.3	3.7
4628.8021	-35.9	8.1	0.122	0.034	-0.7	3.5
4628.8054	-23.4	4.7	0.134	0.033	2.8	5.2
4628.8070	-41.7	8.1	0.144	0.039	1.7	4.4
4628.8086	-31.3	7.7	0.157	0.047	-4.3	4.1
4628.8103	-45.0	7.7	0.217	0.042	-2.8	3.9
4628.8119	-39.4	8.5	0.113	0.042	-2.6	4.3
4628.8135	-40.5	6.0	0.179	0.037	-3.2	4.2
4628.8151	-47.6	6.8	0.168	0.042	-0.3	3.9
4628.8167	-46.2	6.7	0.192	0.038	-6.4	4.5
4628.8183	-35.3	10.8	0.244	0.041	-6.4	4.2

(continued)

α Tauri: CFHT 1981 time series radial velocity and equivalent width data
(continued)

JD ^a (dy) 2440000+	RV (m s ⁻¹)		$\Delta EW_{866.2}$ (pm)		$\Delta(R - I)$ (mmag)	
	value	σ	value	σ	value	σ
4628.8200	-33.3	4.4	0.157	0.035	2.1	4.5
4628.8216	-45.0	6.5	0.137	0.036	-3.6	4.4
4628.8232	-42.2	6.4	0.107	0.030	-4.0	4.4
4628.8248	-42.6	6.3	0.133	0.031	-3.2	5.3
4628.8265	-37.1	5.9	0.126	0.035	-1.6	3.8
4628.8281	-29.0	7.4	0.090	0.031	-8.0	4.3
4628.8297	-43.5	10.0	0.191	0.034	-0.3	5.2
4628.8313	-46.8	6.2	0.140	0.037	-1.4	4.5
4628.8330	-40.8	7.5	0.131	0.031	-3.6	5.1
4628.8346	-40.4	6.9	0.146	0.038	-3.4	3.7
4628.8363	-35.7	7.2	0.124	0.036	-3.8	4.7
4628.8380	-44.1	6.9	0.199	0.039	-5.7	5.2
4628.8396	-41.4	8.2	0.108	0.032	-1.4	4.1
4628.8412	-43.6	9.2	0.174	0.039	-2.5	4.5
4628.8428	-32.4	9.1	0.145	0.036	-6.7	4.9
4629.6966	16.2	14.0	-0.201	0.051	-3.0	3.5
4629.6978	29.1	7.6	-0.132	0.061	-1.6	5.9
4629.6987	21.1	10.9	-0.224	0.088	11.4	8.5
4629.6996	29.9	10.1	-0.153	0.047	5.2	3.7
4629.7005	22.8	7.7	-0.141	0.056	-3.0	6.2
4629.7014	16.1	8.4	-0.145	0.064	0.1	3.9
4629.7023	0.7	21.1	-0.283	0.048	4.9	3.0
4629.7033	7.6	6.1	-0.115	0.050	6.7	3.8
4629.7042	27.2	10.1	-0.217	0.051	1.1	2.6
4629.7051	21.3	11.4	-0.006	0.039	-3.6	3.6
4629.7060	12.7	4.9	-0.106	0.050	-2.7	4.7

(continued)

α Tauri: CFHT 1981 time series radial velocity and equivalent width data
(continued)

JD ^a (dy) 2440000+	RV (m s ⁻¹)		$\Delta EW_{866.2}$ (pm)		$\Delta(R - I)$ (mmag)	
	value	σ	value	σ	value	σ
4629.7069	10.4	8.0	-0.190	0.055	7.7	3.6
4629.7078	12.4	6.7	-0.214	0.051	-0.4	3.9
4629.7087	-1.3	9.0	-0.084	0.058	-1.5	6.1
4629.7096	31.8	5.7	-0.116	0.046	-5.3	5.8
4629.7105	14.8	6.7	-0.017	0.046	-12.5	6.0
4629.7114	16.6	5.3	-0.064	0.050	2.7	4.9
4629.7123	28.8	10.0	-0.147	0.072	3.0	4.9
4629.7132	12.9	5.7	0.120	0.052	-8.8	5.2
4629.7141	17.6	5.1	-0.052	0.057	2.8	5.0
4629.7150	4.1	11.4	-0.094	0.065	-4.5	5.5
4629.7159	39.7	12.7	-0.129	0.047	-11.0	4.6
4629.7168	-1.0	11.5	-0.141	0.052	-7.4	4.9
4629.7177	4.5	13.2	-0.080	0.051	4.6	5.2
4629.7186	30.5	12.2	-0.134	0.049	5.7	3.6
4629.7195	24.8	7.9	-0.260	0.059	1.4	3.3
4629.7205	23.1	6.2	-0.284	0.044	5.0	2.8
4629.7214	13.4	5.0	-0.243	0.044	6.2	3.1
4629.7223	5.5	9.0	-0.138	0.046	1.4	3.2
4629.7241	16.5	11.5	-0.043	0.042	-3.1	5.7
4629.7251	12.0	4.4	-0.116	0.053	0.5	3.8
4629.7262	16.7	5.4	-0.065	0.050	1.0	4.7
4629.7273	9.0	7.5	-0.207	0.052	5.1	3.4
4629.7284	2.9	11.0	-0.108	0.054	5.9	4.3
4629.7296	14.6	5.6	-0.108	0.052	-6.0	6.0
4629.7307	15.1	5.0	-0.119	0.049	-7.9	5.2
4629.7318	30.3	5.5	-0.229	0.059	7.2	4.7

(continued)

α Tauri: CFHT 1981 time series radial velocity and equivalent width data
(continued)

JD ^a (dy) 2440000+	RV (m s ⁻¹)		$\Delta EW_{866.2}$ (pm)		$\Delta(R - I)$ (mmag)	
	value	σ	value	σ	value	σ
4629.7330	20.1	7.8	-0.021	0.058	-7.2	6.9
4629.7341	18.7	4.8	-0.100	0.080	8.2	6.6
4629.7354	19.3	4.4	-0.102	0.051	2.6	4.9
4629.7366	12.2	10.1	-0.109	0.051	-3.3	5.9
4629.7377	23.4	10.4	-0.180	0.050	-3.0	5.1
4629.7389	31.9	16.5	-0.030	0.037	0.9	4.4
4629.7400	20.2	6.6	-0.114	0.046	4.8	3.7
4629.7411	18.8	5.4	-0.147	0.043	4.8	4.0
4629.7422	18.3	5.2	-0.105	0.059	7.9	4.8
4629.7434	13.9	6.0	-0.137	0.047	-3.4	4.6
4629.7445	14.1	3.9	-0.108	0.040	-7.7	3.9
4629.7456	24.7	5.4	-0.082	0.055	5.0	4.7
4629.7467	30.6	9.0	-0.125	0.053	4.8	3.6
4629.7478	32.6	6.9	-0.099	0.052	1.7	3.2
4629.7489	19.3	9.1	-0.116	0.059	6.3	5.1
4629.7501	18.6	5.7	-0.143	0.047	-3.6	4.7
4629.7512	8.5	8.5	-0.124	0.037	1.1	3.8
4629.7523	9.8	6.7	-0.225	0.042	-1.0	3.3
4629.7534	4.2	13.1	0.215	0.064	-7.2	7.0
4629.7546	4.8	8.1	-0.126	0.050	3.1	5.0
4629.7557	18.2	5.7	-0.039	0.048	-7.9	6.4
4629.7568	10.4	6.9	-0.156	0.041	-3.1	4.4
4629.7731	9.4	11.8	-0.095	0.045	-3.9	5.6
4629.7742	21.9	5.2	-0.097	0.036	-7.0	6.0
4629.7754	13.1	9.7	-0.017	0.045	-2.6	6.8
4629.7765	15.7	8.3	-0.041	0.054	-18.7	6.1

(continued)

α Tauri: CFHT 1981 time series radial velocity and equivalent width data
(continued)

JD ^a (dy) 2440000+	RV (m s ⁻¹)		$\Delta EW_{866.2}$ (pm)		$\Delta(R - I)$ (mmag)	
	value	σ	value	σ	value	σ
4629.7776	22.3	7.8	0.103	0.052	-0.9	6.5
4629.7787	16.5	7.9	0.042	0.045	-3.1	6.9
4629.7799	20.9	11.9	-0.043	0.051	-0.4	7.9
4629.7810	26.0	9.4	-0.036	0.050	-11.2	3.7
4629.7821	18.7	7.8	-0.070	0.049	-21.9	5.8
4629.7832	30.9	11.8	-0.086	0.059	-5.0	9.7
4629.7844	30.6	8.8	-0.216	0.041	-0.1	3.3
4629.7855	25.8	10.3	-0.075	0.055	-3.8	5.8
4629.7866	36.2	11.5	-0.135	0.052	0.8	6.2
4629.7877	13.8	12.7	-0.178	0.040	4.1	3.6
4629.7889	18.0	7.8	-0.053	0.046	-14.1	4.7
4629.7900	18.9	10.9	-0.116	0.046	-15.2	4.7
4629.7911	35.6	7.9	0.056	0.058	-7.0	5.6
4629.7923	16.3	8.1	-0.125	0.049	-12.7	3.2
4629.7934	22.7	10.0	-0.175	0.057	1.1	5.3
4629.7945	21.3	10.0	-0.118	0.046	-1.1	5.5
4629.7957	21.2	7.8	-0.034	0.050	-23.7	9.2
4629.7968	18.0	9.4	0.043	0.049	30.9	9.7
4629.7979	22.9	11.1	-0.201	0.056	35.2	10.3
4629.7990	18.2	8.7	-0.034	0.053	28.5	7.7
4629.8002	29.4	9.9	-0.241	0.055	31.6	9.2
4629.8013	10.0	6.9	-0.006	0.047	18.5	8.9
4629.8024	29.4	8.8	-0.197	0.040	31.0	8.8
4629.8035	21.7	7.9	0.028	0.064	30.0	9.2
4629.8047	23.0	7.2	-0.275	0.049	26.8	8.3
4629.8058	40.1	10.3	-0.097	0.056	38.5	8.1
4629.8069	22.8	7.3	-0.251	0.062	18.0	10.5
4629.8080	22.2	8.1	-0.029	0.055	10.1	9.2
4629.8091	24.9	5.9	0.100	0.061	2.1	6.9
4629.8102	38.6	7.2	-0.020	0.058	8.0	6.6
4629.8114	8.5	10.1	0.009	0.051	15.0	9.2

^a Corrected for the light travel time to the barycenter of the solar system

Table A.8: α Tauri: DAO radial velocity data

JD ^a (dy) 2440000+	RV (m s ⁻¹)		JD ^a (dy) 2440000+	RV (m s ⁻¹)	
	value	σ		value	σ
8563.8741	-142.2	35.9	8955.8444	231.9	33.1
8580.8506	11.3	60.8	8955.8499	212.9	38.7
8621.8210	33.8	15.0	8957.8806	319.5	37.8
8638.7144	-6.4	13.2	9003.7780	304.2	12.1
8639.6832	-68.9	19.0	9004.5586	282.3	13.8
8640.7418	-29.8	13.4	9005.5412	267.9	10.5
8641.6384	-44.6	13.4	9006.6398	230.3	18.9
8643.5988	-71.8	18.1	9053.5842	114.1	31.8
8647.7063	44.3	22.0	9053.5915	81.2	20.8
8828.9868	158.6	36.9	9077.6123	341.5	22.7
8829.9920	248.2	34.4	9077.6241	350.6	27.7
8831.0110	173.7	31.6	9079.6309	329.3	17.0
8831.0170	181.9	29.0	9081.6134	295.1	29.0
8831.9793	115.0	25.7	9081.6254	302.1	16.8
8833.0138	170.4	23.5	9089.6245	255.3	72.0
8833.0184	144.8	23.1	9089.6352	281.6	30.6
8877.9797	345.4	36.9	9187.0176	-23.2	25.5
8879.0502	133.8	31.9	9220.0433	107.2	22.7
8881.0525	239.8	20.6	9220.0463	92.0	19.0
8919.7802	267.7	34.0	9225.0494	-3.0	34.8
8921.0926	253.5	27.3	9226.0483	-26.2	30.7
8922.0433	262.1	24.5			

^a Corrected for light travel time to barycenter of solar system.

Data for JD's 8563.5, 8638.5, 8639.5, 8640.5, 8641.5, 8643.5, and 8647.5 are nightly means.

Table A.9: α Tauri: DAO 1992 time series radial velocity data

JD ^a (dy)	RV (m s ⁻¹)		JD ^a (dy)	RV (m s ⁻¹)	
2440000+	value	σ	2440000+	value	σ
8638.6098	-1.1	15.0	8640.8840	-38.1	16.1
8638.6211	-4.9	15.1	8641.5448	-55.5	14.4
8638.6271	-11.2	14.3	8641.5591	-46.4	12.5
8638.7550	-10.8	11.6	8641.5674	-55.0	13.1
8638.7809	-1.6	11.9	8641.5782	-48.5	13.7
8638.7980	-10.2	11.6	8641.5869	-36.5	13.4
8638.8089	-4.8	12.8	8641.5986	-39.2	15.0
8639.5205	-111.1	55.4	8641.6090	-50.3	16.4
8639.5487	-61.3	11.0	8641.6164	-41.5	13.7
8639.5772	-65.6	8.8	8641.6743	-48.5	12.9
8639.5910	-61.0	8.0	8641.6826	-39.6	11.9
8639.6883	-86.9	58.3	8641.6929	-40.3	10.5
8639.6965	-62.6	11.5	8641.7897	-46.0	15.1
8639.7066	-56.9	14.4	8641.8000	-32.9	12.2
8639.7193	-63.3	13.5	8641.8137	-37.0	8.4
8639.7307	-55.6	11.0	8641.8682	-41.0	6.2
8639.7439	-56.6	13.9	8641.8872	-28.7	8.5
8639.8283	-67.3	10.4	8643.5518	-46.4	19.6
8639.8473	-78.2	11.5	8643.5668	-49.9	8.1
8640.6028	8.0	18.0	8643.5791	-52.6	8.3
8640.6486	-29.8	11.9	8643.5950	-80.8	14.2
8640.6682	-22.6	10.8	8643.6086	-75.5	13.0
8640.6789	-44.6	16.5	8643.6912	-125.3	45.7
8640.7174	-43.2	12.6	8647.6372	38.1	25.6
8640.7264	-51.8	13.8	8647.6459	37.3	16.4
8640.7356	-46.5	14.8	8647.6543	35.6	24.5
8640.7420	-35.0	16.1	8647.7334	29.0	21.4
8640.7715	-28.4	9.9	8647.7442	51.3	31.7
8640.8080	-26.0	14.0	8647.7572	60.0	17.8
8640.8198	-25.8	9.3	8647.7721	59.0	16.5
8640.8406	-4.1	10.3			

^a Corrected for the light travel time to the barycenter of the solar system

Table A.10: ϵ Pegasi: CFHT radial velocity and equivalent width data

JD ^a (dy) 2440000+	RV (m s ⁻¹)		$\Delta EW_{866.2}$ (pm)		$\Delta(R - I)$ (mmag)	
	value	σ	value	σ	value	σ
4754.1159	77.3	21.2	-2.388	0.304	4.4	5.7
4770.1246	66.7	18.7	-2.484	0.308	-1.0	4.5
4771.0930	81.0	16.8	-2.660	0.313	-6.6	6.4
4865.8370	342.4	10.8	-2.706	0.351	-3.7	7.6
4926.8389	144.8	26.2	-1.690	0.303	5.2	9.8
4957.8048	137.3	20.5	-2.403	0.339	-5.5	8.6
5148.0689	166.8	16.9	-2.540	0.368	0.8	8.0
5166.0315	43.7	17.0	-1.481	0.281	3.2	4.6
5276.8733	836.6	19.5	-1.251	0.272	-1.3	7.6
5459.1307	440.9	21.4				
5712.7005	-386.7	10.8	-1.593	0.282	-15.5	7.0
5811.1073	-28.4	12.2	-1.772	0.310	1.1	6.0
5811.1119	-28.0	11.5	-1.866	0.311	2.1	6.1
5865.1216	341.7	14.8	-2.157	0.298	9.7	5.5
5865.1253	350.0	13.1	-2.079	0.296	9.5	5.3
6048.7214	567.2	13.5	-0.861	0.196	-0.3	6.6
6216.1395	-645.5	17.8				
6216.1425	-657.5	16.7				
6283.9765	85.7	18.5	0.423	0.060	-0.3	5.5
6283.9789	62.4	17.1	0.598	0.054	-6.7	7.0
6283.9807	58.6	23.4	0.582	0.045	-4.8	5.5
6393.7918	166.7	16.1	-0.749	0.208	13.1	4.7
7371.9690	-505.6	17.6	-0.173	0.191	4.5	5.6
7371.9705	-506.6	15.4	-0.195	0.184	8.2	6.8
7454.8004	311.9	23.4	0.733	0.101	7.1	7.4
7700.1016	-177.1	15.0	0.140	0.131	2.0	5.5

(continued)

ϵ Pegasi: CFHT radial velocity and equivalent width data (continued)

JD ^a (dy) 2440000+	RV (m s ⁻¹)		$\Delta EW_{866.2}$ (pm)		$\Delta(R - I)$ (mmag)	
	value	σ	value	σ	value	σ
7787.9870	-247.0	11.3	-0.304	0.404	-3.0	5.5
7787.9897	-246.5	11.2	-0.480	0.414	1.0	4.6
7788.8809	-236.1	10.4	-0.432	0.373	-13.5	7.3
7788.8831	-247.8	9.6	-0.404	0.364	-1.6	5.9
8112.9592	-479.0	12.0	0.193	0.135	-16.6	7.9
8113.9712	-470.0	13.4	0.350	0.111	-17.9	7.9
8406.0900	343.4	13.7	-0.981	0.189	5.0	6.3
8406.0928	339.8	15.6	-0.883	0.176	3.5	6.4
8406.0952	351.9	16.5	-0.856	0.174	5.1	6.4
8406.0976	336.5	16.1	-0.898	0.181	5.6	6.1
8471.8549	840.9	17.0	-3.131	0.326	-0.1	8.1
8471.8570	862.0	19.1	-3.121	0.317	12.0	9.3
8471.8587	843.8	18.1	-3.155	0.317	3.1	10.8
8471.8603	848.1	18.3	-3.109	0.315	0.7	10.4
8471.8620	856.3	18.3	-3.093	0.314	9.5	8.7
8578.7903	-182.2	13.3	-2.203	0.275	-10.7	7.4
8578.7930	-171.4	12.9	-2.250	0.280	-14.4	8.3
8818.0630	-269.3	12.1	-0.634	0.201	-10.1	7.4
8818.0670	-274.8	12.6	-0.673	0.205	-7.5	6.9
8818.0704	-267.4	11.0	-0.710	0.208	-14.9	6.7

^a Corrected for the light travel time to the barycenter of the solar system.

Table A.11: ϵ Pegasi: DAO radial velocity data

JD ^a (dy) 2440000+	RV (m s ⁻¹)		JD ^a (dy) 2440000+	RV (m s ⁻¹)	
	value	σ		value	σ
6232.9089	-351.1	29.2	8832.8764	15.2	34.8
6233.9105	-328.2	25.7	8880.7998	239.7	36.2
8444.9593	892.0	51.6	8920.7811	460.5	35.3
8812.9692	-79.2	37.0	9186.0040	-79.4	37.7
8828.8511	85.7	26.5	9224.8925	1.9	67.6

^a Corrected for the light travel time to the barycenter of the solar system.

Appendix B

Derivatives For $W_0'(\chi)$ Coefficients

The calculation of the derivatives used in forming the $W_0'(\chi)$ coefficients is entirely consistent with the difference equation method we use to solve the equation of transfer. At the user's discretion, the difference equations can be solved using either the fourth-order Hermitian (Auer, 1976), the second-order spline collocation (Kunasz and Hummer, 1974), or the original second-order Feautrier (Mihalas, 1978) method. For simplicity, we demonstrate the derivative calculation using the original Feautrier method, and the reader is referred to Mihalas (1978) for related equations. The generalization to the other methods is straightforward.

We define $I_d(\mu_i)$ as the monochromatic specific intensity at depth d and angle $\cos^{-1} \mu_i$, for $i = 1, \dots, N$, where N is the number of discrete angles used. Following M78, Eq. (6-12), we define the symmetric average of the specific intensity:

$$u_d(\mu_i) \equiv \frac{1}{2}[I_d(\mu_i) + I_d(-\mu_i)]. \quad (\text{B.1})$$

Since all quantities are monochromatic, we have dropped the wavelength subscripts. This leads to the second order equation of transfer for u_d [M78, Eq. (6-17)]:

$$\mu^2 \left[\frac{\partial^2 u_d(\mu_i)}{\partial \tau_d^2} \right] = u_d(\mu_i) - S_d . \quad (\text{B.2})$$

We assume a simplified source function that allows for continuum scattering:

$$\begin{aligned} S_d &= \alpha_d \int_0^1 u_d(\mu) d\mu + (1 - \alpha_d) B(T_d) \\ &= \alpha_d \sum_k w_k u_{d,k} + (1 - \alpha_d) B(T_d) , \end{aligned} \quad (\text{B.3})$$

where w_k is the angle-integration weight for the k th angle point. In this equation, $B(T_d)$ is the monochromatic Planck function evaluated at temperature T_d and α_d is the ratio of the continuum scattering to the total opacity.

To aid in the discretization of the equation of transfer [Eq. (B.2)], we define:

$$\Delta \tau_{\pm} = \frac{1}{2} \left[\left(\frac{\kappa}{\kappa_R} \right)_d + \left(\frac{\kappa}{\kappa_R} \right)_{d\pm 1} \right] |(\tau_R)_{d\pm 1} - (\tau_R)_d| , \quad (\text{B.4})$$

where κ is the total opacity, κ_R is the Rosseland mean opacity, and τ_R is the corresponding optical depth. We also define:

$$\Delta \tau_0 = \frac{1}{2} (\Delta \tau_- + \Delta \tau_+) . \quad (\text{B.5})$$

The discretized form of the equation of transfer [M78, Eq. (6-30)] is then given as:

$$\begin{aligned} - \left(\frac{\mu_i^2}{\Delta \tau_0 \Delta \tau_-} \right) u_{d-1,i} + \left[1 + \frac{\mu_i^2}{\Delta \tau_0} \left(\frac{1}{\Delta \tau_-} + \frac{1}{\Delta \tau_+} \right) \right] u_{d,i} \\ - \alpha_d \sum_k w_k u_{d,k} - \left(\frac{\mu_i^2}{\Delta \tau_0 \Delta \tau_+} \right) u_{d+1,i} = L_{di} . \end{aligned} \quad (\text{B.6})$$

The thermal source terms are contained in \vec{L}_d :

$$L_{di} = (1 - \alpha_d)B(T_d) . \quad (\text{B.7})$$

This leads to the matrix equation [M78, Eq. (6-31)]:

$$-\vec{A}_d\vec{u}_{d-1} + \vec{B}_d\vec{u}_d - \vec{C}_d\vec{u}_{d+1} = \vec{L}_d . \quad (\text{B.8})$$

The diagonal components of \vec{A}_d , \vec{C}_d and \vec{B}_d are:

$$(A_d)_{ii} = \frac{\mu_i^2}{\Delta\tau_0} \frac{1}{\Delta\tau_-} , \quad (\text{B.9})$$

$$(C_d)_{ii} = \frac{\mu_i^2}{\Delta\tau_0} \frac{1}{\Delta\tau_+} , \quad (\text{B.10})$$

and

$$(B_d)_{ii} = 1 + (A_d)_{ii} + (C_d)_{ii} - \alpha_d w_i . \quad (\text{B.11})$$

In the original Feautrier method, the off-diagonal components of \vec{A}_d and \vec{C}_d are 0. The off-diagonal components of \vec{B}_d are:

$$(B_d)_{ik} = -\alpha_d w_k . \quad (\text{B.12})$$

We solve the difference equations starting at depth because no back-substitution is needed when we are concerned with the surface flux only.

With this scheme, the vector \vec{u}_d is calculated from

$$\vec{u}_d = \vec{D}_d\vec{u}_{d-1} + \vec{v}_d , \quad (\text{B.13})$$

where \vec{D}_d and \vec{v}_d are defined by

$$(\vec{B}_d - \vec{C}_d\vec{D}_{d+1})\vec{D}_d = \vec{A}_d \quad (\text{B.14})$$

$$(\vec{B}_d - \vec{C}_d \vec{D}_{d+1}) \vec{v}_d = (\vec{L}_d + \vec{C}_d \vec{v}_{d+1}) \quad (\text{B.15})$$

for depths $d = D - 1, \dots, 2$ (D being the lower boundary). These equations have a different form than M78, Eqs. (6-39)-(6-41), because of the reverse order of solution. Special forms of Eqs. (B.6) through (B.15) are required at the boundaries (see A76 and M78).

Once the solution of Eqs. (B.14) and (B.15) is completed, we calculate the surface flux:

$$H = \int_0^1 \mu u(\mu) d\mu = \sum_{k=1}^N \mu_k w_k \nu_{1k}. \quad (\text{B.16})$$

The corresponding derivative is given by

$$\frac{\partial H}{\partial g f} = \sum_{k=1}^N \mu_k w_k \frac{\partial \nu_{1k}}{\partial g f}. \quad (\text{B.17})$$

Using the chain rule on Eqs. (B.14) and (B.15), we derive

$$\begin{aligned} & [\vec{B}_d - \vec{C}_d \vec{D}_{d+1}] \frac{\partial \vec{D}_d}{\partial g f} = \\ & \frac{\partial \vec{A}_d}{\partial g f} - \left[\frac{\partial \vec{B}_d}{\partial g f} - \vec{C}_d \frac{\partial \vec{D}_{d+1}}{\partial g f} - \frac{\partial \vec{C}_d}{\partial g f} \vec{D}_{d+1} \right] \vec{D}_d \end{aligned} \quad (\text{B.18})$$

and

$$\begin{aligned} & [\vec{B}_d - \vec{C}_d \vec{D}_{d+1}] \frac{\partial \vec{v}_d}{\partial g f} = \frac{\partial \vec{L}_d}{\partial g f} + \vec{C}_d \frac{\partial \vec{v}_{d+1}}{\partial g f} + \frac{\partial \vec{C}_d}{\partial g f} \vec{v}_{d+1} \\ & - \left[\frac{\partial \vec{B}_d}{\partial g f} - \vec{C}_d \frac{\partial \vec{D}_{d+1}}{\partial g f} - \frac{\partial \vec{C}_d}{\partial g f} \vec{D}_{d+1} \right] \vec{v}_d. \end{aligned} \quad (\text{B.19})$$

We show the partial derivatives for the components of \vec{A}_d as an example of the other matrices:

$$\frac{\partial (A_d)_{ii}}{\partial g f} = \frac{\partial (A_d)_{ii}}{\partial \Delta \tau_+} \frac{\partial \Delta \tau_+}{\partial g f} + \frac{\partial (A_d)_{ii}}{\partial \Delta \tau_-} \frac{\partial \Delta \tau_-}{\partial g f}, \quad (\text{B.20})$$

where

$$\frac{\partial(A_d)_{ii}}{\partial\Delta\tau_+} = -\frac{2\mu_i^2}{\Delta\tau_-(\Delta\tau_+ + \Delta\tau_-)^2}, \quad (\text{B.21})$$

$$\frac{\partial(A_d)_{ii}}{\partial\Delta\tau_-} = -\frac{2\mu_i^2(\Delta\tau_+ + 2\Delta\tau_-)}{\Delta\tau_-^2(\Delta\tau_+ + \Delta\tau_-)^2}, \quad (\text{B.22})$$

and

$$\frac{\partial\Delta\tau_{\pm}}{\partial gf} = \frac{1}{2} \left[\left(\frac{\partial\kappa/\partial gf}{\kappa_R} \right)_d + \left(\frac{\partial\kappa/\partial gf}{\kappa_R} \right)_{d\pm 1} \right] \times |(\tau_R)_{d\pm 1} - (\tau_R)_d|. \quad (\text{B.23})$$

Similar logic is used for the other derivatives. Note that once Eqs. (B.14) and (B.15) are solved at depth d , the entire right hand sides of Eqs. (B.18) and (B.19) are known and the solution for the partial derivatives follows. Eventually, the calculations reach the stellar surface, the boundary conditions are solved, and Eqs. (3.8) and (B.17) are used to determine the coefficients $W'_0(\chi)$.

As shown above, in principle this method can be formulated for a scattering continuum. In the examples presented in the text, we treated scattering as ordinary absorption (without stimulated emission) because it makes little difference in the results for cool stars of solar abundance. Under this treatment, $\alpha = 0$ and all of the Feautrier matrices become diagonal; thus, the derivative matrices are also diagonal and simple multiplication and division may be used.

Appendix C

Solar Intensity Atlas vs. Synthetic Spectrum

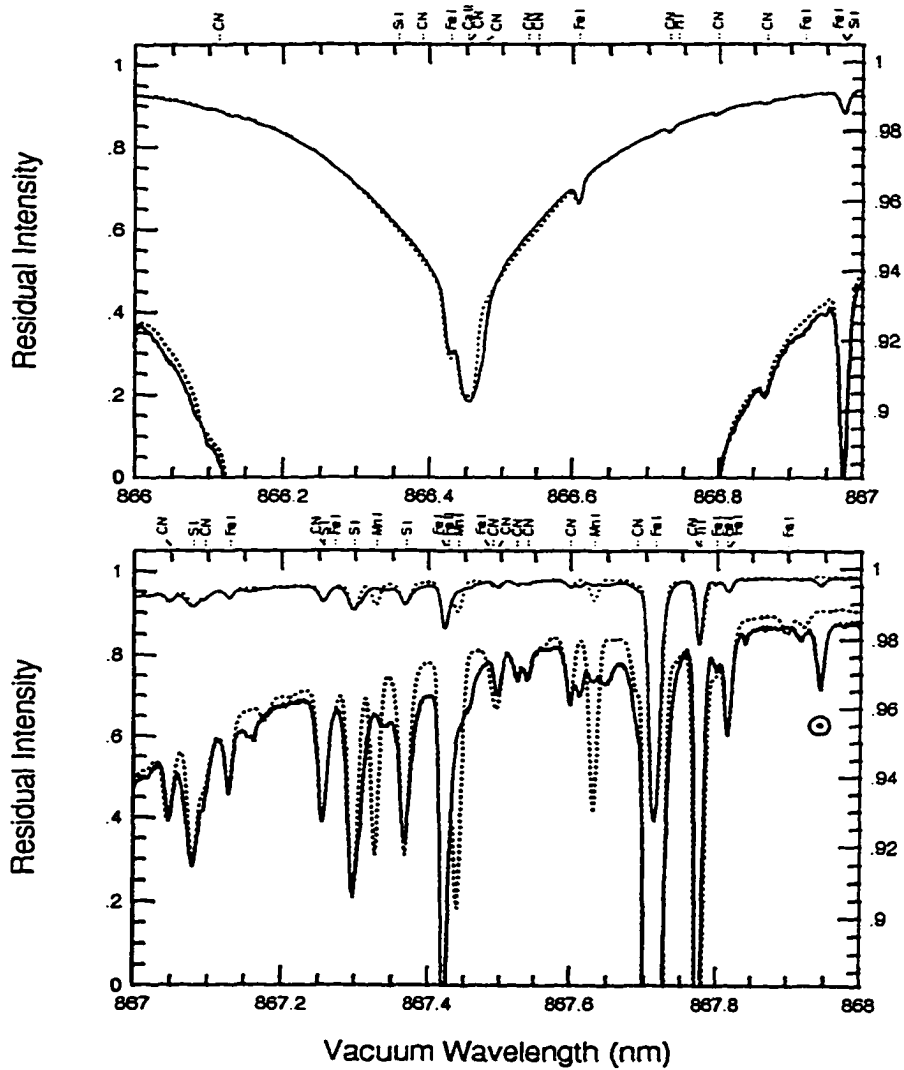


Figure C.2: Continuation of the comparison of the residual intensity from the solar central intensity atlas (solid line) and the synthetic intensity spectrum (dotted line).

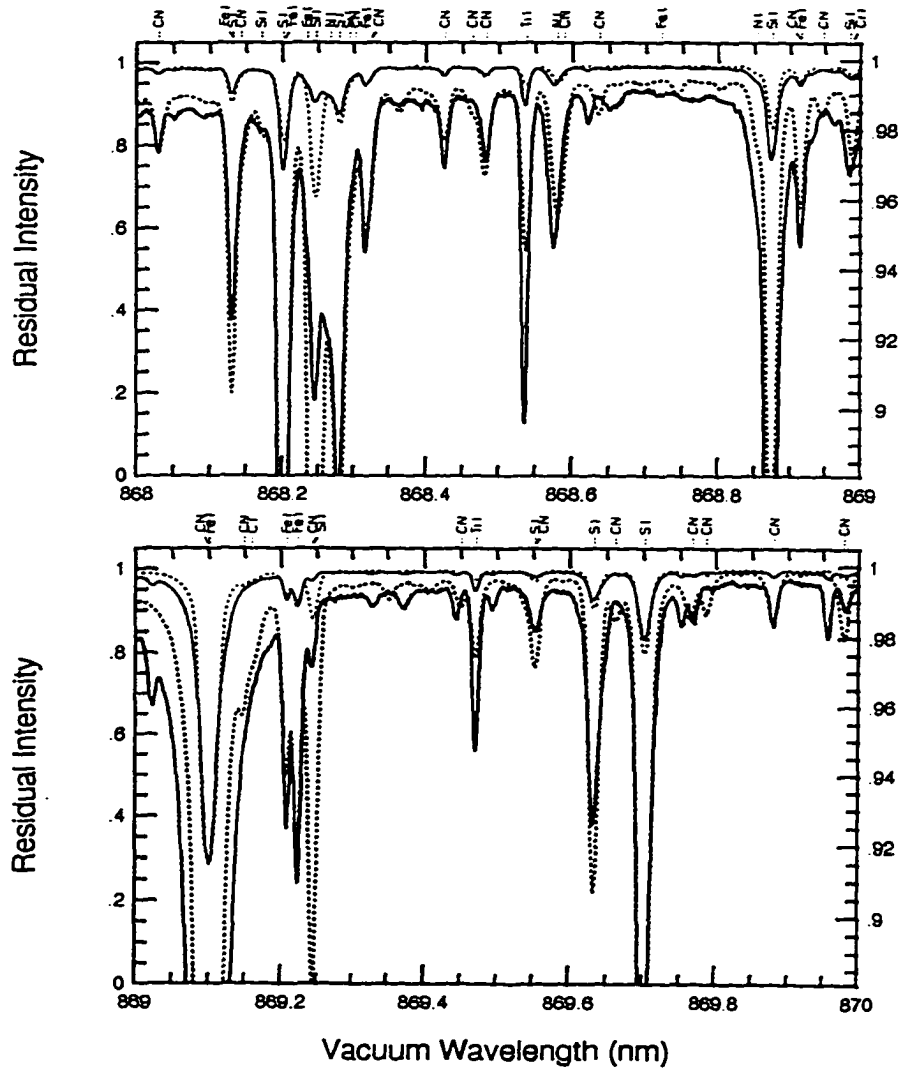


Figure C.3: Continuation of the comparison of the residual intensity from the solar central intensity atlas (solid line) and the synthetic intensity spectrum (dotted line).

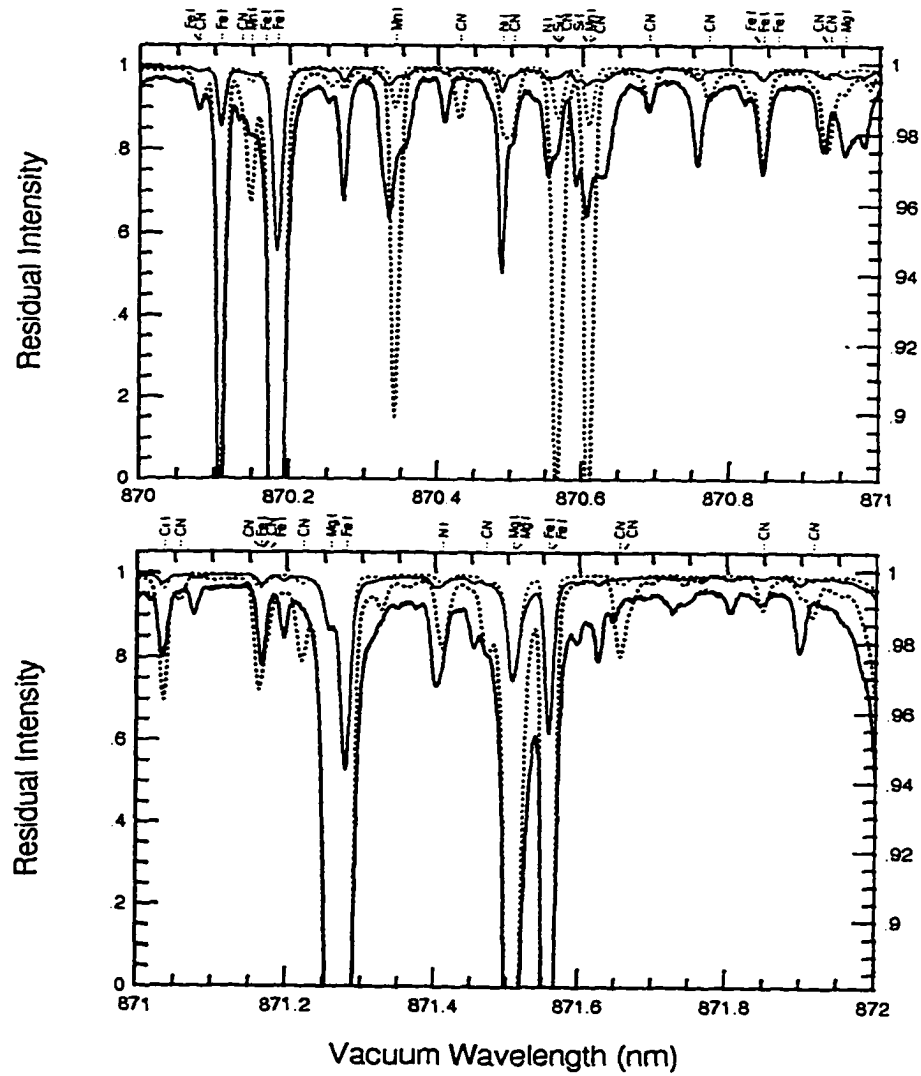


Figure C.4: Continuation of the comparison of the residual intensity from the solar central intensity atlas (solid line) and the synthetic intensity spectrum (dotted line).

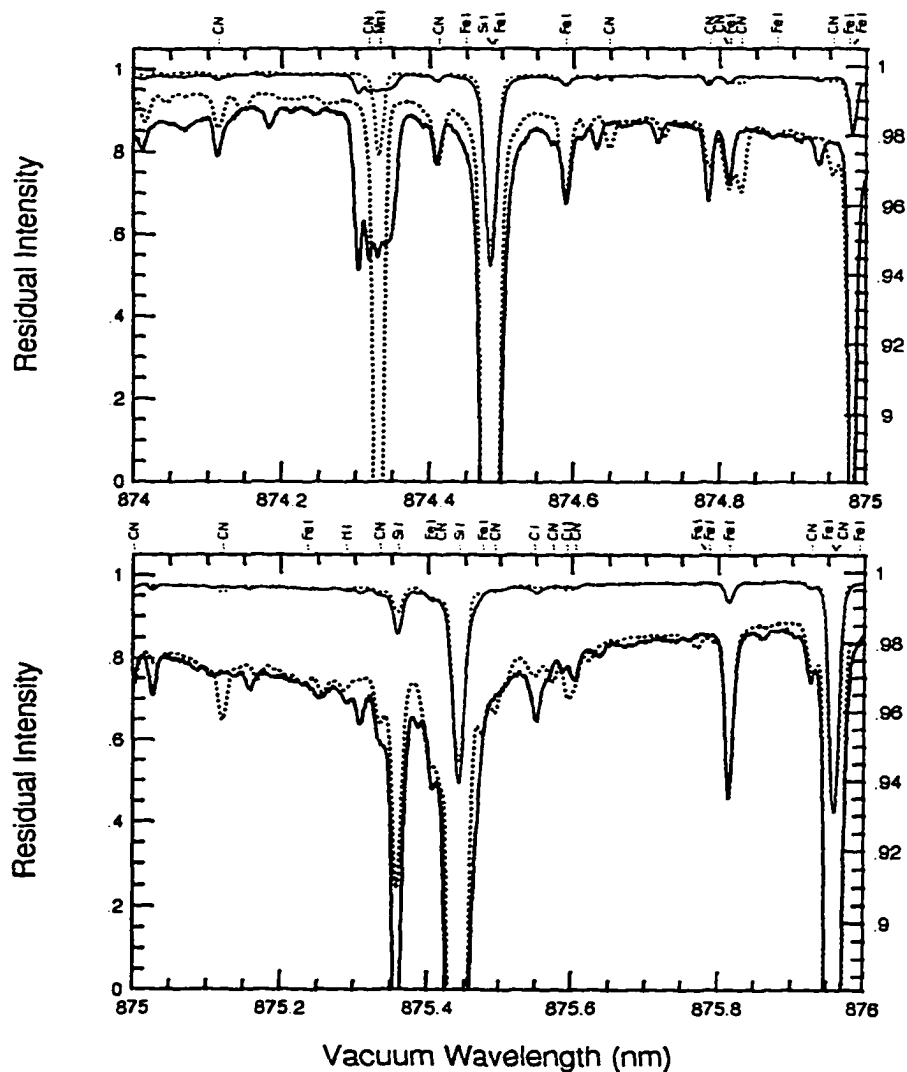


Figure C.6: Continuation of the comparison of the residual intensity from the solar central intensity atlas (solid line) and the synthetic intensity spectrum (dotted line).

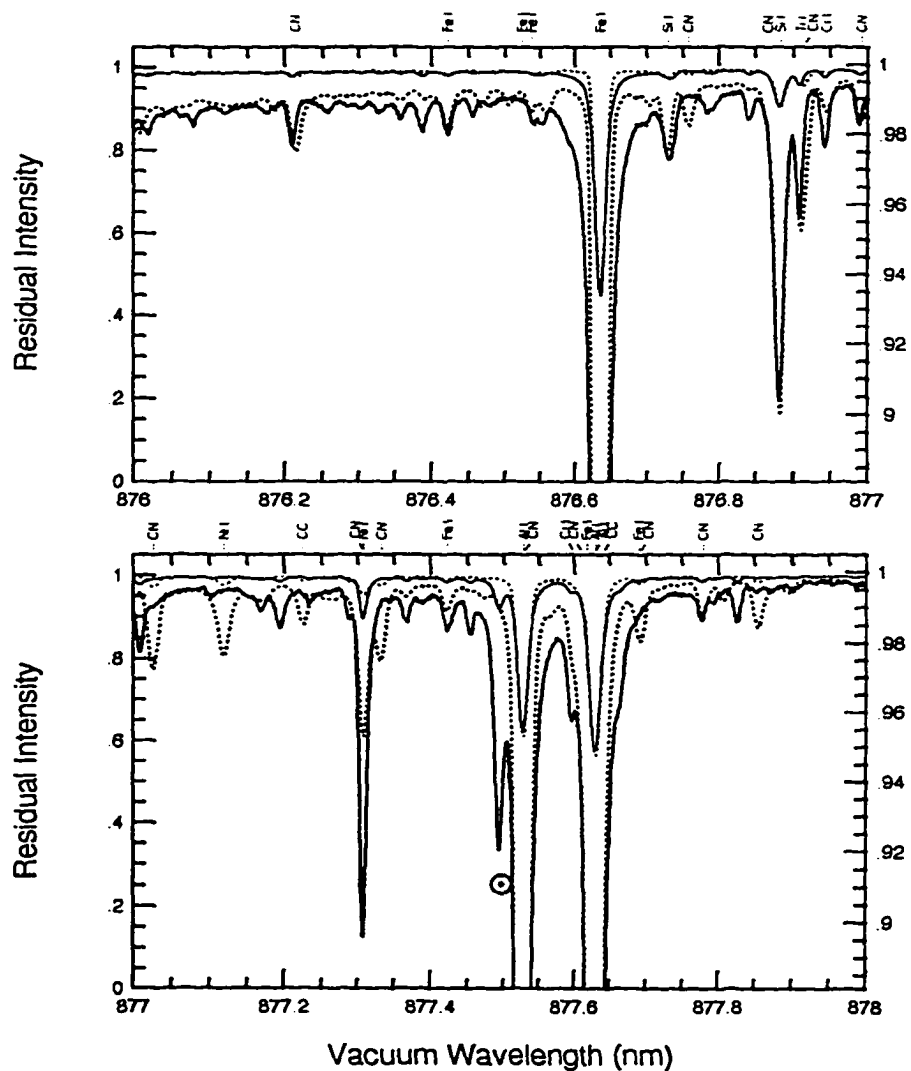


Figure C.7: Continuation of the comparison of the residual intensity from the solar central intensity atlas (solid line) and the synthetic intensity spectrum (dotted line).

Appendix D

Pre-SSynth Manual Pages

The pre-SSynth manual example reproduced on the following pages is shown in the format produced by the Unix operating system. The manual pages provide a convenient, flexible means of providing all of the information needed for experienced or new users of the SSynth programs. These pages will be updated as the spectrum synthesis programs become more streamlined and efficient. A copy of all of the manual pages for the pre-SSynth and SSynth programs is available in the physics reading room (Elliott 105) and via anonymous FTP:

`coho.phys.uvic.ca`

in the directory: `pub/larson/ssynthman`. Within the Physics and Astronomy Department, the manual pages can also be accessed on-line on the Sun system through the command:

`man -M /min2/home/larson/ssynth/man procedure`

Manual pages for the post-SSynth process are planned for the near future.

NAME

PRESYNTH - summary of procedures used to preprocess the line lists used in synthetic spectra calculations.

DISCLAIMER

These programs should not be used blindly. They assume the user has at least a basic knowledge of the wavelength interval being synthesized (that is, the strong wavelengths in and around the region, species which may affect the spectral region, etc.), and of stellar atmospheres, radiation transfer, and the equation of state.

DESCRIPTION

The "presynth" routines consist of a number of preliminary steps which are outlined briefly here. The user should refer to the specific manual pages for more details on running the individual C-shell executable scripts.

In general, one should reserve a sizeable (approx. 1 megabyte per Angstrom being extracted) scratch-disk allocation to process the line lists as duplication of the line lists is unavoidable.

presynth0k.csh -- select subsample from Kurucz CD-ROMs

presynth0j.csh -- select subsample from Jorgensen SCAN tapes

presynth1k.csh -- add and/or interpret broadening parameters, reformat list, summarize line comments, interpret molecular codes

presynth1j.csh -- add broadening coefficients, separate isotopic lines, reformat list, interpret molecular codes

presynth2.csh -- merge Kurucz and Jorgensen CN linelists; sort and concatenate atomic and molecular line lists

hazelist.csh -- generate an artificial line list from the whole line list for use in deriving the equivalent width coefficients; script calls presynth3.csh

presynth3.csh -- convert ASCII format to binary (96-byte/line) format for full line list; for artificial line list, when automatically called from hazelist.csh, step also converts the data to 104-byte/line (but no sorting)

presynth4.csh -- combines a number of executable c-shell scripts to implement the line-elimination method,

which removes the user-defined "ultraweak" lines from the line list

linehaze.csh -- a modified SSynth run which calculates the equivalent width coefficients

tabewcoeff.csh -- EW coefficients tabulated as a function of species and elo at a given central wavelength

calcew.csh -- program reads the complete line list, combines each line's gf value with the interpolated EW coefficient value to calculate the EW; accumulated blocking determined and line list filtered according to a preset line-blocking error; lines marked according to line strength. Presort called to add additional binary data and sort on the three fields and by segment for the final preparation of the line list for ssynth_main.csh

CONTROL FILES

presynth0k.csh:

rcd1lines.cnt rcd18lines.cnt rcd23lines.cnt

presynth0j.csh: rjorg.cnt

presynth1k.csh:

rcd1lines.cnt rcd18lines.cnt rcd23lines.cnt

presynth1j.csh: rjorg.cnt

presynth2.csh: none

hazelist.csh: program creates control file

presynth3.csh: none for complete ASCII line list (no sort)

presynth4.csh:

scale.cnt ss_haze.cnt accblk_lim.cnt linenviron.cnt
newatmos.cnt

DIRECTORY STRUCTURE

In your root .cshrc file, insert the following line (after all primary paths): source {yourdirectoryname}/.cshrc_ssynth

In your root .login file, insert the following line (after all primary paths): source {yourdirectoryname}/.login_ssynth

The c-shell executables expect an environment-set directory structure. The following example should be used to set the directory environments with the appropriate user-defined directories substituted where needed.

CONFERENCES, PUBLICATIONS, REPORTS

Conference Presentations (non-refereed)

- Larson, A. M., Vandenberg, D. A., and DePropris, R. 1996, "The Effect of Rotation on the Luminosity Functions of Globular Clusters," (poster), B.A.A.S., January, 1996
- Walker, G. A. H., Larson, A. M., Irwin, A. W., Yang, S. L. S., and Walker, A. R. 1996, "Intriguing, Low-amplitude Periodicity in the Radial Velocities of δ Sagittarii," (poster), B.A.A.S., January, 1996
- Larson, A. M., Irwin, A. W., Yang, S. L. S., Goodenough, C., Walker, G. A. H., Bohlender, D. A., and Walker, A. R. 1993, "The RV Variability of Yellow Giants," in IAU Colloquium No. 139, *New Perspectives on Stellar Pulsation and Pulsating Variable Stars*, (eds.) J. M. Nemec and J. M. Matthews (Cambridge, Cambridge University), p. 384
- Larson, A. M., and Irwin, A. W., 1995, "A Tabular Approach for Calculating Line Haze in Stellar Spectra", in *Proceedings of the Workshop on Laboratory and Astronomical High Resolution Spectra*, (eds.) A. J. Sauval, R. J. Blomme, N. Grevasse (ASP Publications, San Francisco), p. 561
- Yang, S. L. S., Larson, A. M., Irwin, A. W., Goodenough, C., Walker, G. A. H., Walker, A. R. and Bohlender, D. A. 1993, "The HF Precise Radial Velocity Programme at DAO," in IAU Colloquium No. 139, *New Perspectives on Stellar Pulsation and Pulsating Variable Stars*, (eds.) J. M. Nemec and J. M. Matthews (Cambridge, Cambridge University), p. 383

Journals, Reports:

- Larson, A. M., Irwin, A. W., Yang, S. L. S., Goodenough, C., Walker, G. A. H., Walker, A. R., and Bohlender, D. A. 1993, "A Ca II 8662 Index of Chromospheric Activity: the Case of 61 Cygni A," *PASP*, 105, 332
- Larson, A. M., Irwin, A. W., Yang, S. L. S., Goodenough, C., Walker, G. A. H., Walker, A. R., and Bohlender, D. A. 1993, "A Low-Amplitude Periodicity in the Radial Velocity and Chromospheric Emission of Beta Geminorum," *PASP*, 105, 825
- Larson, A. M. and Irwin, A. W., 1996, "An Efficient Method for Dealing with Line Haze in Stellar Spectra," *A&AS*, 117, 189
- Robb, R. M., Ouellette, J., and Larson, A. 1995, "Archival Hubble Space Telescope Observations of IC4182," *JRASC*, 89, 161
- Walker, G. A. H., Bohlender, D. A., Walker, A. R., Irwin, A. W., Yang, S. L. S., and Larson, A. M. 1992, "Gamma Cephei: Rotation or Planetary Companion?" *ApJ*, 396, L91

Walker, G. A. H., Walker, A. R., Irwin, A. W., Larson, A. M., Yang, S. L. S., and Richardson, D., 1995, "A Search for Jupiter-Mass Companions to Nearby Stars," *Icarus*, 116, 359

Yang, S. L. S., Larson, A. M., Irwin, A. W., Walker, G. A. H., and Walker, A. R. 1993, "Alpha Orionis (Betelgeuse)" IAU Circular #5716

Work in progress

Larson, A. M., Irwin, A. W., Yang, S. L. S., Walker, G. A. H., and Walker, A. R. 1996, "Intriguing Variability in the Radial Velocity, Chromospheric Emission, and $(R - I)$ of δ Sagittarii" (submitted)

VandenBerg, D. A., Larson, A. M., and DePropris, R. 1996, "The Effect of Rotation on Globular Cluster Luminosity Functions"

Larson, A. M. *et al.* 1996, "Detection of a Low-Amplitude, 1.84-dy Period in the Relative Radial Velocities of α Tauri"